Spectroscopic and Structural Analysis of Oxygen-Activating Nonheme Diiron Enzymes and Related Synthetic Models

A Dissertation
SUBMITTED TO THE FACULTY OF
UNIVERSITY OF MINNESOTA
BY

Andrew James Jasniewski

IN PARTIAL FULFILLMENT OF THE REQUIREMENTS
FOR THE DEGREE OF
DOCTOR OF PHILOSOPHY

Professor Lawrence Que, Jr., Adviser

May 2017

Acknowledgements

I would first like to thank my adviser Professor Lawrence Que, Jr., for taking me into his group and providing the opportunity to work on a variety of projects with a high degree of freedom. While we butted heads at times, he always encouraged me to dive into the project and find more details to strengthen my ideas. I also had the good fortune to collaborate with Professor John Lipscomb on the CmlA and CmlI projects during my time here. With these projects I found myself outside of my comfort zone, but Prof. Lipscomb helped guide me through and, as a result, I developed a strong biochemical perspective that I will use for the rest of my career. These two mentors helped shape me into an independently-minded scientific investigator.

During my graduate studies, I worked with many friends in the Que lab, and for this I am grateful. Particularly, Dr. Kathy Van Heuvelen trained me as an undergraduate researcher at the University of Wisconsin – Madison and piqued my interest in bioinorganic chemistry. Years later, I was able to work with her again in the Que lab. Dr. Scott Kleespies helped convince me to come to UMN, and was always around to work through the problems that inevitably arose. Thank you to the XAS team members Dr. Matthew Cranswick, Dr. Kathy Van Heuvelen, Dr. Greg Rohde, Ang Zhou, Dr. Caleb Allpress, Dr. Apparao Draksharapu and Dr. Erik Farquhar for being part of the days spent collecting and analyzing XAS data. Thanks to Dr. Scott Kleespies, Dr. Apparao Draksharapu and Professor Wesley Browne for troubleshooting in the Raman room with me. A big thanks to BioCave members Drs. Anna Komor, Lisa Engstrom, Brent Rivard, and Van Vu for working with a stubborn spectroscopist and answering my silly biochemical questions. A special thanks to Dr Mayank Puri, Professor Dr. Johannes Klein, Dr. Wei-Min (Seesaw) Ching, Shuangning Xu, Patrick Crossland and Seul Ah Lee for good times.

I would also like to thank my collaborators across many different projects. As a spectroscopist, I relied heavily on the hard work of others in order to obtain samples to run. The biochemical projects would have never got off the ground without the repeated contributions from Drs. Anna Komor, Cory Knoot, Lisa Engstrom and Brent Rivard. On the synthetic side, I have had fruitful collaborations with Drs. Mayank Puri, Jai Prakash, Apparao Draksharapu, Alireza Shokri and Johannes Klein and there is continued work on the Fe-Ce project with Patrick Crossland, Professor Julio Lloret-Fillol, Dr. Zoel Codola and Professor Miquel Costas. All of these collaborations have allowed me to gain experience addressing a wide array of challenges across several disciplines.

Finally, I would like to thank my friends and family for all of the love over the years. Thanks to my family for the check-ins, and emotional support – especially the time spent together during visits to the Twin Cities. Aunt June gave me a home away from home and Aunt Sandy brought home with her wherever she went. I was lucky enough to run into a great group of people during the first week of grad school and without Laura, Gereon and Sean, I would have surely gone off the deep end. My good friends Sean and Morgan have kept in touch and are always game to entertain my crazy ideas. Lisa and Nate helped me out when times were rough and for that I am grateful. I thank Brent and Hannah and Ben and Lindsay for always welcoming me into their homes and allowing me to be part of the family. Epic thanks go out to the D&D crew, Pat, Caleb, Teresa, Nova, Mayank, Seesaw, Subhasree and Sasha for the many adventures after work. Minnesota was always more fun to explore with Greg, Mayank and Nirja. There is of course my partner in crime, Anna. I am so lucky to spend time with such a kind and supportive person.

Dedication

This thesis is dedicated to questioning precedent. Precedents in science are comforting and previously published works provide trends to observe and patterns to follow. However, these works are frozen at the time they are published and the comfort they can bring, in the absence of regular reflection and scrutiny, can lead to complacency. Then science becomes no more than a tradition to adhere to. We should always strive to understand why things are done, why models are used, and be critical of the analysis along the way. Always ask questions, and be open to see things from a new perspective, especially when new facts and precedent collide.

Abstract

The general mechanism of O_2 activation by nonheme diiron enzymes begins when the diferrous iron cluster binds dioxygen. The diiron cluster is oxidized to a peroxo-diferric intermediate that in some cases reacts directly with substrates, and in others becomes further activated *via* the cleavage of the O–O bond, leading to the generation of a potent high-valent oxidant that is the active oxidant for the cycle. Peroxo-diferric intermediates are of high interest because they are crossroads between the use of peroxo-diferric or high-valent oxo intermediate as the active oxidant in diiron-cluster-mediated oxidase and oxygenase chemistry.

Understanding this O_2 activation process requires structural characterization of enzymatic peroxo-diferric species. Spectroscopic methods, like electronic absorbance, X-ray absorption (XAS), and resonance Raman (rR) spectroscopies are used to probe a rich landscape of oxygen-activated intermediates and obtain detailed structures of these species. Through systematic study, insight can be gained into the mechanisms of these biological systems and ultimately this insight can be used to understand how Nature has chosen to use peroxo-diferric intermediates for a variety of different functions.

In Chapter 2, X-ray diffraction and XAS were used to characterize various form of the enzyme CmlA to understand how O_2 is regulated in the presence and in the absence of its non-ribosomal peptide synthetase (NRPS) bound substrate. In Chapter 3, the intermediate species on the O_2 activation pathway of the human enzyme deoxyhypusine hydroxylase (hDOHH), including the μ-1,2-peroxo species, were studied using XAS. The structural analysis of the active sites of the various hDOHH species provided insight into the reaction mechanism for the system. In Chapter 4, XAS and rR studies on the unusual peroxo-diferric species of the *N*-oxygenase CmlI were carried out. The spectroscopic analysis of the peroxo intermediate describes a new peroxo binding geometry for diiron enzymes, a μ-1,1-peroxo species. In Chapter 5, detailed XAS characterization of various synthetic peroxo-diferric and oxoiron(IV) model complexes is described. Overall, this thesis demonstrates the power of structural characterization by

complementary spectroscopic methods to support and generate enzymatic mechanistic hypotheses.

Table of Contents

List of Figures

List of Tables

Chapter 1 : Oxygen Activation by Nonheme Diiron Enzymes and the Generation of Peroxo Intermediates: Finding Structure–Function Relationships.

1.1 – Functional Overview of Dioxygen Activation by Diiron-Cluster-Containing Proteins

Oxygen activation by transition metal cofactors is a four electron process by which molecular oxygen is reduced in a stepwise manner to form potent metal-based oxidants that can facilitate reactions with organic substrates. O_2 has two unpaired electrons in the ground state, which makes direct reaction with singlet organic substrates very slow. Metal-based oxidants overcome the energy barrier associated with the change in spin state to react with organic molecules in a kinetically viable manner. Nature employs metalloenzymes as means to control the oxygen activation process and use the generated oxidants to facilitate critical reactions.

One class of oxygen activating metalloenzymes is the diiron-cluster-containing protein family, which uses a 4-helix bundle protein fold and a histidine and carboxylate rich coordination environment to bind transition metal centers.[1, 2] These proteins activate O_2 at ambient temperature and pressure to catalyze reactions like the biomineralization of iron by ferritins,[3] hydroxylation of C–H bonds by bacterial multicomponent monooxygenases (BMM) such as soluble methane monooxygenase (sMMO),[4, 5] toluene/o-xylene monooxygenase (ToMO),[6] and toluene-4-monooxygenase (T4MO),[7] the biosynthesis of RNA to DNA by ribonucleotide reductase (RNR),[8] the synthesis of alkanes from fatty aldehydes by aldehyde deformylating oxygenase (ADO),[9, 10] fatty acid desaturation by Δ^9 stearoyl-acyl carrier protein desaturase (Δ^9D),[11] the cross-linking of tyrosine and valine residues in R2-like ligand-binding oxidase (R2lox),[12, 13] and arylamine *N*-oxygenation by AurF[14] and CmlI.[15] An additional member of this protein family, hemerythrin (Hr), carries oxygen by reversibly binding O_2 to a diiron cluster supported by a 5-His-2-carboxylate ligand framework.[16] There are other diiron enzymes that do not share the 4-helix bundle fold with the superfamily but are still capable of O_2 activation. For example, the human enzyme deoxyhyupsine hydroxylase (hDOHH) facilitates the post-translational modification of the eukaryotic translational initiation

factor 5A using a 4-His-2-carboxylate framework in a HEAT repeat protein fold motif,[17] the *β*-hydroxylase CmlA from the biosynthetic pathway of the antibiotic chloramphenicol uses a 3-His-4-carboxylate motif in a metallo-*β*-lactamase fold,[18] and *myo*-Inositol oxygenase (MIOX) breaks down the signaling molecule myo-inositol to D-glucuronate using a 4-His-2-carboxylate framework in an HD-domain fold.[19]

While some of these diiron proteins like sMMO, RNR and Hr have had crystal structures since the 1990s, the rest have been crystallized during the past decade. Over half of the recently crystallized were solved within the last 2 years, demonstrating the field's strong interest in understanding the structure of this class of enzymes. In the absence of a protein crystal structure, X-ray absorption spectroscopy (XAS) can be used to generate a structure, as this method accurately determines distances between a transition metal cofactor (in this case, Fe) and the close contact atoms, which includes primary sphere ligands (L) and the 2nd Fe center in diiron enzymes.[20] Even when a crystal structure is available, XAS provides a valuable means of structural comparison and at times can provide a more accurate structural metrics than XRD methods. XAS provides a dynamic, solution state structure that can be more informative than a solid state XRD structure, as crystal structures can be distorted by crystal packing forces or photoreduction from the X-ray beam.

XAS generates two complementary sets of information. The X-ray absorption near edge structure (XANES) region provides information about the electronic environment and coordination geometry of the metal centers, reflected in the K-edge energy and pre-edge area, respectively. The K-edge energy can additionally be used to track the change in metal oxidation state during data collection to determine the extent of radiation damage or photoreduction that occurs. This type of monitoring is generally not easy to do during XRD data collection. The extended X-ray absorption fine structure (EXAFS) region provides the structural metrics. The accuracy of Fe–L distances determined from EXAFS is ±0.02 Å,[21] compared to accuracy on the order of ~0.1 Å for

protein crystallography. XAS and crystallography together are powerful tools to analyze nonheme diiron active site structure.

The first step in the reaction pathway for oxygen activation by a diiron enzyme is the binding of dioxygen to the diferrous cofactor (Figure 1.1A). As a result, each iron center is oxidized to Fe^{III} while O_2 is reduced to peroxide (O_2^{2-}), generating a peroxo-diferric intermediate (Figure 1.1 B). In some enzymes, the peroxo-diferric intermediates have been shown to directly react with substrates,[15, 22-25] but in the well-studied canonical examples of sMMO and RNR, the peroxo ligand is further reduced, breaking the O–O bond and generating high-valent (Fe^{IV}_2 or $Fe^{III}Fe^{IV}$) intermediates that are responsible for substrate oxidation.[4, 26, 27] In a third pathway, T4MO has been proposed to generate a mixed valent $Fe^{II}Fe^{III}$-superoxo species that serves as the active oxidant.[28]

The MIOX system deviates substantially from the other diiron-cluster-containing proteins in the method of O_2 activation. The active form of MIOX is a mixed valent $Fe^{II}Fe^{III}$ species with the myo-inositol substrate bound to the Fe^{III} center, which coordinatively saturates the Fe center. O_2 is then proposed to bind to the coordinatively unsaturated Fe^{II} center, which generates a superoxo-diferric intermediate. This superoxo species is implicated as the active oxidant for the system.[29, 30] The available structural characterization for the MIOX system is limited, so this system will not be further discussed in this chapter.

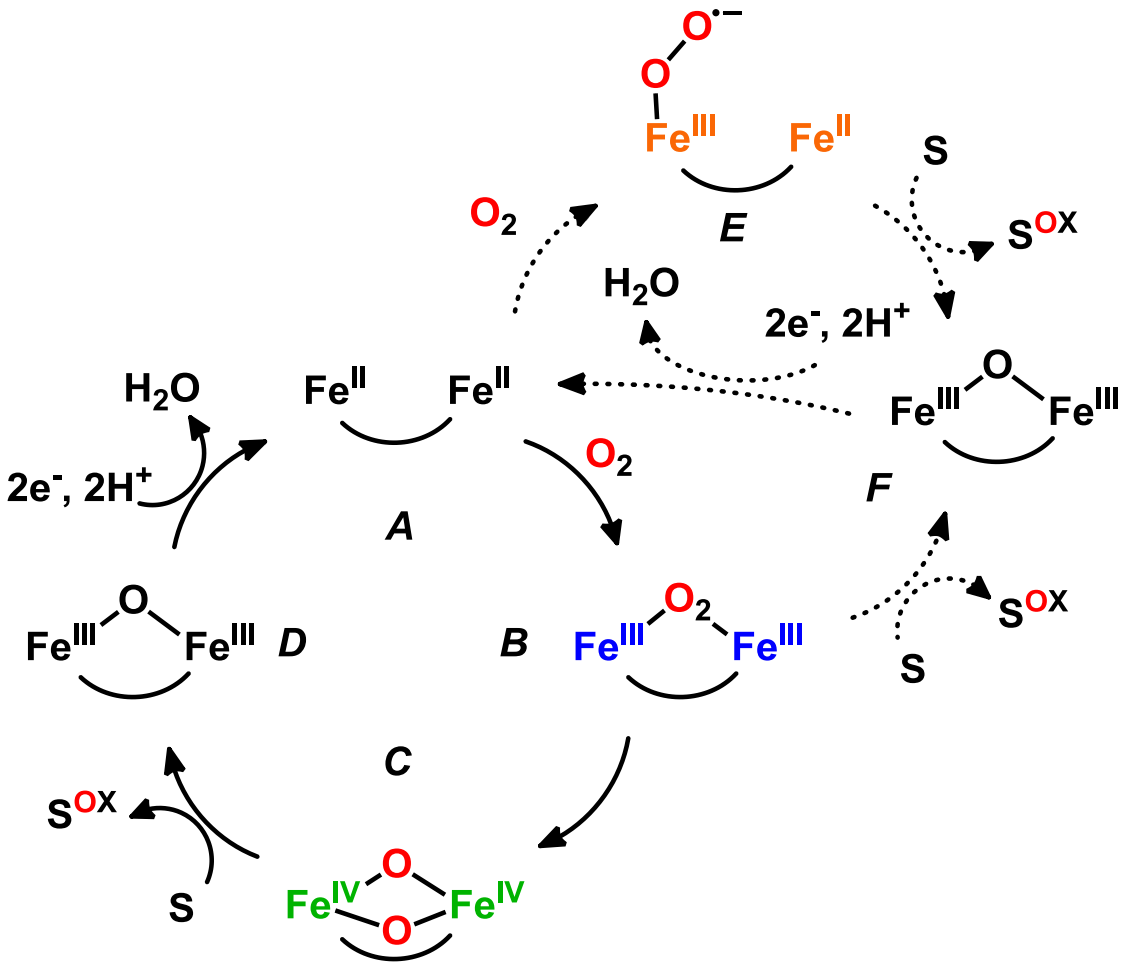

Figure 1.1. Generalized O_2 activation cycle for nonheme diiron enzymes. A is the diferrous starting point of of O_2 activation; B is a peroxo-diferric species; C is the high-valent active oxidant in the cycle, represented here as the bis(μ-oxo)diiron(IV) species **Q** from sMMO; D and F represent the resting diferric state; E is the mixed valent superoxo species proposed for T4MOH. Representative examples: sMMO proceeds through the A→B→C→D cycle; CmlI proceeds through the A→B→F cycle; T4MOH proceeds through the A→E→F cycle.

This chapter provides an overview of the structural characterization and spectroscopic properties of diferrous and peroxo-diferric species found in diiron systems, and concludes with structure-function relationships of the peroxo-diferric intermediates. These intermediates are important crossroads during enzymatic reaction cycles, as sometimes peroxo species are reactive, but in other cases the peroxo ligand is required to

become further activated for proper catalysis. Spectroscopic characterization and structural analysis make it possible to better understand the O_2 activation process, and how Nature chooses to use peroxo-diferric intermediates.

1.2 – Diferrous Enzyme Structures and Properties

Diferrous iron centers are the starting point of catalytic cycles for most nonheme diiron enzymes. As precursors to peroxo-diferric intermediates the structures of diferrous species can dictate the types of peroxo ligand binding modes that are possible. Consequently, these geometric restrictions influence the reactivity of the diiron enzyme. Enzymatic diferrous species have been characterized by a wide variety of spectroscopies, including XRD, XAS, and Mössbauer spectroscopy. The findings from these studies are summarized in this section.

1.2.1 – Structural Characterization of Diferrous Intermediates by XRD and EXAFS

There are three types of active site structures that have been observed in protein crystals from X-ray diffraction (XRD) studies, termed Class 1, Class 2, and Class 3 in this work. Class 1 contains diferrous intermediates that use exclusively a μ-1,3-carboxylate bridging motif (Figure 1.2, A), with two protein derived carboxylate ligands holding the metal centers in the active site. This motif is observed in crystals of RNR, Δ^9D, Mn^{II} substituted AurF, and CmlI (PDB codes 1PFR, 1AFR, 2JCD, and 5HYH, respectively), generally with long M•••M distances between 3.6 and 4.1 Å (Table 1.1). The diferrous form of ADO also shares this binding motif, but maintains a much shorter Fe•••Fe distance at 3.1 Å (PDB code 4RC6).

The second class of diferrous active site, Class 2, utilizes single atom bridging ligands in addition to μ-1,3-carboxylate bridges. The single atom bridges are derived

from μ-1,1-carboxylate and/or solvent ligands (Figure 1.2, B). This motif is observed in crystal structures of sMMOH, Mn^{II} substituted ToMOH, T4MOH, diiron R2lox, frog M ferritin and Hr (PDB codes 1FYZ, 2IND, 3DHI, 4XBV, 4LQN, 1HMD, respectively), with M•••M distances between 3.3 and 3.6 Å (Table 1.1). As their single atom bridge, sMMOH, ToMOH, T4MOH and R2lox employ a glutamate residue that binds in a bidentate coordination mode to one metal center while bridging between both metal centers in a μ-1,1-mode. In addition, sMMOH and ToMOH have a solvent derived μ-aqua ligand and a μ-1,3-carboxylate that bridge, and T4MOH just has a μ-1,3-carboxylate. In contrast, frog M ferritin and Hr use μ-1,3-carboxylate bridges (one in ferritin, two in Hr) and a μ-hydroxo ligand.

The final class of diferrous active site, Class 3, exclusively uses single atom bridges to maintain the diiron cluster (Figure 1.2, C). The only crystallographically characterized example is CmlA (PDB code 5KIK), which has an aspartic acid residue that bridges in a μ-1,1-mode and is opposite a μ-hydroxo bridge, which helps maintain an Fe•••Fe distance of 3.3 Å (Table 1.1).

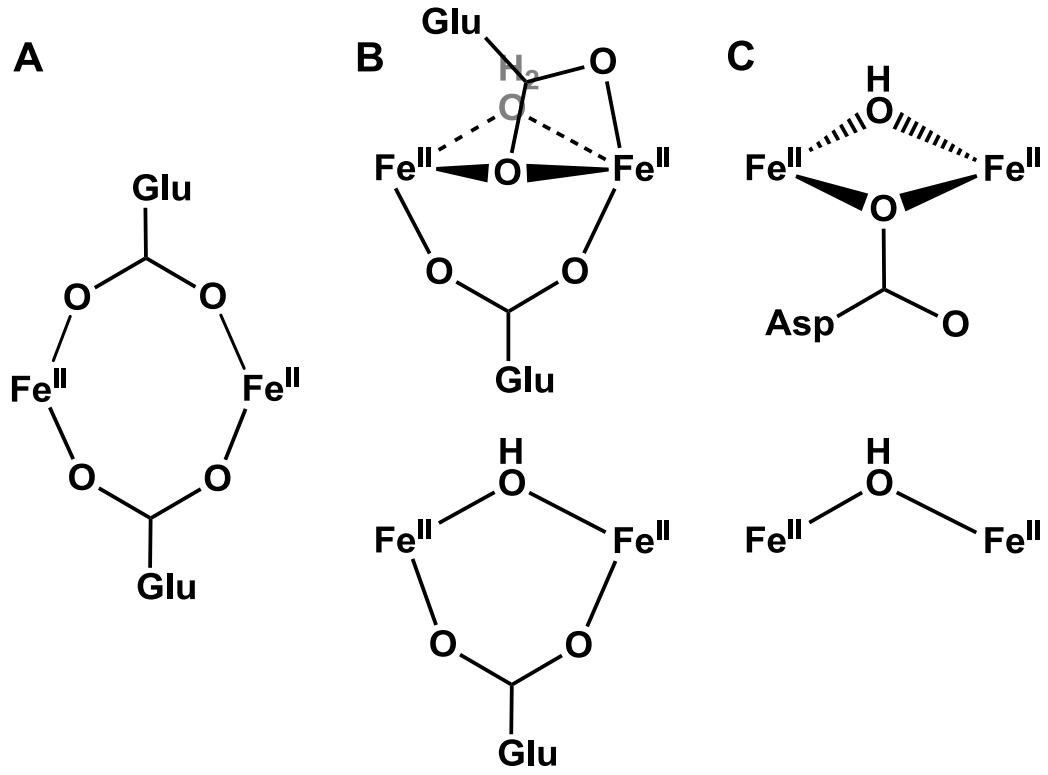

Figure 1.2. Summary of diferrous active site structural classes. A: Class 1 uses exclusively μ-1,3-carboxylate ligands; B: Class 2 uses single atom bridges in addition to μ-1,3-carboxylate ligands; C: Class 3 only uses single atom bridging ligands, without support from μ-1,3-carboxylate bridges.

The crystallographically-derived Fe•••Fe distance can to some extent be correlated with the structural class of the active site. Generally, Class 1 has distances at 3.6 Å and above, and Class 2 has distances between 3.3 and 3.6 Å. Class 3 has only one crystallographically characterized example which has an Fe•••Fe distance of 3.3 Å, and this distance overlaps with Class 2. Additionally, there is overlap at ~3.6 Å between Class 1 and Class 2. Thus, metal-metal separation alone is not indicative of the diferrous active site structure.

EXAFS analysis has also been employed to acquire solution state structural metrics of the diferrous forms of nonheme diiron proteins. Of the eight systems that have parallel XRD and XAS studies, five (sMMOH, ToMOH, frog M ferritin, R2lox, CmlA) yield structural parameters, including the Fe•••Fe distance, that agree between the techniques (Table 1.1). In these systems XRD provides a three-dimensional picture of the

diiron centers, while EXAFS can provide accurate bonding metrics, which together provide an accurate structural picture of the active site. EXAFS can also be used to identify differences between the solid and solution state, if they exist. Having a solution state structure is beneficial to accurately understanding the mechanism of O_2 activation of a particular system.

The three systems that have XRD and EXAFS that do not agree are RNR R2 (3.9 Å XRD vs. 3.41 Å XAS), Hr (3.3 Å vs. 3.57 Å), and CmlI (3.6 Å vs. 3.35 Å). In the case of RNR R2, the wild type (WT) enzyme was used for XRD experiments, [31] whereas a W48A/D84E variant was used in the XAS experiments.[32] The D84E mutation affects a primary sphere carboxylate ligand, so the variance in the Fe•••Fe distance is due, at least in part, to a difference in the coordination geometry of the WT enzyme and the W48A/D84E variant.

The discrepancy in the Hr structures has no clear source. In 1988, Stern and co-workers collected EXAFS data for deoxy (Fe^{II}_2) and oxy (Fe^{III}_2-OOH) Hr and found Fe•••Fe distances of 3.57 and 3.24 Å, and correctly assigned μ-OH and μ-O ligands, respectively.[33] Higher resolution (2.0 Å) crystal structures became available in 1991, revealing Fe•••Fe distances at 3.3 Å for deoxy- and oxyHr.[34] The bridging ligands for deoxy- and oxyHr, as well as the Fe•••Fe for oxyHr from the 1988 XAS analysis, agree with the XRD results, while the Fe•••Fe for deoxyHr does not. To date, this discrepancy has not been resolved.

For CmlI the discrepancy may be due to the solid-state nature of protein crystals. The diferrous crystal is obtained by soaking a crystal of a μ-1,2-peroxo-diferric species in dithionite,[35] resulting in a Class 1 type active site with an Fe•••Fe distance of 3.6 Å. The solution state EXAFS-derived distance is 3.35 Å, consistent with a single atom bridge and a Class 2 active site (See Chapter 4 for more details). In this case, the differences in the XRD and XAS results can be attributed to the inability of the crystal structure to reorganize after chemical reduction.

Finally, in the absence of a crystal structure, XAS is often the best method to obtain a structural model. For example, hDOHH currently has no crystal structure of the diferrous form, so EXAFS analysis was used to develop a structural model for hDOHH of a μ-hydroxide bridged diferrous center with an Fe•••Fe distance of 3.47 Å.[36] This initially appears to put hDOHH into Class 2, however, a crystal structure of the peroxo-diferric form of hDOHH demonstrated that the two glutamate residues in the active site are bound in a monodentate mode,[17] and would unlikely be able to bridge in a μ-1,3-mode. Thus, hDOHH is more consistent with a Class 3 active site, similar to that of CmlA.

1.2.2 – Structural Characterization of Diferrous Intermediates from XANES Analysis

XANES analysis provides additional information about the electronic environment and symmetry of the Fe centers. The K-edge energy is the energy required to liberate a 1s core electron from a Fe nucleus, and generally corresponds to the electronic environment of the metal center. As the oxidation state of the metal increases, the K-edge usually moves to higher energy, as seen in Figure 1.3. The pre-edge feature is a transition that increases in intensity the more the coordination environment distorts away from centrosymmetry (Figure 1.3, right). Thus, the area of the pre-edge feature can help distinguish the coordination environment of the Fe centers.

The K-edge energies of available diferrous species are found from 7121.4 to 7122.7 eV,[13, 36-38] a 1.3 eV range. Despite having the same oxidation states as assigned by Mössbauer spectroscopy, these enzymes do not have the same K-edge energy, demonstrating that K-edge energy is affected by more than just oxidation state.[39-42] Therefore, analysis of K-edge energies alone is not sufficient to determine oxidation state of an Fe center. The context of the coordinating ligands and electronic properties of the Fe centers is required for accurate interpretation of the K-edge results.

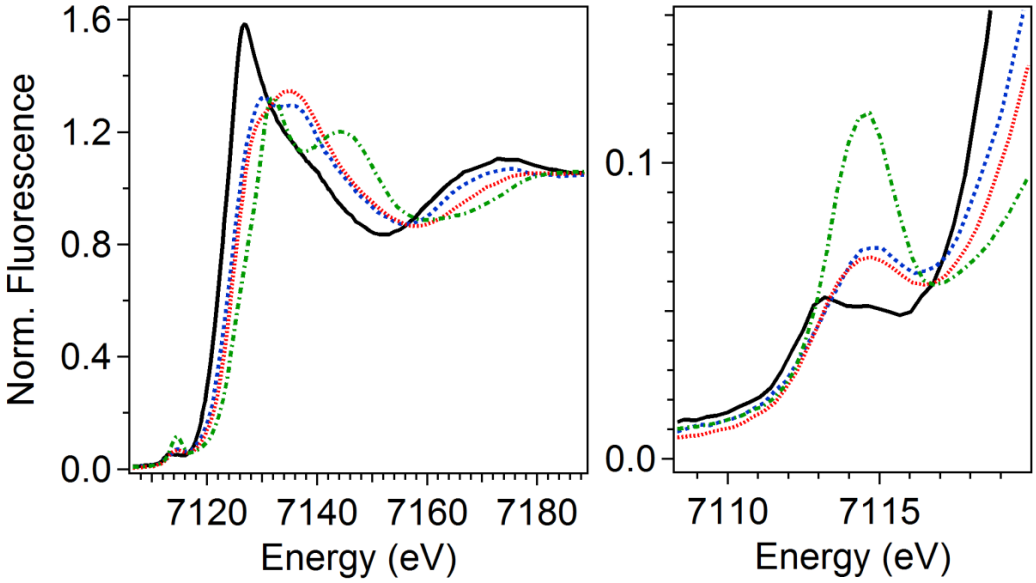

Figure 1.3. Fe K-edge XAS fluorescence spectra (normalized) of the XANES region. Representative spectra of diferrous (black solid, CmlI), peroxo-diferric (red dotted, CmlI; blue dashed, OxyHr) and oxoiron(IV) species (green dash dot).

Analysis and comparison of pre-edge features provides insight into the coordination geometry of metal centers, as the feature is sensitive enough to distinguish between five-coordinate and six-coordinate Fe centers. The coordination environment is important in O_2 activating systems, as open coordination sites on the Fe are required in order to bind O_2.

Six of the diiron systems presented here have reported pre-edge areas for the diferrous form, which range from 8.4 to 13.6 units (Table 1.1). Based on XAS of synthetic systems, six-coordinate centers range from 4 to 6 units, with an average of ~5 units, and five-coordinate centers range from 9 to 13 units, with an average of ~11 units.[43, 44] CmlA (8.4 units), CmlI (8.4 units) and hDOHH (8.6 units) have all been assigned by XAS as having six-coordinate Fe centers. The pre-edge values for these systems fall higher than the range of synthetic six-coordinate centers, but lower than the range of synthetic five-coordinate centers. The crystal structure of CmlA also shows six-

coordinate Fe atoms, demonstrating that the assignment based on XANES is accurate for the system.

Newly available XANES data and better understanding of the relationship between XANES data and coordination number, provides an opportunity to clear up discrepancies in the literature. For example, the pre-edge area of sMMOH was found to be ~10 units in two different studies, with one study assigning two five-coordinate Fe centers and the other assigning the same pre-edge feature to a structure with one five- and one six-coordinate Fe center.[45, 46] In the latter study, ToMOH had a pre-edge of 10.5 units, and was assigned similarly. For comparison, the crystal structure of sMMOH features each Fe center with 5 coordination sites filled by ligands bound between 2.1 and 2.4 Å, and a loosely coordinated μ-solvent ligand with Fe1-O at 2.5 Å and Fe2-O at 2.7 Å.[47] A similar picture is observed with the Mn^{II}-substituted ToMOH crystal structure, but with the μ-solvent ligand having distances of Mn1-O at 2.8 Å and Mn2-O at 2.2 Å.[48] It is conceivable that in solution this loosely bound solvent does not sufficiently perturb the Fe centers such that they can be considered five-coordinate. This analysis is consistent with MCD studies.[49] Based on corroborating structural studies, and on comparison to more recent Fe K-edge XAS analyses, the pre-edge areas of sMMOH and ToMOH are more consistent with an assignment of five-coordinate Fe centers.

The last available set of XANES data from diferrous systems comes from frog M ferritin,[37] with a pre-edge area of 13.6 units. The pre-edge value was not definitively assigned to either six- or five-coordinate centers. Reevaluation based on the range of values presented above leads to the assignment of five-coordinate Fe centers. This is consistent with the diferrous crystal structure,[50] which features one five-coordinate Fe center and one six-coordinate center with a loosely bound solvent ligand at 2.5 Å.

1.2.3 – Spectroscopic Characterization of Diferrous Active Sites by Mössbauer Spectroscopy

Mössbauer spectroscopy is used in the analysis of diiron active sites to acquire the isomer shift (δ), which is sensitive to the electronic state of the Fe nucleus, and the quadrupole splitting (ΔE_Q), which is sensitive to the local electric field around each Fe center.[51] Together these parameters can be used to determine Fe oxidation state, as well as the local coordination environment around each Fe center. Diferrous active sites can have two different electronic ground states. One is an anti-ferromagnetically (AF) coupled S = 0 system, where the Fe centers have unpaired electron spins that are opposite in magnitude (positive or negative). The other is a ferromagnetically coupled S = 4 system where the Fe centers have unpaired electron spins that have the same magnitude. These two ground states can be distinguished using various spectroscopic analyses including, Mössbauer, electron paramagnetic resonance (EPR) and magnetic circular dichroism (MCD) spectroscopies. For an overview on the electronic structures of nonheme diiron active sites, see a recent review by Solomon and Park in ref [52].

The δ values for the diferrous proteins presented here fall between 1.20 and 1.39 mm/s (average of 1.28 mm/s), consistent with high spin S = 2 Fe centers (Table 1.2). The ΔE_Q values have a much wider range from 2.13 to 3.36 mm/s (average of 2.96 mm/s), as the ligand identity and particular coordination environment of each Fe center have a larger effect on this parameter.

There does not appear to be a correlation in the Mössbauer parameters between structural class or by ligand framework, other than that every system is close to the average value (δ = 1.28 mm/s, ΔE_Q = 2.96 mm/s). For instance, by crystallography sMMOH, ToMOH, T4MOH and R2lox all have essentially the same active site structure and 2-His-4-carboxylate ligand framework; however, ToMOH and T4MOH have inequivalent Fe sites, whereas the other two do not (Table 1.2). Additionally, the Mössbauer parameters of asymmetrically bound Fe centers, as determined by crystallography, do not always reflect Fe site inequivalency. AurF, CmlI, CmlA and deoxyHr have two distinct Fe sites with unequal numbers of His ligands as determined by XRD studies. However, only CmlI and CmlA have two sets of Mössbauer parameters,

consistent with two distinct Fe sites. Based on these findings, drawing structural conclusions based on Mössbauer analysis alone is not straight forward, and should be done with caution.

Table 1.1. Selected structural parameters of diferrous active sites from XRD and XAS studies. Distances are in angstroms. [a] from ref [45]. [b] from ref [46].

Protein	K-edge (eV)	Pre-edge area (units)	Fe•••Fe (XRD)	Fe•••Fe (EXAFS)	Bridge type	PDB code	Resolution (Å)	Ref
Ec R2-RNR	-	-	3.9	3.41	μ-1,3-carboxylato	1PFR	2.2	*31, 32*
Δ^9D	-	-	4.1	-	μ-1,3-carboxylato	1AFR	2.4	*53*
ADO	-	-	3.1	-	μ-1,3-carboxylato	4RC6	2.9	*54*
AurF	-	-	3.6 (Mn^{II})	-	μ-1,3-carboxylato	2JCD	2.11	*55*
CmlI	7122.1	8.4	3.6	3.35	μ-1,3-carboxylato μ-hydroxo	5HYH	2.03	Ch. 4, *35*
sMMOH	-	10,[a] 9.6[b]	3.4 C	3.43,[a] 3.29[b]	μ-1,1-carboxylato, μ-aquo, μ-1,3-carboxylato	1FYZ	2.15	*45-47*

Table 1.1 (continued). Selected structural parameters of diferrous active sites from XRD and XAS studies. Distances are in angstroms. [a] from ref [43.] [b] from ref [44.]

Protein	K-edge (eV)	Pre-edge area (units)	Fe•••Fe (XRD)	Fe•••Fe (EXAFS)	Bridge type	PDB code	Resolution (Å)	Ref
ToMOH	-	10.5	3.3 (Mn^{II})	3.37	μ-1,3-carboxylato, μ-1,1-carboxylato μ-aquo	2IND	2.2	*46, 48*
T4MOH	-	-	3.4	-	μ-1,1-carboxylato, μ-1,3-carboxylato	3DHI	1.68	*56*
Frog M ferritn	7122	13.6	3.5	3.43	μ-1,3-carboxylato, μ-hydroxo	4LQN	1.59	*37, 50*
R2lox	7121.4	-	3.6	3.64	μ-1,1-carboxylato, μ-1,3-carboxylato	4XBV	1.8	*13*
Hr	-	-	3.3	3.57	μ-1,3-carboxylato, μ-hydroxo	1HMD	2.0	*33, 34*
CmlA	7121.5	8.4	3.3	3.26	μ-1,1-carboxylato, μ-hydroxo	5KIK	2.2	*38*
hDOHH	7122.7	8.6	-	3.47	μ-hydroxo	-	-	*36*

Table 1.2. Summary of coordination environment and Mössbauer parameters for ferrous nonheme diiron proteins. Class refers to the assigned structural classification; coordination refers to the coordination number for each Fe center based on XRD and XAS studies; Ligands refers to the diiron ligand framework where H is histidine and C is a carboxylate ligand.

Species	**Class**	**Coordination**	**Ligands**	**δ (mm/s)**	**ΔE_Q (mm/s)**	**ref**
Ec R2-RNR	1	5	2H/4C	1.26	3.13	*57*
Δ^9D	1	5	2H/4C	1.30, 1.30	3.04, 3.36	*58*
ADO	1	5	2H/4C	1.3	3.0	*25*
AurF	1	5	3H/4C	1.24	3.06	*59*
CmlI	1/2	5/6	3H/4C	1.25, 1.23	3.13, 2.80	*15*
sMMOH	2	5	2H/4C	1.30	3.01	*45, 60*
ToMOH	2	5	2H/4C	1.32, 1.39	3.06, 2.13	*24*
T4MOH	2	5	2H/4C	1.31, 1.31	3.21, 2.68	*7*
Frog M ferritin	2	5	2H/4C	1.31	3.00	*61*
R2lox	2	6	2H/4C	1.27	2.97	*62*
Hr	2	5,6	5H/2C	1.20	2.89	*63*
CmlA	3	6	3H/4C	1.30, 1.21	2.75, 2.90	*64*
hDOHH	3	6	4H/2C	1.29, 1.29	3.26, 2.90	*65*

1.3 – Enzymatic Peroxo-Diferric Intermediate Structure and Properties

Peroxo-diferric species have been studied for decades, but there has been a boom in the identification of new intermediates in the past 20 years. There is an increased interest in structural nuances of these intermediates due to recent discovery of diferric peroxo species that are active on native enzymatic cycles. Peroxo intermediates also precede high-valent intermediates and insight from peroxo structures will assist in understanding the mechanisms used for O–O bond cleavage.

1.3.1 – Generation of Peroxo-Diferric Species

As depicted in Figure 1.1 (A → B), the generation of peroxo-diferric intermediates in nonheme diiron systems starts with molecular oxygen binding to a diferrous active site. In Hr, this process is fast with a first order rate constant on the order of 10^3 s^{-1} at 25 ºC.[66] The other diiron systems presented here react with O_2 to form peroxo intermediates with rate constants on the order of 10^1 to 10^2 s^{-1} (Table 1.3). In systems like sMMOH and R2 RNR, accumulation of enzymatic peroxo intermediates is thwarted by rapid rates of decay (Table 1.3). Stopped flow and rapid freeze quench techniques are necessary to observe these transient intermediates. In some systems, like CmlA, R2lox, and T4MOH, no accumulation of a transient peroxo intermediate has been reported in kinetic studies. More recently, longer lived peroxo-diferric species have been identified in Δ^9D,[67] AurF,[59] CmlI,[15] and hDOHH,[65] which last from minutes to days which allows for easier preparation and handling of these intermediates.

1.3.2 – Spectroscopic Characterization of Peroxo-Diferric Species by UV-Vis and Resonance Raman Spectroscopies

The signature peroxo-to-Fe^{III} ligand to metal charge transfer (LMCT) transition associated with peroxo-diferric intermediates has a maximum in the electronic absorption

(UV-vis) spectrum between 450 and 725 nm,[15, 25, 59, 61, 63, 65, 67-70] and can be used as a marker in experiments. The UV-vis spectrum of oxyHr can been seen in Figure 1.4. Strangely, in ToMOH there was no visible chromophore associated with the assigned peroxo intermediate, and this species was instead identified by Mössbauer spectroscopy and reactivity studies.[24] This is the only diferric peroxo intermediate for which there is not a chromophore in the visible region.

A powerful tool to aid in the structural characterization of peroxo-diferric intermediates is resonance Raman (rR) spectroscopy. By using a laser with a wavelength close to that of the peroxo-to-iron LMCT transition (Figure 1.4), it is possible to observe vibrations of the atoms associated with, or coupled to, the chromophore.[71] Specifically, the O–O stretching vibration (ν(O–O)) is characteristic of a particular binding mode of a peroxo ligand. In isolation, the ν(O–O) does not assign the binding geometry of the peroxo ligand, and studies of synthetic peroxo models with known structures provide valuable benchmarks against which to compare the biological intermediates (see Section 1.4). The ν(O–O) values observed for the peroxo intermediates range from 791 to 898 cm^{-1} (Table 1.3). Initially this vibration was assigned based on comparison to the stretches of gaseous O_2 (1556 cm^{-1}), the superoxide stretch of KO_2 (1146 cm^{-1}) and hydrogen peroxide (880 cm^{-1}). Additionally, O–O stretching frequencies can be identified from isotope labeling experiments, where peroxo intermediates are generated with $^{18}O_2$ and/or $^{16}O^{18}O$. Hooke's law can be used to predict the expected change in the ν(O–O) using different isotopes from the following simplified relationship for diatomic vibrations:

$$\nu_2 = \nu_1 \sqrt{\frac{\mu_1}{\mu_2}}$$

where ν_1 and ν_2 are Raman shifts of the vibration in cm^{-1} and μ_1 and μ_2 are the reduced mass of the diatomic unit, given by:

$$\mu = \frac{M_1 M_2}{M_1 + M_2}$$

where M_1 and M_2 are the mass of the two atoms involved in the vibration in grams. The reduced mass for $^{16}O_2$ is 8, and for $^{18}O_2$ is 9, so if a putative ν(O–O) was observed at 850 cm^{-1}, the $^{18}O_2$-generated peroxo would have a predicted shift of 49 cm^{-1}.

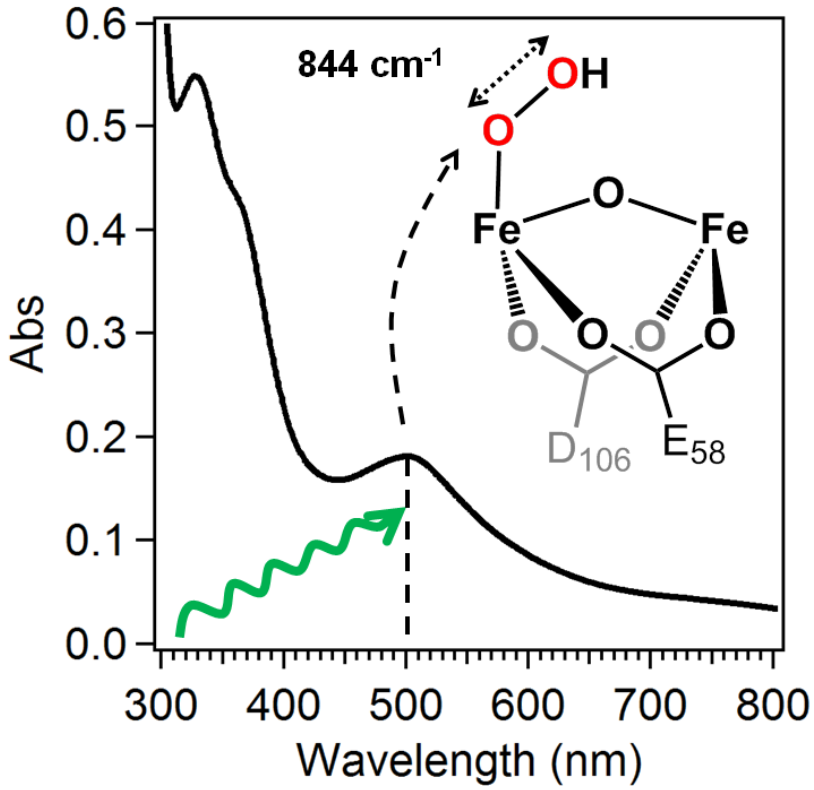

Figure 1.4. Simplified diagram for resonance Raman data collection of peroxo-diferric intermediates. The absorption spectrum is of OxyHr (provided by Dr. Anna Komor) with a peroxo-to-iron(III) LMCT transition at ~500 nm, marked by the vertical dashed line. Excitation by a laser with similar wavelength (green curved line) into the LMCT band results in observation of resonance enhanced vibrations, such as the O–O stretch at 844 cm^{-1}.

Resonance Raman has been used to identify several peroxo ligand binding modes in biological peroxo-diferric species. The most common is the *cis*-μ-1,2-peroxo binding mode which is found in RNR, Δ^9D, frog M ferritin and hDOHH, and is characterized by a ν(O–O) between 851 and 898 cm^{-1} and visible absorption features between 600 and 700 nm (Table 1.3). sMMOH is also proposed to have a μ-1,2-peroxo binding mode based on the visible absorption max at 725 nm and comparison of Mössbauer parameters with known *cis*-μ-1,2-peroxo species,[69, 70, 72] but neither rR nor XAS characterization of the peroxo species has been reported. Of these intermediates characterized by rR, Class 1

active sites have ν(O–O) on the higher end of the range, whereas Class 2 and 3 active sites have values close to 850 cm^{-1}.

Additional peroxo binding modes have been identified from the well-studied oxyHr and the newly discovered CmlI OxyHr has a ν(O–O) at 844 cm^{-1} derived from a terminal hydroperoxo ligand bound to one of the Fe centers (Figure 1.4). This assignment was also confirmed by XRD studies.[34, 73] The ν(O–O) for the end-on hydroperoxo species falls just below the 850 – 900 cm^{-1} range for μ-1,2-peroxo intermediates. The peroxo intermediate from CmlI has an ν(O–O) at 791 cm^{-1}, which is even lower from the μ-1,2-peroxo range than oxyHr. Based on this unusual O–O stretch and subsequent XAS characterization, the peroxo binding mode was assigned as μ-1,1-peroxo (see Chapter 4 for more details).

The remaining peroxo intermediates of ADO, AurF and ToMOH currently have no rR characterization, so definitive assignment of the peroxo binding mode is not possible. Mössbauer and UV-vis spectroscopy, in conjunction with mechanistic studies, has led to several proposed structures which are summarized in Table 1.3 and Table 1.5.[24, 25, 59, 74]

1.3.3 – Structural Analysis of Peroxo-Diferric Species by Mössbauer Spectroscopy

Mössbauer parameters for the peroxo intermediates also help to distinguish structural features of the active site and a summary of these parameters are found in Table 1.3 and Table 1.4. Overall, the isomer shifts range from 0.48 to 0.68 mm/s (average of 0.58 mm/s), and have been assigned to high spin S = 5/2 Fe^{III} centers that are AF coupled to an overall ground state of S = 0. The values for quadrupole splitting range from 0.23 to 1.92 mm/s (average of 1.06 mm/s), which has a difference in values not dissimilar from the diferrous active sites ($\Delta\Delta E_Q$ = 1.69 mm/s for Fe^{III}_2, 1.23 mm/s for Fe^{II}_2). Subdividing further, the peroxo intermediates assigned to a μ-1,2-peroxo binding geometry have values on the higher end of the range (δ = 0.55 – 0.68 mm/s, ΔE_Q = 0.88 –

1.90 mm/s) with an average isomer shift of 0.62 mm/s and average quadrupole splitting of 1.34 mm/s. The isomer shift and quadrupole splitting values for the remaining intermediates (ADO, AurF, CmlI, ToMOH, Hr) have ranges that overlap with those of the μ-1,2-peroxo species (δ = 0.48 – 0.62 mm/s, ΔE_Q = 0.23 – 1.92 mm/s) but with lower averages of δ = 0.55 mm/s and ΔE_Q = 0.81 mm/s. One of the ΔE_Q values for Hr (1.92 mm/s) is an outlier for the series (Table 1.3) and in the absence of this parameter the average value would drop further to ~0.68 mm/s. Based on this analysis, the Mössbauer parameters can, in this case, be used to distinguish μ-1,2-peroxo binding modes from other binding modes. A μ-1,2-peroxo species will have larger values for isomer shift and quadrupole splitting, closer to δ = 0.62 mm/s and ΔE_Q = 1.34 mm/s, on average, compared to peroxo intermediates that have different binding geometries.

An interesting observation from the Mössbauer parameters is the change in the number of inequivalent Fe sites going from diferrous to peroxo-diferric species. Four of the five μ-1,2-peroxo species maintained the same Fe site inequivalency as in the diferrous state (Δ^9D, sMMOH, frog M ferritin, hDOHH), with RNR changing from one type of Fe site in the diferrous form to two Fe sites in the peroxo form. However, the number of inequivalent sites is different within the peroxo intermediates, as sMMOH and frog M ferritin have one set of Mössbauer parameters and the rest have two (Table 1.3). Of the remaining five intermediates, only CmlI maintained the same number of inequivalent Fe centers upon changing oxidation state. This analysis should serve to reinforce that Mössbauer spectroscopy alone is not adequate to generally assign the structure in diiron active sites.

1.3.4 – Structural Characterization of Peroxo-Diferric Species by XRD and XAS

The bonding metrics of peroxo-diferric active sites come from a combination of XRD and XAS (Table 1.5), but only a few systems have been amenable to these types of study. The active site structure of oxyHr was first pieced together from a combination of spectroscopic analyses, including rR and XAS studies, and was ultimately confirmed by a

high resolution crystal structure (PDB code 1HMO, 2.0 Å).[34] The diiron center is coordinated in a similar way as in the diferrous form, with an Fe•••Fe distance of 3.3 Å and a single atom (μ-oxo) bridge that was observed in both XRD and XAS experiments.[33] The hydroperoxo moiety is terminally bound to one Fe center, and rR[75] determined that the hydroperoxo ligand is hydrogen bonded to the μ-oxo bridge and featured a O_{peroxo}•••O_{oxo} distance of ~3 Å (Figure 1.5A). The crystals of oxyHr were grown from a solution of the oxyHr intermediate, which requires a highly stable peroxo species.

Crystals of hDOHH peroxo (PDB code 4D50) were also obtained directly from a solution of the intermediate, as the half-life of the peroxo species is on the order of days.[17] The active site structure is unlike other diiron systems, as there are no bridging carboxylate ligands. The two pseudo-octahedral Fe centers are each bound by protein ligands (2-His-1-Glu) in a meridional motif with a μ-hydroxo bridging between them. The binding geometry of the peroxo ligand is a μ-1,2-peroxo mode, in agreement with rR studies,[65] and the coordination sphere is capped off by terminal solvent derived ligands (Figure 1.5B). Interestingly, the peroxo ligand is bound in a hydrophobic pocket, on the opposite side of the cluster from the proposed substrate binding channel, which was suggested to contribute to the high stability of the peroxo species.[17] The Fe•••Fe distance was found between 3.7 and 3.8 Å (two different active sites), with Fe–O_{peroxo} distances at ~2.2 Å. However, the metrics did not agree with those determined by XAS, which were 3.41 and 1.98 Å, respectively.[36] This indicates that the crystals of hDOHH were photoreduced in the X-ray beam, a well-known issue with crystallographic studies of metalloenzymes.[76-78] The photoreduction can be mitigated in XAS studies, as the K-edge energy can be monitored during data collection and the physical spot that is being hit by the X-ray beam can be moved.

When protein crystals cannot be directly obtained from a solution of the species of interest, in some cases the intermediate may be generated in crystallo. To generate the peroxo species, first crystals of the reduced form are obtained, followed by introduction of an oxidant and in some cases substrate. This method has been successful in generating both peroxo intermediates[35, 79, 80] and catching various steps along a reaction pathway.[28,

[81] The structure of a unique peroxo species obtained in this manner was from the human form of L ferritin. Crystals of apo-L-ferritin, were soaked in a solution containing ferrous iron in the presence of O_2.[80] The resulting structure was a surface exposed trimer of μ-1,2-peroxo-diferric species, with 3 iron centers supported by a μ^3-oxo ligand (PDB code 5LG8, Figure 1.5C). Each peroxo unit (or pair of Fe centers) is supported by a μ-1,3-carboxylate bridge in addition to the μ^3-oxo. Interestingly, there are no histidine ligands supporting the Fe centers, which is distinct from all of the other presented diiron active sites. The Fe•••Fe distances for the three units are 3.2, 3.3 and 3.5 Å with Fe–O_{oxo} bond lengths of 1.8, 2.0 and 2.0 Å. The O–O bond lengths are all 1.5 Å with proximal Fe–O_{peroxo} distances between 2.3 and 2.6 Å and distal Fe–O_{peroxo} distances between 3.1 and 3.4 Å. The Fe–O bond lengths are rather long, as synthetic models generally have bond lengths between 1.8 to 2.0 Å. These elongated distances may be indicative of radiation damage to the crystal.

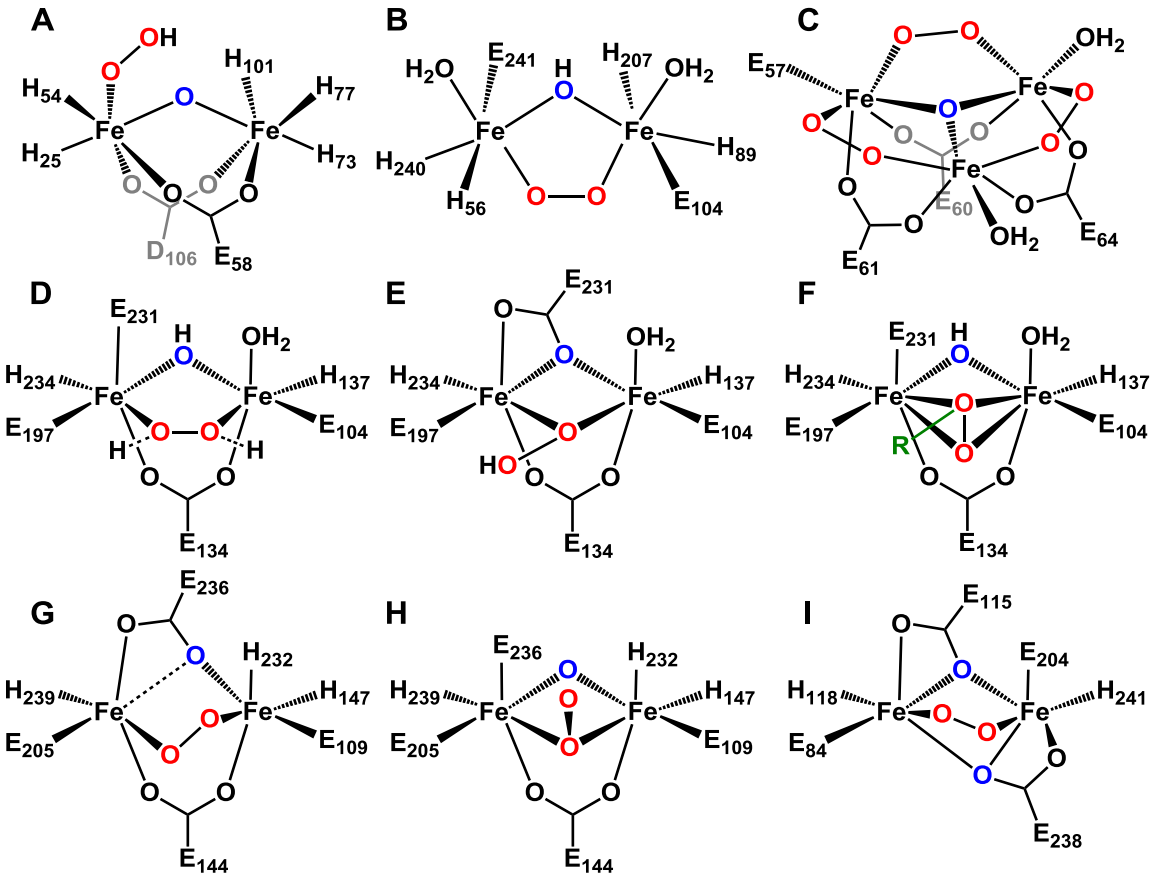

Figure 1.5. Structures of peroxo-diferric intermediates from nonheme diiron proteins. Peroxo ligands are red, single atom bridging ligands are blue. A: OxyHr, from XRD; B: hDOHH, from XRD and XAS; C: human L ferritin, from XRD; D: T4MOH μ-1,2-peroxo, from XRD; E: T4MOH Q228A μ-1,1-(hydro)peroxo, from XRD; F: T4MOH μ-η^2:η^2-arylperoxo, R represents toluene, from XRD; G: CmlI μ-1,2-peroxo, from XRD; H: CmlI μ-1,1-peroxo, from XAS; I: Proposed μ-1,2-peroxo for RNR and/or frog M ferritin, residue numbering from W48A/D84E RNR, from XAS.

The crystal structure of T4MOH was obtained by a slightly different method. Crystals of as-isolated T4MOH complexed with the effector protein T4MOD were soaked in H_2O_2 oxidant (PDB code 3I63). The use of H_2O_2 as a means to bypass the O_2-diferrous binding step and go directly to the peroxide intermediate is called the "peroxide-shunt"[82] and in T4MOH, H_2O_2 can be used for catalysis.[79] The result is two six-coordinate Fe centers bridged by a μ-1,3-carboxylate, a solvent derived single atom bridge *syn* to the His ligands and a μ-1,2-peroxo ligand *anti* to the His ligands (Figure 1.5D). One Fe center has a terminal solvent derived ligand, and the remaining coordination sites are filled by monodentate Glu ligands. The Fe•••Fe distance is 3.4 Å,

the Fe-O_{peroxo} distances are 2.2 and 2.4 Å, and the Fe-μ-O_{sol} distances of 2.1 and 1.9 Å. This differs from the proposed structure of sMMOH[83] in that the solvent derived single atom bridge in T4MOH is replaced by a μ-1,1-carboxylate that is bound in a bidentate mode to one Fe center in sMMOH, similar to the class 2 active site (see Figure 1.2). The Fe-O_{peroxo} bond lengths in this system are also longer than observed in synthetic peroxo-diferric models, which Bailey and Fox suggest is indicative that the peroxo ligand may be protonated, and could serve to weaken the Fe-O bonds.[79] As H_2O_2 is the source of the oxidant, this possibility is plausible, though there are no examples of diiron-H_2O_2 adducts against which to compare. Single crystal analysis would be required to acquire electronic absorption or resonance Raman data to further characterize this intermediate, as there is no observed accumulation in solution.

Recently, two more peroxo intermediates were crystallized from the T4MOH system using a similar strategy to the H_2O_2 generated complex.[28] A μ-1,1-peroxo species was generated using a Q228A variant where the reduced T4MOHD complex was crystallized anaerobically and the crystallization solution was bubbled with O_2 (PDB code 5TDV). The two six-coordinate Fe centers are bridged by a μ-1,1-peroxo, μ-1,3-glutmate, and a μ-1,1-glutamate residue bound in the same orientation as the diferrous structure of the WT T4MOHD,[56] maintaining an Fe•••Fe distance of 3.2 Å (Figure 1.5E). The Fe–O distances from the μ-1,1-glutamate ligand are at 2.1 Å, similar to the single atom bridge from the T4MOH μ-1,2-peroxo structure. The O–O distance is 1.5 Å and the proximal Fe–O_{peroxo} distances are also rather long at 2.4 and 2.5 Å. This may indicate some degree of photo reduction, and/or that the peroxo ligand is protonated. DFT calculation suggests that protonatation is possible, as a hydroperoxo species yields bond lengths that are congruent with those observed in the crystal structure.[28] The distal Fe–O_{peroxo} distances are 3.5 and 3.6 Å and the O atom is pointing into the substrate binding pocket.

A μ-η^2:η^2-peroxo species was generated using WT T4MOHD using the same method as the Q228A variant, but in the presence of the toluene substrate (PDB code 5TDT). In this active site, the Fe centers are bridged by single atom μ-solvent derived

ligand, μ-1,3-glutamate, and a μ-η^2:η^2-peroxo ligand (Figure 1.5F). Additionally, one O atom from the peroxo ligand (called $O2_{peroxo}$) appears to have bonded to the C4 position of a toluene molecule present in the active site. The O–O bond is 1.4 Å and the Fe–$O1_{peroxo}$ distances are both at 2.7 Å, and the Fe–$O2_{peroxo}$ distances are at 2.5 and 2.8 Å. These very long Fe–O distances clearly demonstrate that the peroxo ligand is not tightly bound to the diiron cluster. DFT geometry optimization suggests that this intermediate is consistent with a mixed valent $Fe^{II}Fe^{III}$-arylperoxo species; however, the oxidation states of the Fe centers are not possible to determine from the XRD structures.[28] This series of T4MOH structures is intriguing, as it demonstrates that the 2-His-4-carboxylate-supported active site is versatile and can accommodate three distinct peroxo binding geometries, two of which (μ-1,1-(hydro)peroxo and μ-η^2:η^2-peroxo) have never been structurally characterized in diiron before. Interestingly, the peroxo species of T4MOH are not observed in the solution state, despite the very similar active site structure to sMMOH and other systems where peroxo species have been observed. On the other hand, there have been no reports of an sMMOH peroxo intermediate generated in an analogous manner to T4MOH.

CmlI has also been shown to accommodate different peroxo binding geometries through XRD and spectroscopic studies.[15, 35] A crystal of a 33 amino acid truncated variant of CmlI, CmlIΔ33, was obtained.[35] The crystallization media, in the presence of air, generated H_2O_2 and the resulting structure was of a μ-1,2-peroxo species (PDB code 5HYG) with μ-1,3-carboxylate and a pseudo-μ-1,1-carboxylate bridging protein ligand similar to the Q228A variant of T4MOH (Figure 1.5G). The "pseudo" distinction is made for the μ-1,1-carboxylate as the Fe–O distance are 2.2 and 2.6 Å, which is on average longer than the 2.1 Å distance found in Q228A T4MOH, but the diiron cluster is able to maintain an Fe•••Fe distance of 3.3 Å. In comparison to the other peroxo structures presented, the Fe–O_{peroxo} distances for CmlIΔ33 are 1.8 and 2.0 Å, which agree with synthetically derived peroxo-diferric structures. The Fe–O_{distal} distances are at 2.8 and 2.9 Å and an O–O distance of 1.5 Å. This peroxo species can also be generated from diferric WT or Δ33 CmlI in solution using H_2O_2. A broad visible absorption band at 600 nm

appears in the presence of excess hydrogen peroxide, consistent with a μ-1,2-peroxo binding geometry.[35] However, if O_2 is introduced to the reduced form of the WT or Δ33 enzyme, a different peroxo intermediate is generated, with a visible absorption band at 500 nm.[15] The structure of the 500 nm intermediate in WT CmlI has been assigned through a combination of XAS and rR studies as a μ-1,1-peroxo species (see Chapter 4 for the detailed analysis). The iron centers are bridged by a μ-oxo ligand with Fe–O distances of 1.83 Å, a μ-1,1-peroxo with a proximal Fe–O distances of 1.98 Å and a distal Fe–O distance of 2.82 Å (Figure 1.5H) A μ-1,3-carboxylate ligand is also assumed to bind to the cluster, though there is no direct evidence of this from XAS. The diiron cluster maintains an Fe•••Fe distance of 3.35 Å, consistent with the crystallographically characterized peroxo species above.

Of these structurally characterized peroxo species, there are a few common features that the proteins use in peroxo-diferric intermediates. The Fe•••Fe distance falls between 3.2 and 3.5 Å across four peroxo binding geometries (Table 1.5). The diiron core is held together with μ-1,3-carboxylate bridges, in addition to single atom bridging ligands in every active site. In the diiron enzymes, Fe–O_{peroxo} bond lengths tend to be on the long side (>2.0 Å) regardless of O_2 binding mode, which is the result of either photoreduction or the protonation state of the peroxo ligand.

The remaining two enzymatic peroxo species are from RNR and frog M ferritin, and their characterization by EXAFS raises some interesting questions about their active site structure. Through spectroscopic analysis, both RNR and frog M ferritin have been assigned a μ-1,2-peroxo binding mode.[32, 61, 68, 84] Based on this peroxo binding assignment, Fe•••Fe distances between 3.2 and 3.5 Å could be anticipated for these short lived peroxo intermediates. However, EXAFS analysis yields distances of 2.50 and 2.53 Å for RNR and frog M ferritin, respectively.[32, 37] To rationalize these results, it was suggested that multiple single atom μ-1,1-carboxylate ligands could account for the short Fe•••Fe distance (Figure 1.5I), based on multiple μ-oxo bridged Fe, and Mn model complexes. Indeed, single atom bridging by μ-1,1-carboxylate ligands is observed in the crystal structures of CmlI[35] and T4MOH,[28] however, there is no crystallographically

characterized diiron active site with two of this type of carboxylate ligand. Additionally, there have been no characterized synthetic peroxo-diferric intermediates with Fe•••Fe distances < 3.0 Å (see Section 1.4). While the dynamic nature of the solution state could allow for a reorganization of the protein fold and allow for multiple μ-1,1-carboxylate bridges, further characterization is required to understand the active site structures of peroxo species with short Fe•••Fe distances.

1.3.5 – Structural Characterization of Peroxo-Diferric Intermediates by XANES Analysis

The reported XANES analyses for enzymatic peroxo-diferric intermediates is restricted to three species, the μ-1,1-peroxo CmlI, frog M ferritin and hDOHH.[36, 37] Similar to the observations from the diferrous clusters, the K-edge energies are not found at the same energy despite having the same oxidation state. Frog M ferritin has a K-edge at 7124 eV, and CmlI and hDOHH have energies at 7124.9 and 7125.6 eV, respectively. This is 1.6 eV range for peroxo-diferric species, which makes definite assignment of Fe oxidation state difficult with single K-edge energies.

The pre-edge features of the enzyme species are varied, but useful comparisons to synthetic models can be instructive. From synthetic complexes, six-coordinate (μ-oxo)diferric species have pre-edge areas between 13 and 17 units, with an average of 14.5 units.[44, 85] hDOHH has a pre-edge of 12.4 units, which is below the range of μ-oxo dimers, and consistent with assignment as a μ-hydroxo species.[36] The pre-edge area of the ferrtin peroxo species is just inside of the range for μ-oxo dimers (13.6 units), but there is no evidence from EXAFS supporting the presence of a μ-oxo bridge.[37] This could point to a possible μ-hydroxo or μ-1,1-carboxylate bridge at ~2 Å, consistent with the EXAFS analysis. The peroxo species of CmlI has a much higher value for the pre-edge area at 19.2 units. This exceeds the range of reported μ-oxo dimers, which indicates a high degree of distortion in the CmlI active site. This distortion is consistent with XAS and rR analyses.

Table 1.3. Summary of rates of formation and spectroscopic characterization for peroxo-diferric intermediates of nonheme diiron proteins. k_{form} and k_{decay} refer to the first order rate constants for peroxo intermediate formation and decay. [a] temp. between 4-5 ºC. [b] temp. between 20 – 25 ºC. [c] k_{obs}. [d] half-life. [e] k_{on} ($M^{-1}s^{-1}$). [f] calculated first order rate constant. [g] numbers from $^{18}O_2$ and D_2O substitutions in parenthesis and brackets, respectively. [h] proposed structure based on limited structural characterization.

Species	k_{form} (s^{-1})	k_{decay} (s^{-1})	**δ (mm/s)**	**ΔE_Q (mm/s)**	**ν(O–O)[g] (cm^{-1})**	**Mode**	**ref**
Ec R2-RNR	2.0[a]	0.26[a]	0.60, 0.66	1.47, 1.68	870 (-46)	μ-1,2	*32, 68*
Δ^9D	-	0.45×10^{-3} [b]	0.64, 0.68	1.06, 1.90	898 (-54)	μ-1,2	*67, 86*
ADO	0.75[a]	0.17×10^{-2} [a]	0.48, 0.55	0.49, 1.23	-	μ-η^2:η^2/μ-1,1[h]	*25*
AurF	147[b, c]	0.08[b, c]	0.54, 0.61	0.66, 0.35	-	μ-1,2/μ-1,1–OOH[h]	*59*
CmlI		~3 h[a, d]	0.62, 0.54	-0.23, -0.68	791 (-43)	μ-1,1	*15*, Ch. 4
sMMOH	9.1[a], 25[a]	2.6[a], 0.4[a]	0.66	1.51	-	μ-1,2[h]	*69, 70, 72*
ToMOH	26[a]	0.045[a]	0.55	0.67	-	μ-1,1-OOH[h]	*24*
Frog M ferritin	80[b]	3[b]	0.62	1.08	851 (-51)	μ-1,2	*37, 61, 84*
Hr	1.2×10^7 [b, e] (1.6×10^3 [f])	-	0.54, 0.51	1.92, 1.09	844 (-46) [+4]	η^1-OOH	*63, 66, 73, 87*
hDOHH	-	>24 h[b, d]	0.55, 0.58	1.16, 0.88	855 (-44)	μ-1,2	*65*

Table 1.4. Analysis of Mössbauer parameters from enzymatic peroxo-diferric intermediates. [a] units of mm/s.

Type of Complex	δ[a]			ΔE_Q[a]		
	Low	**High**	**Average**	**Low**	**High**	**Average**
All Enzyme Peroxo	0.48	0.68	**0.58**	0.23	1.92	**1.06**
Enzyme μ-1,2-peroxo	0.55	0.68	**0.62**	0.88	1.90	**1.34**
Enzyme not μ-1,2-peroxo	0.48	0.62	**0.55**	0.23	1.92	**0.81**

Table 1.5. Selected structural parameters of peroxo-diferric active sites from XRD and XAS studies. Distances are in angstroms. [a] Resolution from XRD experiments. [b] range of Fe•••Fe values from the peroxo-diferric trimer.

Enzyme	K-edge (eV)	Pre-edge area (units)	Fe•••Fe (XRD)	Fe•••Fe (EXAFS)	Bridge type	Binding Mode	PDB code	Res.[a] (Å)	Ref
Ec R2-RNR	-	-	-	2.50	μ-1,1-carboxylato	μ-1,2	-	-	*32*
CmlI	7124.9	19.2	-	3.35	μ-1,3-carboxylato μ-oxo	μ-1,1	-	-	Ch. 4
CmlI	-	-	3.3	-	μ-1,3-carboxylato μ-1,1-carboxylato	μ-1,2	5HYG	2.03	*35*
T4MOH	-	-	3.4	-	μ-1,3-carboxylato μ-solvato	μ-1,2	3I63	2.09	*79*
T4MOH	-	-	3.2	-	μ-1,3-carboxylato, μ-1,1-carboxylato	μ-1,1	5TDV	2.0	*28*
T4MOH	-	-	3.3	-	μ-1,3-carboxylato μ-solvato	μ-η^2:η^2	5TDT	1.82	*28*
Frog M ferritn	7124	13.3	-	2.53	μ-1,1-carboxylato	μ-1,2	-	-	*37*
Human L Ferritin	-	-	3.2-3.5[b]	-	μ-1,3-carboxylato, μ^3-oxo	μ-1,2	5LG8	1.98	*80*
Hr	-	-	3.3	3.24	μ-1,3-carboxylato, μ-oxo	η^1-OOH	1HMO	2.0	*33, 34*
hDOHH	7125.6	12.4	3.8 (3.7)	3.41	μ-hydroxo	μ-1,2	4D50	1.7	*17, 36*

1.4 – Synthetic Peroxo-Diferric Intermediate Structure and Properties

Synthetic complexes are used as spectroscopic and structural surrogates for enzyme active sites before protein structural metrics become available. Model complexes can be systematically altered through stepwise synthesis and can be exposed to harsh conditions like extremes of pH and temperature in an effort to trap transient intermediates; methods that are generally not compatible with the biochemistry. The development of a synthetic library of spectroscopic parameters has been critical to assigning metalloenzyme structure and spectroscopic features. However, most of the characterized synthetic peroxo-diferric complexes have μ-1,2-peroxo binding geometries and use primarily neutral N-donor supporting ligands. Therefore, these complexes provide limited points of comparison to enzymatic peroxo-diferric intermediates with alternative peroxo binding geometry.

1.4.1 – Synthetic Approaches to Modeling the Diiron Active Site

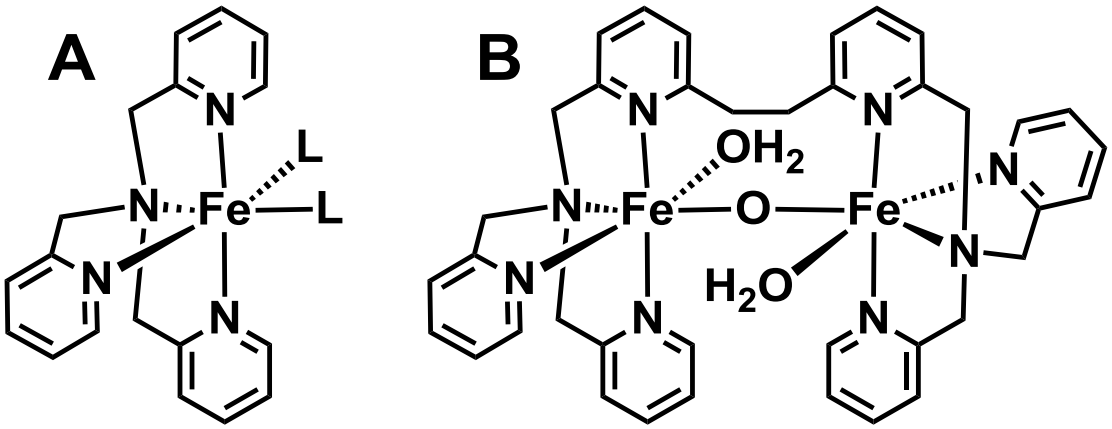

Figure 1.6. Examples of synthetic mononuclear and dinuclear nonheme iron complexes. A: mononuclear iron complex supported by the TPA ligand; B: a dinuclear iron complex supported by the 6-HPA ligand.

Synthetic models generally employ supporting ligands with N-donors such as tertiary amines and pyridines and O-donors like carboxylate and alkoxide ligands to mimic histidine and glutamate ligands, respectively. This allows for the complexes to approximate the geometry and energy levels of the protein derived ligands in diiron active sites. Some of the ligands, like the N-donor ligand TPA (TPA = tris(2-

pyridylmethyl)amine) support tetradentate binding to the Fe center, leaving two *cis* labile sites and generate a monoiron complex (Figure 1.6A).[88] These monoiron species can be dimerized to synthetically yield a diiron cluster. Other approaches involve the synthesis of a dinucleating ligand like 6-HPA (6-HPA = 1,2-bis[2-{bis(2-pyridylmethyl)amino-methyl}-6-pyridyl]ethane), which chemically links two TPA monomers and forces the two Fe centers to generate a dimeric species (Figure 1.6B).[89] Both of these approaches have been successfully used to trap and study peroxo-diferric intermediates.

Two strategies have been developed to generate synthetic peroxo-diferric complexes. One is synthesizing a diferrous complex and bubbling O_2 into the solution to generate a peroxo species[90-100, 101 3704] and the other strategy is the use of a diferric complex and H_2O_2 in a peroxide-shunt type reaction.[89, 102-108] Both strategies have benefits and drawbacks. Use of O_2 as an oxidant is clean, as it can be introduced into a solution without additives, but ferrous iron is required for these reactions. If an O_2 sensitive complex is used, the complex needs to be more carefully handled outside of an anaerobic environment like a glove box. Use of hydrogen peroxide with ferric complexes can be done with stoichiometric H_2O_2 in ideal conditions, and the peroxo species can be formed *via* ligand exchange. However, hydrogen peroxide is diluted in water (30% hydrogen peroxide is widely available), which can interfere with the desired chemistry, and using more concentrated hydrogen peroxide (70 to 90%) is an explosion risk. The intermediates from either method tend to be more stable than their enzymatic counterparts, particularly at lower temperatures. Several of these intermediates have been crystallized[91, 94, 103, 109] and many more have been characterized by XAS analysis.[96, 100, 105, 110-112]

1.4.2 – UV-vis Spectral Properties of Synthetic Peroxo-Diferric Complexes

The peroxo-to-iron(III) LMCT transition in synthetic peroxo-diferric complexes have intense visible absorption maxima between ~570 to 700 nm, yielding a blue or green color. As seen in Table 1.6, most of the synthetic complexes have been assigned

with a μ-1,2-peroxo binding mode, and as such, the visible absorption features are similar to the enzymatic peroxo species.

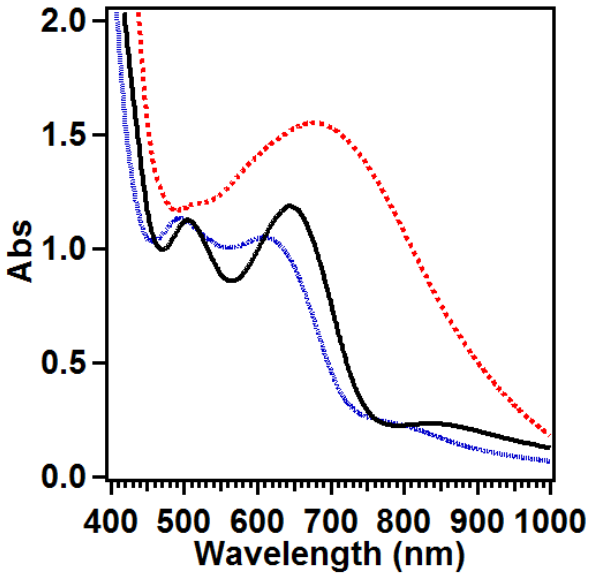

Figure 1.7. Representative UV-vis spectra of synthetic peroxo-diferric intermediates. The spectra of **1** (black solid), **7** (Blue dotted) and **11** (red dashed) are shown, taken at -40 ºC in MeCN. Spectrum of **7** provided by Dr. Jai Prakash. See Table 1.6 for complex definitions.

Synthetic models with a μ-oxo bridge have an additional feature at ~500 nm that can be assigned to the oxo-to-iron(III) LMCT transition. In the (μ-1,2-peroxo)(μ-oxo)diferric complexes **1**, **2**, **3**, **5** and **5-Me** (for complex definitions see Table 1.6) all have two distinct features corresponding to the oxo and peroxo LMCT transitions (Figure 1.7, black solid). These complexes can all be generated using O_2 as an oxidant.[92, 111] Complexes **4** and **6** are also (μ-1,2-peroxo)(μ-oxo)diferric species, but with a single broad LMCT transition in the visible region.[105, 108] The binuclear complexes studied by Kodera and co-workers (**7** – **9**)[89, 104, 111, 113] at low temperatures (~40 ºC) in the presence of H_2O_2 are proposed to generate (μ-1,2-peroxo)(μ-oxo)diferric species. However, the absorption features associated with **7** – **9** are less distinct than in the O_2 generated complexes (**1**, **2**, **3**, **5** and **5-Me**), presumably because the peroxo and oxo LMCT transitions in **7** – **9** appear to be broadened, and overlap each other (Figure 1.7, blue dotted).

Synthetic complexes can also be generated with μ-OR ligands, where OR can be a μ-hydroxo or μ-alkoxo ligand. When the μ-oxo bridging peroxo species **1** and **2** are treated with acid, they generate μ-hydroxo peroxo species (**1-H**, **2-H**).[103, 110] These intermediates have red shifted visible absorption features that have an increased intensity compared to the μ-oxo form. The protonation is reversible through the addition of base and UV-vis features associated with the (μ-oxo)(μ-1,2-peroxo) species are recovered. Complexes **10**, **11**, **11-O_2PPh$_2$**, **11-η^1-O_2PPh$_2$**, **12**, **13**, **13-Me$_4$**, and **13-amide$_4$** all have dinucleating ligands with a μ-alkoxo bridge as part of the framework,[94, 95, 97, 98, 106, 112] and all but **12** have been reported to form using O_2 as an oxidant. These complexes tend to have a single, intense feature assigned to the peroxo-to-iron(III) LMCT transition. The spectrum for **11** is shown in Figure 1.7 (red dashed).

There are several examples of peroxo intermediates (**14-OBz**, **14-PPA**, **16**) that do not have a single atom bridging ligand. These complexes are instead supported by two μ-1,3-carboxylate ligands.[90, 91, 99] Interestingly, the LMCT transitions for **14-OBz** and **14-PPA** are at 682 and 694 nm, respectively, whereas **16**, which has a similar proposed overall structure has a feature at 580 nm. Complex **15** is proposed to have no additional supporting ligands, only a μ-1,2-peroxo ligand, with a visible absorption maximum at 685 nm.[107]

The majority of the characterized synthetic peroxo-diferric species have μ-1,2-peroxo binding modes, but there are several examples of complexes that do not. Complex **17** uses bulky carboxylate ligands to support a peroxo intermediate with a broad absorption feature ~500 nm.[93] Spectroscopic analysis has led to a proposed μ-η^1:η^2-peroxo binding geometry for this species (see Chapter 5 for more details). Terminally bound hydroperoxo-diferric species have also been trapped and characterized. Complex **18** has the most characterization with an absorption feature at 484 nm,[96] while **3-OOH** and **6-OOH** were identified using rR from a mixture of several intermediate species.[101, 108]

1.4.3 – Characterization of Synthetic Peroxo-Diferric Complexes by Resonance Raman Spectroscopy

The study of synthetic peroxo complexes by rR spectroscopy has helped to establish a possible range of ν(O–O) values for different peroxo ligand binding modes, although as most synthetic peroxo species form a μ-1,2-peroxo, the utility of comparison to synthetic complexes is limited. An analysis of the values of ν(O–O) for the peroxo species presented here is summarized in Table 1.6 and Table 1.7. Across all of the assigned μ-1,2-peroxo intermediates, the O–O vibration ranges from 826 to 928 cm^{-1} (average of 870 cm^{-1}). This overall range can be further subdivided into groups based on the bridging ligands. The (μ-oxo)(μ-1,2-peroxo) species have a ν(O–O) range from 826 to 874 cm^{-1}, and (μ-OR)(μ-1,2-peroxo) species (where μ-OR represents a μ-hydroxo or μ-alkoxo ligand) have a range of values between 845 and 928 cm^{-1}, with average values of 848 and 888 cm^{-1}, respectively. Based on the average values, species with μ-oxo ligands have lower a ν(O–O) than species with μ-OR ligands, but the overlapping range is not useful to distinguish between these two types of complexes. Peroxo intermediates without a single atom bridge have a range of values between 861 and 888 cm^{-1}, a narrow range, but one that overlaps with the μ-oxo and μ-OR peroxo complexes. The average ν(O–O) falls between the μ-oxo and μ-OR complexes with a value of 875 cm^{-1}. The enzymatic μ-1,2-peroxo species have a range of ν(O–O) between 851 and 898 cm^{-1}, with an average of 867 cm^{-1}. On the surface, this suggests that the enzymatic peroxo intermediates, on average, are less consistent with a (μ-oxo)(μ-1,2-peroxo) core. Based on the structural analysis presented in the previous section, this appears to be true.

Upon close scrutiny of the (μ-oxo)(μ-1,2-peroxo) data, complexes **7 – 9** appear to have a systematic difference from the other members of the group. As mentioned above, the absorption maxima of **7 – 9** are similar to the UV-vis features of the other μ-oxo species, but with peaks that are broader than the other μ-oxo counterparts. The reported ν(O–O) values for these complexes have a tight range between 826 and 835 cm^{-1}, which is much lower than the ~850 cm^{-1} average across all μ-oxo species (Table 1.7). Removal

of **7 – 9** from the other μ-oxo species does not significantly affect the average (855 vs 848 cm^{-1}) but the range narrows to 844 – 874 cm^{-1} (from a 47 cm^{-1} to a 30 cm^{-1} range). XAS experiments show that (see Section 1.4.5) **7** has a similar diiron core to **1** and **3**, but an O–O stretch ~20 cm^{-1} lower than the other two. Based on analysis by Brunold et al., the ν(O–O) in μ-1,2-peroxo species is affected by the Fe-O-O angle, with smaller angles corresponding to smaller values for ν(O–O).[90] This is due to the amount mechanical coupling of Fe–O and O–O vibrations. The lower ν(O–O) in **7 – 9** possibly indicates that the type of ligand framework used decreases the Fe-O-O angle, and subsequently results in the lower ν(O–O) compared to complexes like **3**. However, this is at odds with the observations from available XAS structures. An alternative interpretation is that the peroxo ligand in **7 – 9** may not be bound in a μ-1,2-peroxo mode.

Terminal hydroperoxo-diferric species have lower ν(O–O) values than μ-1,2-peroxo intermediates, between 806 and 841 cm^{-1} (average of 826 cm^{-1}). Interestingly, two of the three hydroperoxo species (**3-OOH**, **6-OOH**) are supported by ligands that also generate μ-1,2-peroxo intermediates, showing the versatility of some of the supporting ligands. The remaining complex, **17**, has a ν(O–O) of 822 cm^{-1},[93] which places it outside of the range of μ-1,2-peroxo complexes. Complex **17** is proposed to have a μ-η^1:η^2-peroxo binding mode, despite being in the range of terminal hydroperoxo species.

As observed in Table 1.7, the ranges for ν(O–O) values based on structural differences have substantial overlap. Generalization to structure from these values can be cautiously made, but supplementary information is required for accurate determination of structure. Additional features in the rR spectrum, like Fe–O–Fe, Fe–O_2, Fe–O, and Fe–O_2–Fe vibrations can be used as markers for different peroxo-diiron core structures. However, these are not commonly reported (for a list of additional rR features of peroxo-diferric intermediates, see Table 2 from ref [110]).

1.4.4 – Structural Analysis of Synthetic Peroxo-Diferric Intermediates by Mössbauer Spectroscopy

Mössbauer analysis is applied to the synthetic peroxo-diferric complexes in an effort to characterize the effect of the ligand environment on the isomer shift and quadrupole splitting (Table 1.7). The Fe^{III} centers in the synthetic peroxo-diferric complexes are generally characterized as high spin S = 5/2 centers that AF couple to a ground spin state of S = 0, similar to enzymatic peroxo-diferric intermediates. The isomer shift values range from δ = 0.23 to 0.66 mm/s (average of 0.52 mm/s) and quadrupole splitting values range from ΔE_Q = 0.49 to 1.76 mm/s (average of 1.24 mm/s) across all peroxo-diferric species (Table 1.6 and Table 1.7). Dividing more finely, μ-1,2-peroxo species have ranges of δ = 0.35 to 0.66 mm/s and ΔE_Q = 0.62 to 1.76 mm/s, with average values of δ = 0.54 mm/s and ΔE_Q = 1.29 mm/s. This is essentially the same as when all peroxo-diferric species are included, however, most of the complexes presented are μ-1,2-peroxo species. Regardless of bridging ligands, the range of Mössbauer parameters overlaps, but the average values seem to differ. The μ-oxo, μ-OR and no single atom bridge species have average values of δ = 0.49 mm/s and ΔE_Q = 1.45 mm/s, δ = 0.56 mm/s and ΔE_Q = 1.19 mm/s and δ = 0.59 mm/s and ΔE_Q = 1.16 mm/s, respectively (Table 1.7). The available data suggests that isomer shift increases with a decrease in the strength of the auxiliary bridging ligands. Following this trend, the enzyme μ-1,2-peroxo species have an average of δ = 0.62 mm/s, as they generally employ μ-OH and μ-1,1-carboxylate ligands.

The quadrupole splitting does not appear to have a discernible trend, as the μ-oxo species have the highest average value of 1.45 mm/s, the μ-OR species and those intermediates with no single atom bridge have values at ~1.20 mm/s, and the enzyme species have an average at 1.34 mm/s. The ΔE_Q parameter may be sufficiently sensitive such that the ligand identity contributes a great deal to this parameter. Thus, ligand identity should be taken into account when making generalizations of peroxo-diferric intermediates using Mössbauer parameters. For example, the two terminal hydroperoxo

species with available parameters have average values of δ = 0.42 mm/s and ΔE_Q = 1.26 mm/s, which don't compare particularly well to those of OxyHr (δ = 0.51, 54 mm/s and ΔE_Q = 1.09, 1.92 mm/s). However, complex **18** is an accurate structural model to OxyHr, with two μ-1,3-carboxylate and a μ-oxo bridge as well as a terminal hydroperoxo ligand, and has δ = 0.49, 0.53 mm/s and ΔE_Q = 1.15, 1.76 mm/s, which compare quite well to OxyHr.[96]

1.4.5 – Structural Characterization of Synthetic Peroxo-Diferric Intermediates by XRD and XAS

The relative stability of synthetic peroxo complexes has led to the structural characterization of many μ-1,2-peroxo species, the results of which are summarized in Table 1.8. The acid base pair of **2** and **2-H** were crystallized and studied by Suzuki and co-workers (Figure 1.8A).[103] The crystal structure of **2** has a μ-oxo and a μ-peroxo ligand disordered over two positions, so detailed analysis of bond lengths will be carried out with caution. The Fe•••Fe distance of **2** is 3.17 Å, with average Fe–O_{oxo} bonds of ~1.73 Å and Fe–O_{peroxo} bonds of ~ 2.1 Å. In comparison, **2-H** has metrics corresponding to an Fe•••Fe distance of 3.395 Å, Fe–μ-OH bonds of 1.943 and 2.006 Å, and Fe–O_{peroxo} bond lengths of 1.887 and 1.867 Å. These two structures demonstrate that upon protonation of the μ-oxo bridge, the diiron core expands.

XAS studies of frozen solutions of peroxo complexes with analogous diiron structures to **2** and **2-H** agree with the crystallographically derived metrics. Peroxo complexes with μ-oxo ligands have Fe•••Fe distances between 3.13 and 3.16 Å with Fe–O_{oxo} distances of ~1.8 Å and Fe–O_{peroxo} distances between 1.8 and 1.9 Å.[102, 105, 110, 111] The only other characterized μ-OH peroxo complex is **1-H**, which has an Fe•••Fe distance of 3.41 Å, and an Fe–O distance of 1.91 Å for both the μ-hydroxo and μ-1,2-peroxo ligands.[110]

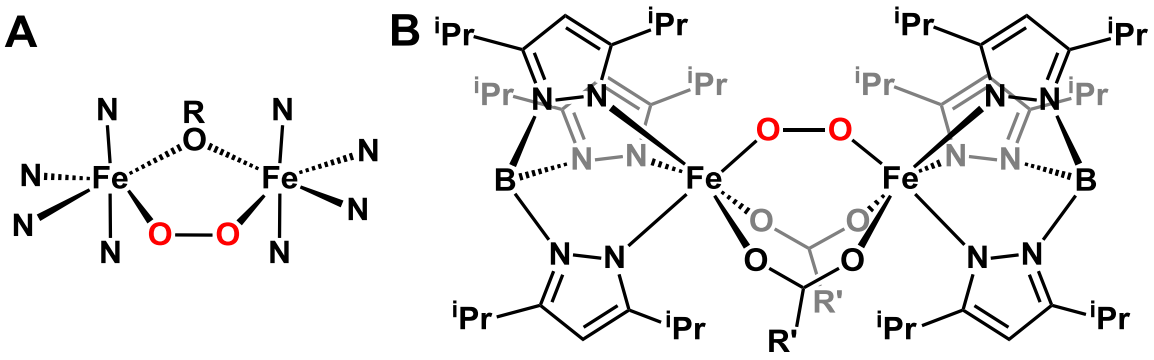

Figure 1.8. Structures of synthetic peroxo-diferric intermediates. Peroxo ligand atoms are red. A: a representative structure of (μ-1,2-peroxo)(μ-OR)diferric species, where μ-OR represents a single atom bridge. The N atoms represent the N/O-donors of the synthetic ligands used; B: the crystal structure of **14-PPA** where R'COO represents phenylacetate.

As mentioned previously, complexes **7 – 9** have interesting O–O vibrations that don't fall in the range of other (μ-oxo)(μ-1,2-peroxo)diferric species. XAS analysis has been carried out on **7** (see Chapter 5 for the full analysis) and **9** to clarify the source of the unusual vibration.[111] The structural parameters of **7** are almost identical to those of **3**, with Fe•••Fe distances at 3.15 and 3.14 Å and Fe–O distances at 1.86 and 1.85 Å, respectively (Table 1.8).[102] However, the ν(O–O) values for **7** and **3** are 826 and 847 cm^{-1} (Table 1.6), and therefore, these vibrations do not appear to reflect the structural metrics. Based on DFT calculation,[111] **3** should have an Fe-O-O angle of ~118º, and based on the similarity by XAS of **3** and **7**, complex **7** should also have a similar angle. This would indicate that mechanical coupling cannot alone explain the difference in ν(O–O) between **3** and **7**. However, XAS is limited to providing radial distances from the Fe center, and cannot provide the three-dimensional position of atoms in space. Therefore, if the peroxo ligand in **7** were distorted out of the Fe–O–O–Fe plane, the Fe–O distance might remain the same from EXAFS analysis but would change the Fe–O–O angle, and the mechanical coupling along with it. The pre-edge area of **7** is 13.2 units and is very similar to **3**, which has a value of 12.5 units. This suggests that a substantial distortion in the peroxo ligand is unlikely. It is therefore possible that the 826 cm^{-1} stretch from **7** belongs to a peroxo species that is different from μ-1,2-peroxo species. Another incongruence with complexes **7 – 9**, is the 0.1 Å shorter Fe•••Fe distance of **9**, at 3.04 Å.[111] Despite this difference in

Fe•••Fe distance, the ν(O–O) of **9** at 830 cm^{-1} is essentially the same as that of **7**, and the K-edge and pre-edge values are almost identical as well. These discrepancies require further analysis to fully understand the structure (Table 1.8).

Another system that yielded a crystal structure of a μ-1,2-peroxo species is **11**. The μ-OR core of **11** has similar structural parameters to the μ-OH bridged peroxo complexes **1-H** and **2-H**, with an Fe•••Fe distance of 3.463 Å, Fe–O_{alkoxo} and Fe–O_{peroxo} bond lengths of 1.991 Å and 1.881 Å, respectively. This demonstrates that in synthetic complexes, μ-alkoxo and μ-hydroxo ligands will have similar effects to the structure. Complex **11** is an ideal candidate for studying the effect of a carboxylate ligand on a peroxo-diferric diiron core, as the crystals of ferrous precursors with carboxylate-like ligands were readily obtained.[112] A diphenylphospinate ligand was introduced to **11** as a carboxylate ligand surrogate, and two species were identified, **11-$\eta^1$$O_2PPh_2$** and **11-$O_2PPh_2$**. From XAS studies, **11-$\eta^1$$O_2PPh_2$** was determined to have the phosphinate ligand bound in a monodentate mode to one of the Fe centers. Structural metrics of Fe•••Fe at 3.47 Å, Fe–O_{alkoxo} at 2.04 Å and an Fe–O_{peroxo} at 1.88 Å were observed. These metrics agree well with those of **11**. However, when the phosphinate binds in a μ-1,3-mode in **11-O_2PPh$_2$**, the Fe•••Fe distance contracts to 3.25 Å, concomitant with a decrease in ν(O–O) from 897 to ~850 cm^{-1}.[112] This shows that carboxylate coordination, in the presence of a single atom bridge, can have a substantial effect on the structure of the diiron core, and the strength of the O–O bond.

A crystal of a μ-1,2-peroxo species without a single atom bridge, **14-PPA**, was also obtained (Figure 1.8B).[91] This model complex has an anionic supporting ligand, in addition to two μ-1,3-carboxylate bridges. The Fe–O_{peroxo} distances are 1.876 and 1.906 Å, with an Fe•••Fe distance of 4.000 Å, which is much longer than any of the metal separations observed in the enzymatic peroxo species (Table 1.5). This indicates that the single atom bridge is important for restricting the Fe•••Fe between 3.2 and 3.4 Å. Interestingly the Mössbauer parameters (δ = 0.66 mm/s, ΔE_Q = 1.40 mm/s)[91] are quite similar to the average values for the enzyme μ-1,2-peroxo species (δ = 0.62 mm/s, ΔE_Q =

1.34 mm/s), despite the structural incongruence. This should further reinforce that proper context is required for applying Mössbauer parameters in structural analyses.

The terminally bound hydroperoxo-diferric intermediates do not have much structural characterization, primarily because **3-OOH** and **6-OOH** came from a mixture of at least two different peroxo species. Under these conditions, XAS analysis can be difficult to accurately interpret. However, complex **18** was generated in high yield, EXAFS data was collected.[96] A short Fe–O distance consistent with a μ-oxo bridge was observed at ~1.8 Å, and an Fe•••Fe distance was found at 3.16 Å. Coincidentally, this Fe•••Fe distance is similar to the (μ-oxo)(μ-1,2-peroxo) species (Table 1.8). Complex **18** in comparison to **14-PPA**, supports the notion that single atom bridges are important for maintaining a Fe•••Fe distance between 3.2 and 3.4 Å.

Table 1.6. Mössbauer and resonance Raman parameters for synthetic peroxo-diferric complexes in this chapter. [a] numbers in parentheses refer to the isotope shift from $^{18}O_2$. [b] peroxo ligand binding geometry. [c] ν(O–O) and shift calculated from analysis of a Fermi doublet. [d] two independent O–O vibrations were observed.

Complex	δ (mms^{-1})	ΔE_Q (mms^{-1})	ν(O–O)[a] (cm^{-1})	Binding[b] Mode	Ref
1	0.55	1.43	854 (-47)	μ-1,2	*110*
2	0.50	1.46	847 (-33)	μ-1,2	*103*
3	0.54	1.68	847 (-44)	μ-1,2	*102,111*
4	-	-	874 (-38)	μ-1,2	*105*
5	-	-	844 (-44)	μ-1,2	*111*
5-Me	-	-	853 (-45)	μ-1,2	*111*
6	0.49	0.62	867 (-48)	μ-1,2	*108, 114*
7	0.35	1.64	826 (-51)	μ-1,2	*89, 115*
8	0.48	1.66	835 (-51)	μ-1,2	*113*
9	0.53	1.67	816 (-45), 830	μ-1,2	*104 111*
1-H	0.57, 0.56	1.35, 0.96	925 (-53)	μ-1,2	*110*
2-H	0.50	1.31	908 (-47)	μ-1,2	*103*
10	0.58, 0.65	0.74, 1.70	-	μ-1,2	*94*
11	-	-	900 (-50)	μ-1,2	*95*
11-O_2PPh_2	0.56	-1.26	845, 853 (-42)	μ-1,2	*112*
11-$\eta^1O_2PPh_2$	0.53	-1.03	897 (-49)	μ-1,2	*112*

Table 1.6. (continued) Mössbauer and resonance Raman parameters for synthetic peroxo-diferric complexes in this chapter. [a] numbers in parentheses refer to the isotope shift from $^{18}O_2$. [b] peroxo ligand binding geometry. [c] ν(O–O) and shift calculated from analysis of a Fermi doublet. [d] two independent O–O vibrations were observed.

Complex	δ (mms^{-1})	ΔE_Q (mms^{1})	ν(O–O)[a] (cm^{-1})	Binding[b] Mode	Ref
12	-	-	884	μ-1,2	*106*
13	-	-	877, 893 (-51)	μ-1,2	*95*
13-Me$_4$	-	-	908 (-47)[c]	μ-1,2	*97*
13-amide$_4$	-	-	887(-48), 873 (-48)[d]	μ-1,2	*98*
14-OBz	-	-	876 (-48)	μ-1,2	*90*
14-PPA	0.66	1.40	888 (-46)	μ-1,2	*91*
15	-	-	876 (-50)	μ-1,2	*107*
16	0.47, 0.63	0.88, 1.20	861 (-50)	μ-1,2	*99*
17	0.65, 0.52	1.27, 0.71	822 (-43)	μ-η^1:η^2	*93*
18	0.53, 0.49	1.76, 1.15	841 (-43)	η^1-OOH	*96*
6-OOH	0.43, 0.23	0.49, 1.64	806 (-44)	η^1-OOH	*108, 114*
3-OOH	-	-	831 (-47)	η^1-OOH	*101*

1 = $[Fe^{III}_2(O_2)(O)(BnBQA)_2]^{2+}$, BnBQA = *N*-benzyl-*N*,*N*-bis(2-quinolinylmethyl)amine; **2** = $[Fe^{III}_2(\mu\text{-}O)(O_2)(6\text{-}Me_2BPP)_2]^{2+}$, 6-$Me_2$BPP = bis(6-methyl-2-pyridylmethyl)-3-aminopropionate; **3** = $[Fe^{III}_2(O)(O_2)(6\text{-}Me_3TPA)_2]^{2+}$, 6-$Me_3$TPA = tris(6-methyl-2-pyridylmethyl)amine; **4** = $[Fe^{III}_2(O_2)(\mu\text{-}O)(IndH)_2]^{2+}$, IndH = 1,3-bis(2'-pyridylimino)isoindoline; **5** = $[Fe^{III}_2(\mu\text{-}O)(O_2)(BQPA)_2]^{2+}$, BQPA = bis(2-quinolylmethyl)-*N*-2-pyridylmethylamine; **5-Me** = $[Fe^{III}_2(\mu\text{-}O)(O_2)(6\text{-}Me\text{-}BQPA)_2]^{2+}$, 6-Me-BQPA = bis(2-quinolylmethyl)(6-methylpyridyl-2-methyl)amine]; **6** = $[Fe^{III}_2(O_2)(\mu\text{-}O)(PB)_4]^{2+}$, PB = (–)- 4,5-pinenebipyridine; **7** = $[Fe^{III}_2(6\text{-}HPA)(O_2)(O)]^{2+}$, 6-HPA = 1,2-bis[2-{bis(2-pyridylmethyl)amino-methyl}-6-pyridyl]ethane; **8** = $[Fe^{III}_2(O_2)(\mu\text{-}O)(BPG_2E)]$, BPG_2E = 1,2-bis[2-(N-2-pyrid-ylmethyl-N-glycinylmethyl)-6-pyridyl]ethane; **9** = $[Fe^{III}_2(\mu\text{-}O)(O_2)(OAc)(BPPE)]^{+}$, BPPE = 1,2-bis[2-(bis(2-pyridyl)methyl)-6-pyridyl]ethane; **1-H** = $[Fe^{III}_2(O_2)(OH)(BnBQA)_2]^{3+}$; **2-H** = $[Fe^{III}_2(\mu\text{-}OH)(O_2)(6\text{-}Me_2BPP)_2]^{1+}$; **10** = $[Fe^{III}_2(Ph\text{-}bimp)(O_2)(OBz)]^{2+}$, Ph-bimp = 2,6-Bis[bish2-(1-methyl-4,5-diphenylimidazolyl)methyljaminomethyl]-4-methylphenolate; **11** = $[Fe^{III}_2(O_2)(N\text{-}Et\text{-}HPTB)(OPPh_3)_2]^{3+}$, *N*-Et-HPTB = tetrakis(2- benzimidazolylmethyl)-2-hydroxy-1,3-diaminopropane; **11-O_2PPh$_2$** = $[Fe^{III}_2(O_2)(O_2PPh_2)(N\text{-}Et\text{-}HPTB)]^{2+}$; **11-$\eta^1$$O_2PPh_2$** = $[Fe^{III}_2(O_2)(N\text{-}Et\text{-}HPTB)(\eta 1\text{–}O_2PPh_2)(MeCN)]^{2+}$; **12 =** $[Fe^{III}_2(O_2)(5\text{-}Me\text{-}HXTA)(OAc)]^{2+}$, 5-Me-HXTA = *N*,*N*'-(2-hydroxy-5-methyl-1,3-xylylene)bis(*N*-carboxymethylglycine); **13** = $[Fe^{III}_2(HPTP)(O_2)(OBz)]^{2+}$, HPTP = *N*,*N*,*N*',*N*'-Tetrakis(2-pyridylmethyl)-1,3-diaminopropan-2-olate; **13-Me$_4$** = $[Fe^{III}_2(Me_4\text{-}HPTP)(O_2)(OBz)]^{2+}$, Me_4-HPTP = *N*,*N*,*N*',*N*'-Tetrakis(6-methyl-2-pyridylmethyl)-1,3-diaminopropan-2-olate; **13-amide$_4$ =** $[Fe^{III}_2(HTTPDO)(O_2)(OBz)]^{2+}$, HTPPDO = *N*,*N*,*N*',*N*'-Tetrakis(6-pivalamido-2-pyridylmethyl)-1,3-diaminopropan-2-ol; **14-OBz** = $[Fe^{III}_2(O_2)(Tp^{iPr2})_2(OBz)_2]$, Tp^{iPr2} = tris(3,5-diisopropyl-1-pyrazolyl)borate; **14-PPA** = $[Fe^{III}_2(O_2)(Tp^{iPr2})_2(PPA)_2]$, PPA = phenylacetic acid; **15** = $[Fe^{III}_2(O_2)(NN)_4(MeCN)_2]^{4+}$, NN = 2–(2'–pyridyl)–N–methylbenzimidazole; **16** = $[Fe^{III}_2(O_2)(BXDK)(O_2CPhCy)_2(py)_2]$, HO_2CPhCy = 1-phenylcyclohexanecarboxylic acid; **17** = $[Fe^{III}_2(dxlCO_2)_4(O_2)(Py)_2]$, $dxlCO_2^-$ = 2,6-bis[(2,6-dimethylphenyl)methyl]-4-*tert*-butylbenzoate; **18** = $[Fe^{III}_2(OOH)(\mu\text{-}O)(Ph_4DBA)(DPE)_2]^{+}$, H_2Ph_4DBA = Dibenzofuran-4,6-bis(diphenylacetic acid), DPE = dipyrrolidinoethane; **6-OOH** = $[Fe^{III}_2(OOH)(\mu\text{-}O)(PB)_4]^{3+}$; **3-OOH** = $[Fe^{III}_2(OOH)(\mu\text{-}O)(OH)(6\text{-}Me_3TPA)_2]^{2+}$.

Table 1.7. Analysis of Mössbauer and rR parameters of synthetic peroxo-diferric intermediates. [a] Units of mm/s. [b] Units of cm^{-1}. [c] μ-OR represents a μ-hydroxo or μ-alkoxo ligand.

Type of Complex	**δ[a]**			**ΔE_Q[a]**			**ν(O–O)[b]**		
	Low	**High**	**Average**	**Low**	**High**	**Average**	**Low**	**High**	**Average**
Fe^{III}-peroxo	0.23	0.66	**0.52**	0.49	1.76	**1.24**	-	-	**-**
All μ-1,2-peroxo	0.35	0.66	**0.54**	0.62	1.70	**1.29**	826	928	**870**
All μ-1,2-peroxo (removed **7 – 9**)	0.47	0.66	**0.56**	0.62	1.70	**1.22**	844	928	**876**
μ-oxo, μ-1,2-peroxo	0.35	0.55	**0.49**	0.62	1.68	**1.45**	826	874	**848**
μ-oxo, μ-1,2-peroxo (removed **7 – 9**)	0.49	0.55	**0.52**	0.62	1.68	**1.30**	844	874	**855**
μ-OR[c], μ-1,2-peroxo	0.50	0.65	**0.56**	0.74	1.70	**1.19**	845	928	**888**
μ-1,2-peroxo, no μ-OR[c]	0.47	0.66	**0.59**	0.88	1.40	**1.16**	861	888	**875**
7 – 9	0.35	0.53	**0.45**	1.64	1.67	**1.66**	826	835	**830**
η-OOH	0.23	0.53	**0.42**	0.49	1.76	**1.26**	806	841	**826**
Enzyme μ-1,2-peroxo	0.55	0.68	**0.62**	0.88	1.90	**1.34**	851	898	**867**
OxyHr	0.51	0.54	**-**	1.09	1.92	**-**	-	-	**844**

Table 1.8. Structural parameters from XRD and XAS analysis of synthetic peroxo-diferric complexes. Distances in angstroms. [a] peroxo ligand binding geometry.

Complex	K-edge (eV)	Pre-edge area (units)	Fe•••Fe (XRD)	Fe•••Fe (EXAFS)	Bridge type	Binding mode[a]	Ref
1	7124.2	15.1	-	3.16	μ-oxo	μ-1,2	*110*
2	-	-	3.171	-	μ-oxo	μ-1,2	*103*
3	7123.6	12.5	-	3.14	μ-oxo	μ-1,2	*102*
4	7124.2	13.3	-	3.13	μ-oxo	μ-1,2	*105*
5	7122.7	16.4	-	3.13	μ-oxo	μ-1,2	*111*
5-Me	7122.8	16.6	-	3.15	μ-oxo	μ-1,2	*111*
7	7123.2	13.2	-	3.15	μ-oxo	μ-1,2	Ch. 5
9	7123.6	13.6	-	3.04	μ-oxo	μ-1,2	*111*
1-H	7123.3	13.8	-	3.46	μ-hydroxo	μ-1,2	*110*
2-H	-	-	3.395	-	μ-hydroxo	μ-1,2	*103*
10	-	-	3.328	-	μ-phenolate, μ-1,3-carboxylate	μ-1,2	*94*

Table 1.8. (continued) Structural parameters from XRD and XAS analysis of synthetic peroxo-diferric complexes. Distances in angstroms. [a] peroxo ligand binding geometry.

Complex	K-edge (eV)	Pre-edge area (units)	Fe•••Fe (XRD)	Fe•••Fe (EXAFS)	Bridge type	Binding mode[a]	Ref
11	-	-	3.463	-	μ-alkoxo,	μ-1,2	*109*
11-O_2PPh$_2$	7126.2	15.8	-	3.25	μ-alkoxo, μ-phosphinato	μ-1,2	*112*
11-$\eta^1$$O_2PPh_2$	7126.3	16.1	-	3.47	μ-alkoxo	μ-1,2	*112*
14-PPA	-	-	4.000	-	μ-1,3-carboxylate	μ-1,2	*91*
17	7123.6	9.6	-	3.33	μ-1,3-carboxylate	μ-η^1:η^2	Ch. 5, *93*
18	-	-	-	3.16	μ-oxo	η^1-OOH	*96*

1.5 – The Reactivity of Peroxo-Diferric Intermediates

Dioxygen activation by sMMOH has been thoroughly investigated, and many intermediate species have been identified along the reaction pathway,[4, 5] including the peroxo-diferric intermediate, **P**.[69, 70, 72] Intermediate **P** directly precedes the high-valent active oxidant **Q**, which has been characterized as a bis-μ-oxodiiron(IV) species.[45, 83] As sMMOH shares a common protein fold and similar ligand framework with many other diiron enzymes,[31, 35, 47, 48, 53-56] and **P** intermediates had been identified using these systems, the working hypothesis was that diiron enzymes activated oxygen *via* mechanisms similar to that of sMMOH (Figure 1.1, A → B → C → D). Indeed, a high-valent $Fe^{III}Fe^{IV}$ intermediate **X** was identified in RNR,[26, 27] consistent with this idea. However, to date, RNR is the only other diiron system that has direct spectroscopic evidence of a high-valent intermediate of this nature.

More recently, a growing number of **P** intermediates have been found to be capable of carrying out oxidation reactions directly. **P** from sMMOH is capable of oxidizing electron-rich substrates like diethyl ether, ethanol and propionaldehyde.[22, 23] A peroxyhemiacetal intermediate in ADO is proposed to be competent for substrate oxidation,[25] and *N*-oxygenation of aryl-amine substrates is facilitated through **P** intermediates of AurF and CmlI.[15, 59] On the other hand, the **P** intermediate from Δ^9D was unable to effect desaturation of the native substrate.[86] The reason for the differences in the reactivity of **P** intermediates is unclear, but analysis of structural features, like the peroxo binding geometry, may shed light on the issue.

1.5.1 – The Reactivity of μ-1,2-Peroxo-Diferric Intermediates

The **P** intermediates with a μ-1,2-peroxo binding mode ($\mathbf{P}_{\mu 1,2}$) have been implicated in many reaction pathways. As discussed in Section 1.3, the sMMOH, RNR,

Δ^9D, frog M ferritin, T4MOH and hDOHH enzymes all have a $\mathbf{P_{\mu 1,2}}$ intermediate. In sMMOH, the $\mathbf{P_{\mu 1,2}}$ is on the pathway of the native cycle,[69, 70, 72] and converts to intermediate **Q**, which is responsible for the oxidation of methane. In D84E-RNR, hDOHH and frog M ferritin the decay of the $\mathbf{P_{\mu 1,2}}$ species has been correlated with tyrosyl radical formation,[116] hypusine product formation,[65] and ferric cluster formation,[61] respectively. These results support the notion that $\mathbf{P_{\mu 1,2}}$ species are on the native reaction pathways of diiron systems.

Of the $\mathbf{P_{\mu 1,2}}$ intermediates, only sMMOH has been shown to directly react with substrates,[22, 23] which demonstrates that $\mathbf{P_{\mu 1,2}}$ intermediates can be reactive. Aside from sMMOH, the direct oxidation capability of peroxo species is unclear. Interception of the $\mathbf{P_{\mu 1,2}}$ species of RNR by exogenous substrates has not been reported, the hypusine formation reaction by hDOHH is very slow (~24 h to completion at room temperature), and in ferritin the $\mathbf{P_{\mu 1,2}}$ has been shown to stoichiometrically generate H_2O_2.[117] In addition, the Δ^9D $\mathbf{P_{\mu 1,2}}$ intermediate is unreactive towards the native substrate under single turnover conditions,[67, 86] which suggests that the $\mathbf{P_{\mu 1,2}}$ species of Δ^9D is not reactive, and may not be on the native pathway.

The synthetic peroxo complexes can also shed light on the nature of the reactive capability of $\mathbf{P_{\mu 1,2}}$ species. In general, synthetic $\mathbf{P_{\mu 1,2}}$ complexes are quite stable and unreactive, however, reactivity has been observed in some cases. When nitric acid is added to **1** at -40 ºC, the μ-hydroxo species **1-H** is generated.[110] As **1-H** decays, a new species with an S = 1/2 EPR signal appears in ~25% yield that is proposed to be a high-valent $Fe^{III}Fe^{IV}$ intermediate. A similar species with a S = 1/2 signal is observed (~30% yield) when perchloric acid is added to **3**,[118] but in both cases the mechanism of this transformation is unknown. Complex **7** is proposed to undergo reversible O–O bond scission to generate a μ-oxodiiron(IV) species with two terminal oxo ligands, but the peroxo intermediate was not directly shown to be reactive.[89, 115] Complex **13** was shown to facilitate an oxygen atom transfer (OAT) reaction to triphenylphosphine,[119] whereas

complex **16** shows no OAT reactivity but solvent oxidation products are observed upon thermal decomposition at high temperatures.[120]

$\mathbf{P}_{\mu 1,2}$ species appear to be reactive in some cases, but it is not possible to draw stronger conclusions with the available data. They are capable of conversion to high-valent intermediates in some enzymatic and synthetic systems, but this is not universally observed.

1.5.2 – The Reactivity of the Peroxo-Diferric Species of T4MOH

The fruitful T4MOH system has yielded three distinct crystallographically characterized peroxo-diferric intermediates to date, a $\mathbf{P}_{\mu 1,2}$ species,[79] an μ-η^2:η^2-peroxo species ($\mathbf{P}_{\eta 2,2}$),[28] and a μ-1,1-(hydro)peroxo species ($\mathbf{P}_{\mu 1,1}$).[28] In addition to demonstrating the versatility of diiron active sites to accommodate multiple peroxo binding modes, it allows for the assessment of the reactivity of these peroxo species. Interestingly, there is no evidence for the accumulation of any of these crystallized peroxo species in the solution state. This is consistent with studies of ToMOH, which identified a single peroxo-diferric intermediate by Mössbauer parameters alone.[24]

The $\mathbf{P}_{\mu 1,2}$ species of T4MOH was obtained by exposing H_2O_2 to crystals of the diferric form of the enzyme. No substrate soaking studies were conducted with this crystallized intermediate, so there is no direct evidence that the $\mathbf{P}_{\mu 1,2}$ species is reactive. However, the peroxide shunt reaction was studied using T4MOH,[79] and the H_2O_2-mediated reaction was ~600 fold slower at toluene hydroxylation compared with the reaction with O_2. This is an indication that a $\mathbf{P}_{\mu 1,2}$ species in T4MOH could be reactive, but is not the native active oxidant for the system. Without a direct connection between the $\mathbf{P}_{\mu 1,2}$ intermediate and the solution state kinetics, the reactive nature of this species is unclear.

The $\mathbf{P}_{\eta 2,2}$ intermediate of T4MOH is generated from a crystal of the diferrous form of the enzyme that is soaked in toluene substrate and exposed to O_2. In the crystal

structure, the O_2 ligand is bonded with the C4 position of the toluene substrate present in the active site, and to the diiron cluster in a $\mathbf{P}_{\eta 2,2}$ mode. With longer incubation time in O_2 crystals of the enzyme-product complex are observed, in which the product *p*-cresol is bound in a μ-1,1 mode (PDB code 5TDU). This subsequent enzyme-product complex demonstrates that the $\mathbf{P}_{\eta 2,2}$ intermediate is on the reaction pathway.[28] This may indicate that T4MOH generates a $\mathbf{P}_{\eta 2,2}$ species that is capable of attacking the C=C double bond of toluene. However, DFT calculations predict that an $Fe^{II}Fe^{III}$-superoxo intermediate (Figure 1.1, E) is responsible for the initial attack on toluene and that the $\mathbf{P}_{\eta 2,2}$ species is an $Fe^{II}Fe^{III}$-peroxo intermediate.[28] While not directly responsible for substrate oxidation, the $\mathbf{P}_{\eta 2,2}$ intermediate supports the idea that a $\mathbf{P}_{\mu 1,2}$ species is not on the native reaction pathway for T4MOH, in contrast to other enzymes like sMMOH and hDOHH. Additionally, T4MOH joins a number of other iron enzyme systems that have invoked Fe^{III}-superoxide species as active oxidants, and not a high-valent intermediate like **Q**.[29, 121-123]

The $\mathbf{P}_{\mu 1,1}$ intermediate is generated from a Q288A variant of T4MOH in a method analogous to the $\mathbf{P}_{\eta 2,2}$ species. DFT predicts that the μ-1,1-peroxo is likely a hydroperoxo species from geometry optimization calculations,[28] but the protonation state cannot be discerned from the XRD experiment. No toluene was present in the crystallization media, so there is no direct evidence for the reactivity of the $\mathbf{P}_{\mu 1,1}$ species. However, the position of the distal peroxo oxygen overlaps with the position of the C3 carbon of toluene from the $\mathbf{P}_{\eta 2,2}$ structure. This likely rules out the $\mathbf{P}_{\mu 1,1}$ intermediate from the native reaction cycle, as substrate positioning appears to be important to achieve proper reactivity in T4MOH.[28] Coincidentally, the Lippard group has proposed a reactive $\mathbf{P}_{\mu 1,1}$ hydroperoxo intermediate in the ToMOH system as the active oxidant based on Mössbauer studies.[24, 74] While T4MOH and ToMOH are not identical, their active sites and target substrates are closely related. In light of the $\mathbf{P}_{\mu 1,1}$ hydroperoxo from T4MOH being off pathway, the putative peroxo intermediate structure of ToMOH may need to be reassessed.

The T4MOH enzyme demonstrates that $\mathbf{P}_{\mu 1,2}$ and $\mathbf{P}_{\eta 2,2}$ may both be reactive, but $\mathbf{P}_{\eta 2,2}$ is on the native reaction pathway. This system provides the first crystallographic evidence to support that $\mathbf{P}_{\eta 2,2}$ intermediates are catalytically competent in diiron enzymes. The proposed ferric superoxo intermediate as the active oxidant also departs from the mechanisms that invoke high-valent intermediates, like in sMMOH.

1.5.3 – The Reactivity of the Peroxo-Diferric Species of CmlI

As discussed in Section 1.3 and later in Chapter 4, there are two different peroxo-diferric intermediates that can be isolated from CmlI; a $\mathbf{P}_{\mu 1,2}$ that was crystallographically characterized,[35] and a $\mathbf{P}_{\mu 1,1}$ species that was deduced from XAS and rR studies. The CmlI $\mathbf{P}_{\mu 1,2}$ species is generated from the addition of excess hydrogen peroxide, but unlike in T4MOH, a new absorption band corresponding to the peroxo species is observed in solution. This intermediate is very stable, with no observed decay over several hours at 4.5 ºC and exposure of the $\mathbf{P}_{\mu 1,2}$ intermediate to the native substrate yields no product.[35] This definitively shows that $\mathbf{P}_{\mu 1,2}$ is unable to facilitate *N*-oxygenation of aryl amine substrates.

The $\mathbf{P}_{\mu 1,1}$ intermediate of CmlI is generated from exposing the diferrous enzyme to O_2, and has a half-life of ~3 h at 4 ºC.[15] Unlike the $\mathbf{P}_{\mu 1,2}$ intermediate, the $\mathbf{P}_{\mu 1,1}$ intermediate rapidly decays upon addition of the native substrate, to yield the aryl-nitro product.[124] A **P** intermediate from AurF facilitates a similar *N*-oxygenation reaction,[59] and is proposed to adopt a $\mathbf{P}_{\mu 1,1}$ mode but lacks further structural characterization. CmlI $\mathbf{P}_{\mu 1,1}$ demonstrates that $\mathbf{P}_{\mu 1,1}$ species are viable oxidants, which is in opposition to the crystallographic studies of T4MOH. However, these results are not mutually exclusive, and they suggest that certain **P** species are utilized based on the requirements of the particular substrate. The $\mathbf{P}_{\mu 1,1}$ is sufficient for *N*-oxygenation, but may not be a potent enough oxidant for aromatic or methane hydroxylation. Alternatively, if CmlI generated a ferric-superoxide or high-valent species, there may be a higher chance for deleterious off-pathway reactions. Not all peroxo-diferric intermediates in catalytic pathways are alike,

and Nature has selected for variation in the types of **P** species used by diiron enzymes. While there are many examples of $\mathbf{P}_{\mu 1,2}$ intermediates, there are far fewer with other peroxo binding geometries. Future experiments should focus on the discovery and characterization of new $\mathbf{P}_{\eta 2,2}$ and $\mathbf{P}_{\mu 1,1}$ species from synthetic and biological sources.

1.6 – Conclusion

The active sites of nonheme diiron proteins are varied and are specialized for a wide range of physiological function. Through analysis of diferrous and peroxo-diferric intermediates, it becomes possible to gain insight into how structure may affect the reactivity of diiron active sites. However, caution must be used when using a single spectroscopic method to make structural conclusions. For example, K-edge energies to have been used to determine oxidation state, but, as demonstrated above, the K-edge energy varies significantly with ligand character as well as oxidation state. Another example is found in Mössbauer parameters, which provide valuable oxidation state information but do not show definite correlations to geometry. Spectroscopic analysis using a robust combination of Mössbauer, rR and XAS techniques is a valuable way to structurally characterize intermediates that are inaccessible by X-ray diffraction methods.

In this thesis, combined spectroscopic and structural analyses will be used to study O_2 activating nonheme diiron enzymes from several different systems. The first system is CmlA, and a combination of XAS, XRD and kinetics studies are used to understand the effect of the O_2 binding to the diferrous active site in the presence and absence of the protein-bound substrate. Next, the hDOHH system is studied using XAS analysis of several forms of the enzyme along the O_2 reaction pathway to better understand the active site structure. The final enzyme system studied is CmlI and a combination of resonance Raman and XAS analysis are used to determine the active site structure of a novel peroxo-diferric intermediate. The final part of this thesis is the XAS

analysis of various synthetic complexes, ranging from peroxo-diferric species to oxoiron(IV) complexes.

Chapter 2 : A Carboxylate Shift Regulates Dioxygen Activation by the Diiron Nonheme *β*-Hydroxylase CmlA upon Binding of a Substrate-Loaded Nonribosomal Peptide Synthetase

The content of this chapter was reproduced with permission from:

Jasniewski, A. J.; Knoot, C. J.; Lipscomb, J. D.; Que, L., Jr. A Carboxylate Shift Regulates Dioxygen Activation by the Diiron Nonheme *β*-Hydroxylase CmlA upon Binding of a Substrate-Loaded Nonribosomal Peptide Synthetase. *Biochemistry*, **2016**, *55*, 5818 – 5831

2.1 – Introduction

The biosynthesis of the natural product antibiotic chloramphenicol is carried out in *Streptomyces venezuelae* by utilizing the nonribosomal peptide synthetase (NRPS) CmlP.[125, 126] The chloramphenicol precursor L-*para*-aminophenylalanine (L-PAPA) is covalently attached to the phosphopantetheine (Ppant) arm of the thiolation (T) domain of CmlP via the action of the associated adenylation (A) domain.[127] In the first step of the biosynthesis, the tailoring monooxygenase CmlA catalyzes β-hydroxylation of the bound L-PAPA.[64] The active site of CmlA contains a dinuclear iron center in an unusual metallo-β-lactamase protein fold.[18, 64] CmlA is the archetypal member of a newly recognized family of diiron enzymes that carry out essential oxygenase reactions in natural product biosynthesis. The as-isolated CmlA stabilizes the diiron cluster in the fully oxidized diferric state. The crystal structure shows that the irons are bridged by a μ-oxo-ligand and an unusual μ-1,1-carboxylate of D403 (Figure 2.1, PDB ID 4JO0).[18]

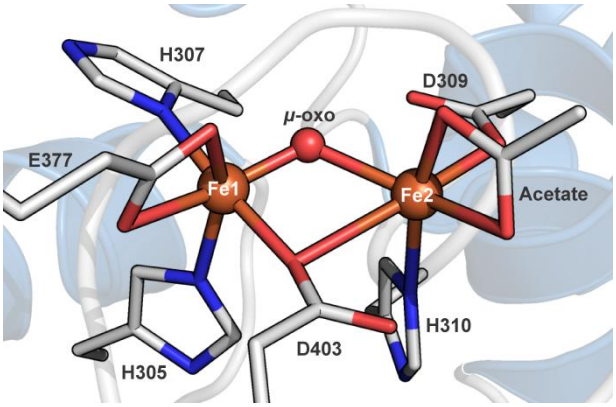

Figure 2.1. Active site diiron cluster of the diferric CmlA (**WT^{Ox}**) from PDB ID 4JO0. Carbon atoms are shown in gray, oxygen atoms in red, nitrogen in blue, and iron atoms are shown as brown spheres.

Another unusual feature is the presence of a chelated acetate derived from the crystallization medium occupying two ligands sites on Fe2 of the cluster. The remaining cluster ligands occupy all of the coordination sites of both irons so that there are no free sites to interact with additional exogenous ligands. CmlA is primed to react with O_2 by

reduction of each iron to the ferrous state. However, the resulting diferrous enzyme reacts very slowly with O_2 ($t_{1/2} \approx 1$ min at 4 °C).[64] This slow rate is not significantly affected by the addition of CmlP without L-PAPA bound, but it is accelerated 1000-fold by CmlP with covalently bound L-PAPA ($CmlP_{AT}$~ L-PAPA). The basis for this acceleration is unclear, but it must involve opening of sites on one or both irons for O_2 binding with subsequent O_2 activation to allow the observed conversion of bound L-PAPA into the *β*-hydroxylated product.

The regulation of O_2 activation is a common feature of oxygenase enzymes, but the mechanisms by which this occurs are quite varied. For example, in the *α*-ketoglutarate (*α*-KG) dependent oxygenases, O_2 activation occurs only after both the co-substrate *α*-KG and the hydrocarbon substrate are bound in the active site.[128-131] This guarantees that substrate is present and in position to be hydroxylated when the Fe(IV)=O oxidant is generated. In contrast, soluble methane monooxygenase (sMMO) employs a different strategy by sequestering the activated oxygen species such that only the small methane molecule has rapid access to the active site.[132-134] Both access of O_2 to the diiron cluster and control of the size-selective "pore" that admits CH_4 into the active site are controlled by binding of a regulatory protein. The most similar regulatory mechanism to that of CmlA is used by stearoyl-acyl carrier protein (ACP) Δ^9-desaturase, where the ACP-bound substrate must bind to the hydroxylase in order to activate O_2 at the diiron cluster.[11, 86] Both the sMMO and ACP Δ^9-desaturase regulatory schemes invoke shifts in the positions of cluster ligands, in particular Asp or Glu carboxylates, to control O_2 binding and activation by the cluster. It is unknown whether CmlA employs a similar strategy for the regulation of O_2 activation.[135-138]

In order to probe the mechanism of O_2 activation by CmlA, structural characterization of the active diferrous form of the enzyme and its complex with CmlP and CmlP~L-PAPA is required. Here we report the X-ray crystal structure of diferrous CmlA, but co-crystallization of its key complexes with CmlP and CmlP~L-PAPA could not be achieved. We have shown previously that X-ray absorption spectroscopy can

provide structural insight into the diiron cluster of CmlA.[139] Here we use this technique to study the nature of the complex between reduced CmlA and a functional CmlP variant ($CmlP_{AT}$) with and without L-PAPA covalently attached. This approach reveals a specific diiron cluster carboxylate ligand that appears to regulate reactivity with O_2. Mutagenesis of this key ligand, combined with structural and kinetic characterization provides insight into the complex interplay of substrate and the CmlA diferrous cluster that allows the regulated activation of O_2 for the highly specific hydroxylation of L-PAPA.

2.2 – Experimental Procedures

2.2.1 – Enzyme Overexpression, Purification, Amino Acid Loading, and Mutagenesis.

The chloramphenicol biosynthetic enzymes utilized here were overexpressed in an *E. coli* host with an N-terminal histidine tag and purified using immobilized metal affinity chromatography (IMAC) with a His-Pur Ni-NTA resin (Thermo Scientific). Following IMAC purification, the enzymes were dialyzed into 50 mM HEPES buffer, pH 7.5, with two exchanges of buffer. The enzymes were stored at -80 °C. For this and the previously reported work,[64] the CmlP coding sequence in the expression construct was truncated to remove the C-terminal reductase domain, leaving only A and T domains, termed $CmlP_{AT}$. $CmlP_{AT}$ was co-expressed in *E. coli* with the Sfp phosphopantetheinyl transferase from *B. subtilis* which catalyzed the attachment of the Ppant cofactor to the CmlP T domain *in vivo*.[64] L-PAPA substrate was purchased as the HCl salt from Sigma Aldrich and was used without further purification. $CmlP_{AT}$ was either covalently loaded with L-PAPA after purification and frozen for later use or loaded immediately prior to performing the experiments. The typical loading reactions contained 2.5 mM L-PAPA, 2.5 mM ATP, 1 mM tris(2-carboxyethyl)phosphine (TCEP) and 10 mM $MgCl_2$ in 0.1 M Tris-HCl pH 8.5. The loading reactions were incubated for 3 h at 4 °C or for 1.5 h at 22

°C while stirring. The excess reagents were then removed and the buffer exchanged using dialysis against HEPES buffer or a PD-10 desalting column (GE Healthcare). Attachment of the Ppant cofactor and L-PAPA was confirmed using liquid chromatography-coupled electrospray ionization mass spectrometry (LC-ESI MS) of the whole proteins. The proteins were separated *via* reverse-phase chromatography using an Acquity UPLC C4 column in a linear gradient from water / 0.1 % formic acid to 97% acetonitrile / 0.1 % formic acid. Samples were ionized and analyzed using a Waters Synapt G2 QTOF instrument at the University of Minnesota Chemistry Department mass spectrometry laboratory.

The E377D mutant of CmlA was generated with a Quickchange II site-directed mutagenesis kit (Agilent Technologies) using the pET28a CmlA expression construct as a template. The mutation was introduced using the following oligonucleotides:
GCCCTTCCTCGGCGATCACGGCGACCTGC (forward)
GCAGGTCGCCGTGATCGCCGAGGAAGGGC (reverse)

2.2.2 – X-ray Crystallography

Crystals of CmlA were acquired and prepared for data collection using the methods previously reported.[18] For chemical reduction of the WT CmlA crystals, the crystals were prepared in a low-O_2 atmospheric chamber (Belle Laboratories) and single crystals soaked for 10-15 min in Ar-sparged cryoprotectant containing 10 mM sodium dithionite and 10 μM methyl viologen. The samples were then flash-frozen directly in liquid nitrogen. Diffraction data were collected at the Structural Biology Center at the Advanced Photon Source (Argonne National Laboratories, Argonne, IL) on beamline 19-ID at 100 K. The data were indexed, integrated, and scaled using the HKL2000 software package.[140] The CCP4 suite v. 6.3.0 was used to generate the final models. The data were phased in Refmac5 [141] using direct Fourier-phasing with a model of the reported structure of WT CmlA.[18] The structure was modeled using Coot v. 0.8.2 [142] and refined using Refmac5.[141] At no point during the refinement process were the iron-ligand bond

distances explicitly restrained. The final model quality was assessed using the Protein Data Bank validation server.

2.2.3 – X-ray Absorption Spectroscopy

Protein samples for X-ray absorption spectroscopy (XAS) contained either 2 mM CmlA (~4 mM Fe) or CmlA with 2.5 mM $CmlP_{AT}$ or $CmlP_{AT}$~L-PAPA. The samples were prepared in an anaerobic glove bag (Coy). Each sample contained 50 μM methyl viologen as mediator and 5 mM sodium dithionite in 50 mM HEPES pH 7.5 supplemented with 25% glycerol as cryoprotectant. Samples were frozen in an isopropanol/ dry ice bath (-65 °C) then moved to liquid nitrogen for storage and transfer to the synchrotron. Iron K-edge X-ray absorption spectra were collected on SSRL beam lines 7-3 and 9-3 using a 30 element and 100 element (respectively) solid state Ge detector (Canberra) with a SPEAR storage ring current of ~500 mA at a power of 3.0 GeV. The incoming X-rays were unfocused using a Si(220) double crystal monochromator, which was detuned to 40% of the maximal flux to attenuate harmonic X-rays. For chemically reduced WT CmlA (**WT^R**), **WT^R** with $CmlP_{AT}$ (unloaded $CmlP_{AT}$, **WT^RU**), **WT^R** with $CmlP_{AT}$~L-PAPA substrate (**WT^RS**) and chemically reduced E377D CmlA (**$E377D^R$**) 12, 16, 11 and 16 scans (respectively) were collected from 6882 eV to 8000 eV at a temperature (~10 K) that was controlled by an Oxford Instruments CF1208 continuous flow liquid helium cryostat. An iron foil was placed in the beam pathway prior to the X-ray ionization chamber I_0 and scanned concomitantly for an energy calibration, with the first inflection point of the edge assigned to 7112.0 eV. A "9" μm Mn filter (3 μm + 6 μm) and a Soller slit were used to increase the signal to noise ratio of the spectra for **WT^R** and **WT^RS**. A 3 μm filter was used for the collection of **WT^RU** and **$E377D^R$**. Photoreduction was monitored by scanning the same spot on the sample twice and comparing the first derivative peaks associated with the edge energy during collection.

The detector channels from the scans were examined, calibrated, averaged, and processed for extended X-ray absorption fine structure (EXAFS) analysis using

EXAFSPAK [143] to extract χ(k). Theoretical phase and amplitude parameters for a given absorber-scatterer pair were calculated using FEFF 8.40 [144] and were utilized by the "opt" program of the EXAFSPAK package during curve fitting. Parameters for each species were calculated using a model derived from the crystal structure of CmlA. In all analyses, the coordination number of a given shell was a fixed parameter and was varied iteratively in integer steps, while the bond lengths (R) and mean-square deviation (σ^2) were allowed to freely float. The amplitude reduction factor S_0 was fixed at 0.9, while the edge-shift parameter E_0 was allowed to float as a single value for all shells. Thus, in any given fit, the number of floating parameters was typically equal to (2 x num shells) + 1. **WT^R**, **WT^{R}U**, and **WT^{R}S** have a k range of 2 – 14 Å^{-1}, and **E377D^R** has a range of 2 – 13.5 Å^{-1}. Pre-edge analysis was performed on data normalized in the "process" program of the EXAFSPAK package, and pre-edge features were fit between 7108 eV to 7118 eV using the Fityk[145] program with pseudo-Voigt functions composed of 50:50 Gaussian/Lorentzian functions. One function was fit as the baseline underneath the pre-edge peak and two functions were used to fit the remaining pre-edge feature. The area was calculated by multiplying the height and the full width at half-maximum (FWHM) of each fitted function, adding these component functions together and multiplying by 100 to achieve convenient values.

2.2.4 – Stopped-flow Transient Kinetics

The reaction between CmlA and O_2 with and without CmlP$_{AT}$ or CmlP$_{AT}$~L-PAPA was monitored using a SX.18MV stopped-flow spectrophotometer from Applied Photophysics. The experiments were conducted using the methods described previously.[18, 64] All reported reactions were performed at 4.5 °C in 50 mM HEPES buffer pH 7.5. For reactions containing both CmlA and CmlP, the enzymes were mixed prior to loading on the instrument in order to allow the enzyme complex to form before reacting with O_2. The reaction traces were mathematically fit using the Pro-Data Viewer software from Applied Photophysics as a sum of exponential functions of the form

$$A_{t,obs} = A_{\infty} + \sum_{i=1}^{n} A_i e^{\left(-\frac{t}{\tau i}\right)}$$

where A_i is the observed amplitude of phase i (of n) in absorbance units, τ_i^{-1} is the reciprocal relaxation time of the phase (RRT, s^{-1}), t is time (s) and A_∞ is the absorbance at the end of the reaction. Unless the steps in the reaction of the enzyme complex with O_2 are kinetically irreversible, each RRT will not directly correlate with a discrete microscopic rate constant.[146]

2.3 – Results

2.3.1 – X-ray Crystal Structure of Chemically Reduced CmlA

The crystal structure of diferrous **WT^R** (Figure 2.2) was solved to a maximal resolution of 2.2 Å. The R_{work} and R_{free} for the final model were 18.0% and 21.3%, respectively. Details of the diffraction data collection and model refinement are given in Table 2.1.

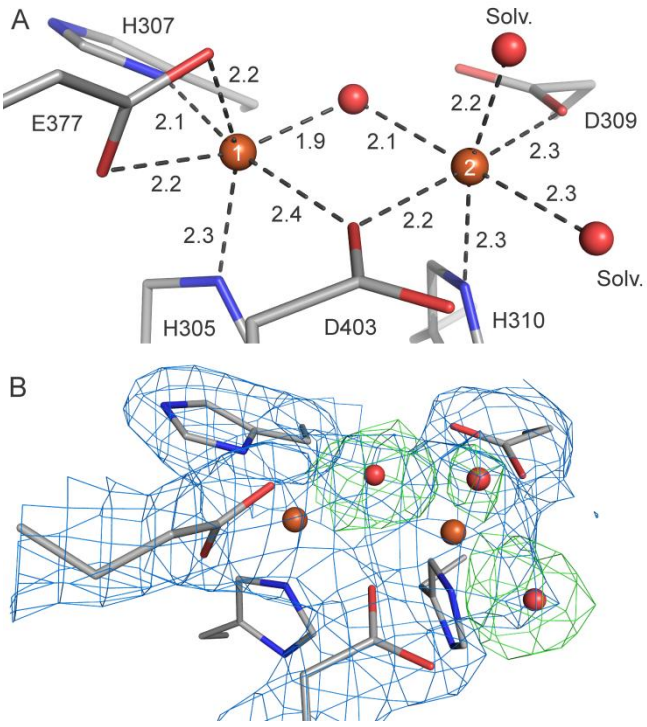

Figure 2.2. The diiron cluster observed in the X-ray crystal structure of CmlA in its chemically reduced state (**WT^{R}**). (A) Bond distances for the iron and first-sphere ligands, given in Å. (B) Electron density map of **WT^{R}**. The blue mesh is the $2|F_o|-|F_c|$ map contoured at 1.5 σ and the green mesh is the $|F_o|-|F_c|$ omit map for the solvent-derived ligands contoured at +4.5 σ. Atom coloring is as in Figure 2.1.

The overall protein structure of the reduced enzyme (PDB ID 5KIK) is superimposable with that of the as-isolated diferric CmlA (**WT^{Ox}**) and the backbone atom RMSD over the length of the whole protein is 0.2 Å. Similarly, the diiron cluster exhibits very few changes relative to the as-isolated cluster.[18] Both metals are six-coordinate in pseudo-octahedral ligand environments. Fe1 retains the H305, H307, bidentate E377, and D403 protein ligands and a monoatomic solvent-derived bridge (Figure 2.2, A). The bridge is likely to be hydroxide based on the observed bond distances in the crystal structure and cluster charge-balance considerations. Fe2 is coordinated by D309, H310 and D403 protein ligands, the mono-atomic bridge and two solvent-derived ligands.

Table 2.1. Diffraction data collection and model statistics

	WT CmlA chemically reduced	**CmlA E377D variant**
PDB ID	5KIK	5KIL
Data collection		
Space group	$P4_3 2_1 2$	$P4_3 2_1 2$
Cell dimensions		
a, b, c (Å)	153.53, 153.53, 93.04	153.95, 153.95, 92.55
α, *β*, γ (°)	90, 90, 90	90, 90, 90
Wavelength (Å)	0.97918	0.97933
Resolution (Å)	50-2.20	50-2.72
Total/Unique reflections	488258/ 58432	217968/ 30307
R_{merge} (%) [a,b]	13.2 (56.0)	10.2 (47.1)
I/σI [a]	27 (5.4)	29 (4.8)

Completeness (%) [a]	98.9 (98.6)	99.7 (99.9)
Redundancy [a]	8.4 (6.8)	7.2 (7.5)
Model Refinement		
Resolution (Å)	44.8-2.20	38.5-2.72
R_{work}, R_{free}, test set (%)	0.180, 0.213, 5.3	0.202, 0.262, 5.1
Average B, all atoms ($Å^2$)	57	63
ESU (Å)[c]	0.098	0.229
Protein atoms in model	4209	4110
RMSDs		
Bond lengths (Å)	0.013	0.019
Bond angles (°)	1.71	1.97
Ramachandran analysis		
Favored (%)	97	91
Allowed (%)	3	8
Outlier (%)	0	1

All data collected on synchrotron beamline APS SBC-CAT 19ID-D
[a] Highest resolution shell is shown in parentheses
[b] $R_{sym} = \Sigma_{hkl}\Sigma_i |I_{hkl,i} - \langle I \rangle_{hkl}|/\Sigma_{hkl}\Sigma_i|I_{hkl,i}|$, where I_{hkl} is the intensity of a reflection and $\langle I \rangle_{hkl}$ is the average of all observations of the reflections in the dataset
[c] Estimated overall coordinate error (ESU) based on maximum likelihood
RMSD, root mean square deviation from ideal geometry

These solvent molecules occupy the two coordination sites where acetate was bound in the as-isolated crystal structure[18] and, based on the observed bond distances, are likely to be aqua ligands. Evidence for the presence of the solvent-derived ligands is shown in Figure 2.2B as strong residual electron density in the ligand-omit map (green mesh). Although these crystals were grown and chemically reduced in the presence of 0.1 M potassium acetate as co-precipitant (the same conditions as the previously reported structure), there was no evidence in the electron density map for acetate chelation of Fe2. This is consistent with overall loss of two positive charges upon cluster reduction with coincident loss of the labile acetate and protonation of the μ-oxo-bridge to hydroxide prior to freezing. The Fe•••Fe distance is 3.3 Å. The hydroxide bridge-Fe bond distances

are 1.9 Å and 2.1 Å for Fe1 and Fe2, respectively, whereas both μ-oxo bridge-Fe bond distances in the as-isolated structure are roughly 1.8 Å.[18, 139] The overall increase in iron-ligand bond distances for the chemically reduced cluster is expected upon reduction of both iron ions to the ferrous state. The cluster retains the μ-1,1-bridging D403 carboxylate. This results in a cluster that has a μ-OH and protein-derived μ-1,1-carboxylate bridges. Because both iron ions are coordinately saturated, there is no obvious binding site available for O_2.

2.3.2 – XAS of Chemically Reduced Diferrous CmlA and Diferrous CmlA:CmlP$_{AT}$~L-PAPA

To date, a co-crystal of CmlA with its substrate CmlP$_{AT}$~L-PAPA has not been obtained. Consequently, we have used Fe-K-edge XAS to provide insight into potential changes in the active site structure of CmlA upon interaction with substrate (Table 2.2 and Table 2.3). The position of the rising Fe K-edge energy, found in the X-ray absorption near edge structure (XANES) region, generally reflects the oxidation state of the Fe centers. The K-edge energy of the **WT^{R}** is 7121.5 eV, which is close to that found for the diferrous forms of the ferroxidase center in frog M ferritin (7122.0 eV)[37] and the R2-like ligand binding oxidase (7121.4 eV).[13] When **WT^{R}** is mixed with L-PAPA-tethered CmlP$_{AT}$, the enzyme-substrate complex is formed (**WT^{R}S**), and the measured K-edge blue-shifts in energy to 7122.2 eV, which is still consistent with diferrous centers. For comparison, the control sample of **WT^{R}** mixed with CmlP$_{AT}$ without a tethered L-PAPA (**WT^{R}U**) shows a K-edge energy of 7121.7 eV, comparable to that of **WT^{R}**. The other characterized CmlA species, **WT^{Ox}**, has a K-edge energy of 7126.8 eV, which is at much higher in energy than those of these diferrous species.[139] Although there was a possibility that the diiron cluster might be partially photoreduced in the crystal structure of **WT^{Ox}**,[18] the K-edge energy observed for the XAS sample is most consistent with a diferric species and shows no hint of photoreduction during data collection.[139]

The pre-edge portion of the XANES region of the XAS samples includes a feature due to forbidden 1s → 3d transitions in first-row transition metal compounds.[147] The intensity of this feature is governed by the degree of distortion from centrosymmetry at the metal center, so the less centrosymmetric metal centers have pre-edge features with higher intensity, as reflected by a larger peak area. The metal coordination number can be accurately assessed by comparing the observed pre-edge areas to XANES data of well characterized synthetic complexes.[43, 44, 85] The X-ray fluorescence spectra showing the pre-edge region are shown in Figure 2.3. Individual pre-edge fits can be found in the Supplementary Information (Figure 2.12 – Figure 2.14).

Table 2.2. Pre-edge parameters for non-heme diiron enzyme species.

Species	K-edge energy (eV)	Pre-edge Area (units)	Assignment
WT^R	7121.5	8.4	6C – Fe^{II}_2
WT^RU	7121.7	7.4	6C – Fe^{II}_2
WT^RS	7122.2	11.4	5C – Fe^{II}_2
$E377D^R$	7122.8	10.4	5C – Fe^{II}_2
WT^{Ox} [a]	7126.8	13.4	6C – Fe^{III}_2
sMMOH [b]	-	10	5C – Fe^{II}_2
Frog M ferritin [c]	7122	13.6	5/6C – Fe^{II}_2
DOHH [d]	7122.7	8.6	6C – Fe^{II}_2

[a]Data from ref. [139], [b]data from ref [45], [c] ferritin ferroxidase center from ref [37], [d]deoxyhypusine hydroxylase (DOHH) from ref [36]. Assignment column refers to the assigned coordination environment of the Fe centers.

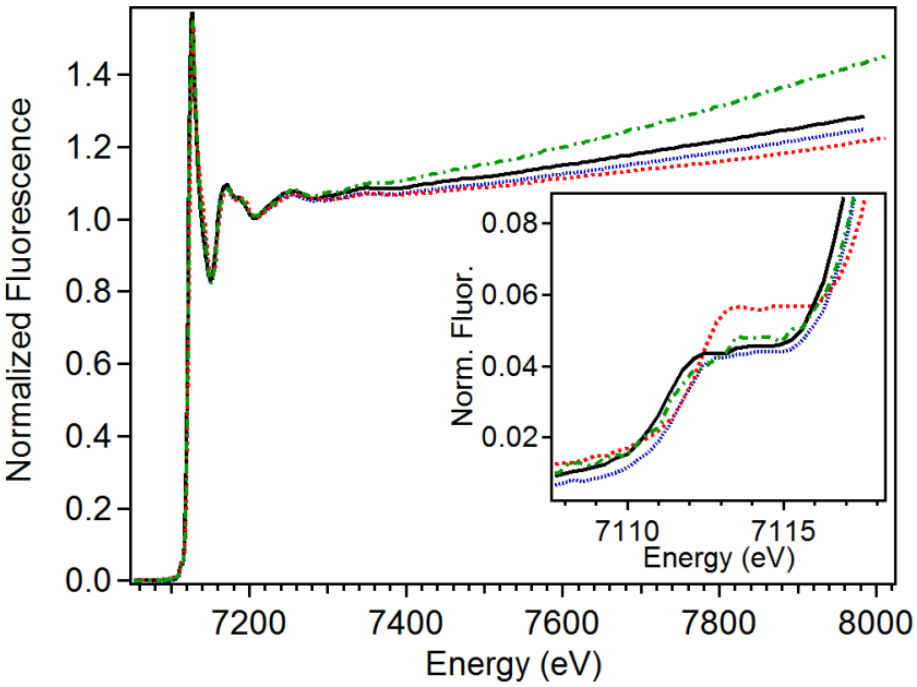

Figure 2.3. XANES region of **WT^{R}** (black solid), **WT^{R}U** (green dash-dot), **WT^{R}S** (blue dotted) and **E377D^{R}** (red dashed). Inset: Zoom-in of pre-edge region.

WT^{R} has a pre-edge peak centered on 7113.4 eV with a total area of 8.4 units. This value falls between those typical of six-coordinate (~5 units) and five-coordinate (~11 units) diferrous centers[43] and is consistent with the six-coordinate geometry established by X-ray crystallography. **WT^{R}S** has a peak centered at 7113.3 eV with an area of 11.4 units. This value indicates an increased distortion from centrosymmetry at the iron and suggests that at least one of the two iron ions in the active site has become five-coordinate. The pre-edge feature of **WT^{R}U** is found at 7113.0 eV with an area of 7.4 units, which is very similar to the pre-edge area of **WT^{R}** and consistent with six-coordinate iron centers. For comparison, the **WT^{Ox}** species shows a feature reported at 7114.9 eV with an area of 13.4 units.[139] As the pre-edge area generally increases with an increase in the iron oxidation state, this observation is consistent with a six-coordinate (μ-

oxo)diferric cluster (~14.5 units),[85] which is corroborated by the crystal structure of **WT^{Ox}**.[18]

EXAFS analysis provides bond distances and close contacts near the iron centers. The final fits for each species are summarized in Table 2.3, and detailed individual fit protocols and figures can be found in the Supporting Information (Table 2.5 – Table 2.7, Figure 2.15 – Figure 2.17). It should be noted that coordination numbers determined from EXAFS fits have an inherent uncertainty of ±25% due to difficulties in accurately extracting amplitude information from the observed interference pattern from the XAS experiment.[21] Thus EXAFS analysis is used to determine average metal-scatterer distances, while XANES analysis sheds better light on coordination number.[148]

The Fourier transformed EXAFS data (FT) for the CmlA samples generally exhibit a prominent feature below R+Δ < 2 Å representing the first coordination sphere about each Fe center; weaker features are found at higher R+Δ values arising from outer-sphere scatterers (Figure 2.4). In the **WT^{R}** data (Figure 2.4, black), the major feature can be fit with 5 N/O scatterers at 2.15 Å and 1 O/N at 1.97 Å (Table 2.3). The longer 2.15 Å distance is assigned to the protein-derived histidine and carboxylate ligands as well as to the terminally-bound solvent molecules observed in the crystal structure of **WT^{R}**. The assignment of the protein-derived ligands is based on metal-ligand distances found in the crystal structures of non-heme diiron proteins.[14, 18, 31, 34, 53, 149-152] The imidazole ligands arising from histidines have Fe–N distances that generally fall in the range of 2.0 – 2.5 Å, with an average of 2.2 Å, regardless of the ferrous or ferric oxidation state. Carboxylate-derived Fe–O distances have a similar range but depend on the binding mode of the carboxylate ligand (i.e. monodentate versus bidentate, terminal versus bridging). Additionally, in synthetic iron(II) complexes, Fe^{II}–OH_2 distances can range from 2.04 – 2.16 Å, consistent with this assignment.[105, 153-158] The Fe–O/N scatterer at 1.97 Å is assigned to the hydroxo bridge between the metal centers, as synthetic (μ-hydroxo)diferrous complexes have Fe^{II}–μ-OH distances as short as 1.97 Å.[92, 159, 160] This assignment would agree with the single atom bridge observed in the crystal structure of

WT^{R} and give rise to a diiron(II) active site with an overall neutral charge. Mössbauer studies of **WT^{R}** reveal a diiron(II) center with weak antiferromagnetic coupling (J ~ 12 cm^{-1}).[64] Such a J value would be consistent with the hydroxo bridge identified from EXAFS analysis.[160, 161]

Table 2.3. EXAFS parameters from the final fits of the reported CmlA species.

	Fe-N/O			Fe•••C/N/O			Fe•••Fe			Fe•••C				GOF	
Fit	**N**	**R(Å)**	**$\sigma^2(10^{-3})$**	**N**	**R(Å)**	**$\sigma^2(10^{-3})$**	**N**	**R(Å)**	**$\sigma^2(10^{-3})$**	**N**	**R(Å)**	**$\sigma^2(10^{-3})$**	**E_o**	**F**	**F'**
WT^R	5	2.15	4.32	0.5	2.57	1.50	1	3.26	6.22	4	3.09	2.46	-10.8	106	373
	1	1.97	2.53							3	4.26	3.18			
WT^RU	4.5	2.13	5.32				1	3.32	2.08	4	3.15	3.78	-0.65	399	623
	0.5	1.95	2.39							3	3.56	3.41			
										3	4.31	4.35			
WT^RS	5	2.13	4.53				1	3.25	3.49	5	3.07	3.30	-12.9	123	417
	1	1.94	1.12							4	4.31	1.91			
$E377D^R$	4	2.12	4.63				1	3.26	7.22	3	3.05	3.09	-10.0	128	470
	1	1.95	4.25							3	4.35	1.99			
WT^{Ox} [a]	5	2.10	4.97	1	2.53	1.09	1	3.32	5.36	2	3.09	1.19	-	-	-
	1	1.80	4.41							1	3.93	5.13			
										4	4.36	3.80			

[a]Data from ref. [139]

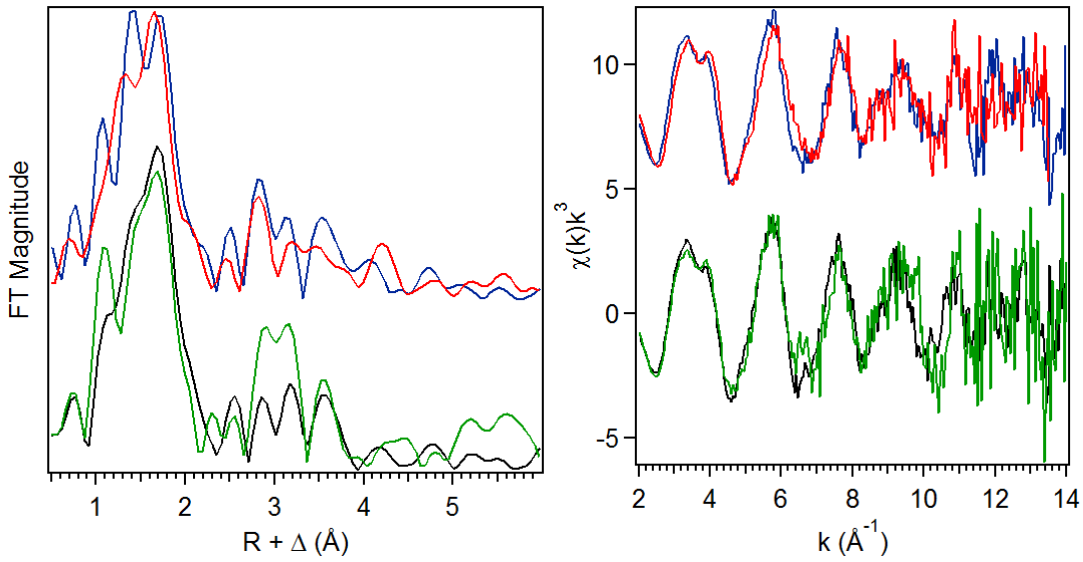

Figure 2.4. Left: Fourier transform of the unfiltered EXAFS data for **WT^{R}** in black, **WT^{R}U** in green, **WT^{R}S** in blue, **E377D^{R}** in red. Right: Unfiltered EXAFS data for CmlA species.

WT^{R} also exhibits four additional features at distances beyond the first coordination sphere that can be fit by introducing scattering atoms not directly ligated to the iron centers, namely a carbon atom from a bidentate carboxylate at 2.57 Å, the outer-sphere C/N-atoms of the imidazole rings of the histidine ligands at 3.09 and 4.26 Å, and the other Fe in the dinuclear active site at 3.26 Å. Such features have been found in the EXAFS data for several non-heme diiron enzymes, [162-164] including for **WT^{Ox}**.[139] The C scatterer at 2.57 Å arises from the bridgehead carbon of a bidentate carboxylate ligand terminally bound to an iron center in the CmlA active site cluster. This carboxylate binding mode is observed in the crystal structure of **WT^{R}** presented above, and in the crystal structure and EXAFS analysis of **WT^{Ox}**.[18, 139] However, the best fit gives an occupancy of 0.5 for this scatterer; attempts to increase this value to 1 (Table 2.5, fit 12) result in a scatterer with a mean-squared deviation (σ^2) of 6.68 × 10^{-3} Å^2, which is quite large for a single-atom scatterer. This N = 0.5 assignment is consistent with only one Fe center having a bidentate carboxylate ligand, which is congruent with the crystal structures of **WT^{R}** and **WT^{Ox}**.[18] The additional C/N scatterers at 3.09 and 4.26 Å are

associated with the non-ligated C/N-atoms of the imidazole rings of the histidine ligands and have been found at similar distances in the EXAFS data for various non-heme diiron enzymes.[139, 162-164] Lastly, there is an Fe scatterer at 3.26 Å, which is also observed in the EXAFS analysis of $\mathbf{WT^{Ox}}$ [139] and in agreement with the crystallographic results for $\mathbf{WT^{R}}$.

The EXAFS analysis of $\mathbf{WT^{R}S}$ shows small changes in the diiron site structure as $\mathbf{WT^{R}}$ combines with the L-PAPA-tethered $CmlP_{AT}$ (Figure 2.4, blue). The Fe–N/O scatterer distances in the inner coordination sphere have contracted slightly to 2.13 Å and 1.94 Å, respectively (Table 2.3). Similarly, the Fe•••Fe distance at 3.25 Å, and the Fe•••C/N scatterer distances at 3.07 Å and 4.31 Å are not much different from the corresponding values found for $\mathbf{WT^{R}}$, indicating that no major rearrangement of the diferrous core has occurred. The main difference between $\mathbf{WT^{R}S}$ and $\mathbf{WT^{R}}$ is the absence of a Fe•••C scatterer at ~2.6 Å found in the fit of $\mathbf{WT^{R}}$, suggesting that the carboxylate moiety is no longer bound in a bidentate fashion. The simplest way to account for this change without significant impact on the diiron site structure is for the bidentate carboxylate to switch to a monodentate binding mode upon substrate binding. Such a scenario would be supported by the increase in the pre-edge area observed for this complex (Table 2.2), signaling a decrease in the coordination number of the iron centers. Although the best fit favors a coordination number of six, the corresponding fit with a coordination number of five is only slightly worse (Table 2.6, Fit 18 vs Fit 15). Taken together, the XANES and EXAFS data support the notion that E377 becomes monodentate upon binding of the L-PAPA-tethered $CmlP_{AT}$ to $\mathbf{WT^{R}}$ to open up a coordination site for subsequent O_2 binding.

The EXAFS analysis of the control sample $\mathbf{WT^{R}U}$ affords a best fit with a set of scatterers and distances that is similar to that of $\mathbf{WT^{R}S}$ (Table 2.7). However, in $\mathbf{WT^{R}U}$ the σ^2 value for the single O/N scatterer at 1.94 Å assigned to the hydroxo bridge is unusually high (8.3×10^{-3} Å^2) when N = 1 (Table 2.7, fit 11). When the N value for this scatterer is lowered to 0.5, its σ^2 value decreases significantly to an acceptable value (3.2×10^{-3} Å^2) with a slight decrease in the distance to 1.92 Å (Table 2.7, fit 19). An N value of 0.5 for the short Fe-O scatterer would suggest that the hydroxo bridge becomes

unsymmetrically bound in this sample, and a longer Fe–μ-OH distance would end up in the 2.13-Å subshell. The best fit (Table 2.7, fit 23) has a N = 4.5 for the 2.13 Å subshell and N = 0.5 for the now 1.95 Å Fe-O scatterer. Extra carbon scatterers at 3.56 Å also improve the fit, and are consistent with assignment to the C_β atom of an N_δ-bound histidine ligand (Table 2.7, fit 22 vs 23).[36] In addition, the EXAFS fit does not include the carbon scatterer at ~2.6 Å that is associated with the terminal bidentate carboxylate found in the crystal structure of **WT^R** and observed in its EXAFS fit. This result would be consistent with this carboxylate no longer coordinating in a bidentate mode upon binding of untethered $CmlP_{AT}$ to **WT^R**. The conversion of a bidentate carboxylate to a monodentate binding mode could free up a Fe binding site and decrease the Fe coordination number, as observed for **WT^{R}S**. However **WT^{R}U** has a smaller pre-edge area than **WT^{R}S** with a value typical for six-coordinate iron centers (Table 2.2), so a solvent molecule may occupy this site instead.

2.3.3 – Rationale for Cluster Ligand Modification.

Our past studies have shown that **WT^R** and **WT^{R}U** are effectively unreactive with O_2, while **WT^{R}S** reacts rapidly and yields hydroxylated product. Based on the XAS analysis of **WT^R** and **WT^{R}S**, the notable differences are the change in coordination number as established by the pre-edge analysis and the loss of the 2.57 Å scatterer assigned to the bridgehead carbon of a chelating carboxylate ligand. The crystal structure of **WT^R** clearly shows that there is only one candidate for this scatterer: the carboxylate of E377. This result suggests that binding of the NRPS with its tethered L-PAPA amino acid may induce a carboxylate shift at E377 from a bidentate to monodentate binding mode, resulting in the loss of the bridgehead carbon scatterer and opening up a coordination site at this Fe to activate the cluster to react with O_2. In order to test this hypothesis, we generated the E377D variant of CmlA. The rationale for this mutation was that decreasing the number of carbon atoms on the side-chain by one would be expected to shorten the reach of this residue, preventing it from chelating Fe1, and forcing the D377 carboxylate to adopt a monodentate coordination mode. We hoped to generate a

structural mimic of our hypothesized **WT^{R}S** complex, and use it to test the possibility that E377 assumes a monodentate mode in the reactive complex.

2.3.4 – Characterization of CmlA E377D.

As-isolated E377D (**E377D^{Ox}**) has a near-UV optical feature like that of **WT^{Ox}** but blue-shifted about 20 nm (Figure 2.5). This band has been assigned to an oxo-to-Fe^{3+} ligand-to-metal charge-transfer transition.[64] The similar intensity of this band relative to that in WT is consistent with the retention of a μ-oxo bridge in the variant. This chromophore disappears upon chemical reduction (**E377D^{R}**), thereby providing a means to follow the reaction with O_2 by monitoring cluster re-oxidation to the diferric state (see below). Product formation by E377D was assessed using whole-protein mass spectrometry as described in the Experimental Procedures. The results of these experiments show that E377D is unable to generate the hydroxylated product (Figure 2.18). Fluorescence experiments were conducted to observe whether the lack of product formation is due to a change in the binding of $CmlP_{AT}$~L-PAPA to the E377D variant. As seen in Figure 2.19, **WT^{Ox}** and **E377D^{Ox}** have the same behavior when mixed 1:1 with $CmlP_{AT}$~L-PAPA, indicating that binding is likely not affected by the E377D mutation.

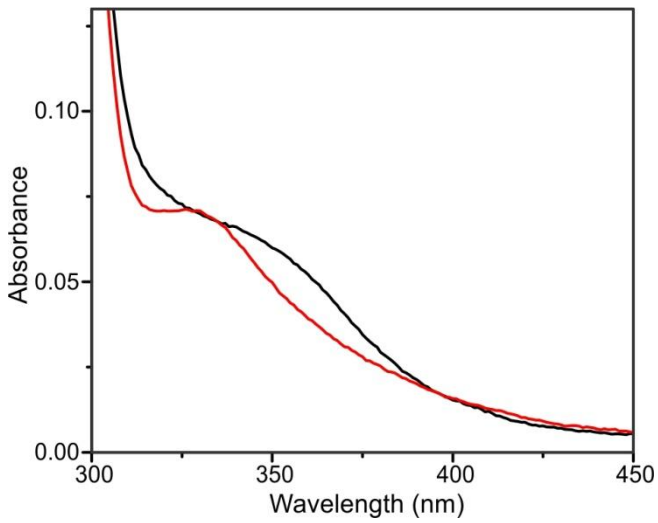

Figure 2.5. Comparison of the as-isolated UV/vis spectra for WT CmlA (**WT^{Ox}**) (black line) and **E377D^{Ox}** (red line). Both enzymes are shown at roughly the same concentration based on the absorbance at 280 nm.

2.3.5 – X-ray Crystal Structure of As-Isolated E377D^{Ox} CmlA

The diiron cluster found in the crystal structure of **E377D^{Ox}** (PDB ID 5KIL) is shown in Figure 2.6. E377D crystals diffracted poorly relative to those of the **WT^{Ox}**, and the final structure was modeled at a maximal resolution of 2.7 Å. The final R_{work} and R_{free} for the model were 20.2% and 26.2%, respectively. Details of the data collection and refinement are given in Table 2.1. Attempts to generate crystals of the chemically reduced form of the mutant **E377D^{R}** resulted in a considerable loss in diffraction quality, preventing us from determining the structure of the reduced variant at a tractable resolution. However, XAS data were successfully collected on **E377D^{R}**, and the results are discussed in the next section. As with **WT^{R}**, no significant changes in the protein backbone of **E377D^{Ox}** were observed relative to the as-isolated WT enzyme structure (Figure 2.6, A and B).

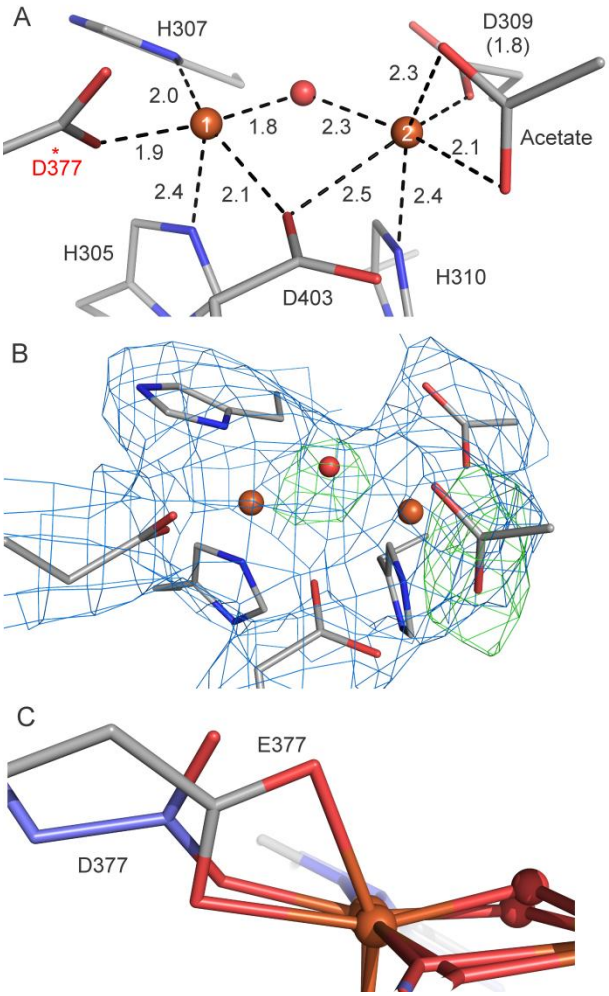

Figure 2.6. Details of the diiron active site observed in the X-ray crystal structure of E377D CmlA in the as-isolated state (**E377D^{Ox}**). (A) Bond distances for the iron and first-sphere ligands, given in Å. The mutated residue D377 is starred for clarity. (B) Electron density map of **E377D^{Ox}**. The blue mesh is the $2|F_o|-|F_c|$ map contoured at 1.0 σ and the green mesh is the $|F_o|-|F_c|$ omit map for the μ-oxo bridge and acetate contoured at +4 σ. (C) Overlay of **WT^{R}** and **E377D^{Ox}** clusters showing the coordination of residue 377. Atom coloring is as in Figure 2.1 except the carbon atoms of the variant are shown in purple in panel C.

With the exception of a dramatic change in the coordination mode of the position 377 residue, the cluster in **E337D^{Ox}** is similar to that of the as-isolated **WT^{Ox}**.[18] Due to the shortening of the E377 residue side-chain by one carbon atom, D377 is no longer able to chelate Fe1 and instead coordinates in a monodentate mode (Figure 2.6C). Thus, Fe1 is five-coordinate and has a vacant site *trans* to H305. Fe2 remains six-coordinate and a

chelated acetate ligand is found at the same site as in **WT^{Ox}**.[18] The oxo-bridge is still present in the E377D cluster based on the strong positive ligand-omit density (Figure 2.6B, green mesh). This is also consistent with the relatively intense near-UV optical feature of the as-isolated enzyme noted above. The crystal structure of E377D shows that both iron ions are retained and that the diiron cluster has not been greatly perturbed by the introduction of the mutation. Indeed, the structure shows that the mutation has had the desired localized effect of converting the binding mode of the Fe1 ligand from bidentate in the WT enzyme to a monodentate mode in the variant.

2.3.6 – XAS Characterization of E377D^{R}

XAS studies of E377D were pursued in order to gain insight into the structure of the chemically reduced variant **E377D^{R}** and to compare structural metrics to those of the WT complexes discussed above. XANES analysis of **E377D^{R}** yielded a K-edge energy of 7122.8 eV (Figure 2.3, red), which is similar to what was found for **WT^{R}**, **WT^{R}U** and **WT^{R}S** and consistent with diferrous centers (Table 2.2). The differences among these four enzyme species could be due to the change in the carboxylate ligand (E377 for **WT^{R}** and D377 for **E377D^{R}**) as well as its binding mode. Others have shown that the K-edge energy can be sensitive to the effective nuclear charge, [40] ligand identity and hardness [39] and the metal spin state.[42] **E377D^{R}** has a pre-edge peak centered at 7113.6 eV that was fit with an area of 10.4 units (Figure 2.20). This higher value compares well with that of **WT^{R}S** (11.4 units) and suggests that at least one of the two irons in the diferrous active site has become five-coordinate.

Two sets of parameters (Table 2.8, fit 15 vs 18) fit reasonably well with the experimental EXAFS data for **E377D^{R}** (Figure 2.21). The difference between the two fits is in the number of scatterers in the Fe–N/O subshell at ~2.1 Å. Fit 15 has 5 Fe–N/O scatterers at 2.10 Å with a single Fe–O scatterer at 1.91 Å, whereas fit 18 has 4 Fe–N/O scatterers at 2.12 Å with a single Fe–O scatterer at 1.94 Å. The coordination number of five for fit 18 is more consistent with the pre-edge area (Table 2.2), and the scattering distances for the primary coordination sphere are identical to those of **WT^{R}S** within error. On the other hand, fit 15 has an Fe–O scatterer assigned to the hydroxo bridge that is

much shorter than the shortest 1.97 Å Fe^{II}-OH distance established by synthetic precedent. For these reasons, fit 18 is favored as the best fit for **E377D^{R}**. The remaining scatterers in the best fit are 1 Fe at 3.26 Å, and C/N atoms at 3.05 Å and 4.35 Å from bound histidines. As expected, a carbon scatterer at ~2.6 Å was not required to fit the EXAFS data; introduction of such a scatterer led to its shift to the 3.05-Å carbon shell or to the 2.12-Å nitrogen shell upon refinement. The absence of this scatterer is consistent with a lack of a bidentate carboxylate ligand, which was the rationale for making this variant. This result is also in agreement with the crystal structure of **E377D^{Ox}** presented above.

2.3.7 – Transient Kinetic Comparison of the WT and E377D Reaction with the NRPS and O_2.

The XAS studies of the **E377D^{R}** mutant show that this variant is a reasonable structural mimic of the activated **WT^{R}S** complex. We next compared the O_2-reactivity of this mutant to that of the WT enzyme. Using stopped-flow spectroscopy, we probed the reactions of **WT^{R}** and **E377D^{R}** with O_2 in the presence or absence of $CmlP_{AT}$ or $CmlP_{AT}$~L-PAPA (Figure 2.7). All experiments were performed at 4.5 ºC in 50 mM HEPES and the enzymes were reacted with O_2-saturated buffer (roughly 1 mM O_2 after 1:1 mixing) to establish pseudo-first-order conditions. The time courses were fit to multiple summed exponential equations as described in Experimental Procedures to yield reciprocal relaxation times (τ^{-1}, RRTs) and phase amplitudes. The results of the fitting are given in Table 2.4. Most time courses required two large amplitude phases with relatively large RRTs. In all experiments, very slow phases were also observed that, based on the observed RRTs, likely arise from cluster autooxidation in CmlA molecules that are not complexed with $CmlP_{AT}$~L-PAPA. However, the two fastest phases account for most of the observed absorbance change at 340 nm. The observation of two phases implies two steps, but it does not indicate whether the steps are sequential or parallel. However, because the large spectroscopic change observed for each phase can be attributed solely to oxidation of the cluster, the data are more consistent with independent oxidation

pathways originating from some unknown difference in the protein structure. In Table 2.4, the phases are grouped based on the magnitude of the corresponding RRTs.

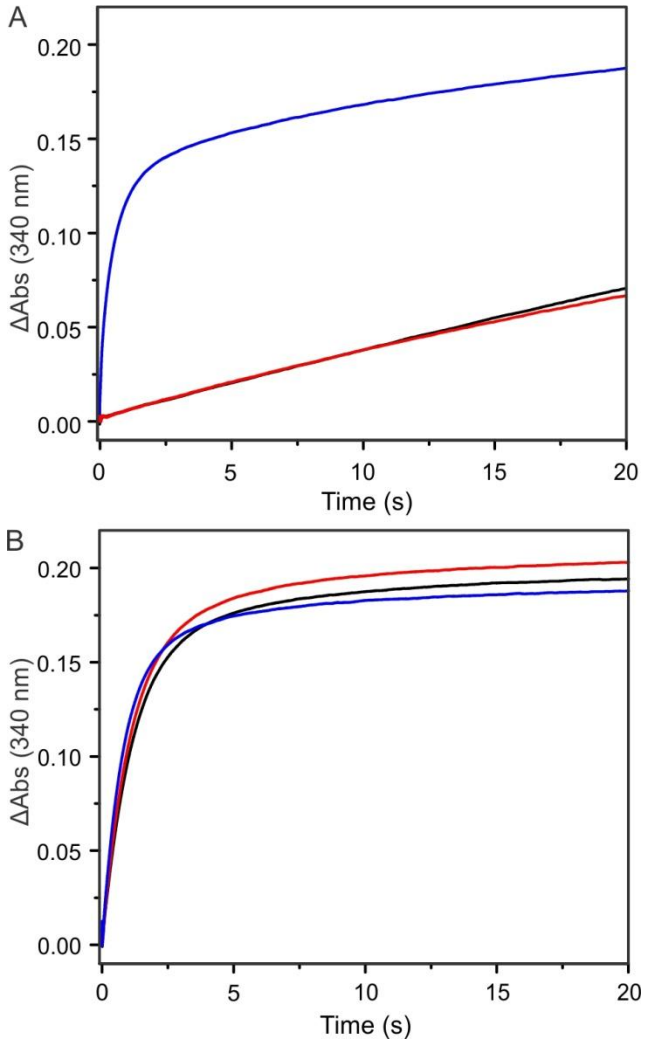

Figure 2.7. Stopped-flow transient kinetic time courses of the CmlA:CmlP reaction monitored at 340 nm. (A) Reaction of **WT^{R}** with $CmlP_{AT}$ and O_2. With O_2 (black), with $CmlP_{AT}$ and O_2 (red), and with $CmlP_{AT}$~L-PAPA and O_2 (blue). (B) Reaction of **E377D^{R}** CmlA with $CmlP_{AT}$ and O_2. With O_2 (black), with $CmlP_{AT}$ and O_2 (red), and with $CmlP_{AT}$~L-PAPA and O_2 (blue). Reactions were performed in 50 mM HEPES pH 7.5 at 4.5 °C and contained 75 μM CmlA ± 100 μM $CmlP_{AT}$ and 0.95 mM O_2.

Table 2.4. Transient kinetic reaction parameters[a]

	τ_1^{-1} (s^{-1})	τ_2^{-1} (s^{-1})
WT^R + O_2	0.016 ± 0.001	
WT^R + $CmlP_{AT}$ + O_2	0.034 ± 0.01	0.010 ± 0.001
WT^R + $CmlP_{AT}$~L-PAPA + O_2	14 ± 2	2.0 ± 0.3
E377D^R + O_2	0.89 ± 0.03	0.12 ± 0.07
E377D^R + $CmlP_{AT}$ + O_2	1.0 ± 0.1	0.21 ± 0.07
E377D^R + $CmlP_{AT}$~L-PAPA + O_2	1.3 ± 0.1	0.27 ±0.1
WT^R + $CmlP_{AT}$~L-Tyr + O_2	12 ± 1	2.1 ± 0.1
WT^R + $CmlP_{AT}$~D-Tyr + O_2	0.14 ± 0.01	0.036 ± 0.001

[a]All values were determined at 4.5 °C. Errors represent one standard deviation. Reactions contained 75 μM chemically reduced CmlA ± 100 μM $CmlP_{AT}$ and 0.95 mM O_2.

As we have previously observed, in the absence of $CmlP_{AT}$, **WT^R** re-oxidizes very slowly when exposed to O_2.[64] This process can be fit with only a single exponential phase (τ^{-1} = 0.016 s^{-1}). Upon addition of $CmlP_{AT}$ having a Ppant linker but lacking L-PAPA (**WT^{R}U** plus O_2), the reaction becomes biphasic. However, the RRTs remain comparable to those observed in the absence of the NRPS (τ_1^{-1} = 0.034 s^{-1}, τ_2^{-1} = 0.010 s^{-1}). In the presence of $CmlP_{AT}$~L-PAPA, the reaction (**WT^{R}S** plus O_2) dramatically accelerates (τ_1^{-1} = 14 s^{-1}, τ_2^{-1} = 2 s^{-1}), as expected based on the regulatory role of $CmlP_{AT}$~L-PAPA.

Analogous experiments were performed with **E377D^R**. Even in the absence of $CmlP_{AT}$, the auto-oxidation of **E377D^R** exhibited two exponential phases. The RRTs were 8-55 times faster than **WT^R** oxidation under the same conditions (τ_1^{-1} = 0.89 s^{-1}, τ_2^{-1} = 0.12 s^{-1}). In the presence of $CmlP_{AT}$ only, the reaction accelerated slightly more (τ_1^{-1} = 1.0 s^{-1}, τ_2^{-1} = 0.21 s^{-1}). Notably, when **E377D^R** was reacted with $CmlP_{AT}$~L-PAPA the reaction was observed to again only experience a slight additional acceleration (τ_1^{-1} = 1.3 s^{-1}, τ_2^{-1} = 0.27 s^{-1}).

2.4 – Discussion

Tightly controlled O_2 activation is a hallmark of oxygenase enzymes.[132, 165, 166] Regulatory mechanisms that modulate the formation of reactive oxygen species prevent highly potent oxidants that form during catalysis from causing cellular damage *via* non-specific reactions. Due to the inherent potency of the high-valent iron-oxygen species formed, the most sophisticated regulatory mechanisms are arguably present in the oxygenase enzymes that hydroxylate unactivated C-H bonds. One such regulatory mechanism has been detected in CmlA and is tied to the binding of the NRPS-bound substrate.[18, 64] The work presented here provides the first insights into the NRPS-mediated catalytic regulation in CmlA. Lessons learned from this work likely extend to many homologues of CmlA in other natural product biosynthetic pathways. By comparing and contrasting the regulatory mechanism in CmlA to those found in other diiron oxygenase families, we gain fundamental insights into the underlying regulatory logic that Nature has devised to control biological O_2 activation in diverse protein scaffolds. These topics and others are discussed below.

2.4.1 – Structural Models of Changes in the Reduced CmlA Diiron Cluster Upon Substrate Binding

The models of the diferrous cluster developed above can be categorized into two groups: the clusters of **WT^{R}** and **WT^{R}U**, having six-coordinate Fe centers, and those of **WT^{R}S** and **E377D^{R}**, having at least one five-coordinate Fe center. The Fourier-transformed EXAFS data for each pair look similar (Figure 2.4, left) but distinct from those of the other pair. Indeed, detailed analysis of the data shows that the distances between most atoms in the clusters present in each of the enzyme species considered here are very similar or identical within error. This observation implies that there are no large scale rearrangements within the cluster upon substrate binding. However, the data also reveal more subtle changes that have a large impact on catalysis. Most importantly, the shift in the coordination mode of a key carboxylate residue appears to be at the heart of

the change from six- to five-coordinate iron centers (Figure 2.8) that is required for much more rapid reaction with O_2. Crystallographic characterization of **WT^R** indicates that E377 is the carboxylate that shifts upon substrate binding. We show here that it is possible to force the shift of the carboxylate of the 377 residue by making the E377D variant. Accordingly, the lack of a bidentate carboxylate ligand evident from the EXAFS spectra of **E377D^R** is consistent with the monodentate D377 ligand observed in the crystal structure of oxidized E377D CmlA.

One potential difficulty with the proposed correlation between a monodentate carboxylate at position 377 and high reactivity with O_2 is found in the EXAFS of **WT^{R}U**, which also lacks the signature 2.6–Å carbon scatterer, but still remains unreactive towards O_2. However, while we cannot assign E377 as a bidentate ligand in **WT^{R}U** based on the EXAFS data, the XAS preedge data are not consistent with having five-coordinate iron centers when compared with the values observed for **WT^{R}S** and **E377D^R**. This observation suggests that E377 may become monodentate in **WT^{R}U** and a solvent molecule fills the vacated site to prevent O_2 binding. For **WT^{R}S**, the bound L-PAPA may prevent solvent binding to facilitate O_2 binding and activation.

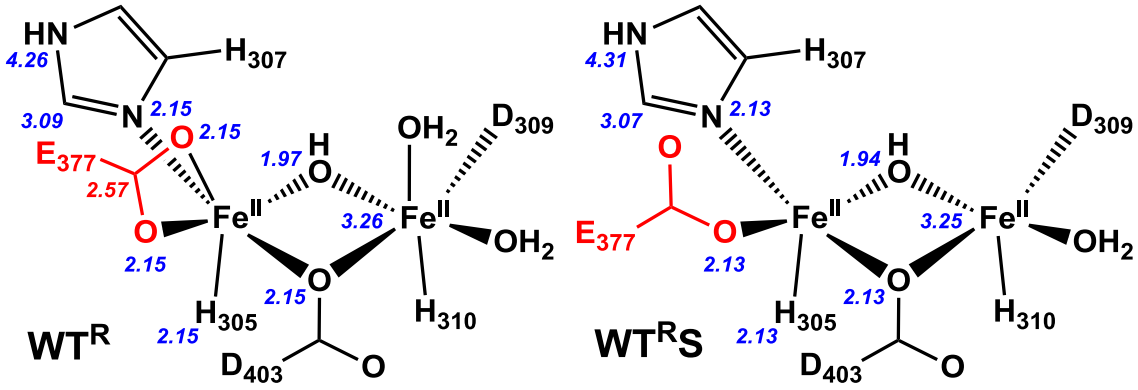

Figure 2.8. Structural models of **WT^R** (left) and **WT^{R}S** (right) as determined by EXAFS analysis. Numbers in italics represent the best fit scattering distances in Å.

2.4.2 – Comparisons of CmlA and sMMOH.

The chemically reduced diiron cluster structure of CmlA is intriguing. To our knowledge there is no synthetic precedent for a (μ-hydroxo)(μ-1,1-carboxylato)diiron(II) core, although synthetic diiron(II) complexes with different combinations of hydroxo and μ-1,3-bound carboxylato bridges are known.[92, 159, 160] The closest analog in an enzyme active site is that found in reduced sMMOH, where the two irons are bridged by a hydroxide, a bidentate carboxylate, and a monodentate carboxylate, the carbonyl oxygen atom of which is also bound to one of the iron atoms (Figure 2.9).[5, 47] Not too surprisingly, the Fe•••Fe distances for reduced CmlA and reduced sMMOH are comparable.

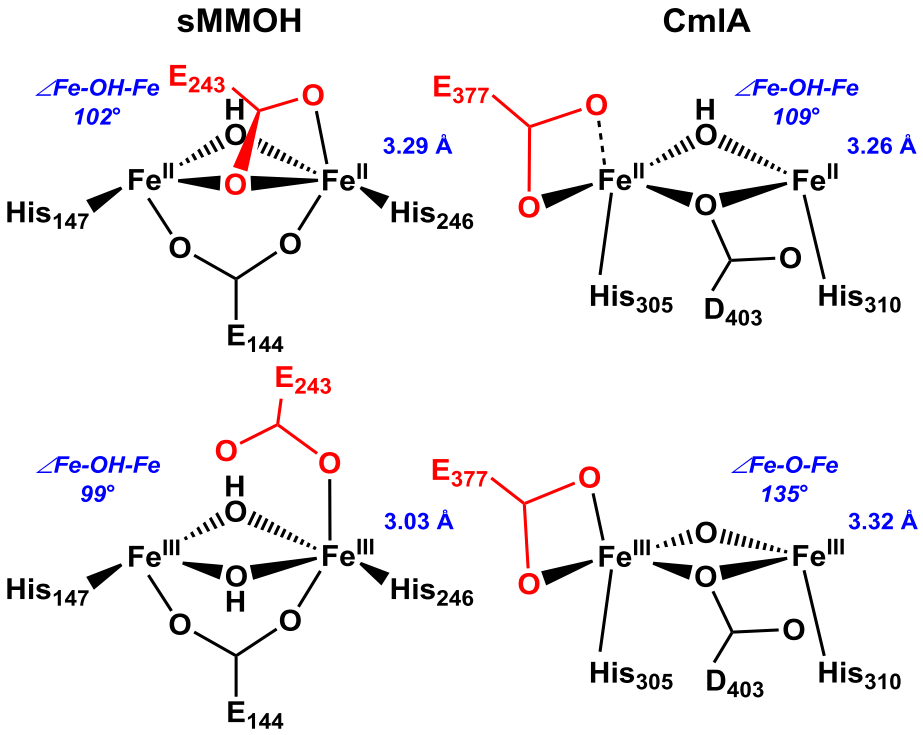

Figure 2.9. Diiron core differences between CmlA and sMMOH upon redox change. Active site models adapted from crystallographic data from refs [5, 18, 47, 150]. Top row: diferrous Fe centers. Bottom row: diferric Fe centers. Left: Fe•••Fe distance contracts while maintaining ∠Fe-O-Fe in sMMOH. Right: ∠Fe-O-Fe increases while maintaining Fe•••Fe distance in CmlA. Distances from EXAFS data from refs [46, 139, 163]. ∠Fe-O-Fe in italics; calculated by assuming a symmetric diiron core, where d(Fe1-O) = d(Fe2-O). Residues shown in red are proposed to shift during the respective catalytic cycles. Both enzymes have μ-1,1-carboxylato residues in the diferrous state (sMMOH E243 and CmlA D403), but only sMMOH E243 is proposed to shift. Some ligands are omitted for clarity.

Interestingly, the Fe•••Fe distance in the diiron cluster of CmlA increases by only 0.06 Å on going from $\mathbf{WT^{R}}$ to $\mathbf{WT^{Ox}}$, due to the maintenance of the 'diamond' core structure (Figure 2.9). Two-electron oxidation and the loss of a proton from the hydroxo bridge mainly result in the increase of the Fe–O–Fe angle, from 110° to 122° based on the crystal structures and from 109° to 135° calculated by using the Fe–O and Fe•••Fe distances obtained from EXAFS analysis. The EXAFS derived distances are more reliable in this case, as the crystal structure of $\mathbf{WT^{Ox}}$ could have been partially photoreduced.[18] Also, the XAS experiments require a much lower radiation dose and the photoreduction is more easily monitored. In contrast, the 3.29-Å Fe•••Fe distance of reduced sMMOH shrinks to 3.03 Å upon oxidation to the diferric form.[46, 47, 163, 167] This dramatic difference can be attributed to the replacement of the 1,1-carboxylate bridge by a hydroxide. Consequently, the Fe–OH–Fe angles of the two forms of sMMOH remain essentially unchanged.

Very recently, some of us have reported EXAFS data for another diiron enzyme, deoxyhypusine hydroxylase (DOHH), that also exhibits a < 0.1 Å change in the Fe•••Fe distance for a series of enzyme species, including its diferric-peroxo intermediate.[36] The relative invariance of the cluster structure was proposed to be a consequence of the unique HEAT-repeat protein fold in DOHH that allowed for rigid cross-domain binding of the 4-His-2-carboxylate ligand framework to the Fe centers. It could be argued that the unusual metallo-β-lactamase fold of CmlA may also innately impart rigidity to the diiron cluster, but our data does not provide us clear insight into the issue. However, the diiron active sites of CmlA and DOHH are somewhat different from each other, with the two carboxylates in the latter enzyme not properly positioned to allow them to act as bridging ligands.

Although no oxygenated intermediates for CmlA have been isolated, the characterization presented here and that of other diiron enzymes provide structural insight into the O_2 activation process. Upon exposure to O_2, reduced sMMOH is converted to intermediate **P**, which is proposed to be a cis μ-1,2-peroxo species.[5, 91, 168] The bridging

OH of reduced sMMOH (Figure 2.9, top left) is *trans* to the bound histidine ligands, facing the open space where methane and O_2 can approach the cluster, and it is weakly bound based on its Fe–O bond lengths of 2.52 and 2.65 Å determined by crystallography.[47] Consequently, it is likely that the μ-1,2-peroxo forms by displacing this OH, leaving the μ-1,1-carboxylato bridge intact (Figure 2.10, left). We have speculated that the shift of this carboxylate back to the terminal monodentate position of diferric sMMOH (Figure 2.9, bottom left) occurs in the subsequent step of the reaction cycle in order to open space for formation of the bis-μ-oxo diamond core of the high-valent intermediate sMMOH **Q**.[83]

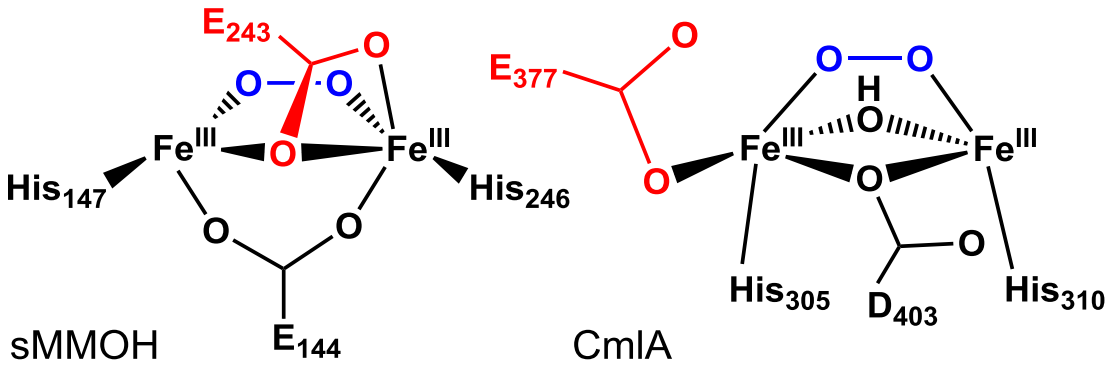

Figure 2.10. Proposed structure of O_2 bound peroxo intermediates for sMMOH (left) and CmlA (right). Structures adapted from PDB codes 1FYZ and 5KIK for sMMOH and CmlA, respectively. Residues shown in red are proposed to shift during the respective catalytic cycles. Atoms in blue are from the peroxo moiety, derived from O_2. Some ligands are omitted for clarity.

A quite different scenario is likely for CmlA based on the structural and spectroscopic studies reported here, despite the overall similarities in the ligand environments of sMMOH and CmlA diiron centers. In the case of CmlA, the bridging OH is *cis* to the histidine ligands (Figure 2.9, top right) and tightly bound with Fe–O distances of ~2 Å, but it does not directly face the open substrate binding pocket. The observed bi- to monodentate shift of terminal residue E377 in response to substrate binding to convert Fe1 from six- to five-coordinate and the retention of all bridging

ligands suggest that an open site is created on Fe1 that could be readily occupied by O_2. This ligand site is adjacent to one of the two solvents bound to Fe2 (Figure 2.2A). Formation of a μ-1,2-peroxo species bridging these ligand sites would orient the peroxo oxygens *trans* to the two His ligands of the iron cluster (Figure 2.10, right). This placement would position the bound oxygen atoms immediately adjacent to the binding site of the CmlP-tethered L-PAPA substrate previously proposed from computational docking (Figure 2.11).[18] The equivalent O_2 binding orientation has also been proposed for sMMOH and all other diiron oxygenases that are known to generate *cis*-μ-1,2 peroxo intermediates except hDOHH.[5, 17, 31, 35, 79, 83, 169] Moreover, the presence of an open coordination site on Fe1 would account for the 1000-fold increase in O_2 binding rate upon formation of the complex with CmlP~L-PAPA. It is interesting to note that formation of a μ-1,2-peroxo intermediate in CmlA in the position proposed here would still retain one of the two initial waters bound to Fe2. This remaining solvent ligand may play an important role by providing a proton required for cleavage of the O-O bond to form the reactive high valent intermediate.[69]

The μ-1,2-peroxo complexes of CmlA and sMMOH proposed here differ in that the peroxo unit of sMMOH forms in the same plane as the μ-1,1-carboxylato bridge of E243, whereas the peroxo unit of CmlA forms in the plane perpendicular to that of the μ-1,1-carboxylato bridge of D403 (Figure 2.10). Despite this difference in orientation, the presence of the rarely observed μ-1,1-carboxylato ligand in the diiron centers of two O_2 activating enzymes raises the question of whether D403 of CmlA might also be mobile in some reaction cycle steps as we have proposed for E243 of sMMOH.[83] However, in contrast to the case for sMMOH, none of the changes in the CmlA ligand structure required to form a peroxo intermediate mandate a shift in the position of the μ-1,1-carboxylato bridge D403. This residue is locked into position by the protein secondary structure and hydrogen bonding, so a shift analogous to that proposed for sMMOH E243 residue is unlikely. CmlA D403 appears to serve a structural function more similar to that of the 1,3-bridging carboxylate E144 of reduced sMMOH. Whereas CmlA D403 is opposite a strongly bound bridging OH, sMMOH E144 is opposite the strongly bound

terminal solvent on Fe1. In each case, it is likely that O_2 does not displace the strong ligand but rather adds in a perpendicular plane to form the peroxo intermediate (Figure 2.10).

It is interesting to consider how the binding of $CmlP_{AT}$~L-PAPA can induce the rearrangement of E377 to begin the cascade of ligand changes that allows O_2 binding and activation. It is known that neither free L-PAPA alone[64] nor **WT^{R}U** (Figure 2.7) can induce rapid O_2 binding. The XAS and minor kinetic changes noted here for **WT^{R}U** show that a complex between CmlA and $CmlP_{AT}$ without L-PAPA bound does form despite the lack of acceleration in O_2 activation. Consequently, it is likely that the precise placement of substrate in the active site by the fully loaded NRPS is necessary. A previous docking simulation of CmlA with $CmlP_{AT}$-L-PAPA showed that the amine group of L-PAPA is positioned within hydrogen bonding distance to E377 as illustrated in Figure 2.11.[18] In support of this proposal, we note that $CmlP_{AT}$ loaded with L-tyrosine but not D-tyrosine can induce O_2 binding and activation by CmlA and only the former is *β*-hydroxylated (Table 2.4 and Figure 2.22). These alternative substrates would differ by the orientation of the substrate amine relative to E377.

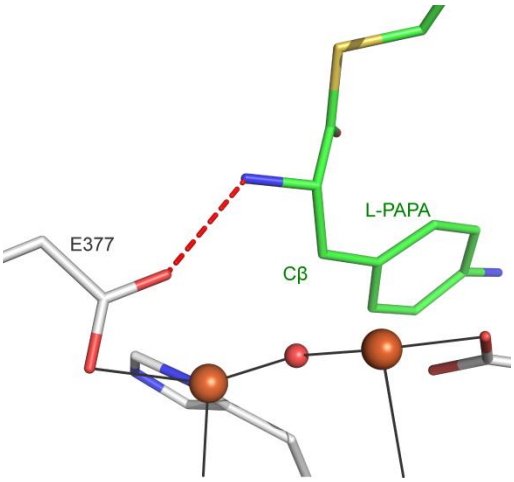

Figure 2.11. Computationally docked model of Ppant-L-PAPA in the active site of **WT^{Ox}**. The amine group of L-PAPA is within hydrogen bonding distance to the carboxylate of E377. Binding of NRPS~L-PAPA could cause a sterically-driven conformational change of E377 to a monodentate mode which triggers the reaction with O_2. The docked model is based on work presented in ref.[18]

2.4.3 – Comparisons of the CmlA Regulatory Mechanism to Those of Other Diiron Enzymes

In sMMOH, the rate constants for the reaction of diferrous enzyme with O_2 and the subsequent generation of intermediates **P** and **Q** are unaffected by the presence or absence of methane or other substrates.[5, 45, 132, 170, 171] This reactivity pattern is quite distinct from that of CmlA where the rate constant for the reaction of O_2 with diferrous CmlA is highly regulated by the binding of CmlP~L-PAPA. We have proposed that sMMOH uses a regulatory mechanism appropriate for selection of a small, highly stable substrate.[132, 171, 172] It sequesters the high-valent intermediate inside the protein and admits methane through a size-selective pore created by a regulatory protein, MMOB, when it forms a complex with sMMOH. CmlA must catalyze similar hydroxylation chemistry but in a stereo- and regiospecific manner with a larger substrate. As a result, access to the cluster is through a much larger channel,[18] which would expose the activated species to solvent and adventitious substrates if it were to be present at the beginning of the reaction cycle. CmlA appears to utilize a more typical strategy for enzymes in which substrate is first delivered and specifically oriented in the active site, and this placement then triggers O_2 binding and activation. In this sense, CmlA is more similar to the acyl-ACP Δ^9-desaturase, which requires binding of the ACP-tethered fatty acid substrate to activate the diiron cluster for reaction.[173] The data presented here indicate that CmlA employs a previously unrecognized carboxylate-shift mechanism to couple O_2 activation to substrate binding.

2.4.4 – Implications of the Inability of E377D to Generate Product.

Mutation of E377 to D377 uncouples the O_2-binding and cluster oxidation reactions, but also abolishes formation of hydroxylated product. The substitution of Asp for Glu has the desired effect of converting the carboxylate ligand from bi- to monodentate. However as illustrated in Figure 2.6C, the shorter carbon skeleton of Asp results in significantly different positioning of the unbound carboxylate oxygen.

Consequently, the putative hydrogen bond with bound L-PAPA would not form in the same way as with E377 (Figure 2.11). Indeed, it is likely that the D377 carboxylate oxygen would be too distant to form any hydrogen bond. Two potential outcomes are: (1) misalignment of the substrate with the activated oxygen species so that uncoupling rather than hydroxylation occurs, or (2) failure to induce release of the solvent from Fe2 so that cluster oxidation rather than cis-μ-peroxo intermediate formation occurs. We favor the latter explanation because cluster oxidation is greatly accelerated even in the absence of $CmlP_{AT}$-L-PAPA.

2.5 – Conclusion

We have shown that a single amino acid change that mimics the bi- to monodentate rearrangement of a diiron cluster carboxylate ligand in the active site of CmlP in response to substrate binding can obviate the strict regulation of O_2 binding and activation by the system. This represents a new type of regulation within the diiron enzyme family and adds to a growing list of regulatory functions mediated by carboxylate ligand reorganization. It is interesting to note that in all cases observed thus far, a carboxylate shift rather than complete carboxylate dissociation occurs.[5, 47, 138, 174] In most cases, the carboxylate ligand remains unprotonated, although the proposed role of a protonated carboxylate ligand in the sMMOH intermediate **P** to **Q** conversion may be a notable exception.[5, 83, 168] Other potential roles for carboxylate ligands include: hydrogen bonding to orient substrates, shifts related to changes in metal coordination number, and alteration of the bridging mode of the cluster engendering changes in its electronic structure. The regulatory mechanism of CmlA showcases several of these modes of action.

2.6 – Supplementary Information

General EXAFS considerations: In the fit tables of EXAFS data, N refers to the number of scatterers used for a particular shell, R is the distance of the scattering shell, σ^2 is the mean-squared deviation (or Debye-Waller factor), E_0 is the edge shift parameter, and the goodness of fit (GOF) parameters are calculated as $F = \sqrt{\sum k^6 \left(\chi_{\exp} - \chi_{calc}\right)^2}$, $F' = \sqrt{\sum k^6 \left(\chi_{\exp} - \chi_{calc}\right)^2 / \sum k^6 \chi_{\exp}{}^2}$. For all fits, the amplitude reduction factor ($S_0{}^2$) was set to 0.9.

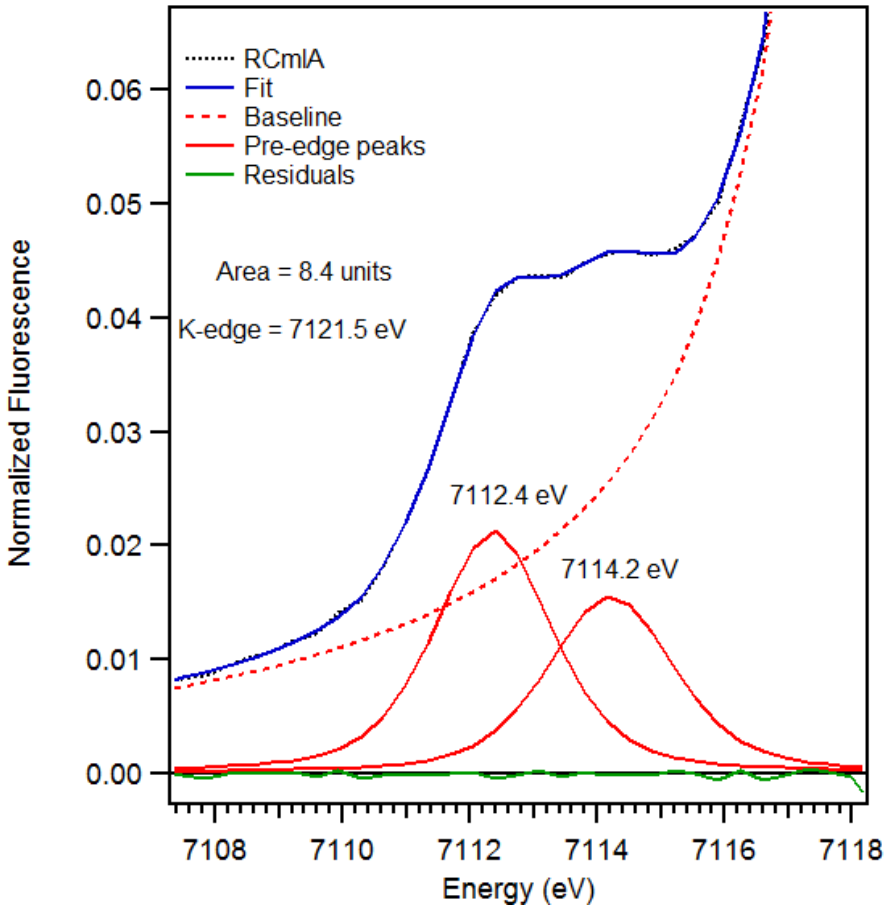

Figure 2.12. Pre-edge region analysis of **WT**$^{\mathbf{R}}$. The experimental data (black dotted), baseline (red dashed), pre-edge peak components (red solid), residuals (green solid) and total fit (blue solid) are shown.

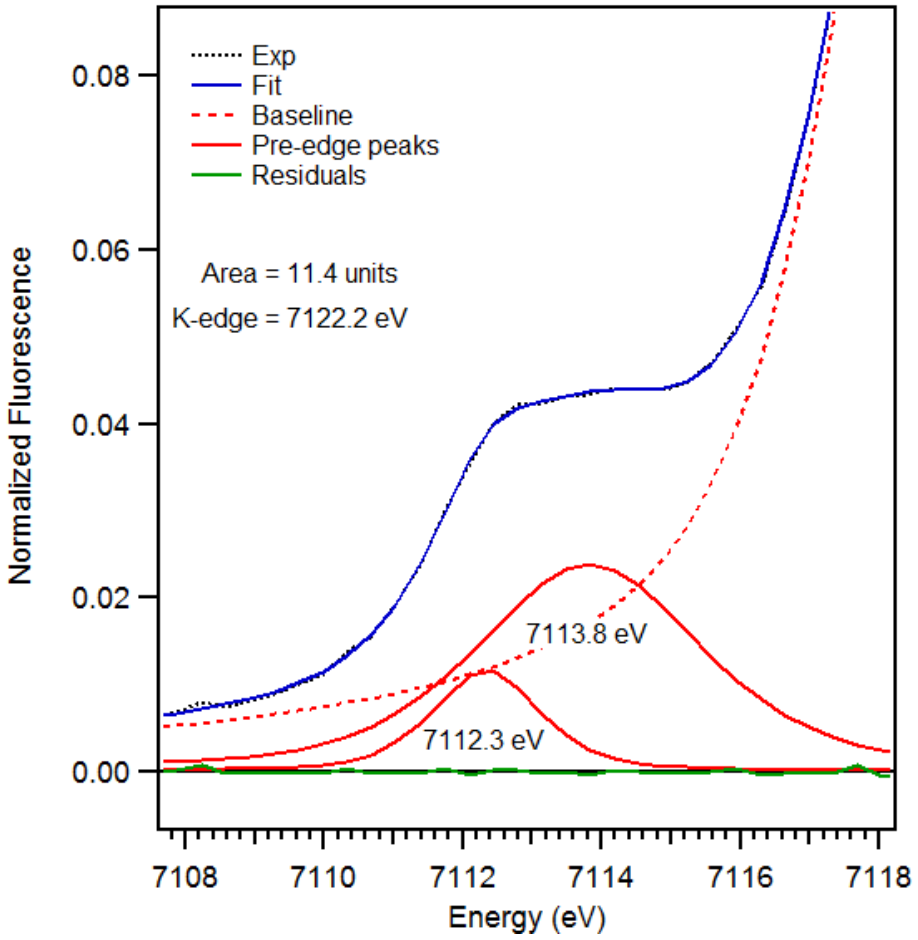

Figure 2.13. Pre-edge region analysis of **WT^{R}S**. The experimental data (black dotted), baseline (red dashed), pre-edge peak components (red solid), residuals (green solid) and total fit (blue solid) are shown.

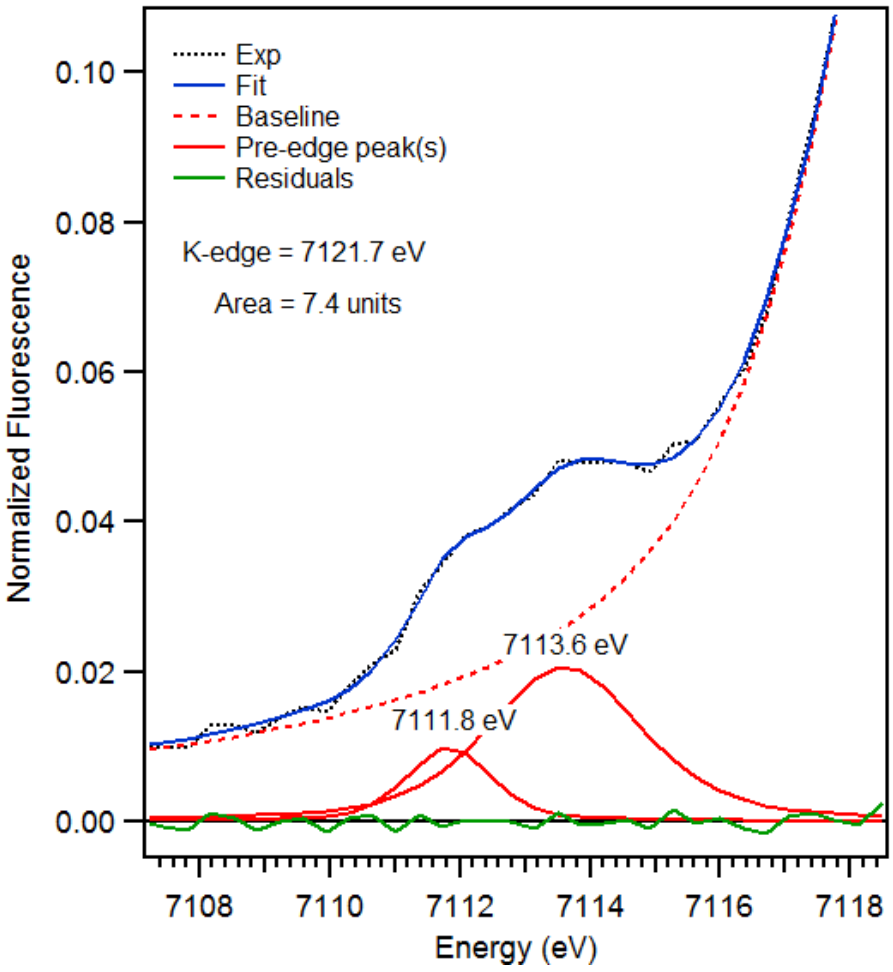

Figure 2.14. Pre-edge region analysis of **WT^{R}U**. The experimental data (black dotted), baseline (red dashed), pre-edge peak components (red solid), residuals (green solid) and total fit (blue solid) are shown.

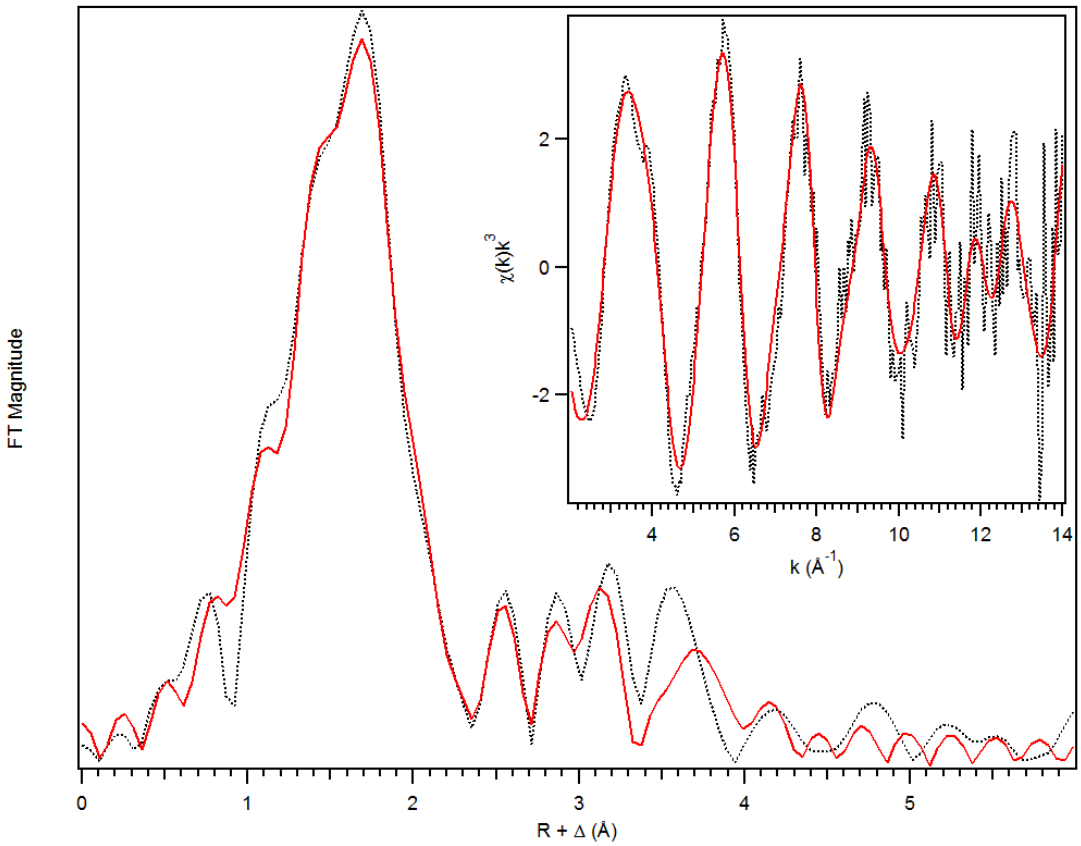

Figure 2.15. Fit (red solid line) of the unfiltered (black dotted) EXAFS data (inset) and corresponding Fourier transform of $\mathbf{WT^R}$ (Table 2.5, Fit 14). Data was fit between k = 2 – 14 $Å^{-1}$.

Table 2.5. Fit parameters for the unfiltered EXAFS data of **WT^{R}**, between k = 2 – 14 Å^{-1}. Fit 14 gives the most reasonable fit of the experimental data.

	Fe-N/O			Fe•••C/N/O			Fe•••Fe			Fe•••C				GOF	
Fit	**N**	**R(Å)**	**$\sigma^2(10^{-3})$**	**N**	**R(Å)**	**$\sigma^2(10^{-3})$**	**N**	**R(Å)**	**$\sigma^2(10^{-3})$**	**N**	**R(Å)**	**$\sigma^2(10^{-3})$**	**E_o**	**F**	**F'**
1	6	2.14	7.87										-8.70	197	509
2	5	2.15	6.4										-7.90	196	508
3	4	2.15	4.89										-7.06	210	526
4	3	2.16	3.29										-6.21	245	568
5	6	2.14	7.96	1	2.57	5.42							-8.59	185	494
6	6	2.14	7.79	1	2.56	6.11				3	3.10	4.44	-8.41	166	467
7	6	2.15	7.91	1	2.56	6.77				1	3.09	-1.70	-8.27	159	458
8	6	2.15	7.87	1	2.56	6.43	1	3.27	6.36	3	3.11	1.21	-8.04	139	428
9	6	2.15	7.86	1	2.55	6.37	1	3.27	6.67	3	3.11	1.25	-7.77	133	419
										2	4.03	2.74			
10	6	2.15	7.85	1	2.56	6.68	1	3.27	6.23	3	3.11	1.10	-7.72	122	400
										2	4.10	3.55			
										3	4.29	5.93			
11	5	2.15	4.49	1	2.57	7.35	1	3.25	6.93	3	3.09	0.86	-10.3	106	373
	1	1.98	2.88							2	4.14	2.68			
										3	4.23	4.48			
12	5	2.15	4.46	1	2.57	6.68	1	3.26	5.92	4	3.09	2.21	-10.5	107	375
	1	1.98	2.84							3	4.26	3.00			
13	5	2.14	4.35	1	2.57	3.49				4	3.09	7.25	-11.4	134	420
	1	1.97	2.60							3	4.25	3.74			
14	**5**	**2.15**	**4.32**	**0.5**	**2.57**	**1.50**	**1**	**3.26**	**6.22**	**4**	**3.09**	**2.46**	**-10.8**	**106**	**373**
	1	**1.97**	**2.53**							**3**	**4.26**	**3.18**			
15	5	2.15	4.33				1	3.26	6.24	4	3.09	2.25	-10.6	110	380
	1	1.98	2.65				1	3.26	6.24	3	4.26	2.92			

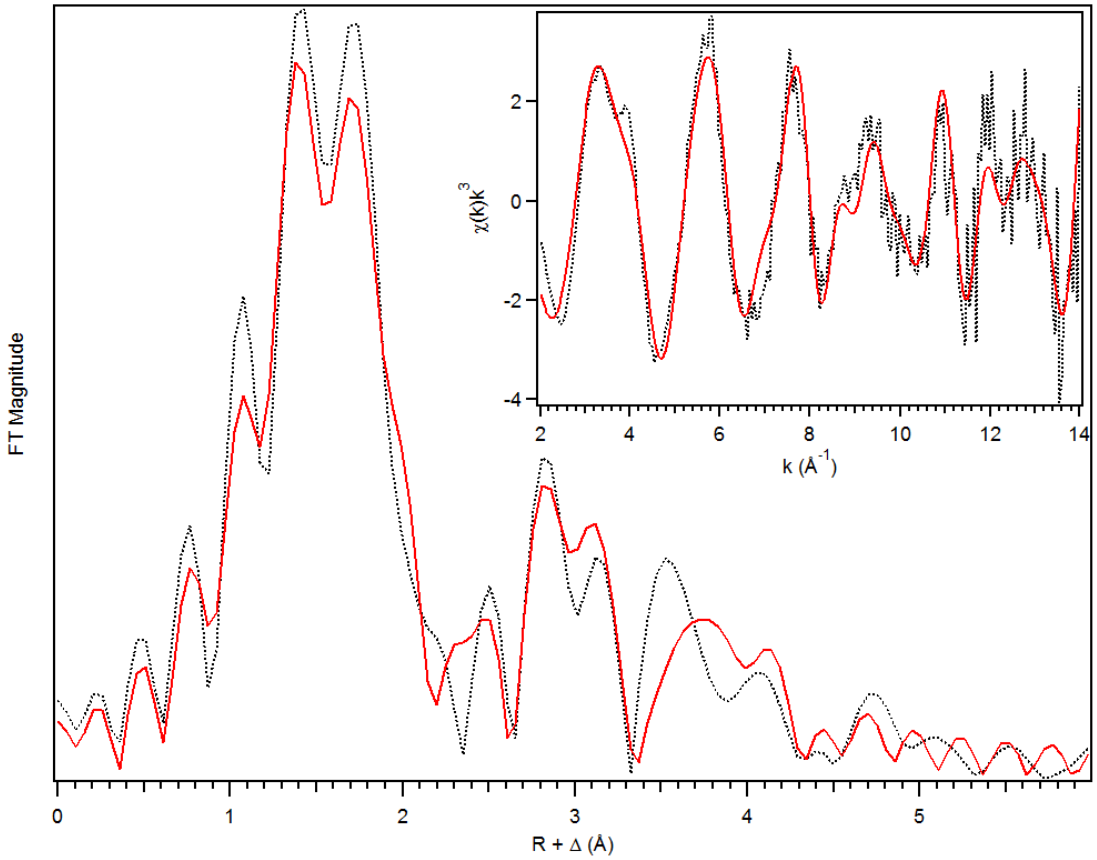

Figure 2.16. Fit (red solid line) of the unfiltered (black dotted) EXAFS data (inset) and corresponding Fourier transform of **WT^{R}S** (Table 2.6, Fit 15). Data was fit between k = 2–14 Å^{-1}.

Table 2.6. Fit parameters for the unfiltered EXAFS data of **WT^{R}S**, between k = 2 – 14 Å^{-1}. Fit 15 gives the most reasonable fit of the experimental data.

	Fe-N/O			Fe•••O/N			Fe•••Fe			Fe•••C				GOF	
Fit	**N**	**R(Å)**	**$\sigma^2(10^{-3})$**	**N**	**R(Å)**	**$\sigma^2(10^{-3})$**	**N**	**R(Å)**	**$\sigma^2(10^{-3})$**	**N**	**R(Å)**	**$\sigma^2(10^{-3})$**	**E_o**	**F**	**F'**
1	6	2.13	9.51										-8.92	249	593
2	5	2.14	7.82										-7.99	249	593
3	4	2.14	6.07										-7.09	259	605
4	4	2.14	3.59	2	1.97	5.44							-14.0	213	548
5	4	2.13	3.56	1	1.95	1.91							-12.5	220	558
6	5	2.12	4.93	1	1.94	1.78							-13.2	211	546
7	5	2.13	5.05	1	1.93	1.90	1	3.28	5.48				-12.6	197	528
8	4	2.14	3.56	2	1.97	5.33	1	3.28	5.5				-13.9	200	531
9	4	2.13	3.55	1	1.95	1.80	1	3.28	5.25				-12.5	205	539
10	4	2.14	3.26	1	1.96	1.49	1	3.25	3.66	5	3.07	3.38	-11.6	153	464
11	5	2.13	4.61	1	1.94	1.34	1	3.25	3.64	5	3.07	3.44	-12.6	143	449
12	4	2.14	3.18	2	1.97	4.76	1	3.25	3.53	5	3.07	3.18	-13.3	146	454
13	5	2.13	4.52	1	1.94	1.07	1	3.25	3.55	5	3.07	3.20	-13.0	124	418
										4	4.29	2.69			
14	5	2.13	4.49	1	1.94	1.12	1	3.25	3.49	5	3.07	3.13	-12.3	118	409
										4	4.23	2.54			
15	**5**	**2.13**	**4.53**	**1**	**1.94**	**1.12**	**1**	**3.25**	**3.49**	**5**	**3.07**	**3.30**	**-12.9**	**123**	**417**
										4	**4.31**	**1.91**			
16	5	2.13	4.52	1	1.95	1.19	1	3.25	3.34	5	3.07	2.96	-12.3	118	409
										4	4.25	1.88			
17	5	2.12	4.68	1	1.94	1.39				5	3.05	7.57	-13.1	189	516
										4	4.31	2.47			
18	**4**	**2.14**	**3.15**	**1**	**1.96**	**1.19**	**1**	**3.25**	**3.55**	**5**	**3.07**	**3.23**	**-12.1**	**133**	**434**
										4	**4.31**	**1.89**			

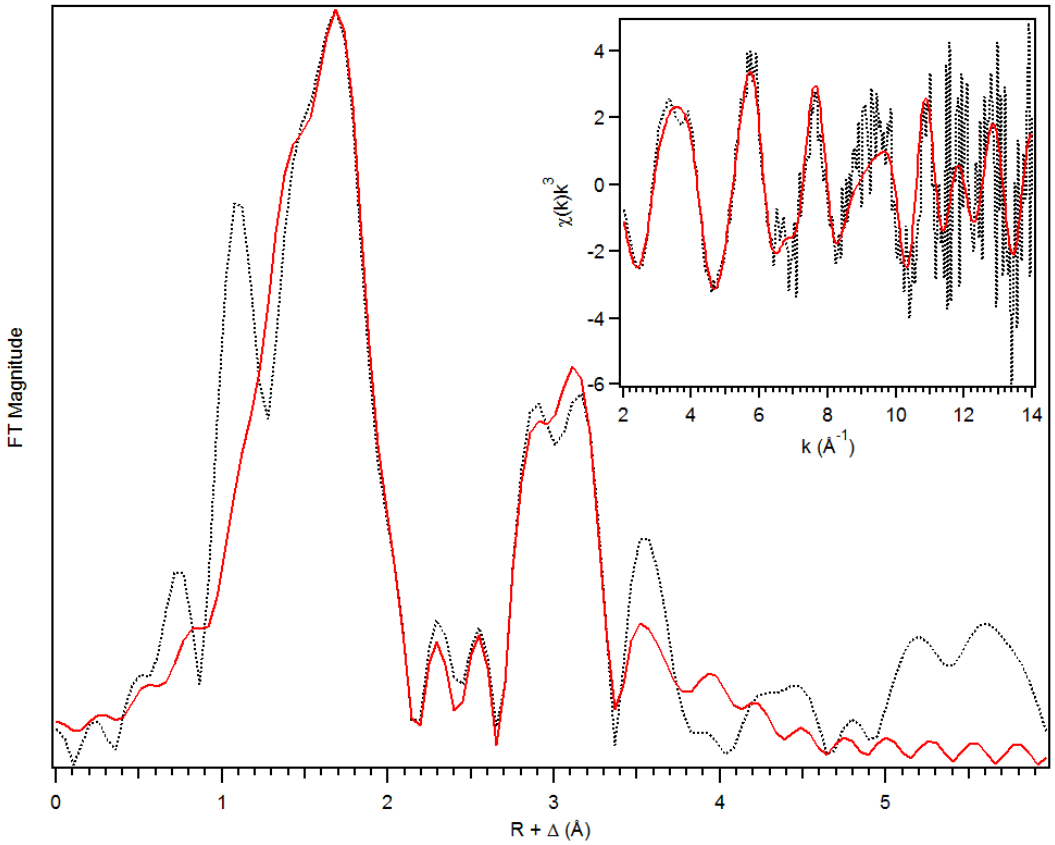

Figure 2.17. Fit (red solid line) of the unfiltered (black dotted) EXAFS data (inset) and corresponding Fourier transform of **WT^{R}U** (Table 2.7, Fit 23). Data was fit between k=2–14 Å^{-1}.

Table 2.7. Fit parameters for the unfiltered EXAFS data of **WT^{R}U**, between k = 2 – 14 Å^{-1}. Fit 23 gives the most reasonable fit of the experimental data.

	Fe-N/O			Fe•••O/N			Fe•••Fe			Fe•••C				GOF	
Fit	**N**	**R(Å)**	**$\sigma^2(10^{-3})$**	**N**	**R(Å)**	**$\sigma^2(10^{-3})$**	**N**	**R(Å)**	**$\sigma^2(10^{-3})$**	**N**	**R(Å)**	**$\sigma^2(10^{-3})$**	**E_o**	**F**	**F'**
1	6	2.12	9.62										-1.16	555	735
2	5	2.13	7.62										0.05	543	726
3	4	2.13	5.71										0.99	541	725
4	3	2.14	3.80										2.01	560	737
5	5	2.12	5.44	1	1.93	4.33							-3.46	524	714
6	4	2.14	3.53	1	1.97	2.80							-2.60	520	711
7	4	2.13	4.23	2	1.97	8.82							-4.53	523	713
8	5	2.13	5.98	1	1.94	6.66	1	3.31	2.97				-1.85	454	664
9	5	2.13	6.22	1	1.93	7.75	1	3.29	1.41	3	3.14	0.60	-2.06	420	639
10	5	2.13	6.19	1	1.94	7.69	1	3.30	1.43	4	3.15	3.20	-1.85	426	643
11	5	2.13	6.31	1	1.94	8.32	1	3.30	1.42	4	3.15	3.00	-1.58	411	632
										3	4.30	5.20			
12	5	2.13	7.77				1	3.32	1.42	4	3.16	3.77	0.36	418	638
										3	4.32	5.37			
13	6	2.12	9.72				1	3.31	1.26	4	3.16	3.08	-0.64	433	648
										3	4.31	5.18			
14	5	2.13	6.30	1	1.93	8.13	1	3.29	1.09	2	2.95	2.48	-2.20	406	628
										5	3.13	1.61			
										3	4.29	5.15			
15	4	2.14	4.83	1	1.98	6.66	1	3.30	1.46	2	2.95	3.76	-1.22	404	626
										5	3.13	2.64			
										3	4.30	5.28			

Table 2.7. (continued) Fit parameters for the unfiltered EXAFS data of **WT^{R}U**, between k = 2 – 14 Å^{-1}. Fit 23 gives the most reasonable fit of the experimental data.

	Fe-N/O			Fe•••O/N			Fe•••Fe			Fe•••C				GOF	
Fit	**N**	**R(Å)**	**$\sigma^2(10^{-3})$**	**N**	**R(Å)**	**$\sigma^2(10^{-3})$**	**N**	**R(Å)**	**$\sigma^2(10^{-3})$**	**N**	**R(Å)**	**$\sigma^2(10^{-3})$**	**E_o**	**F**	**F'**
16	5	2.13	6.20	1	1.93	7.82	1	3.32	2.10	4	3.18	8.23	-1.95	401	624
										3	3.55	2.23			
										3	4.30	3.96			
17	4	2.14	4.72	1	1.98	6.40	1	3.32	2.00	3	3.18	5.79	-1.11	400	623
										3	3.56	3.03			
										3	4.31	4.19			
18	4	2.14	4.33	0.5	1.96	1.69	1	3.33	2.11	3	3.19	6.66	-0.42	399	623
										3	3.56	2.90			
										3	4.31	4.18			
19	5	2.13	6.35	0.5	1.92	3.15	1	3.32	1.67	3	3.18	4.48	-1.34	400	623
										3	3.55	3.23			
										3	4.30	4.21			
20	5	2.13	6.37	0.5	1.93	3.47	1	3.30	1.61	4	3.15	3.78	-0.67	405	627
										3	4.31	5.38			
21	4	2.14	4.86	1	1.99	6.87	1	3.31	1.78	4	3.15	4.31	-0.34	410	631
										3	4.31	5.41			
22	**4.5**	**2.14**	**5.32**	**0.5**	**1.96**	**2.46**	**1**	**3.31**	**1.95**	**4**	**3.14**	**4.90**	**0.22**	**411**	**631**
										3	**4.31**	**5.63**			
23	**4.5**	**2.13**	**5.32**	**0.5**	**1.95**	**2.39**	**1**	**3.32**	**2.08**	**3**	**3.16**	**5.93**	**-0.65**	**399**	**623**
										3	**3.56**	**3.41**			
										3	**4.31**	**4.35**			
24	5.5	2.13	7.34	0.5	1.91	4.36	1	3.31	1.70	4	3.14	3.95	-0.56	415	635
										3	4.31	5.44			

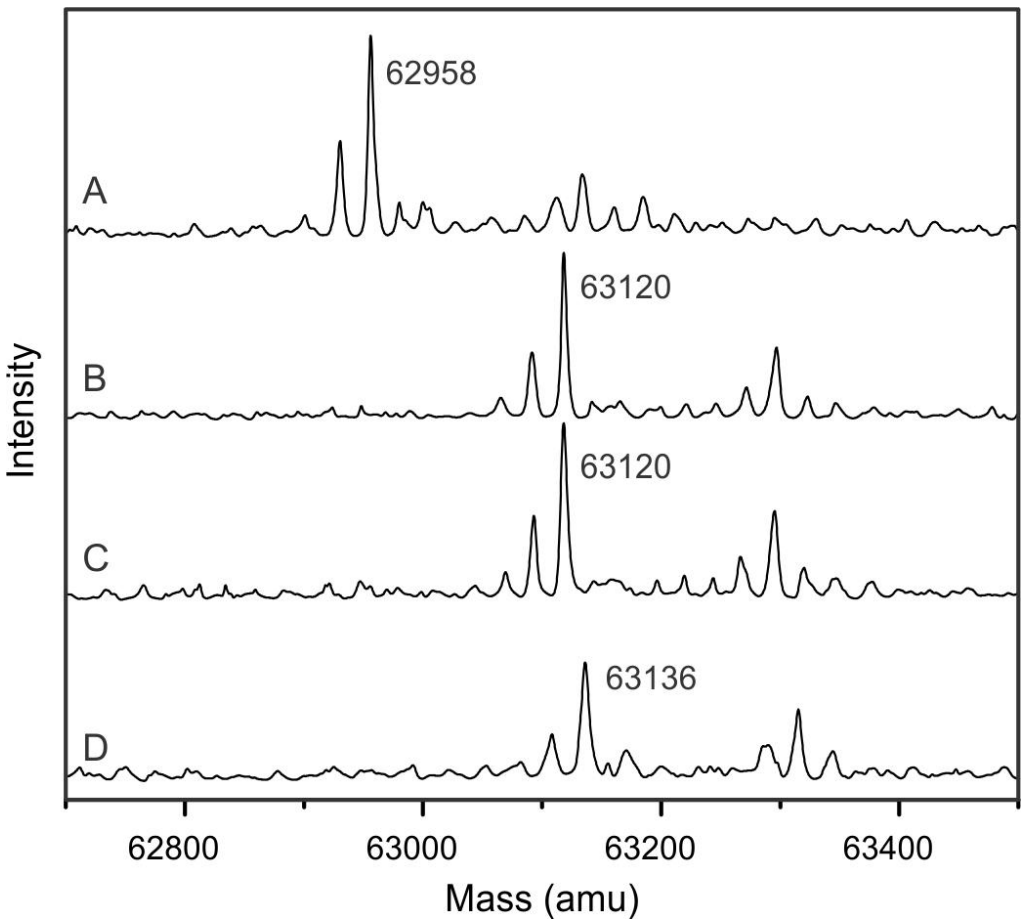

Figure 2.18. Deconvoluted LC ESI-MS protein mass spectra for the $CmlP_{AT}$ reaction products and controls. (A) Unloaded $CmlP_{AT.}$ (B) Reaction product for $\mathbf{WT^{Ox}}$ + $CmlP_{AT}$~PAPA and O_2 control reaction. (C) Reaction product for $\mathbf{E377D^{R}}$ + $CmlP_{AT}$~PAPA and O_2. (D) Reaction product for $\mathbf{WT^{R}}$ + $CmlP_{AT}$~PAPA and O_2. Loading of $CmlP_{AT}$ with L-PAPA results in the expected increase in mass of the protein (+162 amu). No hydroxylated product is detected in the $\mathbf{E377D^{R}}$ reaction, whereas the reaction with $\mathbf{WT^{R}}$ yields an increase in mass (+16 amu) consistent with hydroxylation of L-PAPA. The masses of the major peak are labeled in each reaction in amu.

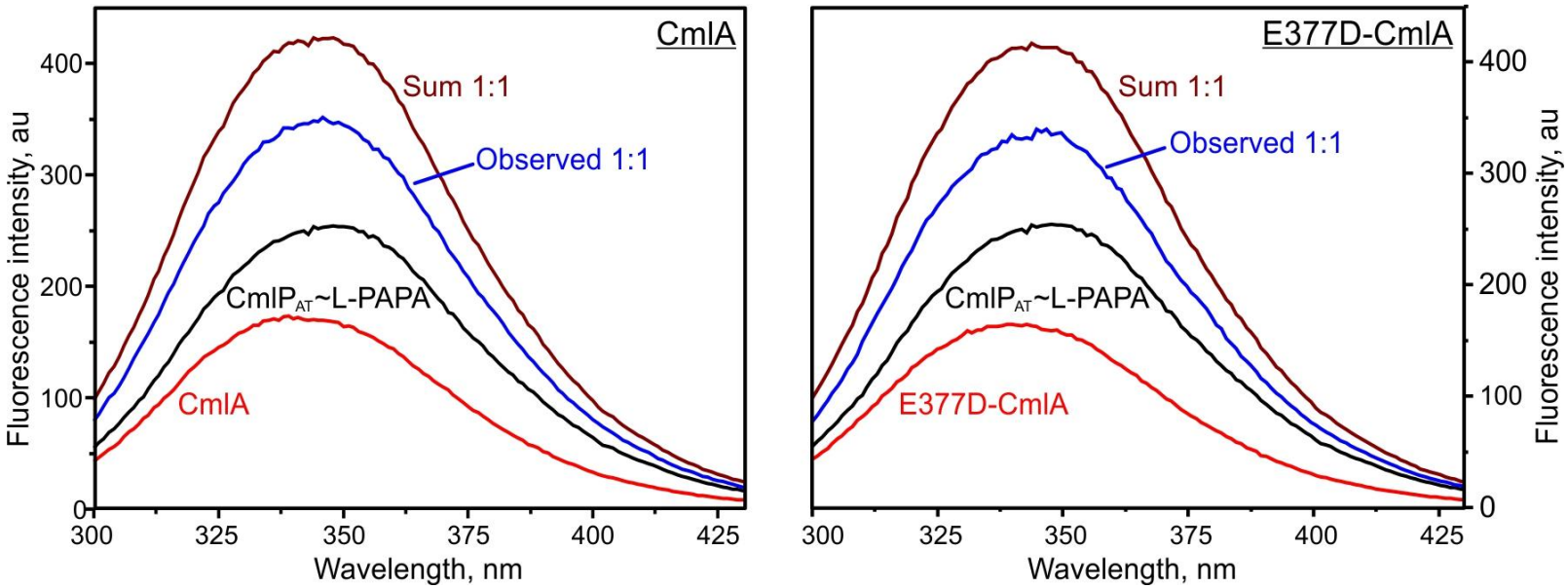

Figure 2.19. Fluorescence emission spectra of CmlA (left) and E377D-CmlA (right) in the presence or absence of CmlP$_{AT}$~L-PAPA. Fluorescence spectra from tryptophan emission (280 nm excitation) are shown for 9 µM (monomer) CmlA (left, red) or E377D-CmlA (right, red), 9 µM CmlP$_{AT}$~L-PAPA (black), the 1:1 mixture of the two proteins at 9 µM final each (blue), and the mathematical sum of the two individual fluorescence spectra (burgundy). The decrease in fluorescence from the mixture shows that a complex forms, and the similarity of the left and right panels indicates that the mutation does not cause a significant change in affinity. The fluorescence is linear with protein concentration in the range selected.

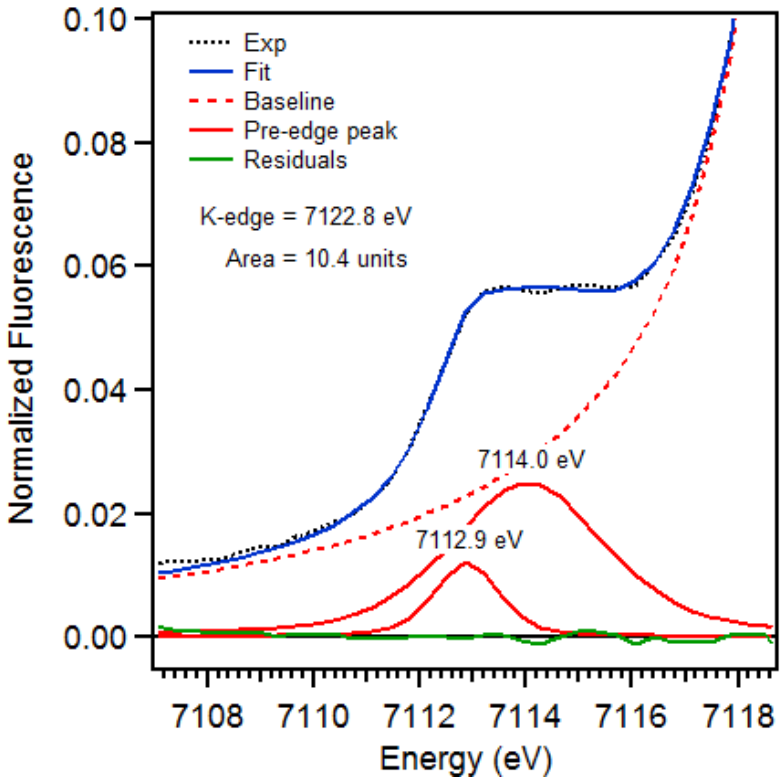

Figure 2.20. Pre-edge region analysis of **E377D^{R}**. The experimental data (black dotted), baseline (red dashed), pre-edge peak components (red solid), residuals (green solid) and total fit (blue solid) are shown.

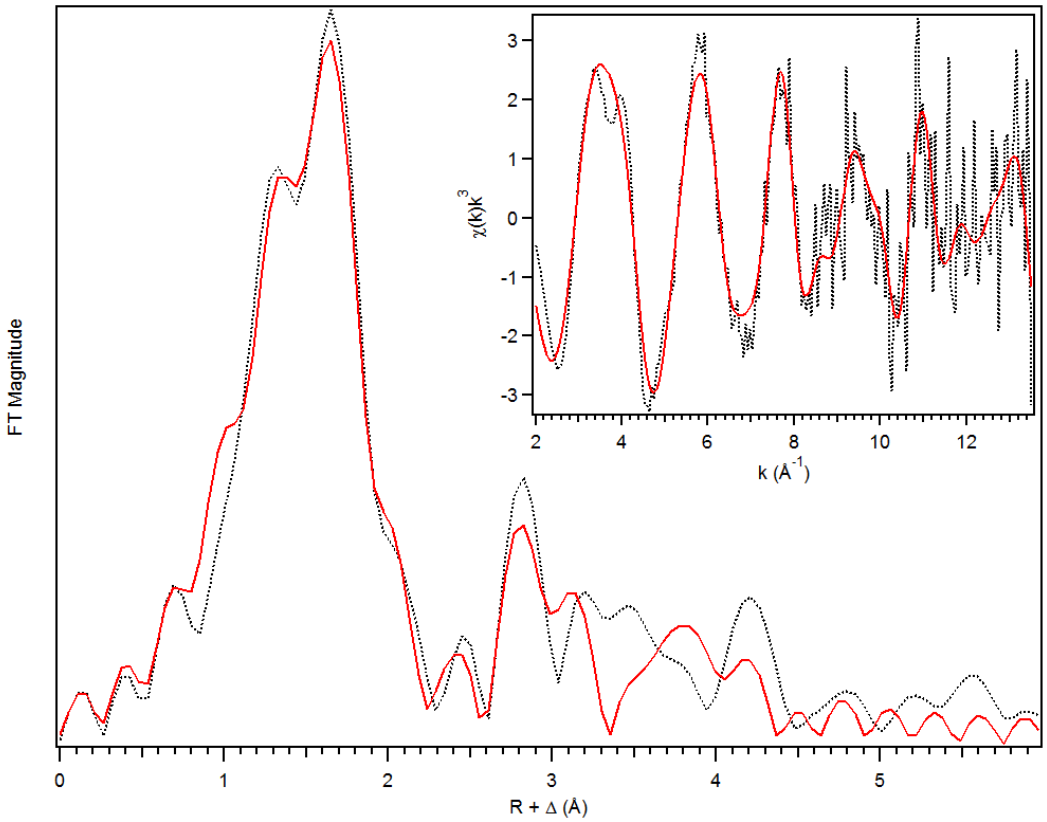

Figure 2.21. Fit (red solid line) of the unfiltered (black dotted) EXAFS data (inset) and corresponding Fourier transform of **E377D** (Table 2.8, Fit 18). Data was fit between k = 2 – 13.5 $Å^{-1}$.

Table 2.8. Fit parameters for the unfiltered EXAFS data of **E377D^{R}**, between k = 2 – 13.5 Å^{-1}. Fit 18 gives the most reasonable fit of the experimental data.

	Fe-N/O			Fe•••O/N			Fe•••Fe			Fe•••C				GOF	
Fit	**N**	**R(Å)**	**$\sigma^2(10^{-3})$**	**N**	**R(Å)**	**$\sigma^2(10^{-3})$**	**N**	**R(Å)**	**$\sigma^2(10^{-3})$**	**N**	**R(Å)**	**$\sigma^2(10^{-3})$**	**E_o**	**F**	**F'**
1	6	2.11	10.81										-8.67	199	586
2	5	2.11	8.92										-7.76	194	578
3	4	2.12	7.02										-6.84	198	584
4	3	2.12	5.03										-5.96	217	613
5	5	2.10	6.28	1	1.90	4.27							-12.4	176	551
6	4	2.11	5.02	1	1.94	4.88							-10.8	179	557
7	4	2.11	5.02	2	1.94	8.36							-13.1	174	548
8	5	2.10	6.34	1	1.90	4.34	1	3.28	8.34				-12.1	169	540
9	5	2.10	5.91	1	1.91	3.60	1	3.25	7.23	3	3.04	3.12	-12.1	142	495
10	5	2.10	5.99	1	1.91	3.88	1	3.26	6.36	4	3.05	5.26	-11.8	143	497
11	5	2.10	5.77	1	1.91	3.29	1	3.23	9.07	2	3.03	0.67	-12.1	141	494
12	5	2.10	5.92	1	1.90	3.69				3	3.02	4.33	-12.1	168	538

Table 2.8. (continued) Fit parameters for the unfiltered EXAFS data of **E377D^{R},** between k = 2 – 13.5 Å^{-1}. Fit 18 gives the most reasonable fit of the experimental data.

	Fe-N/O			Fe•••O/N			Fe•••Fe			Fe•••C				GOF	
Fit	**N**	**R(Å)**	**$\sigma^2(10^{-3})$**	**N**	**R(Å)**	**$\sigma^2(10^{-3})$**	**N**	**R(Å)**	**$\sigma^2(10^{-3})$**	**N**	**R(Å)**	**$\sigma^2(10^{-3})$**	**E_o**	**F**	**F'**
13	5	2.10	5.81	1	1.90	3.27	1	3.24	7.24	3	3.04	3.10	-12.7	128	470
										4	4.41	3.23			
14	5	2.10	5.88	1	1.90	3.48	1	3.24	7.46	3	3.04	2.65	-12.2	134	482
										4	4.24	6.31			
15	**5**	**2.10**	**5.98**	**1**	**1.91**	**3.73**	**1**	**3.24**	**7.22**	**3**	**3.04**	**2.86**	**-11.8**	**127**	**468**
										3	**4.33**	**3.73**			
16	5	2.10	6.02	1	1.91	4.10				3	3.02	4.34	-11.4	153	515
										3	4.34	2.60			
17	5	2.11	6.46	1	1.91	4.85	1	3.29	8.36	3	4.35	2.37	-11.1	154	516
18	**4**	**2.12**	**4.63**	**1**	**1.94**	**4.25**	**1**	**3.26**	**7.22**	**3**	**3.05**	**3.09**	**-10.0**	**128**	**470**
										3	**4.35**	**1.99**			

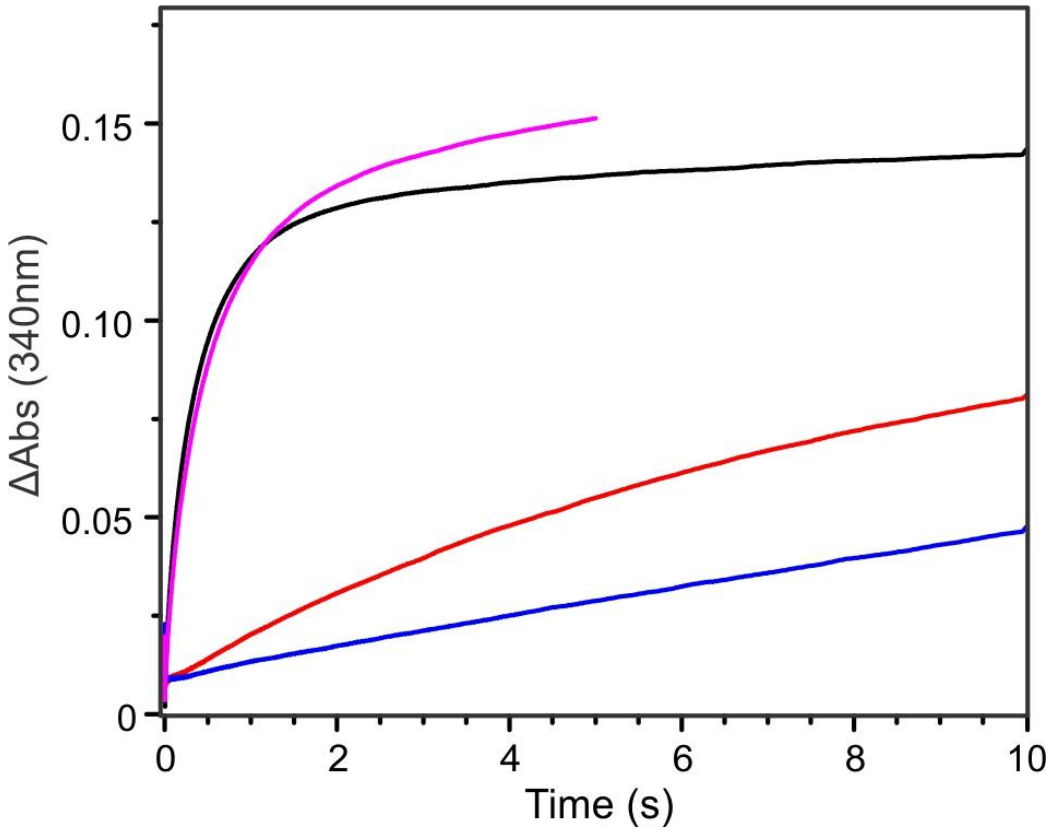

Figure 2.22. Stopped-flow transient kinetic timecourses for the reaction **WT^{R}** with CmlP$_{AT}$~L-Tyr and CmlP$_{AT}$~D-Tyr. Reaction of **WT^{R}** with CmlP$_{AT}$~L-Tyr and O_2 (black), with CmlP$_{AT}$~D-Tyr and O_2 (red). As a comparison, reactions of **WT^{R}** with CmlP$_{AT}$~L-PAPA and O_2 (magenta) and with unloaded CmlP$_{AT}$ (blue) are also shown. Reactions were performed in 50 mM HEPES pH 7.5 at 4.5 °C and contained 75 μM CmlA ± 100 μM CmlP$_{AT}$ and 0.95 mM O_2. Loading of L- and D-Tyr by the CmlP A domain was confirmed using protein LC ESI-MS. Reaction of **WT^{R}** with CmlP$_{AT}$~L-Tyr and O_2 yields hydroxylated protein product (63136 amu) whereas reaction with CmlP$_{AT}$~D-Tyr and O_2 did not yield any detectable hydroxylated product (63120 amu) based on LC ESI-MS analysis.

Chapter 3 : X-ray Absorption Spectroscopic Characterization of the Diferric-peroxo Intermediate of Human Deoxyhypusine Hydroxylase in the Presence of its Substrate eIF5a

The content of this chapter was reproduced with permission of Springer from:
Jasniewski, A. J.; Engstrom, L. M.; Vu, V. V.; Park, M. H.; Que, L., Jr. X-ray absorption spectroscopic characterization of the diferric-peroxo intermediate of human deoxyhypusine hydroxylase in the presence of its substrate eIF5a. *J. Biol. Inorg. Chem.* **2016**, *21*, 605 – 618.

3.1 – Introduction

Members of the ferritin-like protein superfamily are characterized by a four-helix bundle structural motif that generally bind pairs of redox-active metals in a 2-His-4-carboxylate coordination environment.[1, 2] Nonheme diiron members of this family activate O_2 and facilitate a wide variety of reactions, including the biomineralization of iron by ferritins,[3] the biosynthesis of DNA precursors from ribonucleotides by ribonucleotide reductase (RNR),[8] hydroxylation of C–H bonds by the hydroxylase components of bacterial multicomponent monooxygenases such as soluble methane monooxygenase (sMMO)[4, 5] and toluene/o-xylene monooxygenase (ToMO),[6] fatty acid desaturation by Δ^9 stearoyl-acyl carrier protein desaturase (Δ^9D),[11] arylamine *N*-oxygenation by AurF[14] and CmlI,[15] and formation of alkanes from fatty aldehydes by aldehyde deformylating oxygenase (ADO).[9, 10] Among the best studied members of this protein family is sMMO, which has been subjected to intensive crystallographic, spectroscopic and mechanistic investigations.

In 2006, a new nonheme diiron enzyme human deoxyhypusine hydroxylase (hDOHH) was characterized and found to be responsible for the post-translational modification of the eukaryotic translational initiation factor 5A (eIF5A).[175, 176] eIF5A plays an essential role in the regulation of cell proliferation by facilitating peptide synthesis at the ribosome.[177, 178] Inactivation of the enzymes responsible for the post-translational modification of eIF5A results in cell death,[179] making this pathway a potential therapeutic target for the treatment of diseases like malaria and certain cancers.[180] The substrate eIF5A utilizes a unique amino acid residue, hypusine (Hpu), to perform a critically important function[177] and is in fact the only known protein that harbors a Hpu residue.[181] The hypusine is derived from a lysine residue that is first converted to deoxyhypusine (Dhp) by deoxyhypusine synthase (Figure 3.1). This modified eIF5A(Dhp) is the substrate for hDOHH, which activates O_2 and hydroxylates the strong C^{ζ}-H bond to generate the final eIF5A(Hpu) product.[176] As preparations of this

enzyme from heterologous expression cells were reported to be blue in color,[175] we carried out spectroscopic investigations that identified the blue chromophore as the diferric peroxo intermediate of hDOHH (hDOHH-**P**).[65] Importantly, hDOHH-**P** exhibits spectroscopic properties similar to, yet distinct from, those of the peroxo intermediates associated with the canonical nonheme diiron enzymes.[32, 37, 61, 67, 68, 72, 86, 116, 182, 183]

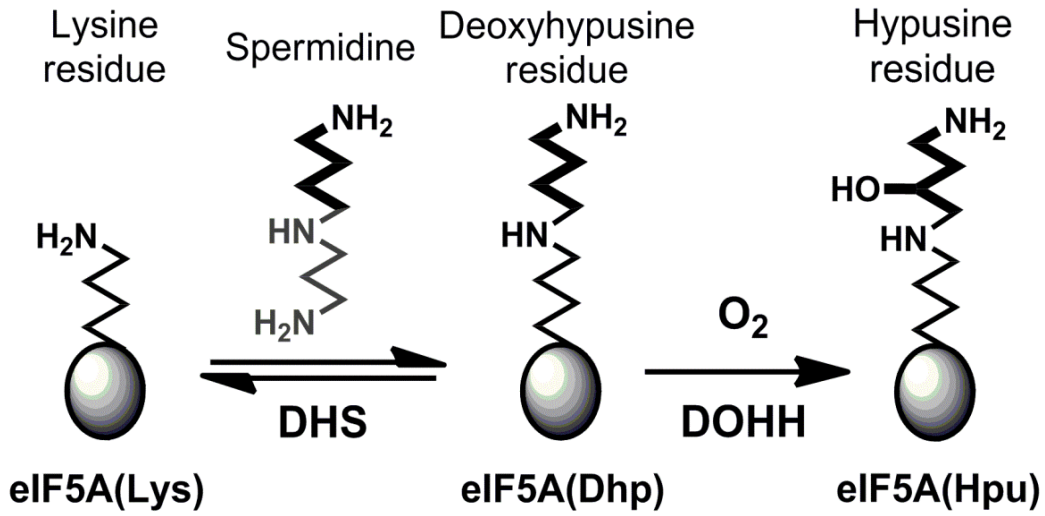

Figure 3.1. Biosynthetic pathway of hypusine on eIF5A. Reproduced with permission from ref [65].

O_2 activation by the majority of diiron enzymes is initiated by dioxygen binding to a diferrous center, generating a diferric peroxo species.[52] Subsequent O–O bond cleavage generates a high-valent diiron-oxo center (Fe(III)Fe(IV) or $Fe(IV)_2$) that effects substrate oxidation,[4, 184] but the detailed steps in the mechanisms by which the O–O unit is converted to the active oxidizing species remains unclear. Most of the enzymatic diferric peroxo species identified to date have fleeting half-lives on the order of seconds to a few minutes,[24, 59, 61, 70] making characterization of these intermediates quite challenging. Additionally, most of the peroxo species described to date can only be accumulated through mutagenesis of the wild type (WT) enzyme[68, 116] or the use of reaction conditions that do not produce product.[86] In contrast, the hDOHH-**P** intermediate

can persist for days but is nevertheless reactive. However, the binding of the eIF5A(Dhp) substrate to hDOHH-**P** significantly accelerates the decay of the peroxo intermediate and concomitantly generates eIF5A(Hpu) product.[65] Unlike members of the ferritin-like protein superfamily, hDOHH does not have a four-helix-bundle structural motif that provides the two histidine and four carboxylate residues that comprise the diiron active site. Instead, hDOHH utilizes HEAT repeat motifs to support a 4-His-2-carboxylate diiron active site, as established by site-directed mutagenesis studies[175] and the recent crystal structure of hDOHH.[17]

Our initial study of hDOHH-**P** by X-ray absorption spectroscopy (XAS) revealed an Fe•••Fe distance of 3.44 Å, but the quality of the data limited the information that could be extracted about the active site.[65] In this follow-up of our earlier effort, we have obtained better XAS data on hDOHH, focusing on five different samples along the reaction pathway, starting with the reduced diferrous state and ending with a diferric product. XAS analysis of these samples reveals that the diiron center of hDOHH maintains a relatively invariant Fe•••Fe distance throughout its redox cycle despite changes in oxidation state, in contrast to the larger variations in Fe•••Fe distance observed for sMMO and the R2 subunit of RNR,[32, 45, 46, 57, 163, 185] the canonical members of the family of nonheme diiron enzymes. This physical constraint imposed on the diiron center of hDOHH has implications on how the peroxo O–O bond can be cleaved and leads us to propose an O_2 activation mechanism for hDOHH that is distinct from that for sMMO and RNR R2.

3.2 – Results

We have used Fe-K-edge X-ray absorption spectroscopy (XAS) to gain insight into the diiron active site structures of a series of hDOHH samples: chemically reduced diferrous hDOHH (hDOHH-**R**), diferric peroxo hDOHH (hDOHH-**P**), hDOHH-**P** bound with substrate, eIF5A(Dhp) (hDOHH-**P•S**) and the diferric species following decay of hDOHH-**P**, both in the presence and absence of substrate (hDOHH-**D•S** and hDOHH-**D**,

respectively). hDOHH-**P** is the as-isolated form of the enzyme, hDOHH-**R** was generated by reacting hDOHH-**P** with dithionite until fully reduced, and hDOHH-**P•S** was prepared by adding eIF5A(Dhp) to a solution of the peroxo species. The peroxo to Fe(III) LMCT transition is maintained in both hDOHH-**P** and hDOHH-**P•S** (Figure 3.8). hDOHH-**D** was generated by allowing hDOHH-**P** to decay at room temperature in an XAS cup until the feature at A_{630} had reached a minimum value, resulting in a yellow colored species. Similarly, hDOHH-**D•S** was prepared by thawing the hDOHH-**P•S** sample and allowing the hydroxylation reaction to run for 72 hours at room temperature in an XAS cup. The previously reported XAS data for hDOHH-**P** was recorded with a k range of only 2-11.8 $Å^{-1}$ and the sample showed evidence of significant photoreduction.[65] Here we present new hDOHH-**P** data with an improved k range of 2-13.5 $Å^{-1}$ and a minimal degree of X-ray photoreduction.

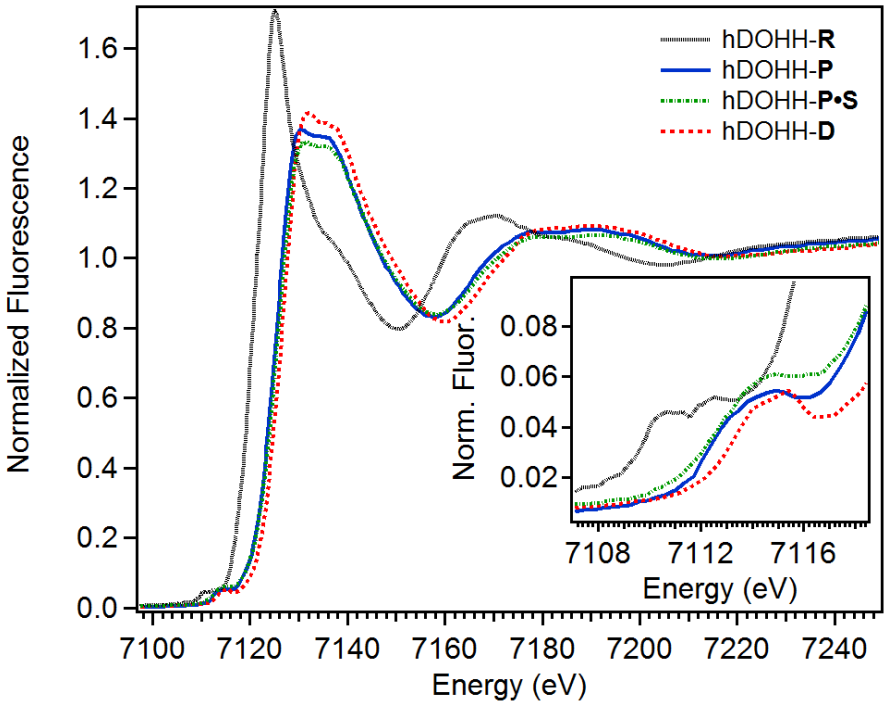

Figure 3.2. XANES region of hDOHH-**R** (black dotted), hDOHH-**P** (blue solid), hDOHH-**P•S** (green dot dash) and hDOHH-**D** (red dash). Inset: zoom in of the pre-edge region.

X-ray absorption near edge structure (XANES) analysis provides information regarding the oxidation state (via the K-edge energy) and symmetry of the diiron centers (via the pre-edge area) in an enzyme active site. The five hDOHH species exhibit Fe K-edge energies consistent with oxidation state assignments that we had previously made by Mössbauer spectroscopy or deduced by UV-vis spectroscopy. The Fe K-edge energy for hDOHH-**R** was found to be 7122.7 eV (Figure 3.2, Table 3.1), which is similar to the K-edge energies reported for the diferrous forms of an R2-like ligand-binding oxidase (7121.4 eV)[13] and frog M ferritin (7122.0 eV).[37] In addition, previous Mössbauer analysis of hDOHH-**R** characterized the metal sites as high spin (S = 2) ferrous iron.[65] The Fe K-edge energy of 7125.6 eV for hDOHH-**P** is consistent with our previous analysis,[65] and is approximately 3 eV higher than that of hDOHH-**R**. Mössbauer spectroscopy of hDOHH-**P** established that the metal centers are in the high spin (S = 5/2) ferric state and are antiferromagnetically coupled.[65] Assuming that the K-edge energy correlates to oxidation state, only a 1 eV jump would be anticipated in going from $Fe(II)_2$ in hDOHH-**R** to $Fe(III)_2$ in hDOHH-**P**. However, in transition metal complexes the ligand identity and hardness,[39] effective nuclear charge,[40] metal-ligand bond length[41] and spin state of the metal[42] all affect the K-edge energy. Given this and the lack of a systematic study of K-edge energies in diiron enzyme systems, the source of this 3-eV difference is not clear. hDOHH-**P•S**, hDOHH-**D**, and hDOHH-**D•S** all have K-edge energies similar to hDOHH-**P** (Table 3.1), consistent with a diferric center in the peroxo and the decayed species in the presence and the absence of substrate.

The pre-edge peak in the XANES region corresponds to forbidden 1s → 3d transitions in transition metal complexes.[147] The intensity of this transition is dependent on the degree of metal 4p mixing into 3d states, and increases as the metal center is distorted from centrosymmetry.[186] By comparing the area under the pre-edge peak, information about the symmetry and general coordination environment of the diiron site can be inferred. The pre-edge feature for hDOHH-**R** is fit by two pseudo-Voigt functions and is centered at 7111.7 eV with an area of 8.6 units (Table 3.1). This area falls between

values typical of 6-coordinate (~5 units) and 5-coordinate diferrous species (~11 units).[43] The pre-edge feature of hDOHH-**P** is centered at 7113.8 eV with an area of 12.4 units. This value is consistent with our previously published data[65] and higher than observed for hDOHH-**R**. hDOHH-**P** is likely 6-coordinate by comparison to synthetic 6-coordinate diferric peroxo complexes, which have pre-edge values that range from 13 – 16 units.[105, 110, 112] In contrast, hDOHH-**P•S** has a pre-edge feature centered higher in energy at 7114.1 eV with an area of 16.2 units, increased from hDOHH-**P**, indicating that the addition of substrate has decreased the symmetry around the diiron center. hDOHH-**D** and hDOHH-**D•S** have a feature centered around 7114.7 eV with areas of 7.8 and 8.6 units, respectively. These values are lower than observed for hDOHH-**P** and are consistent with those of synthetic 6-coordinate (μ-hydroxo)diferric centers, with reported areas of 5 – 9 units.[44]

Table 3.1. XANES analysis of hDOHH species.

Species	K-edge energy (eV)	Peak Position (eV)	Peak Area (units)
hDOHH-**R**	7122.7	7111.7	8.6
hDOHH-**P**	7125.6	7113.8	12.4
hDOHH-**P•S**	7124.9	7114.1	16.2
hDOHH-**D**	7125.2	7114.7	7.8
hDOHH-**D•S**	7125.6	7114.7	8.6

Table 3.2. EXAFS fit distances of hDOHH species.

Species[a]	**N**	hDOHH-**R**		**N**	hDOHH-**P**		**N**	hDOHH-**P•S**		**N**	hDOHH-**D/D•S**	
Fe•••Fe (Å)	1	3.47	(5.18)	1	3.41	(1.86)	1	3.41	(5.44)	1	3.42	(5.09)/(3.51)
Fe-N/O (Å)	4	2.18	(2.78)	3	2.15	(1.95)	4	2.11	(5.61)	4	2.09/2.08	(4.45)/(4.40)
Fe-O/N (Å)	2	2.07	(3.39)	3	1.98	(4.57)	1	1.98	(4.47)	2	1.95	(2.88)
Fe•••C (Å)	3	3.10	(6.20)	-	-		3	3.09	(6.50)	3	3.08	(4.90)/(6.29)
	3	3.68	(4.05)	3	3.58	(2.93)	3	3.56	(3.51)	3	- /3.59	- /(3.30)
	3	4.35	(2.51)	4	4.29	(1.55)	4	4.30	(1.72)			

[a]Numbers in parenthesis are σ^2 values in units of 10^{-3} Å^2. See SI for individual fitting tables.

Additional structural information can be determined from extended X-ray absorption fine structure (EXAFS) analysis, which provides scattering distances for the ligands and close contacts near the Fe centers. The final fits for each species are presented in Table 3.2, and fit tables for individual complexes can be found in Supplementary Information (Section 3.6, Table 3.5 – Table 3.10).

The primary coordination sphere of hDOHH-**P** consists of 3 Fe-N/O scatterers at 2.15 Å with a relatively low Debye-Waller factor (σ^2) of 1.95×10^{-3} Å^2 (Table 3.2) and 3 Fe-O/N at 1.98 Å with higher σ^2 values (4.45×10^{-3} Å^2). The higher σ^2 value for the latter Fe-O/N shell suggests a broader range of distances for the scatterers comprising the 1.98-Å shell. Second and third sphere Fe•••C are fit at 3.58 Å and 4.29 Å, respectively, with reasonable σ^2 values. The Fe•••Fe distance fit for hDOHH-**P** is 3.41 Å, which agrees quite well with the previously reported value of 3.44 Å.[65]

The primary coordination sphere of hDOHH-**R** consists of two shells, both with reasonable σ^2 values (Table 3.2). The first shell contains 4 Fe-N/O scatterers at 2.18 Å, and the second shell contains 2 Fe-O/N scatterers at 2.07 Å. However these two shells are within 0.11 Å of each other, which are just slightly outside of the resolution of the data. The resolution to distinguish one shell from another in a given fit for hDOHH-**R** is determined by the equation:

$$\Delta R = \frac{\pi}{2\Delta k}$$

where ΔR is the resolution and Δk is the difference in the k-space range used. For hDOHH-**R**, ΔR = 0.12 Å. Although these shells are outside the ability to resolve the two shells (0.11 Å), there is an improvement in fit when the 2.07 Å shell is included (Table 3.5, Fit 12 vs Fit 18). Consequently, this shell was included in the best fit for hDOHH-**R**. The Fe•••Fe distance for this species was fit at 3.47 Å, which is only slightly longer than the Fe•••Fe distance of 3.41 Å observed in hDOHH-**P**. Three additional carbon shells were found at 3.10 Å, 3.68 Å and 4.35 Å.

Fitting of hDOHH-**D** resulted in two acceptable fits of the data (Fits A and B, Table 3.8 and Table 3.9). Both fits A and B have similar primary shells and reasonable σ^2

values with 4 Fe-N/O at 2.07 Å and 2.09 Å, respectively. An additional Fe-O/N shell with two scattering atoms is needed for hDOHH-**D**, at similar distances of 1.93 Å for fit A and 1.95 Å for fit B. Significant differences between fits A and B are evident in the Fe•••Fe distances as well as the carbon scattering shells. Fit A has a shorter Fe•••Fe distance at 3.07 Å with a σ^2 of 9.87×10^{-3} Å^2 and 5 Fe•••C at 3.41 Å, while fit B has a longer Fe•••Fe distance at 3.42 Å with a σ^2 of 5.09×10^{-3} Å^2 and 3 Fe•••C at 3.08 Å. Fit A resembles a bis-hydroxo "diamond-core"-like species, if the two Fe-O bonds at 1.93 Å were assigned to μ-hydroxo ligands with a metal-metal separation of 3.07 Å (synthetic models have Fe•••Fe distances between 2.8 Å and 3.1 Å[187-193]). However, the σ^2 for the Fe scatterer at this short distance is unreasonably high. Moreover, a carbon scatterer at 3.41 Å seems unlikely as this has not, to our knowledge, been observed in previously reported species and would require significant movement of the histidine rings (*vide infra*). Fit B differs from fit A by switching the assignments for the scatterers at ~3.1 Å and ~3.4 Å. This model structure would accommodate the longer Fe•••Fe distance of 3.42 Å and has a more reasonable σ^2 value than fit A. Additionally, the carbon scatterer at 3.08 Å is more clearly assigned to the ligands bound to the iron centers (see Discussion). For these reasons, fit B is favored over fit A for hDOHH-**D**, with fit B being more consistent with a single-atom-bridged "open core" species (Table 3.2), with the single atom bridge falling into the shell at 1.95 Å. Our preference of fit B for hDOHH-**D** is supported by the best fit to hDOHH-**D•S**, which consists of four Fe-N/O scatterers at 2.08 Å, two Fe-O/N at 1.95 Å, one Fe•••Fe at 3.42 Å, and three Fe•••C at both 3.08 Å and 3.59 Å (Table 3.2). This congruence in the fits of hDOHH-**D** and hDOHH-**D•S** strengthens our argument for a 3.42 Å Fe•••Fe distance in the decayed species.

The best fit for hDOHH-**P•S** consists of 1 Fe-O/N at 1.98 Å and 4 Fe-N/O at 2.11 Å (Table 3.2). The changes in distance and the number of scatterers for each shell in the first coordination sphere, together with the previously noted increase in pre-edge area, suggest that substrate binding causes a distortion of the diiron active site prior to O–O bond cleavage. The Fe•••Fe distance however remains unchanged at 3.41 Å. Additional

Fe•••C shells at 3.09 Å, 3.56 Å and 4.30 Å are required to achieve a reasonable fit, similar to hDOHH-**R**.

3.3 – Discussion

The importance of peroxo intermediates in the dioxygen activation chemistry of diiron enzymes is underscored by their prominent role in the catalytic cycles proposed for these enzymes. However, detailed study of the chemistry of O–O activation is challenging due to the general instability of these peroxo species and the protein modifications required to observe them.[24, 61, 68, 70, 86, 116] Here, we report a detailed XAS analysis of the diferric-peroxo intermediate from the human hydroxylase, hDOHH. This enzyme is unique within its class as it is purified as a long-lived diferric-peroxo species, thereby facilitating its characterization. Despite it stability, hDOHH-**P** has been shown to carry out substrate hydroxylation,[65] making it the first catalytically competent peroxo intermediate to be characterized from a native enzyme. Our XAS analysis has provided structural information on five species in the reaction cycle.

EXAFS analysis of the five hDOHH samples we have studied show two prominent features in the Fourier-transformed data (see Figure 3.10,Figure 3.12, Figure 3.14, Figure 3.17, Figure 3.19). The taller feature between R+Δ 1.5 - 1.7 Å is assigned to scatterers in the primary coordination sphere of the iron atoms of the diiron active site. The second, less intense feature at R+Δ ~ 3.0 Å is comprised of contributions arising mainly from the other iron atom. Included in the first shell scatterers are the ligating atoms of one glutamate and two histidine residues on each metal center. This ligation scheme was initially deduced from sequence comparisons and site-directed mutagenesis[175] and recently identified from the crystal structure of the enzyme.[17] Crystallographically, imidazole ligands typically give rise to Fe–N bond distances between 2.0-2.5 Å that average to 2.2 Å irrespective of whether the iron is in the +2 or +3 oxidation state.[14, 18, 31, 34, 53, 149-152] This is consistent with the distances observed in all five hDOHH species studied here, with distances ranging from 2.08 – 2.18 Å. Typical Fe–O

bond distances found for carboxylate ligands span a similar range of values (1.9 – 2.6 Å)[14, 18, 31, 34, 53, 149-152] but can vary depending on the binding mode of the carboxylate, i.e. terminal vs bridging or monodentate vs bidentate. In addition to the protein-derived ligands, the diiron center is likely to have solvent-derived ligands with distances that vary among the five hDOHH species, suggesting some variation in the identities and binding modes of these solvent derived ligands but not in the protein derived ligands. Finally, hDOHH-**P** and hDOHH-**P•S** contain one additional ligand unique to these species – a bound O_2 molecule. Our data suggests that dioxygen is likely bound to the diiron(III) center as a 1,2-peroxo bridge.[65] Based on the available structures for synthetic peroxo-bridged diiron(III) complexes,[91, 94, 105, 109, 110] such a ligand would be expected to have Fe–O bond distances of 1.87 – 1.98 Å, consistent with our observed distance of 1.98 Å.

Interestingly, the Fe•••Fe distances found for the five hDOHH complexes vary within a narrow range of 3.41 – 3.47 Å, suggesting that the diiron core dimensions do not change significantly as it undergoes redox transformations. Similar Fe•••Fe distances have been observed in other diiron proteins such as deoxyhemerythrin and reduced sMMO, where the diiron unit has a single-atom bridge and additional bidentate carboxylate bridges.[14, 18, 32, 37, 45, 149, 151] However the hDOHH crystal structure[17] suggests that the two carboxylate ligands of hDOHH are not well positioned to bridge the diiron center but instead bind as terminal ligands. Both the core architecture and the invariant Fe•••Fe distance are features that differ significantly from the approximately 1-Å change in Fe•••Fe distance observed as the diiron active sites of sMMO and *E. coli* RNR convert from the diferrous forms to their respective high-valent intermediates.[45, 57, 194] Presumably, these differences reflect changes in the redox chemistry associated with the diiron centers of each enzyme.

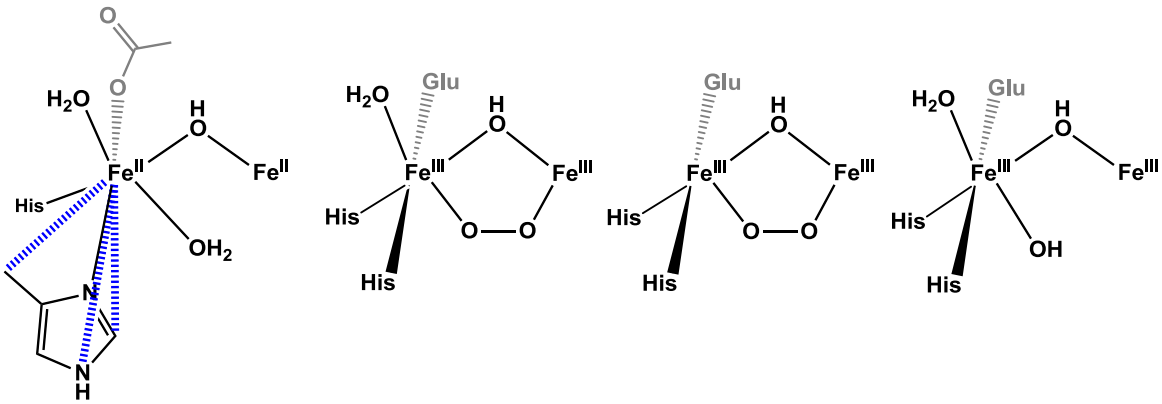

Figure 3.3. Models derived from the EXAFS fits from the samples shown above

Analysis of fits of the EXAFS data for the five samples leads to the proposed diiron site structures shown in Figure 3.3. Based on the iron-ligand bond length comparisons presented above, the six scatterers observed for the first coordination sphere of each Fe atom in the EXAFS fit of hDOHH-**R** can be reasonably assigned in the following manner. The carboxylate and two histidine ligands on each Fe would give rise to one of the two 2.07-Å scatterers and two of the four 2.18-Å scatterers. The three remaining scatterers on each Fe most likely derive from solvent derived exogenous ligands. The second scatterer at 2.07 Å would correspond to a hydroxo bridge between the two ferrous ions, as this distance matches the average Fe^{II}-(μ-OH) distance (2.072 Å) found for a number of (μ-hydroxo)diferrous complexes, which have Fe^{II}–OH distances ranging from 1.99 to 2.21 Å (Table 3.12).[92, 159, 160] On the other hand, corresponding complexes with bridging aqua ligands typically have longer Fe^{II}-μ-OH_2 distances and exhibit a wider range of values (2.13 – 2.40 Å, Table 3.12).[153, 159, 195] A particularly useful diiron(II) complex for comparison is $[Fe_2(\mu\text{-OH})(\mu\text{-OH}_2)(TPA)_2]^{3+}$ (TPA = tris(2-pyridylmethyl)amine),[159] which was found to have respective. Fe^{II}-μ-OH and Fe^{II}-μ-OH_2 bonds averaging 2.07 and 2.17 Å, values that support our proposed assignment of the 2.07-Å scatterer in hDOHH-**R** as a hydroxo bridge. The remaining two scatterers at 2.18 Å have Fe–O distances consistent with either terminal (2.04 – 2.16 Å, Table 3.12)[105, 153-158] or bridging water ligands (2.13 – 2.40 Å),[153, 195] but the Fe•••Fe distance of 3.22 Å

observed for $[Fe_2(\mu\text{-}OH)(\mu\text{-}OH_2)(TPA)_2]^{3+}$ is too short to match the distance deduced for hDOHH-**R**.

hDOHH-**D** and hDOHH-**D•S** are diferric species that form upon decay of hDOHH-**P** respectively in the absence and the presence of the eIF5A substrate, which is indicated by the loss of the visible chromophore associated with the peroxo intermediate. As reported previously, eIF5a binding to hDOHH-**P** significantly destabilizes this intermediate and results in its immediate decay. These two decayed samples give rise to very similar EXAFS spectra and fits. Like hDOHH-**R**, the first coordination spheres of hDOHH-**D** and hDOHH-**D•S** are best fit with two shells of N/O scatterers, 2 at 1.95 Å and 4 at 2.11 Å. The decrease in the Fe-ligand distance for each shell relative to those of hDOHH-**R** is rationalized by the change in iron oxidation state from +2 to +3. We propose that the 2.11Å shell consists of the three protein-derived ligands as well as a terminal solvent ligand, while the 1.95-Å shell can be reasonably assigned to hydroxo ligands. One of the latter scatterers very likely corresponds to the μ-OH bridge found in hDOHH-**R**, as analogous bridges in synthetic diferric complexes have Fe^{III}-(μ-OH) distances between 1.94 Å and 2.02 Å.[103, 188, 193, 196-198] The other scatterer could in principle be assigned to a second hydroxo bridge, but such an $Fe(III)_2(\mu\text{-}OH)_2$ core should give rise to an Fe•••Fe distance much shorter than the 3.41-Å separation found for hDOHH-**D** and hDOHH-**D•S**. Alternatively, the other 1.95-Å scatterer could arise from a terminal hydroxo ligand on each Fe, as synthetic high-spin Fe(III)–OH units have bond distances that fall within the range of 1.82 – 1.93 Å.[199-207] This formulation would also maintain the +1 charge associated with the diiron sites in hDOHH-**R** and h-DOHH-**P** (see below).

The best fit for hDOHH-**P** shows N/O scatterers at 2.15 Å and 3 O/N scatterers at 1.98 Å. The 2.15-Å shell likely consists of two histidine ligands and a terminal water ligand based on bond metrics discussed earlier. The 1.98-Å shell would comprise a terminal carboxylate ligand, the hydroxo bridge (1.94 – 2.02 Å),[103, 188, 193, 197, 198, 208] and the proximal oxygen of a μ-1,2-peroxo ligand (1.86 – 1.94 Å).[91, 94, 109, 112] These results compare well to the parameters found by Suzuki and co-workers in the crystal structure

of $[Fe^{III}_2(\mu\text{-}OH)(\mu\text{-}1,2\text{-}O_2)(L)_2]^+$ (L = bis(6-methylpyridyl-2-methyl)-3-aminopropionate), which has an Fe•••Fe distance of 3.396 Å and average Fe–O and Fe–N distances of 1.95 Å and 2.21 Å, respectively.[103]

The complex of hDOHH-**P** with its substrate eIF5A(Dhp), which we refer to as hDOHH-**P•S**, was also prepared and analyzed by EXAFS. Figure 3.4 shows an overlay of the Fourier transformed (FT) data for hDOHH-**P** and hDOHH-**P•S**, revealing obvious differences between these two species. The feature at R+Δ ~1.5 Å representing the first coordination sphere is shifted to a slightly longer distance in hDOHH-**P•S** compared to hDOHH-**P**. Also, there is a notable feature at ~1.8 Å in hDOHH-**P** that is absent in hDOHH-**P•S**. Lastly, the feature at R+Δ ~ 3 Å, assigned to contributions mainly from the second iron atom, becomes less intense and shifted to a slightly lower R value relative to that in hDOHH-**P**. As hDOHH-**P** and hDOHH **P•S** have identical Fe•••Fe distances based on their respective EXAFS fits, the differences in the feature at R+Δ ~ 3 Å may arise from changes in the multiple scattering features that contribute to this peak. This shows that the hDOHH-**P** active site changes upon substrate binding to hDOHH-**P**, demonstrating that eIF5A binds to the hDOHH enzyme.

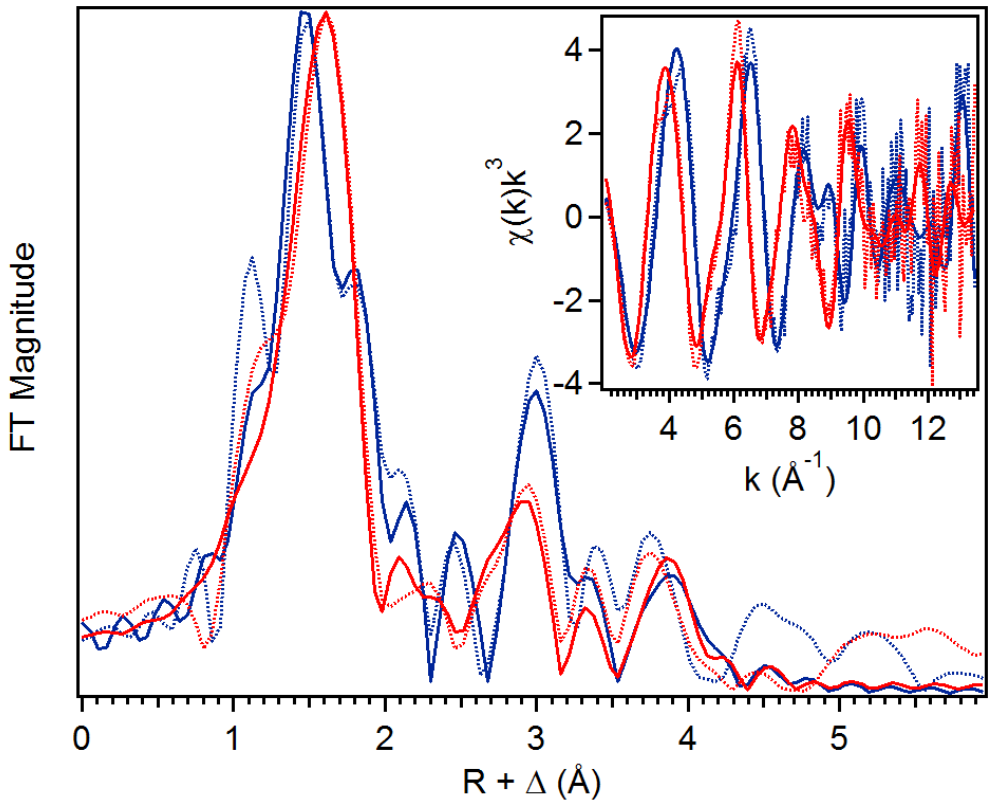

Figure 3.4. Fit (solid line) of the unfiltered (dotted) EXAFS data (inset) and corresponding Fourier transform. k = 2 – 13.5 $Å^{-1}$; hDOHH-**P** (blue, Figure 3.12) hDOHH-**P•S** (red, Figure 3.14).

Intriguingly, the Fe•••Fe distance of hDOHH-**P** is not significantly perturbed by the addition of substrate. However, the changes in the first coordination sphere noted above upon substrate binding result in a larger pre-edge area for hDOHH-**P•S** (16.2 units vs 12.4 for hDOHH-**P**), which is consistent with a larger distortion from octahedral symmetry engendered by a decrease in iron coordination number from 6 to 5. This change is accompanied by alterations in the composition of the first shell of scatterers in the best fit found for hDOHH-**P•S**. Although the average Fe–N/O bond distances for the two hDOHH complexes differ by just 0.01 Å, the shorter 1.98-Å shell now has only one scatterer, while the other shell now consists of four Fe–N/O scatterers at 2.11 Å. Attempts to increase the number of scattering atoms in either the 1.98 Å or 2.11 Å shells resulted in substantial increases in the σ^2 values for the shell of interest (Table 3.7, Fits 19 and 20). The shortening of a three-scatterer shell at 2.15 Å in hDOHH-**P** to a four-

scatterer shell at 2.11 Å corresponds to the shift of a 1.98-Å scatterer into the shell at longer distance. Clearly, there is some rearrangement in the iron coordination spheres upon substrate binding to hDOHH-**P**.

In the fit of hDOHH-**P**, the 1.98-Å subshell consists of three O scatterers, which we have assigned to the μ-OH bridge, the 1,2-bridging peroxo, and a terminal carboxylate ligand. In hDOHH-**P•S**, this shell consists of only one scatterer. As there is no change in the peroxo charge transfer band at 630 nm (Figure 3.8), it would seem likely that the peroxo ligand remains as the only scatterer at 1.98 Å. The carboxylate ligand and the hydroxo bridge would presumably shift into the 2.11-Å shell together with the two His residues concomitant with the loss of the terminal aqua ligand, but we have insufficient data to establish the fates of these ligands.

For all five of the hDOHH samples in this study, there are scatterers included in the fits at distances ranging from 3.1 – 4.3 Å that are likely derived from the imidazole rings of the histidine ligands, as observed for the diiron sites in sMMO and ToMO,[46, 60] methemerythrin and RNR R2,[209] and CmlA.[139] Histidine ligands typically give rise to scatterers at 3.1 and 4.3 Å, which are respectively associated with the C atoms adjacent to the coordinated N atom and the C and N atoms further away (Figure 3.5). Interestingly, no scatterer at ~3.1 Å is required in the fit for hDOHH-**P**. The absence of this carbon shell in hDOHH-**P** could be due to slightly different orientations of the imidazole ring relative to the Fe-N_{His} bond for the four histidines bound to the diiron center, which lead to destructive interference that decreases the contributions of these scatterers to the EXAFS spectrum of hDOHH-**P**. This is visually apparent in the relative intensities of the second-sphere peaks at ~ 3 Å in the Fourier transforms of hDOHH-**P** and hDOHH-**P•S** (Figure 3.4). Similarly, the fits for hDOHH-**D** and hDOHH-**D•S** do not require scatterers at ~4.3 Å. A similar phenomenon was reported for reduced MMOH with the appearance of a new light atom scatterer between 3.2 Å and 4.0 Å upon binding of the accessory protein MMOB,[46] which was rationalized by the contributing amino acid residues becoming more ordered in the MMOH:MMOB complex. We propose that a different ordering of the active site affects the outer-sphere contributions of ligands in hDOHH,

particularly the imidazole rings of histidine, which results in the disappearance of light atom scatterers from the EXAFS fit.

Interestingly, there is an additional scattering interaction at ~3.6 Å observed in most of the species studied here. This feature does not arise from an iron scatterer, as our attempts to introduce an iron atom at 3.6 Å always refined to a distance of 3.4 Å. Moreover, the inclusion of a light scattering atom at this distance improves the fit (See Table 3.5 – Table 3.10). A scatterer at a similar distance has been found in EXAFS studies of sMMO and assigned to multiple scattering pathways involving the β carbon of an N_δ-bound His.[163] Fe•••C distances were collected from available diiron protein crystal structures with N_δ-bound histidine ligands[14, 18, 31, 53, 149-151] or N_ε-bound histidine ligands[14, 18, 34, 152] (Figure 3.5). His ligands bound to Fe through N_δ have Fe•••C_β distances ranging from 3.5 Å to 3.9 Å and Fe•••C_γ distances ranging from 3.1 – 3.6 Å, while those bound to Fe through the Nε position have Fe•••C_ε distances of 3.1-3.5 Å. The 3.58 Å scatterer fits within all of these observed ranges. However, the Fe-N bond lengths that relate to the respective Fe•••C distances can suggest which options best agree with the 3.58 Å scatterer. With a N_ε-bound His ligand and an Fe•••Cε interaction at ~3.6 Å, the Fe-N distance is around 2.3 Å. The same is true for an N_δ-bound His with an Fe•••Cγ distance of ~3.6 Å. These Fe–N distances are longer than our experimentally determined Fe–N range of 2.1-2.2 Å, and so do not support assignment of the 3.58 Å scatterer. A N_δ-bound His with an Fe•••C_β interaction has an Fe–N distance of ~2.2 Å, which agrees with both the multiple scattering and Fe-N observations. We thus propose that the available crystallographic data supports the assignment of the ~3.6 Å scatterer as arising from the C_β-atom of an N_δ-bound His ligand in the XAS samples analyzed herein.

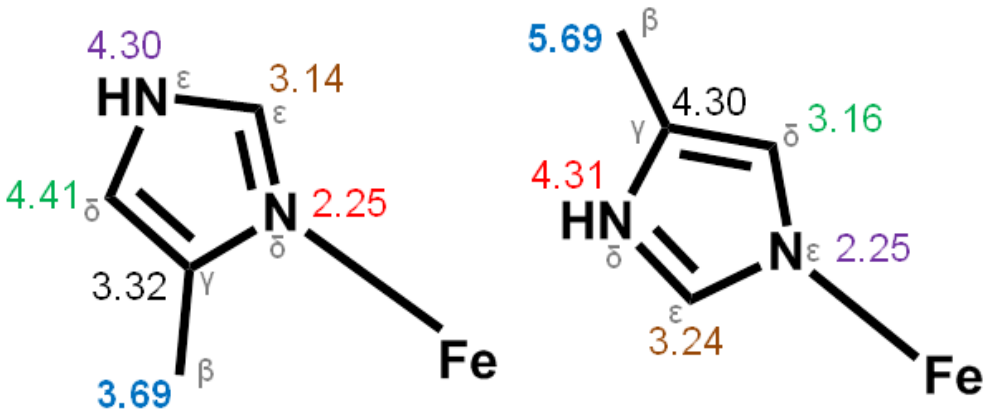

Figure 3.5. Comparison of average Fe•••C/N distances of His ligands bound to Fe at N_δ (left) and Nε (right). Color corresponds to the same atom position in the imidazole ring of His.

A 1.7-Å resolution crystal structure of a truncated form of hDOHH-**P** (hDOHH-$\mathbf{P_T}$) was recently reported by Han *et al.*[17] (PDB ID 4D50), providing the first crystallographic information about this interesting enzyme (Figure 3.6). This structure confirmed the HEAT repeat protein motif predicted by Park and coworkers[175] that distinguishes this enzyme from most diiron enzymes, which are typically found to use a 4-helix bundle structural motif.[1, 2, 9] Additionally, the histidine-rich coordination environment for the diiron center predicted by site-directed mutagenesis experiments[175] was supported by this structure. Lastly, the active site was deduced to have a (μ-solvento)(μ-1,2-peroxo)diiron core structure as suggested by our earlier spectroscopic analysis.[65] However, the metrical information provided by the crystal structure about the diiron site differs considerably from what we have extracted from our XAS analysis. On average, the Fe-ligand distances appear to be 0.1-0.2 Å longer in the crystallographically derived data compared to our EXAFS measurements (Table 3.3), but the latter are likely to be of greater precision (± 0.02 Å).[21]

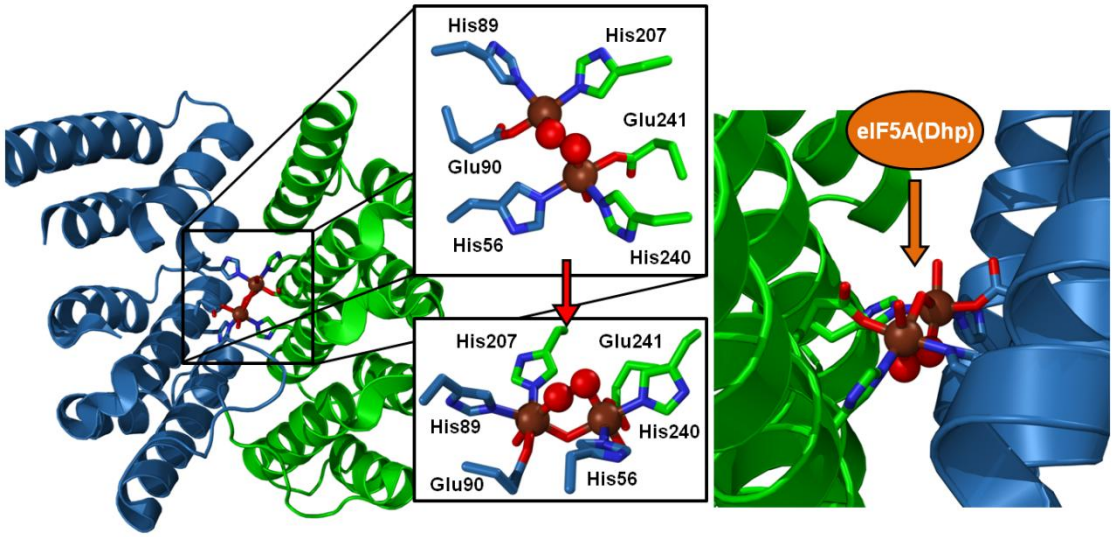

Figure 3.6. Diiron site of hDOHH-**P** generated by PyMOL using PDB ID 4D50. Fe atoms are shown as brown spheres, while peroxo O-atoms are shown as red spheres. Residues from the N-terminal domain are in blue, while residues from the C-terminal domain are in green. Amino acid residues coordinating the diiron site are shown in stick representation. The left panel shows the diiron site within the HEAT repeat motif, while the right panel shows a zoomed-in view showing the peroxodiiron unit within a hydrophobic cleft, with access for the substrate presumably via the less restricted approach.

Table 3.3. Comparison of hDOHH-**P** and hDOHH-$\mathbf{P_T}$.

Ligand type	hDOHH-**P** (Å)	hDOHH-$\mathbf{P_T}$ (Å)
Fe•••Fe	3.41	3.7
Fe-N(His)	2.15	2.3
Fe-O(Glu)	1.98	2.1
Fe-OH_2	2.15	2.2
Fe-μ-OH	1.98	2.2
Fe-O(peroxo)	1.98	2.2

Even more significantly, the diiron core dimensions from the XRD and EXAFS analyses are distinct. The Fe•••Fe distance found in the crystal structure of hDOHH-**P** is 0.3 Å longer than the value found by EXAFS (Table 3.3). The authors of the protein structure paper suggest that the EXAFS-deduced μ-hydroxo bridge may have become protonated during the 48-hour period needed for crystallization, resulting in longer Fe–O_{bridge} bonds and, consequently, a larger Fe•••Fe distance. Alternatively, we suggest that the observed elongation of the Fe•••Fe distance may result from photoreduction of the

diiron(III) center during the XRD experiment, which is a well-recognized problem in metalloenzyme crystallography.[76-78] Photoreduction would also rationalize the elongation of the Fe-ligand bonds observed in the XRD study. Indeed, we have previously noted that hDOHH-**P** is sensitive to photoreduction even under the comparatively mild XAS conditions, as evidenced by an observed downshift in the K-edge energy with increasing exposure to the synchrotron beam.[65] In the XAS experiments reported in this paper, we minimized the effect of photoreduction on our analysis by moving the X-ray beam during the XAS experiments to a fresh spot on the sample surface after each scan.

There are also spectroscopic differences between hDOHH-$\mathbf{P_T}$ used in crystallography experiments and the hDOHH samples prepared for the XAS studies. Han *et al.* note that the visible absorption maximum of hDOHH-$\mathbf{P_T}$ is blue-shifted from ~630 nm to 600 nm, suggesting some perturbation of the peroxo-to-iron(III) charge transfer chromophore. Moreover, while the Mössbauer spectrum collected for the hDOHH-$\mathbf{P_T}$ solution sample showed quadrupole doublets with parameters ($\delta_{1/2}$ = 0.57/0.55 mm s^{-1}, $\Delta E_{Q1/2}$ = 0.85/1.17 mm s^{-1}) similar to those previously reported for hDOHH-**P** ($\delta_{1/2}$ = 0.58/0.55 mm s^{-1}, $\Delta E_{Q1/2}$ = 0.88/1.16 mm s^{-1}),[65] the crystalline material exhibited somewhat different parameters ($\delta_{1/2}$ = 0.62/0.62 mm s^{-1}, $\Delta E_{Q1/2}$ = 0.72/1.25 mm s^{-1}), hinting at a possible structural change.

There may be additional differences in how the His residues are bound to the diiron center. In the crystal structure, they are shown to bind through the N_ε atom, whereas XAS analysis suggests binding via N_δ, due to the presence of a ~3.6 Å carbon scattering shell that is assigned to the His β carbon (*vide supra*). The His ligands are typically N_δ-bound in a number of other crystallographically characterized diiron enzymes,[14, 31, 53, 149-151] with the notable exceptions of hemerythrin[34] and mammalian desaturase[210] where all iron-bound His residues are N_ε-bound. At the present time, we cannot rationalize this difference between the XRD and XAS results.

Table 3.4. Fe•••Fe distances in angstroms of related diiron cores in enzymes[a].

Species	$Fe^{II}Fe^{II}$	$Fe^{III}Fe^{III}$	Peroxo	$Fe^{III/IV}Fe^{IV}$
sMMO	*3.4* [47] 3.43,[45] 3.29 [46]	*3.0* [150] 3.02,[185] 3.03 [163]	-	2.46 [45]
Ec RNR R2	*3.9* [31] 3.41 [32]	*3.3* [211] 3.22 [57]	2.50 [32]	2.79 [57]
St RNR R2	*3.7* [151]	*3.3* [151]	-	-
frog M ferritin	3.43 [37]	2.99 [37]	2.53 [37]	-
Fatty acid desaturases	*4.1* [53]	*3.2* [212] 3.13 [162]	-	-
hDOHH	3.47 [b]	3.42 [b]	3.41 [b]	-

[a] Distances shown in italics derived from X-ray crystallography; all other distances obtained from XAS studies. [b] This work.

An important generalization for the hDOHH series is that the Fe•••Fe distance determined from the XAS studies remains relatively invariant as hDOHH-**R** (3.47 Å) progresses through hDOHH-**P** and hDOHH-**P•S** (3.41 Å) and eventually to hDOHH-**D** (3.42 Å) following decay of the peroxo intermediate. In contrast, larger changes in the Fe•••Fe distances are observed for several diiron enzymes upon oxidation of diiron(II) forms to diiron(III) (Table 3.4). In the case of sMMO, the Fe•••Fe distance contracts by 0.3-0.4 Å by substitution of the monodentate carboxylate bridge in the (μ-1,1-carboxylato)(μ-1,3-carboxylato)diiron(II) core by two hydroxo bridges in the diiron(III) core. For RNR R2 and the fatty acid desaturases, the change in distance upon oxidation of the diferrous form to the diferric form can be even more dramatic from ~4.0 Å to ~3.1 Å in the conversion of the bis(μ-1,3-carboxylato)diiron(II) core to a (μ-oxo)(μ-1,3-carboxylato)diiron(III) core. In these examples, the binding mode of a bridging carboxylate plays a key role in the changes in Fe•••Fe distance due to their versatility in binding a metal center, namely monodentate or bidentate as well as terminal or bridging.[213] However, such a role for carboxylates in hDOHH appears unlikely, as there are only two carboxylate ligands, both of which are positioned within the active site such that only a terminal binding mode is plausible. To maintain the 3.4-3.5 Å Fe•••Fe

distance in hDOHH throughout its catalytic cycle, we propose that the Fe–OH–Fe unit remains intact throughout the series. Further constraints to the Fe•••Fe distance may also be imposed by the unique HEAT repeat protein fold that houses the diiron center in hDOHH, which significantly differs from the 4-helix bundle motif that supports the diiron centers of many nonheme diiron enzymes. In the crystal structure of hDOHH-$\mathbf{P_T}$,[17] each iron is ligated by a histidine and a glutamate from one protein domain and by a second histidine that derives from the second domain (Figure 3.6, left panel), creating a cross-domain interaction that may rigidly position the bound diiron center and could be responsible for the limited change in the Fe•••Fe distance.

Closer scrutiny of the hDOHH-$\mathbf{P_T}$ structure[17] shows the diiron unit to be buried in a narrow hydrophobic pocket, with the peroxo moiety pointing away from where eIF5A is proposed to bind hDOHH (Figure 3.6, right panel). The location and the hydrophobic environment of the peroxo pocket may account for the impressive stability of the peroxo intermediate. However, with this orientation for the intermediate as a starting point, the peroxo ligand would have to undergo rearrangement for it to be effective in substrate hydroxylation. We thus propose a mechanism shown in Figure 3.7 that begins with the (μ-hydroxo)(μ-1,2-peroxo)diiron(III) active site as described by our EXAFS analysis (Figure 3.7 A), with substrate binding initiating a series of steps (Figure 3.7 B-F) that lead to formation of the high-valent diiron oxidant that cleaves the substrate C–H bond. Substrate binding causes the loss of the terminal water ligand on the left Fe followed by the shift of the hydroxo bridge to become a terminal ligand on that Fe (Figure 3.7 B). These changes result in the decrease in coordination number for both Fe's, allowing the μ-1,2-peroxo bridge to twist and isomerize into a side-on bound μ-η^2:η^2-peroxo moiety (Figure 3.7 C). This conversion activates the O–O bond for cleavage to generate a diiron(IV) intermediate (Figure 3.7 D) that carries out substrate hydroxylation (Figure 3.7 E & F).

The high-valent diiron intermediate proposed for hDOHH has a core structure distinct from that associated with sMMO intermediate **Q**. The latter has been shown by EXAFS analysis and resonance Raman spectroscopy to have a bis(μ-oxo)diiron(IV)

diamond core.[45, 83] The Raman evidence that both oxygen atoms bridging the two Fe's in **Q** derive from one O_2 molecule supports the hypothesis of Banerjee et al. that a (μ-η^2:η^2-peroxo)diiron(III) moiety serves as the precursor to **Q**.[83] Our mechanistic proposal relies on this precedent. The more compact core structure established for **Q** with an EXAFS-deduced Fe•••Fe distance of 2.46 Å may not be able to form within the constraints of the hDOHH active site, which appears to impose a relatively invariant Fe•••Fe distance (3.4-3.5 Å) on all five hDOHH complexes described in this study. However both the (μ-η^2:η^2-peroxo)diiron(III) moiety and the open-core isomer of the bis(μ-oxo)diiron(IV) diamond core, respectively proposed in Figure 3.7 C & D, would fit within the Fe•••Fe distance constraints of the hDOHH active site. Although synthetic complexes with (μ-η^2:η^2-peroxo)diiron(III) cores have yet to be described, corresponding dicopper complexes are well known and exhibit Cu•••Cu distances of 3.6 Å for those with planar Cu_2O_2 units;[214-216] in one example, the Cu•••Cu distance can be decreased by conversion to a nonplanar butterfly configuration.[217] On the other hand, there are two precedents for the open-core formulation among synthetic high-valent diiron complexes which have been shown to have respective Fe•••Fe distances of 3.3 and 3.6 Å.[218, 219] In addition, reactivity comparisons among this series of diiron complexes show that the subset with terminal Fe=O units exhibits significantly higher reactivity with respect to H-atom abstraction than those with only bridging oxo units,[220] which led us to speculate that the sMMO-**Q** diamond core may isomerize to an open core in order to be able to cleave the 105-kcal/mol C–H bond of methane. This notion has also been proposed independently on the basis of DFT calculations.[221, 222] In any case, the terminal Fe=O unit in the open core configuration shown in Figure 3.7 D may be well set up to attack the target C–H bond on eIF5A and effect its hydroxylation.

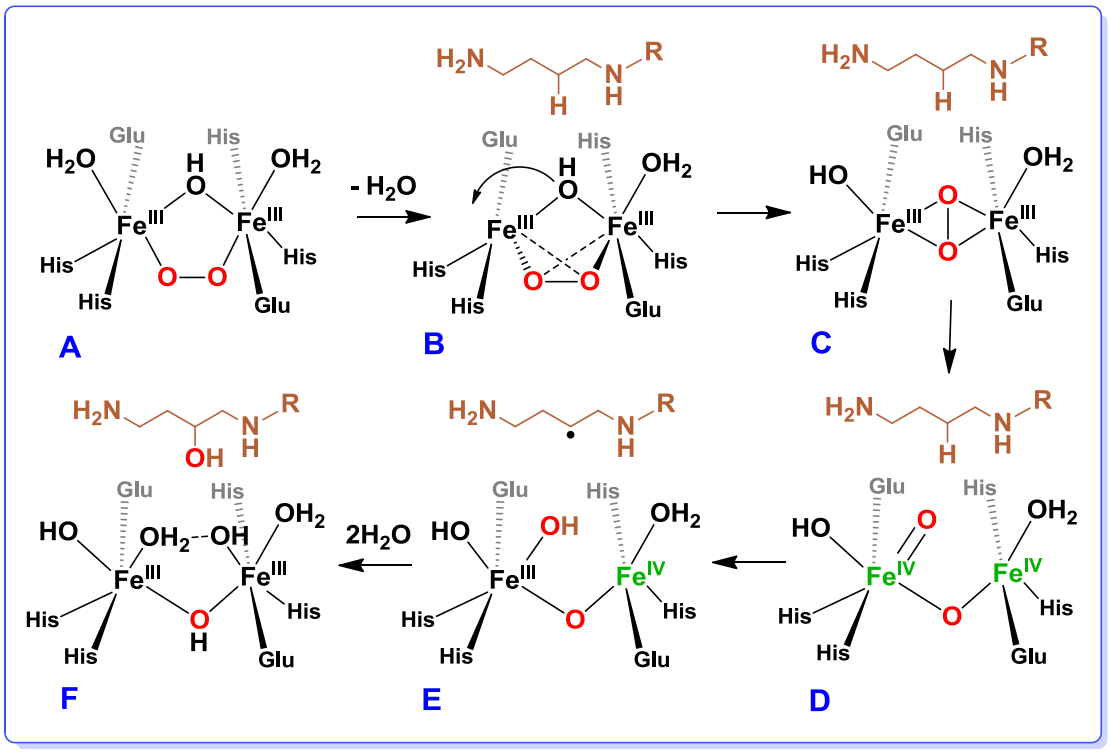

Figure 3.7. Proposed mechanism of O–O bond scission and substrate hydroxylation by hDOHH. A is hDOHH-**P**, B is hDOHH-**P•S**, and F is hDOHH-**D•S**. C, D, and E correspond to yet unobserved intermediates on the reaction pathway.

In summary, we have used X-ray absorption spectroscopy to characterize five different species in the catalytic cycle of hDOHH, including its O_2 adduct hDOHH-**P**, which we propose to have a (μ-hydroxo)(*cis*-μ-1,2-peroxo)diiron(III) center that gives rise to its characteristic blue color and an Fe•••Fe distance of 3.4 Å. These results are in good agreement with the X-ray structure reported for $hDOHH_T$-**P**, making this peroxo intermediate the best characterized to date within the dioxygen activating nonheme diiron enzyme family. hDOHH-**P** resembles peroxo intermediates found for other diiron enzymes in this family such as mutant RNR R2,[68, 182] Δ^9D,[67] and the ferroxidase center of ferritin[84] in exhibiting a ν(O–O) vibration within the 850-900 cm^{-1} range, which has been associated with synthetic (μ-1,2-peroxo)diiron(III) complexes.[105, 110, 112] However, unlike for hDOHH-**P,** available EXAFS data for RNR W48A/D84E R2[32] and the ferroxidase center of ferritin[37] implicate a much shorter Fe•••Fe distance of 2.5 Å, an observation that is difficult to reconcile with the peroxo binding mode derived from the Raman data.[182] A

major difference between hDOHH and most of the other diiron enzymes characterized thus far is the ligand combination that supports the diiron center. Most enzymes in this family utilize a 2-His-4-carboxylate ligand set that is neutralized upon binding of the diiron(II) center. In contrast, hDOHH employs a 4-His-2-carboxylate combination and requires one solvent-derived ligand to be ionized in order to mitigate the excess positive charge engendered by the binding of the diiron(II) center. The same argument may also be applied to justify the presence of a hydroxo bridge in deoxyhemerythrin, which has a 5-His-2-carboxylate binding site.[34] We suggest that the presence of the hydroxo bridge in hDOHH-**P** enhances the structural stability of the peroxo intermediate to allow the Fe scatterer to be observed unequivocally in the EXAFS data.

The differences noted above between hDOHH-**P** and the peroxo intermediates of canonical nonheme diiron enzymes suggest a greater diversity in peroxo binding modes in nonheme diiron active sites than initially imagined. Two other examples support this notion. ToMO gives rise to a peroxo intermediate with no visible chromophore[223] but nevertheless gives rise to a hydroxylated product, while CmlI generates a peroxo intermediate with a visible chromophore at ~500 nm and a much lower ν(O-O) at 791 cm^{-1}, which are inconsistent with a (*cis*-μ-1,2-peroxo)diiron(III) center.[15] Clearly additional work is called for to clarify the questions raised by this work. Despite the structural differences, Nature has selected for these diiron enzymes to catalyze fundamentally similar reactions. In widening the scope of the diiron family of proteins, we can learn more about design principles and structural motifs that are used to control the reactivity in biological systems.

3.4 – Experimental Procedures

Overexpression and Purification of hDOHH: The overexpression and purification were modified from a previously reported procedure.[65] hDOHH was overexpressed using the pGEX-4T-3_*hdohh* plasmid containing the *hdohh* gene in BL21(DE3) pLysS *E. coli* cells. Cells were grown in 4 L of LB growth media using a fermentation flask (New Brunswick) containing 100 μg/mL ampicillin at 37 ^{o}C with air bubbling continuously throughout the growth. Protein expression was induced at an OD_{600} of 0.6 by the

addition of 1 mM IPTG for 4 hours at 30 ^{o}C. The cells were harvested by centrifugation (8000 rpm, 10 min, 4 ^{o}C) and the cell pellet resuspended in ice cold 30 mL Buffer A (50 mM Tris-HCl, pH 7.5) supplemented with 1 mM PMSF. The resuspended cell pellet was stored at -80 ^{o}C. For protein purification, cells were lysed by sonication and cellular debris removed by centrifugation (25,000 rpm, 30 minutes, 4 ^{o}C). The clarified supernatant was rotated with 1 mL GSH-Sepharose resin (GE Healthcare) for four hours at 4 ^{o}C. The protein-bound resin was then poured into two empty PD-10 columns and washed with 50 mL Wash Buffer (50 mM Tris-HCl, pH 7.5, 100 mM NaCl) followed by 25 mL Thrombin Cleavage Buffer (20 mM Tris-HCl, pH 8, 150 mM NaCl, 2.5 mM $CaCl_2$). Thrombin (10 U) was added to the protein-bound resin and incubated overnight at 4 ^{o}C to cleave the GSH affinity tag from hDOHH. Free hDOHH was eluted from the column by the addition of 3 mL Thrombin Cleavage Buffer. Subsequent purification was carried out using a Superdex 200 size-exclusion column (GE Healthcare) and buffer. Blue fractions containing hDOHH-**P** were pooled and concentrated using a Vivaspin concentrator with 10 000 MWCO (Millipore) and stored at -80 ^{o}C.

Overexpression and Purification of eIF5A(Dhp): The overexpression and purification of modified eIF5A(Dhp) was modified from a previously reported procedure.[224] eIF5A(Dhp) was overexpressed using the polycistronic plasmid pST39_*eIF5A/DHS* containing both eIF5A(Lys) and DHS genes in BL21(DE3)pLysS *E. coli* cells.

Sample Preparation: hDOHH-**P** was prepared from as-isolated enzyme following purification. The blue species was concentrated using a Vivaspin concentrator with 10 000 MWCO at 4 ^{o}C in 50 mM Tris-HCl, pH 8, 125 mM NaCl. Glycerol was added for a final concentration of 20% and 4 mM $[Fe]_T$. To make the hDOHH-**P•S** sample, eIF5A(Dhp) was concentrated in Tris-HCl, pH 7.5, 125 mM NaCl and 20% glycerol at 4 ^{o}C using a Vivaspin concentrator. Concentrated hDOHH-**P** (in 50 mM Tris-HCl, 125 mM NaCl) was added to eIF5A(Dhp) on ice at a final ratio of 1.2 eq substrate. Enzyme and substrate were mixed and frozen for a final $[Fe]_T$ of 3.2 mM. The decayed species (hDOHH-**D** and hDOHH-**D•S**) were prepared by thawing the hDOHH-**P** and hDOHH-

P•S XAS samples. The samples were incubated at room temperature until the peroxo absorption feature had reached a minimum value (approximately 48 hours). The samples were then frozen in liquid nitrogen. hDOHH-**R** was prepared by chemically reducing hDOHH-**P** using 7 equivalents dithionite and 0.1 equivalents of methyl viologen at room temperature. The sample was then concentrated, and glycerol was added for a final concentration of 3 mM $[Fe]_T$ in Tris-HCl, pH 8 with 20 % glycerol. All samples were frozen in liquid nitrogen in a small Mössbauer/XAS cup.

X-ray Absorption Spectroscopy: Iron K-edge X-ray absorption spectra were collected on SSRL beam line 7-3 and 9-3 using a 30 element and 100 element (respectively) solid state Ge detector (Canberra) with a SPEAR storage ring current of ~500 mA at a power of 3.0 GeV. The incoming X-rays were unfocused using a Si(220) double crystal monochromator, which was detuned to 40% of the maximal flux to attenuate harmonic X-rays. For hDOHH-**R**, hDOHH-**P**, hDOHH-**P•S**, hDOHH-**D** and hDOHH-**D•S** 14, 12, 9, 12 and 10 scans (respectively) were collected from 6882 eV to 8000 eV at a temperature (~10 K) that was controlled by an Oxford Instruments CF1208 continuous flow liquid helium cryostat. An iron foil was placed in the beam pathway prior to I_0 and scanned concomitantly for an energy calibration, with the first inflection point of the edge assigned to 7112.0 eV. A 3 μm Mn filter and a Soller slit were used to increase the signal to noise ratio of the spectra. Photoreduction was monitored by scanning the same spot on the sample twice and comparing the first derivative peaks associated with the edge energy during collection.

The detector channels from the scans were examined, calibrated, averaged, and processed for EXAFS analysis using EXAFSPAK[143] to extract χ(k). Theoretical phase and amplitude parameters for a given absorber-scatterer pair were calculated using FEFF 8.40[144] and were utilized by the "opt" program of the EXAFSPAK package during curve fitting. Parameters for each species were calculated using a model derived from the crystal structure (PDB code 4D50). In all analyses, the coordination number of a given shell was a fixed parameter and was varied iteratively in integer steps, while the bond lengths (R) and mean-square deviation (σ^2) were allowed to freely float. The amplitude

reduction factor S_0 was fixed at 0.9, while the edge-shift parameters E_0 was allowed to float as a single value for all shells. Thus, in any given fit, the number of floating parameters was typically equal to (2 x num shells) + 1. hDOHH-**P**, hDOHH-**P•S**, and hDOHH-**D** all have a k range of 2 – 13.5 $Å^{-1}$, and hDOHH-**R** has a range of 2 – 15 $Å^{-1}$
Pre-edge analysis was performed on data normalized in the "process" program of the EXAFSPAK package, and pre-edge features were fit between 7108 eV to 7118 eV (for Reduced 7108 eV to 7115 eV) using the Fityk[145] program with pseudo-Voigt functions composed of 50:50 Gaussian/Lorentzian functions.

3.5 – Acknowledgements

This work was supported by the National Institutes of Health grant GM-38767 to L.Q. and postdoctoral fellowship 5F32GM106612-02 to L.M.E. and by the Intramural Research Program of the National Institute of Dental and Craniofacial Research. XAS data were collected on Beamline 7-3 at the Stanford Synchrotron Radiation Lightsource, SLAC National Accelerator Laboratory and at Beamline X3B of the National Synchrotron Light Source (NSLS). SLAC is supported by the U.S. Department of Energy (DOE), Office of Science, Office of Basic Energy Sciences under Contract No. DE-AC02-76SF00515. Use of Beamline 7-3 is supported by the DOE Office of Biological and Environmental Research, and by the National Institutes of Health, National Institute of General Medical Sciences (including P41GM103393). NSLS is a DOE Office of Science User Facility operated for the DOE Office of Science by Brookhaven National Laboratory under Contract No. DE-AC02-98CH10886. We thank Dr. Caleb Allpress for helpful discussions.

3.6 – Supplementary Information

General EXAFS considerations: In the fit tables of EXAFS data, N refers to the number of scatterers used for a particular shell, R is the distance of the scattering shell, σ^2 is the mean-squared deviation (or Debye-Waller factor), E_0 is the edge shift parameter, and the

goodness of fit (GOF) parameters are calculated as $F = \sqrt{\sum k^6 \left(\chi_{\exp} - \chi_{calc}\right)^2}$, $F' = \sqrt{\sum k^6 \left(\chi_{\exp} - \chi_{calc}\right)^2 / \sum k^6 \chi_{\exp}{}^2}$. For all fits, the amplitude reduction factor ($S_0{}^2$) was set to 0.9.

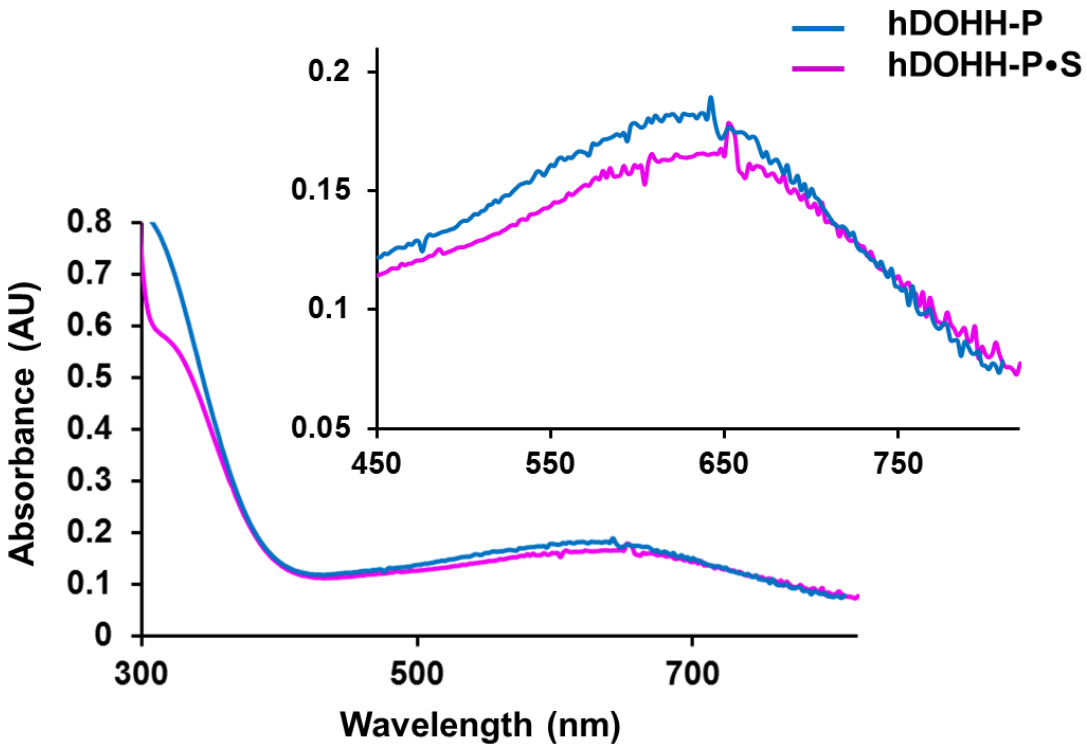

Figure 3.8. UV-visible absorption spectra of hDOHH-**P** (blue) and hDOHH-**P•S** (purple). Concentration of hDOHH-**P** in both samples is 75 μM with 1.2 eq. of eIF5A(Dhp) added to make the hDOHH- **P•S** sample. Both samples were prepared in 50 mM Tris-HCl, 125 mM NaCl buffer with spectra recorded at 25 °C. Inset: zoom in on the 630 nm LMCT transition.

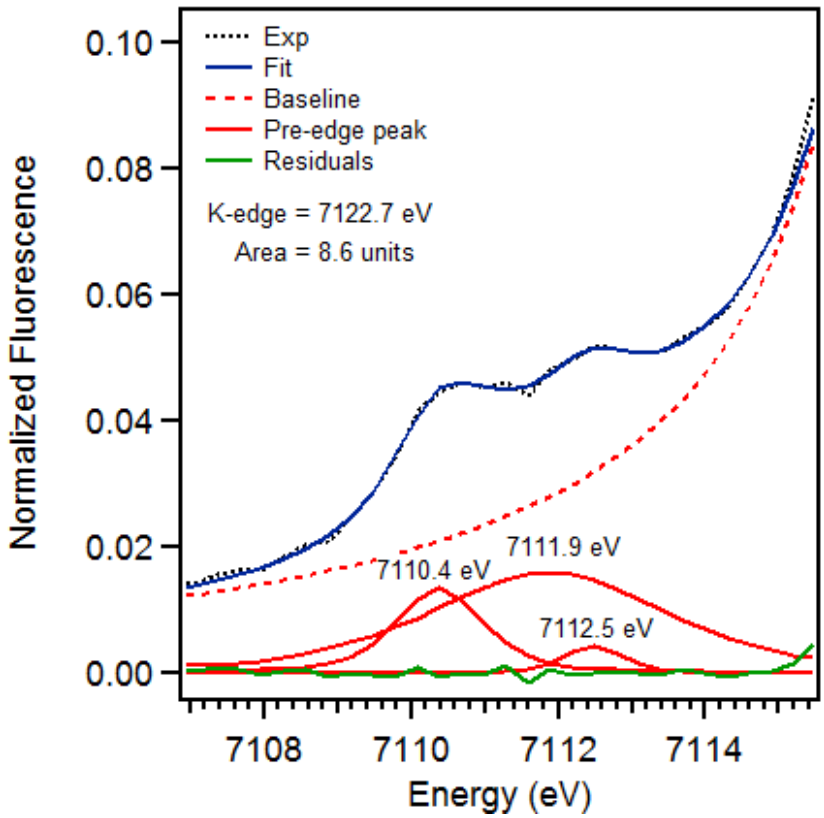

Figure 3.9. Pre-edge region analysis of hDOHH-**R**. The experimental data (black dotted), baseline (red dashed), pre-edge peak components (red solid), residuals (green solid) and total fit (blue solid) are shown.

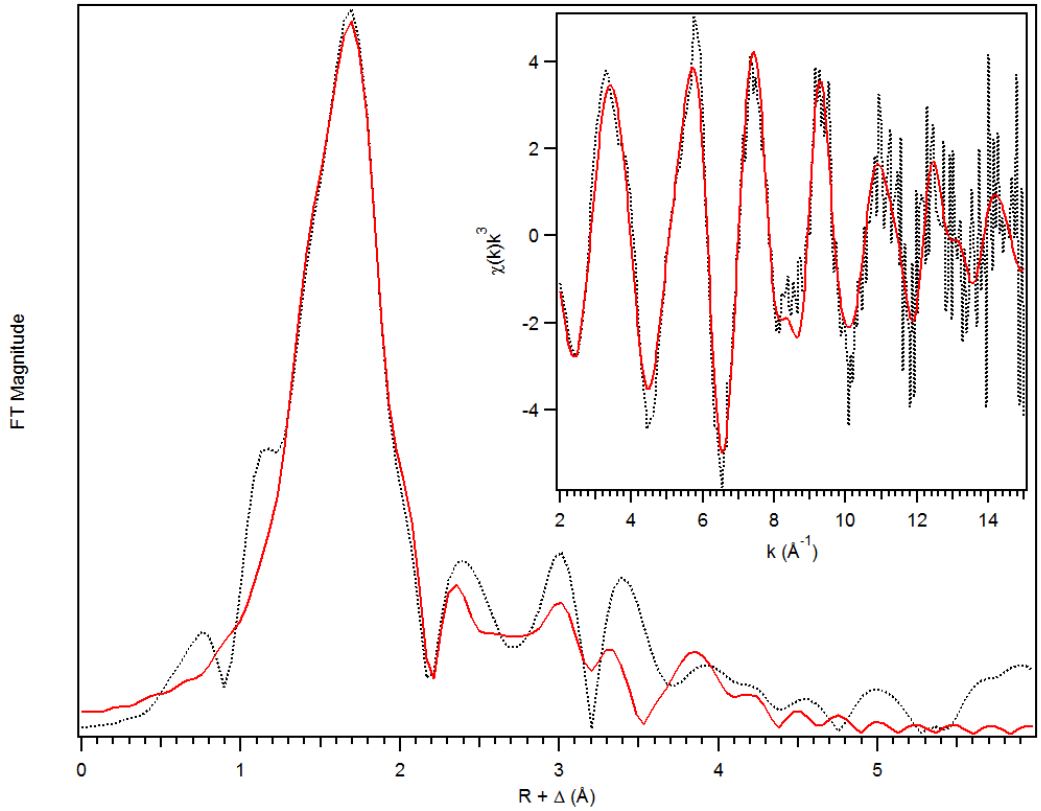

Figure 3.10. EXAFS spectrum of hDOHH-**R**. Fit (red solid line) of the unfiltered (black dotted) EXAFS data (inset) and corresponding Fourier transform (Table 3.5, Fit 12). Data was fit between k = 2 – 15 $Å^{-1}$.

Table 3.5. Fit parameters for the unfiltered EXAFS data of hDOHH-**R**, between k = 2 – 15 $Å^{-1}$. Fit 12 gives the most reasonable fit of the experimental data.

	Fe-N			**Fe-O**			**Fe•••Fe**			**Fe•••C**				**GOF**	
Fit	**N**	**R(Å)**	**$\sigma^2(10^{-3})$**	**N**	**R(Å)**	**$\sigma^2(10^{-3})$**	**N**	**R(Å)**	**$\sigma^2(10^{-3})$**	**N**	**R(Å)**	**$\sigma^2(10^{-3})$**	**E_o**	**F**	**F'**
1	6	2.15	4.71										-5.97	360	509
2	5	2.15	3.73										-5.59	384	526
3	4	2.15	2.71										-5.16	433	558
4	5	2.17	3.01	1	2.05	1.77							-6.97	350	503
5	4	2.18	2.54	2	2.07	3.25							-7.55	347	500
6	5	2.17	3.30	1	2.05	2.27				3	3.11	5.41	-6.21	317	478
7	4	2.18	2.85	2	2.08	3.49				3	3.10	5.49	-6.69	313	475
8	4	2.17	2.64	2	2.07	3.51	1	3.46	7.04	3	3.09	6.58	-7.28	299	464
9	5	2.17	3.04	1	2.05	1.88	1	3.47	7.17	3	3.10	6.48	-6.72	304	468
10	5	2.17	3.19	1	2.05	2.02	1	3.47	7.26	3	3.10	6.56	-6.20	287	453
										4	4.36	3.61			
11	4	2.18	2.99	2	2.08	3.92	1	3.46	7.02	3	3.09	6.54	-6.70	281	450
										4	4.35	3.24			
12	**4**	**2.18**	**2.78**	**2**	**2.07**	**3.39**	**1**	**3.47**	**5.18**	**3**	**3.10**	**6.20**	**-6.80**	**272**	**443**
										3	**3.68**	**4.05**			
										3	**4.35**	**2.51**			

Table 3.5. (continued) Fit parameters for the unfiltered EXAFS data of hDOHH-**R**, between k = 2 – 15 $Å^{-1}$. Fit 12 gives the most reasonable fit of the experimental data.

	Fe-N			Fe-O			Fe•••Fe			Fe•••C				GOF	
Fit	N	R(Å)	$\sigma^2(10^{-3})$	N	R(Å)	$\sigma^2(10^{-3})$	N	R(Å)	$\sigma^2(10^{-3})$	N	R(Å)	$\sigma^2(10^{-3})$	E_o	F	F'
13	5	2.17	3.15	1	2.05	1.85	1	3.47	5.33	3	3.11	6.13	-6.36	277	446
										3	3.68	3.79			
										3	4.36	2.88			
14	5	2.17	3.42	1	2.06	2.32				3	3.11	5.39	-5.70	280	449
										3	4.05	2.01			
										4	4.36	1.81			
15	5	2.17	3.05	1	2.05	1.75	1	3.46	5.07	3	3.69	4.64	-7.01	299	464
										4	4.35	2.57			
16	5	2.16	3.10	1	2.05	2.07	1	3.47	6.10	3	3.10	6.34	-7.05	300	465
										3	3.70	4.78			
17	4	2.17	2.72				1	3.48	5.86	3	3.12	5.85	-4.80	354	505
										3	3.70	3.70			
										4	4.37	2.17			
18	6	2.15	4.71				1	3.48	5.79	3	3.12	5.97	-5.70	286	454
										3	3.69	3.62			
										4	4.37	2.25			

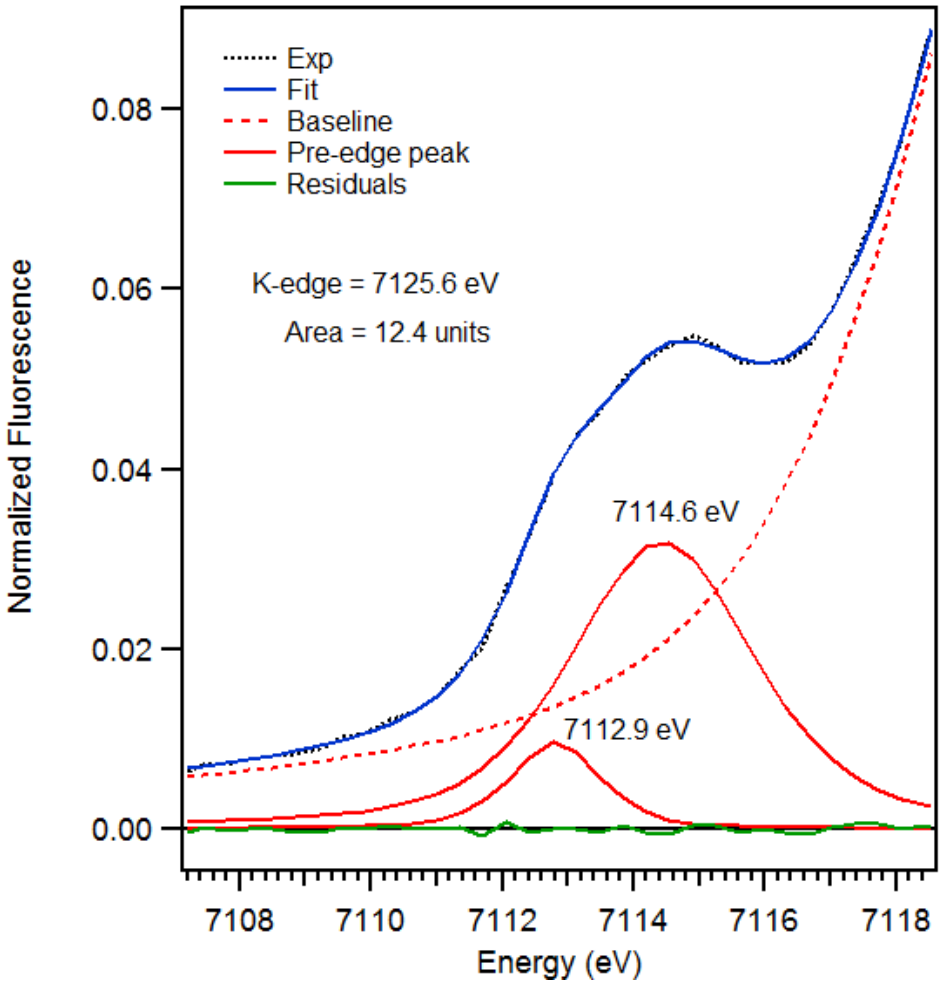

Figure 3.11. Pre-edge region analysis of hDOHH-**P**. The experimental data (black dotted), baseline (red dashed), pre-edge peak components (red solid), residuals (green solid) and total fit (blue solid) are shown

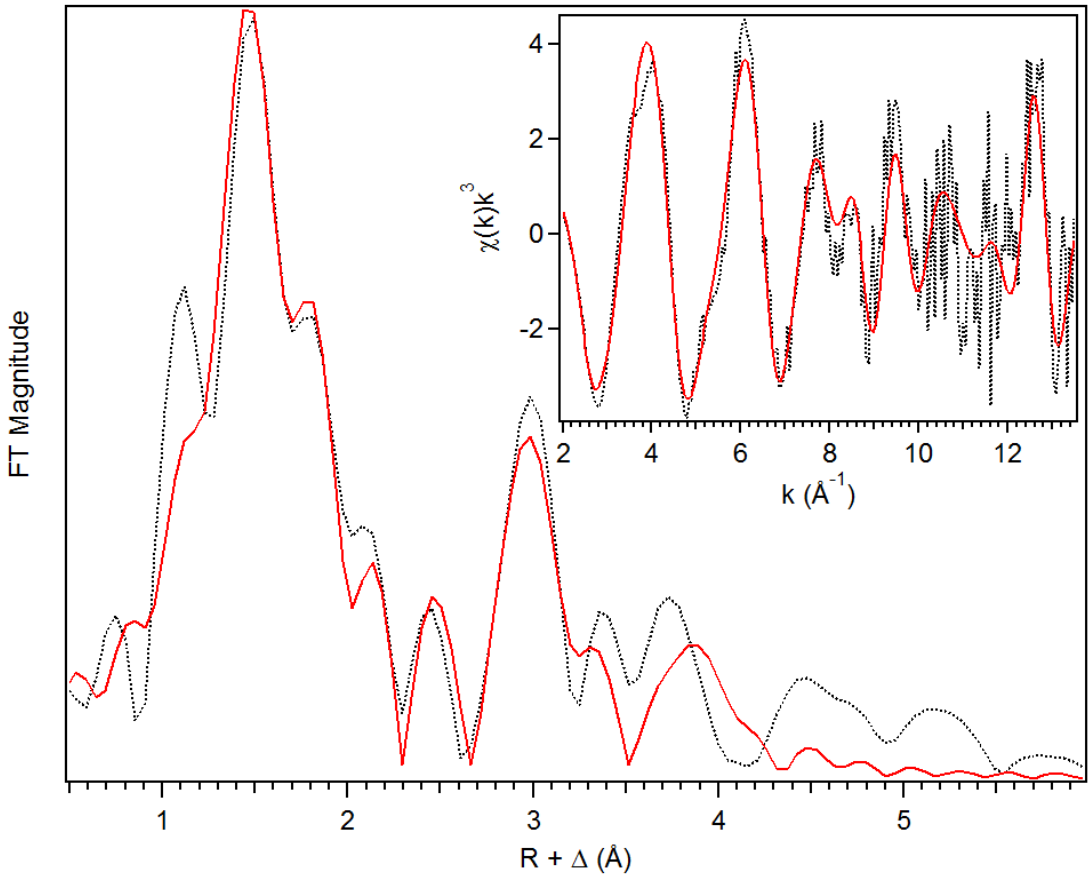

Figure 3.12. EXAFS spectrum of hDOHH-**P**. Fit (red solid line) of the unfiltered (black dotted) EXAFS data (inset) and corresponding Fourier transform (Table 3.6, Fit 14). Data was fit between k = 2 – 13.5 $Å^{-1}$.

Table 3.6. Fit parameters for the unfiltered EXAFS data of hDOHH-**P**, between k = 2 – 13.5 $Å^{-1}$. Fit 14 gives the most reasonable fit of the experimental data.

	Fe-N			**Fe-O**			**Fe•••Fe**			**Fe•••C**				**GOF**	
Fit	**N**	**R(Å)**	**$\sigma^2(10^{-3})$**	**N**	**R(Å)**	**$\sigma^2(10^{-3})$**	**N**	**R(Å)**	**$\sigma^2(10^{-3})$**	**N**	**R(Å)**	**$\sigma^2(10^{-3})$**	**E_o**	**F**	**F'**
1	6	2.08	12.12										0.79	392	637
2	5	2.08	10.51										1.30	410	652
3	4	2.09	8.80										2.31	446	680
4	3	2.11	6.86										3.63	504	723
5	3	2.13	1.44	1	1.97	-1.40							1.19	331	586
6	3	2.15	1.33	2.	1.98	1.73							-0.21	305	562
7	4	2.14	3.10	2	1.96	2.04							-0.32	300	558
8	3	2.15	0.56	2	1.99	0.74							-2.27	297	554
				1	1.90	4.49									
9	3	2.14	1.46	2	1.97	1.82	1	3.42	3.05				-0.79	233	491
10	3	2.14	1.36	2	1.97	1.77	1	3.42	3.33	3	4.30	0.08	-0.60	209	465
11	3	2.14	1.37	2	1.97	1.79	1	3.42	3.30	4	4.30	1.51	-0.51	207	464
12	3	2.15	0.99	2	1.99	1.63	1	3.41	3.21	4	2.29	1.61	-2.09	198	453
				1	1.91	6.68									
13	3	2.14	1.53	2	1.97	1.93	1	3.42	2.03	4	4.30	1.44	-0.78	197	452
										3	3.60	3.31			
14	**3**	**2.15**	**1.95**	**3**	**1.98**	**4.57**	**1**	**3.41**	**1.86**	**4**	**4.29**	**1.55**	**-1.76**	**190**	**444**
										3	**3.58**	**2.93**			

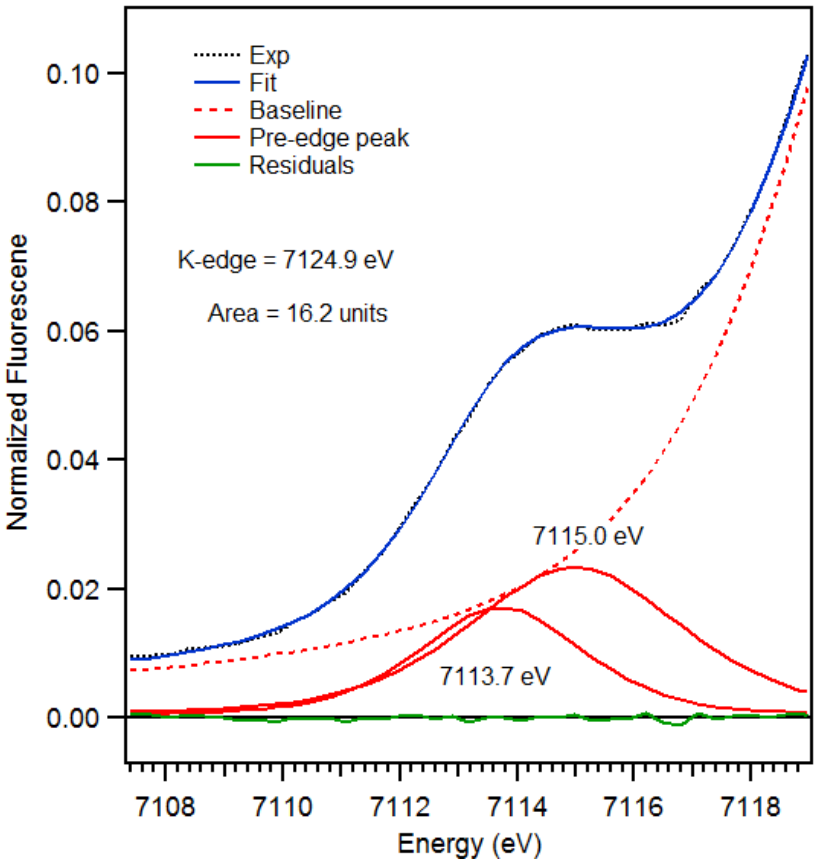

Figure 3.13. Pre-edge region analysis of hDOHH-**P•S**. The experimental data (black dotted), baseline (red dashed), pre-edge peak components (red solid), residuals (green solid) and total fit (blue solid) are shown

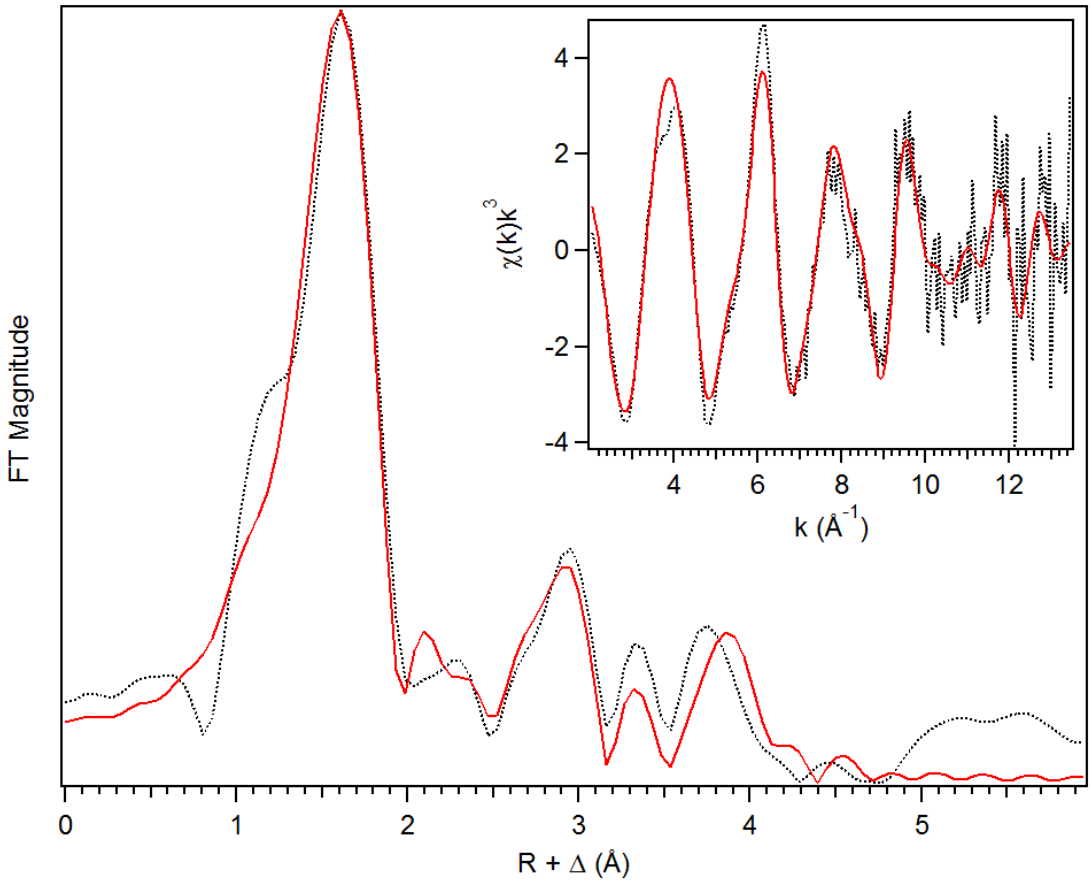

Figure 3.14. EXAFS spectrum of hDOHH-**P•S**. Fit (red solid line) of the unfiltered (black dotted) EXAFS data (inset) and corresponding Fourier transform (Table 3.7, Fit 17). Data was fit between k = 2 – 13.5 $Å^{-1}$.

Table 3.7. Fit parameters for the unfiltered EXAFS data of hDOHH-**P•S**, between k = 2 – 13.5 $Å^{-1}$. Fit 17 gives the most reasonable fit of the experimental data.

	Fe-N			Fe-O			Fe•••Fe			Fe•••C				GOF	
Fit	N	R(Å)	$\sigma^2(10^{-3})$	N	R(Å)	$\sigma^2(10^{-3})$	N	R(Å)	$\sigma^2(10^{-3})$	N	R(Å)	$\sigma^2(10^{-3})$	E_o	F	F'
1	6	2.08	9.45										-4.13	228	540
2	5	2.08	7.76										-3.40	223	553
3	4	2.09	6.06										-2.86	233	546
4	3	2.09	4.29										-2.25	268	585
5	3	2.12	4.15	1	2.00	1.90							-2.51	212	521
6	3	2.10	12.28	2	2.05	5.41							-3.18	208	516
7	4	2.11	6.48	1	1.99	4.77							-3.34	210	518
8	4	2.12	5.70	1	1.99	3.17	1	3.07	7.49				-2.67	169	465
9	4	2.12	5.69	1	1.99	3.00				3	3.10	3.26	-2.67	170	465
10	4	2.11	5.48	1	1.98	3.44	1	3.07	7.44	4	4.30	1.31	-2.65	143	427
11	4	2.11	5.86	1	1.99	3.61	1	3.08	8.0	4	4.30	1.42	-3.00	140	423
										2	3.41	4.02			
12	4	2.10	5.94	1	1.97	5.86				4	4.29	1.30	-4.46	172	469
										2	3.43	1.42			
13	4	2.11	5.50	1	1.97	4.24				4	4.30	1.15	-3.62	134	414
										2	3.43	3.15			
										3	3.09	3.71			
14	4	2.11	5.43	1	1.97	4.05				3	3.09	3.28	-3.62	146	432
										4	4.30	1.16			
15	4	2.10	5.67	1	1.97	4.99	1	3.43	7.95	4	4.29	0.98	-4.44	164	458

Table 3.7. (continued) Fit parameters for the unfiltered EXAFS data of hDOHH-P•**S**, between k = 2 – 13.5 $Å^{-1}$. Fit 17 gives the most reasonable fit of the experimental data.

	Fe-N			**Fe-O**			**Fe•••Fe**			**Fe•••C**				**GOF**	
Fit	**N**	**R(Å)**	**$\sigma^2(10^{-3})$**	**N**	**R(Å)**	**$\sigma^2(10^{-3})$**	**N**	**R(Å)**	**$\sigma^2(10^{-3})$**	**N**	**R(Å)**	**$\sigma^2(10^{-3})$**	**E_o**	**F**	**F'**
16	4	2.1	5.24	1	1.97	3.80	1	3.43	10.99	3	3.09	3.97	-3.87	135	414
										4	4.29	3.99			
17	**4**	**2.11**	**5.61**	**1**	**1.98**	**4.47**	**1**	**3.41**	**5.44**	**3**	**3.09**	**6.50**	**-3.90**	**132**	**411**
										3	**3.56**	**3.51**			
										4	**4.30**	**1.72**			
18	4	2.11	5.75	1	1.98	4.52	1	3.41	5.61	3	3.61	3.20	-4.00	38	421
							1	3.07	11.32	4	4.29	1.92			
19	4	2.10	6.32	2	1.98	10.78	1	3.48	13.37	2	3.38	1.82	-5.34	140	424
							1	3.07	10.03	4	4.28	1.32			
20	5	2.09	7.05	1	1.94	8.36	1	3.07	8.68	3	3.41	5.49	-4.94	148	435
										4	4.28	1.02			
21	4	2.09	5.95	2	1.96	11.61	1	3.40	4.58	3	3.08	7.63	-5.84	134	414
										3	3.59	2.50			
										4	4.28	2.02			
22	4	2.10	5.83	1.5	1.97	8.81	1	3.40	4.99	3	3.08	7.24	-5.14	132	411
										3	3.59	3.17			
										4	4.29	1.66			
23	4.5	2.09	6.41	1.5	1.95	10.26	1	3.41	4.71	3	3.08	7.13	-5.40	135	416
										3	3.60	2.45			
										4	4.29	1.89			
24	4.5	2.10	6.40	1	1.96	7.00	1	3.41	5.18	3	3.09	6.67	-4.56	134	415
										3	3.60	3.12			
										4	4.29	1.87			

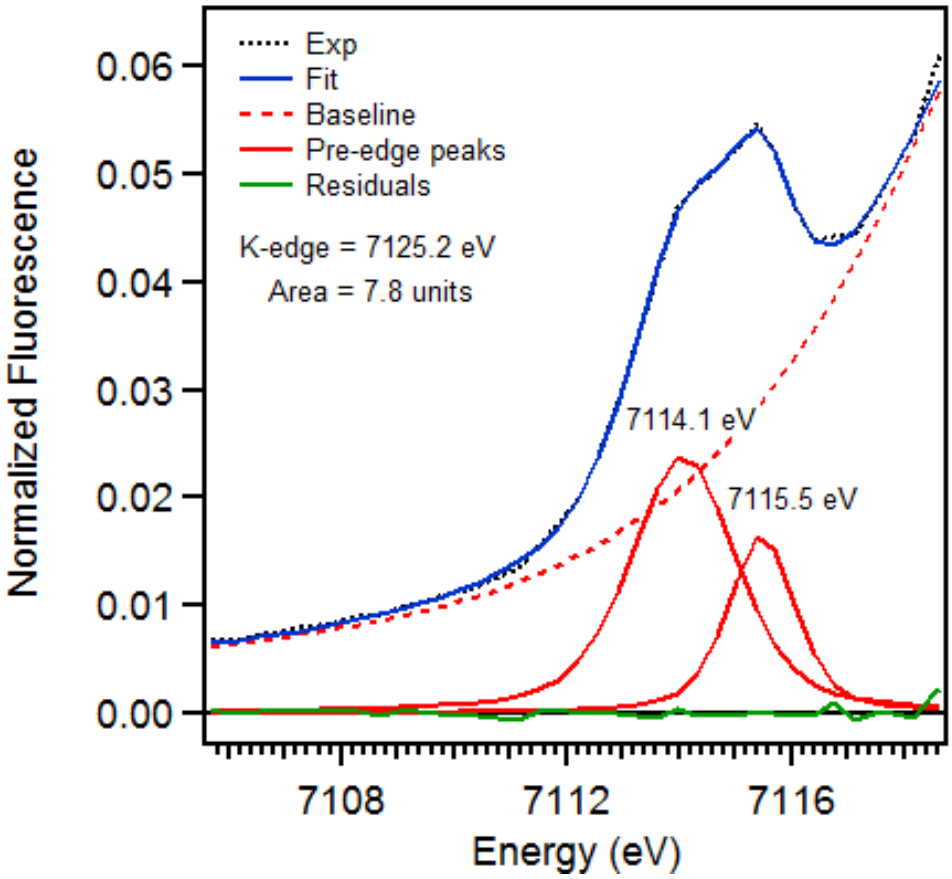

Figure 3.15. Pre-edge region analysis of hDOHH-**D**. The experimental data (black dotted), baseline (red dashed), pre-edge peak components (red solid), residuals (green solid) and total fit (blue solid) are shown.

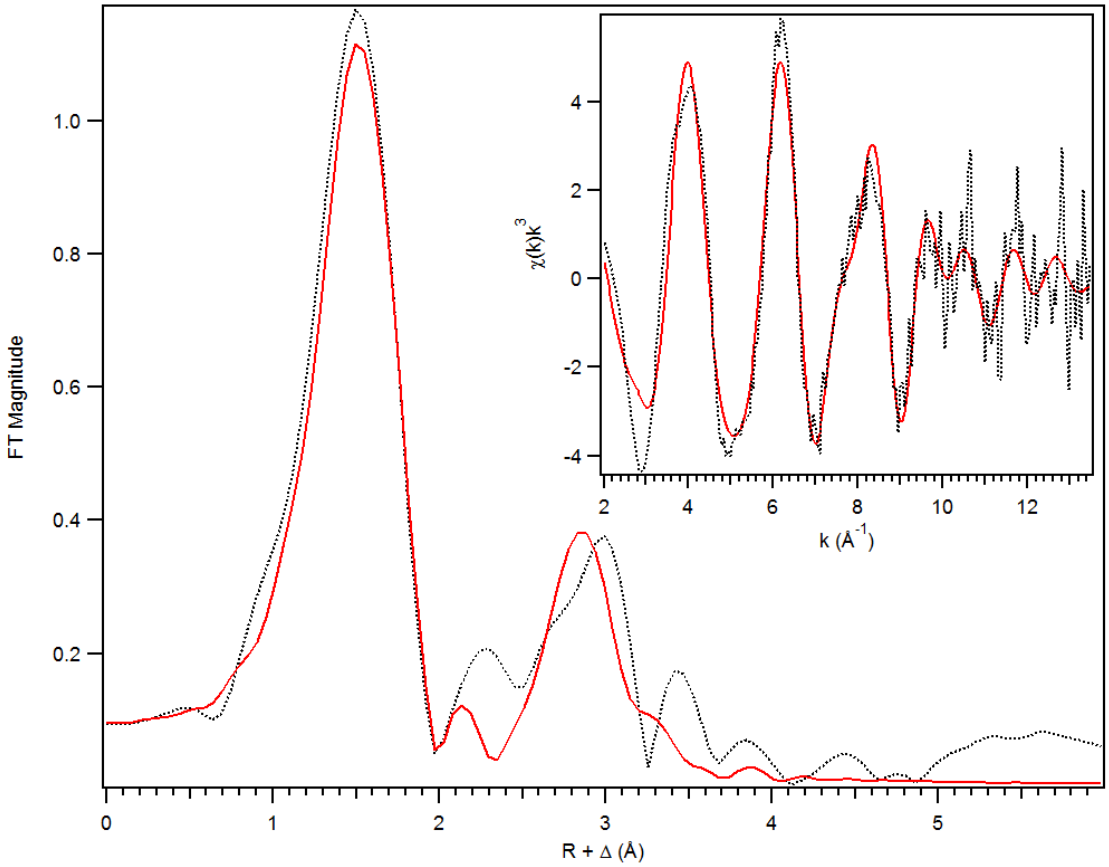

Figure 3.16. EXAFS spectrum of hDOHH-**D**. Fit A (red solid line) of the unfiltered (black dotted) EXAFS data (inset) and corresponding Fourier transform (Table 3.8, Fit 11). Fit A includes an Fe•••Fe distance at 3.07 Å. Data was fit between k = 2 – 13.5 $Å^{-1}$

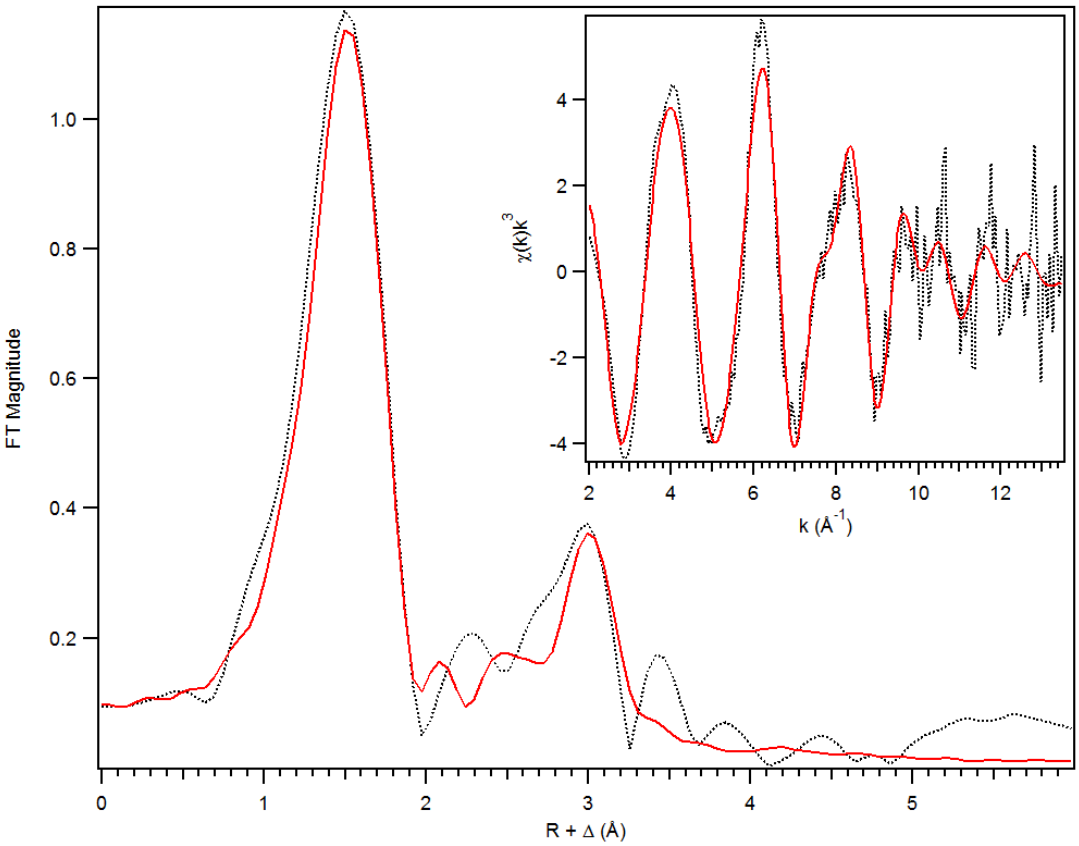

Figure 3.17. EXAFS spectrum of hDOHH-**D**. Fit B (red solid line) of the unfiltered (black dotted) EXAFS data (inset) and corresponding Fourier transform (Table 3.9, Fit 8). Fit B includes an Fe•••Fe distance at 3.42 Å and is the preferred fit for hDOHH-**D**. Data was fit between k = 2 – 13.5 $Å^{-1}$.

Table 3.8. Fit parameters for the unfiltered EXAFS data of hDOHH-**D** Fit A, between k = 2 – 13.5 $Å^{-1}$. Fit 11 gives the most reasonable fit of the experimental data.

	Fe-N			**Fe-O**			**Fe•••Fe**			**Fe•••C**				**GOF**	
Fit	**N**	**R(Å)**	**$\sigma^2(10^{-3})$**	**N**	**R(Å)**	**$\sigma^2(10^{-3})$**	**N**	**R(Å)**	**$\sigma^2(10^{-3})$**	**N**	**R(Å)**	**$\sigma^2(10^{-3})$**	**E_o**	**F**	**F'**
1	6	2.03	8.25										-0.93	233	431
2	5	2.03	6.92										-0.73	273	466
3	4	2.03	5.57										-0.41	340	521
4	5	2.07	5.50	1	1.93	0.87							-0.77	209	409
5	5	2.08	6.35	2	1.94	3.93							-1.52	197	396
6	4	2.09	4.43	2	1.96	2.78							-1.18	207	406
7	3	2.10	2.32	2	1.95	1.74							-0.96	233	431
8	4	2.09	4.58	2	1.95	2.88	1	3.07	6.22				-0.44	151	348
9	4	2.10	4.56	2	1.96	2.68				4	3.09	4.46	0.42	178	377
10	4	2.09	4.36	2	1.95	2.72				4	3.07	7.03	-0.39	127	319
										4	3.43	2.27			
11	**4**	**2.07**	**4.05**	**2**	**1.93**	**2.81**	**1**	**3.07**	**9.87**	**5**	**3.41**	**3.51**	**-2.90**	**133**	**326**

Table 3.9. Fit parameters for the unfiltered EXAFS data of hDOHH-**D** Fit B, between k = 2 – 13.5 $Å^{-1}$. Fit 8 gives the most reasonable fit of the experimental data.

	Fe-N			**Fe-O**			**Fe•••Fe**			**Fe•••C**				**GOF**	
Fit	**N**	**R(Å)**	**$\sigma^2(10^{-3})$**	**N**	**R(Å)**	**$\sigma^2(10^{-3})$**	**N**	**R(Å)**	**$\sigma^2(10^{-3})$**	**N**	**R(Å)**	**$\sigma^2(10^{-3})$**	**E_o**	**F**	**F'**
1	6	2.03	8.23										-0.95	233	431
2	5	2.03	6.91										-0.75	273	466
3	4	2.03	5.56										-0.44	340	521
4	4	2.07	3.60	1	1.93	-0.20							-0.41	237	435
5	4	2.09	4.44	2	1.94	2.82							-1.22	206	405
6	5	2.08	6.39	2	1.94	3.97							-1.49	197	396
7	4	2.08	4.20	2	1.94	2.89	1	3.41	3.97				-1.97	141	336
8	**4**	**2.09**	**4.45**	**2**	**1.95**	**2.88**	**1**	**3.42**	**5.09**	**3**	**3.08**	**4.90**	**-0.69**	**127**	**317**
9	4	2.09	4.25	2	1.94	2.73				5	3.43	3.62	-1.28	125	316
										3	3.09	4.73			
10	4	2.09	4.58	2	1.95	2.74				3	3.10	2.65	0.01	166	364

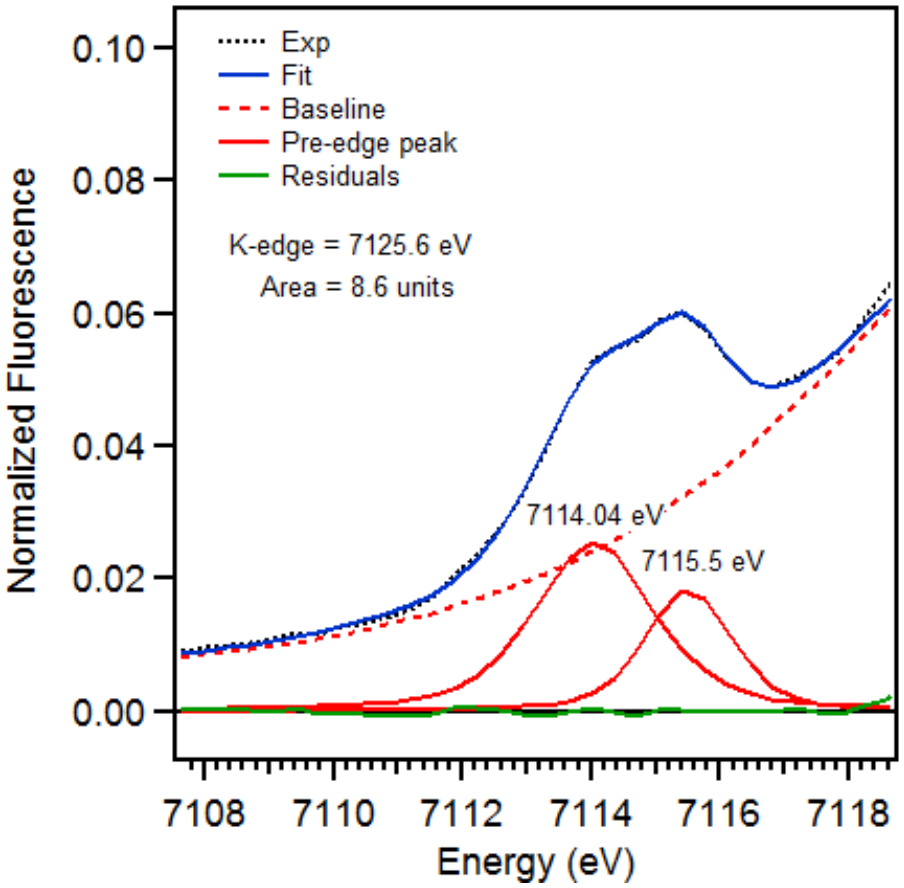

Figure 3.18. Pre-edge region analysis of hDOHH-**D•S**. The experimental data (black dotted), baseline (red dashed), pre-edge peak components (red solid), residuals (green solid) and total fit (blue solid) are shown.

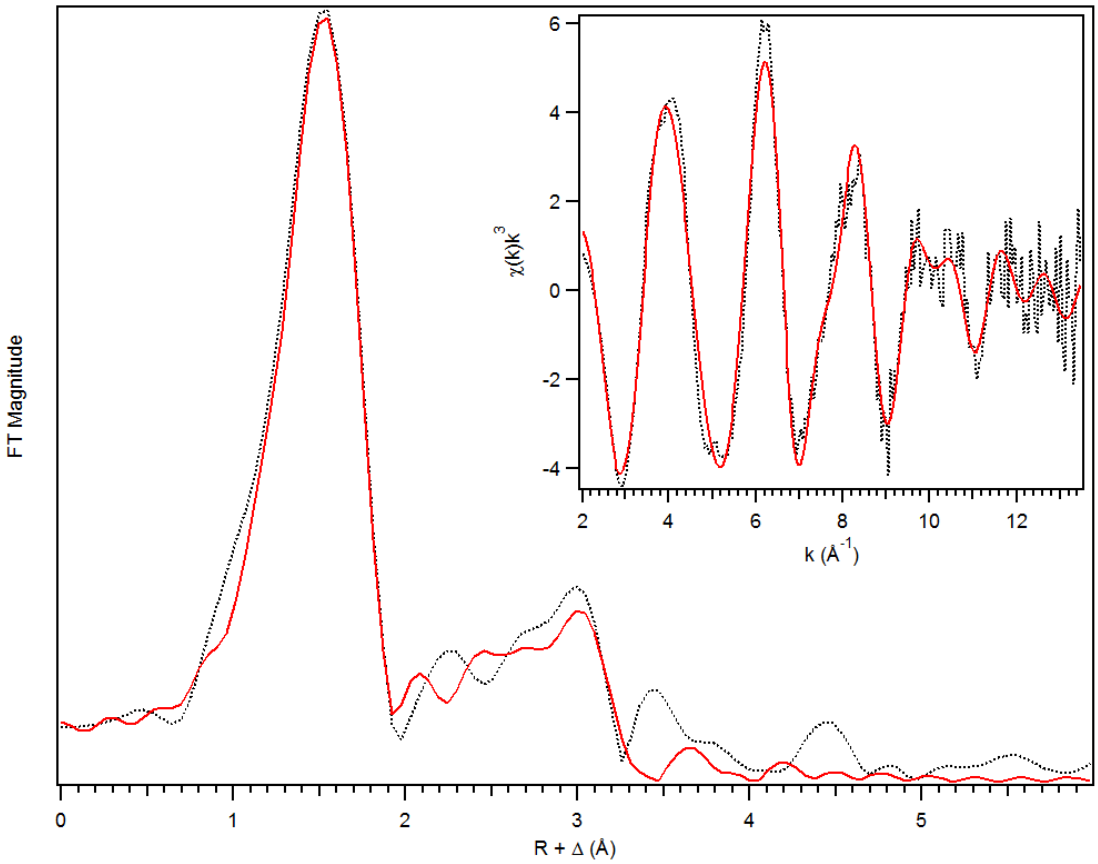

Figure 3.19. EXAFS spectrum of hDOHH-**D•S**. Fit (red solid line) of the unfiltered (black dotted) EXAFS data (inset) and corresponding Fourier transform (Table 3.10, Fit 10). Data was fit between k = 2 – 13.5 $Å^{-1}$.

Table 3.10. Fit parameters for the unfiltered EXAFS data of hDOHH-**D•S**, between k = 2 – 13.5 $Å^{-1}$. Fit 10 gives the most reasonable fit of the experimental data.

		Fe-N			**Fe-O**			**Fe•••Fe**			**Fe•••C**				**GOF**	
Fit	**N**	**R(Å)**	**$\sigma^2(10^{-3})$**	**N**	**R(Å)**	**$\sigma^2(10^{-3})$**	**N**	**R(Å)**	**$\sigma^2(10^{-3})$**	**N**	**R(Å)**	**$\sigma^2(10^{-3})$**	**E_o**	**F**	**F'**
1	6	2.03	7.49										-0.91	181	376
2	5	2.03	6.21										-0.70	218	412
3	4	2.03	4.89										-0.41	284	471
4	3	2.03	3.46										-0.19	391	552
5	5	2.06	5.29	1	1.93	0.95							-0.60	163	356
6	5	2.07	6.59	2	1.94	4.34							-1.39	157	350
7	4	2.08	4.44	2	1.95	2.78							-0.96	161	354
8	4	2.07	4.20	2	1.94	2.79	1	3.42	4.96				-1.54	113	297
9	4	2.08	4.20	2	1.95	2.56	1	3.44	6.17	3	3.08	5.33	-0.45	97	274
10	**4**	**2.08**	**4.40**	**2**	**1.95**	**2.88**	**1**	**3.42**	**3.51**	**3**	**3.08**	**6.29**	**-0.71**	**85**	**258**
										3	**3.59**	**3.30**			
11	4	2.08	4.23	2	1.90	2.56	1	3.44	6.14	3	3.08	5.49	-0.37	94	271
										3	4.27	6.60			
12	4	2.08	4.51	2	1.95	2.96	1	3.42	3.30	3	3.08	6.43	-0.55	77	245
										3	3.59	2.68			
										3	4.27	5.46			

Table 3.11. Component analysis of pre-edge peak fitting for hDOHH species. Pre-edge peaks were fit between 7108 – 7118 eV using PseudoVoigt functions with a 50:50 Gaussian/Lorentzian peak shape.

Species	**Component Position (eV)**	**Component Area (units)**	**Total Area (units)**
hDOHH-**R**	7110.4	1.93	8.6
	7111.9	6.20	
	7112.5	0.43	
hDOHH-**P**	7112.9	1.67	12.4
	7114.5	10.7	
hDOHH-**P•S**	7113.7	5.82	16.2
	7115.0	10.4	
hDOHH-**D**	7114.1	5.40	7.8
	7114.6	2.40	
hDOHH-**D•S**	7114.0	5.64	8.6
	7115.5	2.93	

Table 3.12. Selected distances from crystal structures of ferrous (Fe^{II}) synthetic model complexes[a].

Complex	Fe / Fe_2	Core OH_x	Fe-O (Å)	Term. OH_x	Fe-O (Å)	Fe•••Fe (Å)	<Fe-O-Fe	References
$[Fe_2(\mu\text{-}OH)(\mu\text{-}OH_2)(TPA)_2](OTf)_2$	Fe_2	OH	2.098 2.034	-	-	3.216	95.5 º	*159*
		OH_2	2.132 2.210	-	-	-	102.2 º	
$[Fe_2(\mu\text{-}OH)_2(6\text{-}Me_3\text{-}TPA)_2](OTf)_2$	Fe_2	OH	2.033 2.208	-	-	3.221	98.8 º	*92*
$[Fe_2(\mu\text{-}OH_2)_2(\mu\text{-}O_2CAr^{4F\text{-}Ph})(O_2CAr^{4F\text{-}Ph})_3(THF)_2(OH_2)]$	Fe_2	OH_2	2.229 2.293 2.232 2.152	OH_2	2.115	3.288	93.3 º 97.1 º	*153*
$[Fe_2(\mu\text{-}OH_2)_2(\mu\text{-}O_2CAr^{Tol})_2(O_2CAr^{Tol})_2(THF)_2]$	Fe_2	OH_2	2.326 2.398	-	-	3.043	80.2 º	*195*
$[Fe_2(\mu\text{-}OH)(\mu\text{-}OAc)_2(TACN)_2]ClO_4$	Fe_2	OH	1.987	-	-	3.317	113.1 º	*160*
$[Fe(H_2O)_2(^{Me2,BzIm}TACN)](OTf)_2$	Fe	-	-	OH_2	2.113 2.148	-	-	*154*
$[Fe(LN_3SMe)(H_2O)_3](OTf)_2$	Fe	-	-	OH_2	2.116 2.086 2.098	-	-	*155*
$[Fe(indH)(CH_3CN)(H_2O)_2](ClO_4)_2$	Fe	-	-	OH_2	2.145 2.163	-	-	*105*
$[Fe(H_2O)_6](C_{17}H_{13}O_7S)_2 \bullet 8H_2O$	Fe	-	-	OH_2	2.138 2.155 2.043	-	-	*156*
$[Fe(\kappa N\text{-}nicH)(H_2O)_4]$	Fe	-	-	OH_2	2.135	-	-	*157*
$[Fe(bpe)_4(H_2O)_2](TCNQ)_2$	Fe	-	-	OH_2	2.107 2.109	-	-	*158*

[a] TPA = tri-(2-pyridylmethyl)amine, 6-Me_3-TPA = tri-(6-methyl-2-pyridylmethyl)amine, $O_2CAr^{4F\text{-}Ph}$ = 2,6-di-(p-tolyl)benzoate, TACN = N,N',N''-trimethyl-1,4,7-triazacyclononane, ^{Me2,BzIm}TACN = 1-(2-methyl-1-benzimidazolyl)methyl-4,7-dimethyl-1,4,7-triazacyclononane, indH = 1,3-bis(2'-pyridylimino)isoindoline, $C_{17}H_{13}O_7S$ = bis(4',7-dimethoxyisoflavone-3'-sulfonate), nicH = pyridine-3-carboxylic acid, bpe = trans-1,2-bis(4-pyridyl)ethane, TCNQ = tetracyanoquinodimethane

Table 3.13. Selected distances from crystal structures of ferric (Fe^{III}) synthetic model complexes[a].

Complex	Fe / Fe_2	Core OH_x	Fe-O (Å)	Term. OH_x	Fe-O (Å)	Fe•••Fe (Å)	< Fe-O-Fe	References
$[Fe_2(\mu\text{-}OH)_2(H_2O)_2((CH_3)_2NC_7H_2NO_4)_2]$	Fe_2	OH	1.937 1.986	OH_2	2.033	3.118	105.3 º	*188*
$[Fe_2(\mu\text{-}OH)(\mu\text{-}OAc)_2(HBpz_3)_2]ClO_4$	Fe_2	OH	1.960 1.953	-	-	3.438	123.0 º	*196*
$[Fe_2(\mu\text{-}OH)_2(\mu\text{-}O_2CAr^{Tol})_2(O_2CAr^{Tol})_2(4\text{-}CNPy)_2]$	Fe_2	OH	1.978 1.945 1.997 1.945	-	-	2.831	92.4 º	*193*
$[Fe_2(L^{amine})_2(\mu\text{-}OH)]BPh_4$	Fe_2	OH	2.003 2.017	-	-	3.762	138.6 º	*197*
$[Fe_2(L^{NO2})_2(\mu\text{-}OH)]ClO_4$	Fe_2	OH	1.969 2.003	-	-	3.733	140.1 º	*198*
$[Fe_2(\mu\text{-}O)(OH)(OH_2)(TPA)_2](ClO_4)_3$	Fe_2	O	1.830 1.780	OH OH_2	1.914 2.041	3.389	138.9 º	*199*
$[Fe_2(\mu\text{-}O)(OH)(OH_2)(5\text{-}Et\text{-}TPA)_2](ClO_4)_3$	Fe_2	O	1.826 1.779	OH OH_2	1.907 2.049	3.346	136.3 º	*200*
$[Fe(tnpa)(OH)(PhCOO)]ClO_4$	Fe	-	-	OH	1.876	-	-	*201*
$K[FeH_31(OH)]$	Fe	-	-	OH	1.932 1.921	-	-	*202*
$[Fe_2(L^{Ph4}\text{-}O)(Ph_3CCO_2)(OH)](ClO_4)_2$	Fe_2	OR	2.051 2.008	OH	1.862	3.508	119.6 º	*203*
$[Fe(OH)(L^1)][K(DMF)_3]$	Fe	-	-	OH	1.857	-	-	*204*
$K[Fe0^{iPr}(OH)]$	Fe	-	-	OH	1.876	-	-	*205*
$[Fe_2(N\text{-}Et\text{-}HPTB)(NO)(OH)(DMF)_2](BF_4)_3$	Fe_2	OR	1.952 2.044	OH	1.817 1.823	3.621	130.0 º	*206*

Table 3.13. (continued) Selected distances from crystal structures of ferric (Fe^{III}) synthetic model complexesa.

Complex	Fe / Fe_2	Core OH_x	Fe-O (Å)	Term. OH_x	Fe-O (Å)	Fe•••Fe (Å)	<Fe-O-Fe	References
[Fe_2(N-Et-HPTB)$(OH)_2(DMF)_2$]$(BF_4)_3$	Fe_2	OR	1.979 2.044	OH	1.817 1.823	3.954	129.1 º	*207*
[$Fe_2(\mu$-OH)$_2(\mu$-O_2CAr^{4F-Ph})$(O_2CAr^{4F-Ph})_3(OH_2)$(2-Ph_2P(O)-py)]	Fe_2	OH	1.981 1.955 1.977 1.981	OH_2	2.099	2.973	98.2 º 97.4 º	*187*
[$Fe_2(\mu$-OH)$(OH_2)_2$(4-Ph-hxta)]	Fe_2	OR	2.028 1.989	OH_2	1.994	3.090	104.4 º	*189*
		OH	1.956				100.6 º	
[$Fe_2(\mu$-OH)$_2(OH_2)_2$(Dipic)$_2$]	Fe_2	OH	1.937 1.993	OH_2	2.021	3.089	103.6 º	*190*
[Fe_2(μ-OH)$_2$(μ-O_2CAr^{Tol})$(O_2CAr^{Tol})_3(OH_2)$(Hdmpz)$_2$]	Fe_2	OH	1.945 1.958 2.013 1.953	OH_2	2.013	2.996	100.3 º	*191*
[Fe_2(μ-O_2)$(Ph_3PO)_2$(N-Et-HPTB)]$(BF_4)_3$	Fe_2	OR OO	1.991 1.881	-	-	3.463	120.8 º	*109*
[Fe_2(μ-O_2)(μ-O_2CPh)(Ph-bimp)]$(BF_4)_2$	Fe_2	OR	2.018 2.001	-	-	3.327	111.7 º	*94*
		OO	1.944 1.864					
[Fe_2(μ-O_2)(μ-$O_2CCH_2Ph)_2${HB(pz′)$_3$}]	Fe_2	OO	1.881 1.877	-	-	4.007	-	*91*
[Fe_2(6Me_2-BPP)$_2(\mu$-OH)$(\mu$-O_2)](OTf)	Fe_2	OH	1.943 2.006	-	-	3.395	118.6 º	*103*
		OO	1.887 1.867					

[a]$(CH_3)_2NC_7H_2NO_4$ = bis[4-dimethylamino-2,6-pyridinedicarboxylate], $HBpz_3$ = hydrotris(1-pyrazolyl)borate, O_2CAr^{Tol} = 2,6-di-(p-tolyl)benzoate, 4-CNPy = 4-cyanopyridine, L^{amine} = 2,2'-(2-methyl-2-(pyridin-2-yl)propane-1,3-diyl)bis(azanediyl)bis(methylene)diphenol, L^{NO2} = 2,2' -(2-Methyl-2(pyridine-2-yl)propane-1,3diyl)bis(azanediyl)-bis(methylene)bis(4-nitrophenol), TPA = tri-(2-pyridylmethyl)amine, 5-Et-TPA = 5-ethyl-tri-(2-pyridylmethyl)amine, tnpa = tris(6-neopentylamino-2-pyridylmethyl)amine), H_31 = tris[(N'-tert-butylureaylato)-N-ethy]amine, L^{Ph4}-O = N,N,N′,N′-tetrakis[(1-methyl-2-phenyl-4- imidazolyl)methyl]-1,3-diamino-2-propanolate), L^1 = tris(1-phenyl-2(4-tert-butylanaline))amine, 0^{iPr} = Tris(N-isopropylcarbamoylmethyl)amine, N-Et-HPTB = N,N,N′,N′- tetrakis[2-(1-ethylbenzimidazolyl)]-2-hydroxy-1,3-diaminopropane, O_2CAr^{4F-Ph} = 2,6-di-(p-tolyl)benzoate, 2-$Ph_2P(O)$-py = 2-Pyridyldiphenylphosphine oxide, 4-Ph-hxta = 2- hydroxy-5-phenyl-l,3-xylylenedimethanamine-N,N,N',N'-tetraacetate, Dipic = 2,6-pyridinedicarboxylate, O_2CAr^{Tol} = 2,6-di-(p-tolyl)benzoate, Hdmpz = 3,5-dimethylpyrazole, Ph-bimp = 2,6-bis[bis{2-(1-methyl- 4,5-diphenylimidazolyl)methyl}aminomethyl]-4-methylphenolate, pz' = 3,5-bis(isopropyl)- pyrazole, $6Me_2$-BPP = N,N-bis(6-methyl-2-pyridylmethyl-3-amino-propionic acid

Chapter 4 : An Unprecedented (*μ*-1,1-Peroxo)diferric Structure for the Reactive Orange Peroxo Intermediate of the Nonheme *N*-Oxygenase CmlI

4.1 – Introduction

Nonheme diiron enzymes are capable of facilitating a variety of difficult chemical transformations *via* oxygen activation, including C–H bond hydroxylation, C–C bond desaturation, the generation of alkanes from aldehydes, and *N*-oxygenation of aryl amine substrates, among others.[4, 6, 7, 9-11, 14, 15] The diiron cluster-containing *N*-oxygenase CmlI is a member of this latter class. It serves as a tailoring enzyme on the non-ribosomal peptide synthetase biosynthetic pathway that is responsible for producing the antibiotic chloramphenicol in the soil bacterium *Streptomyces venezuelae*.[64, 127, 225-228] CmlI catalyzes a six-electron oxidation of the aryl-amine precursor to form the aryl-nitro group of the active antibiotic (Figure 4.1).

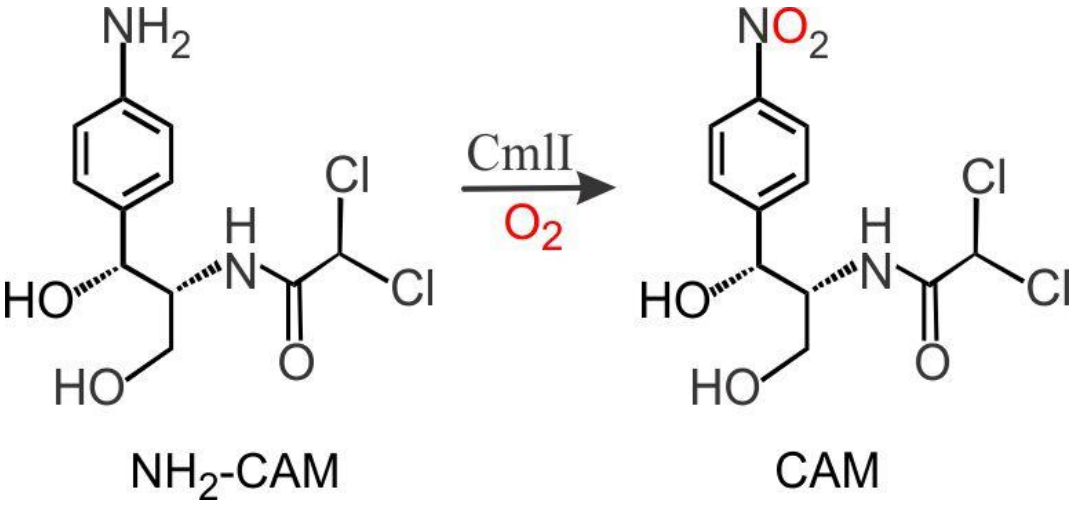

Figure 4.1. Six-electron oxidation of the aryl-amine precursor to the aryl-nitro-containing final product chloramphenicol, catalyzed by the nonheme diiron cluster enzyme CmlI.

Characterization of the aryl-amine conversion by CmlI has provided the strongest evidence to date for a new type of oxidant in diiron-cluster-mediated oxygenation reactions.[124] The canonical scheme for dioxygen activation by diiron-cluster-containing enzymes is based on the well-studied diiron enzyme soluble methane monooxygenase (sMMO). Dioxygen binds to the diferrous form of the enzyme to generate a peroxo-diferric intermediate (**P**), which then undergoes O–O bond cleavage to generate a high-

valent bis(μ-oxo)diiron(IV) cluster (**Q**). **Q** is the reactive intermediate responsible for C–H bond activation in the sMMO catalytic cycle. The R2 subunit of ribonucleotide reductase (RNR) from *E. coli* is another canonical diiron enzyme, which activates O_2 to generate a functionally essential tyrosyl radical. This oxidation is carried out by a high-valent oxidant called **X** with a (μ-oxo)iron(III)iron(IV) core. [57, 229, 230] sMMO and RNR are the only enzymes with diiron active sites for which high-valent iron oxidants have been identified, but they have been widely postulated to be the reactive intermediate formed in most diiron oxygenases.

Diferric-peroxo (**P**) species have been overlooked as oxidants in their own right, which is not surprising, given the types of **P** intermediates found in the classical diiron oxygen activating enzymes, sMMO,[69, 70, 231] RNR R2,[68, 116, 182] and Δ9D.[67] Analysis of these intermediates has suggested that diiron peroxos universally assume the *cis* μ-1,2-peroxo binding mode (Figure 4.2) and that **P** intermediates are not oxidants on the native catalytic cycles except in rare cases of easily oxidized substrates.[22, 23] These assumptions are bolstered by several synthetic peroxo-diferric model complexes for which the X-ray crystal structures are known.[91, 94, 103, 109, 232] These complexes are supported by ligands with N and O rich donors to mimic the histidine and carboxylate rich active sites of the enzymes, and all have been found to contain a *cis* μ-1,2-peroxo binding mode. In addition, these synthetic complexes have been extensively characterized, which provides a set of spectroscopic parameters to which enzymatic **P** species can be compared. However, these biomimetic synthetic peroxos are fairly stable and generally unreactive, and therefore do not provide much insight into the mechanism of oxidation by a **P** species.

The first reactive **P** intermediate was discovered in 2005 by Lippard and co-workers,[22] when they demonstrated that the **P** species of sMMO would directly react with ether and alcohol substrates. However, definitive structural characterization of this **P** intermediate is unavailable. In 2009, a hyperstable ($t_{1/2}$ > 24 hrs at room temperature) *cis* μ-1,2-peroxo species was discovered and characterized[65] from the human enzyme

deoxyhypusine hydroxylase (hDOHH) that decays concomitant with the formation of the native hydroxylated product, demonstrating that stable *cis*-μ-1,2-peroxo species can be activated.[65] In 2013, an example of a peroxo-diferric species serving as the active oxidant was reported.[25] This peroxo species, on the cycle of the enzyme from aldehyde deformylating oxygenase (cADO), was spectroscopically characterized as a peroxy-hemiacetal intermediate, or a diferric peroxo bound to substrate. A final set of examples comes from the related enzymes toluene-4-monooxygenase (T4MO) and toluene/o-xylene monooxygenase (ToMO), which fall into the diiron oxygenase subclass bacterial multicomponent monooxygenases (BMM) with sMMO. A recent crystal structure from T4MO was obtained of an arylperoxo species bound in a μ-η^2:η^2 configuration to the diiron cluster (T4MO$^{\mathbf{P}\eta\mathbf{2}}$),[28] which was shown *in crystallo* to be an intermediate for the hydroxylation of toluene. The putative **P** intermediate of ToMO (ToMO$^{\mathbf{P}}$) isolated from the wild type enzyme is a short-lived ($t_{1/2}$ ~ 15 s) diferric species that appears to be active towards arene substrates, but is identified only by Mössbauer spectroscopy, with no corroborating spectroscopic data (curiously, ToMO$^{\mathbf{P}}$ lacks an optical signature).[24] The Mössbauer parameters significantly differ from those observed for sMMO and other *cis* µ-1,2-peroxo-diferric intermediates, and the structure remains unknown. An inactive **P** intermediate has also been generated from the T201S mutant of ToMO, with spectroscopic signatures that match those of sMMO.[233] These examples provide evidence that diferric peroxos can serve as the active oxidant instead of a high valent species such as **Q** or **X** for some types of substrates.

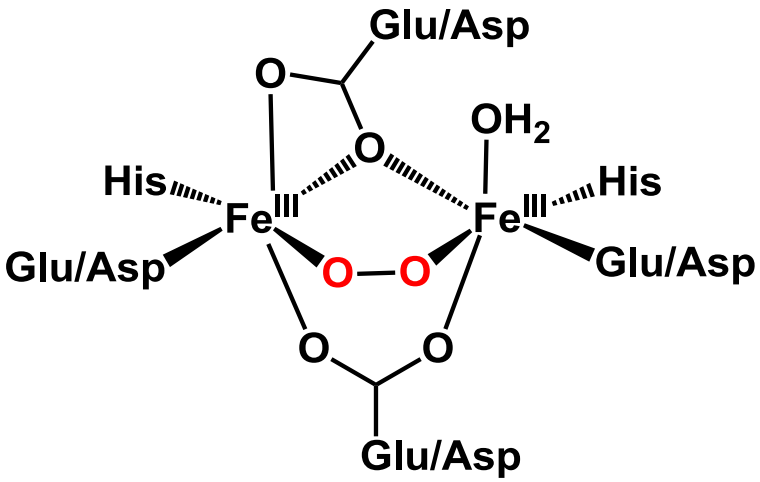

Figure 4.2. General *cis*-(μ-1,2-peroxo)diferric intermediate structure in diiron enzymes.

In the past, geometric assignments of enzymatic **P** intermediates have been largely based on the comparison of their spectroscopic parameters to those of structurally characterized synthetic **P** species. Recently, the X-ray crystal structures of enzymatic **P** intermediates have been determined for hDOHH[17], a truncated CmlI (**CmlIΔ33**),[35]and T4MO (T4MO$^{\mathbf{P}}$ and T4MO$^{\mathbf{P}\eta\mathbf{2}}$).[28, 79] The hDOHH crystal structure confirms the *cis* μ-1,2-peroxo binding mode earlier assigned by resonance Raman studies, although the Fe•••Fe distance in hDOHH suggests that the crystallized enzyme may have suffered from photoreduction by the X-ray beam, which is a well known issue in metalloenzyme crystallography.[76-78] Therefore, the specific distances should be viewed with some skepticism. The **CmlIΔ33** crystallized **P** also shows a *cis*-μ-1,2-peroxo binding mode, but the species does not react with substrate, nor does it have the same UV-vis absorption spectrum as the known active **P**. Consequently, the crystallized CmlI peroxo is not thought to be the active or native peroxo. Two different peroxo species have been crystallized from the T4MO system, with different peroxo binding modes.T4MO$^{\mathbf{P}}$ was prepared by soaking crystals of diferric T4MO in H_2O_2, resulting in a *cis*-μ-1,2-peroxo binding geometry. T4MO is active *via* the peroxide shunt,[82] though the reaction is ~600 times slower than that carried out with the native biological reductants and O_2. The more

recent crystal structure of T4MO$^{\mathbf{P}\eta^2}$, was prepared from soaking diferrous crystals of T4MO toluene, then exposing to O_2. As mentioned above, this resulted in a reactive μ-η^2:η^2-arylperoxo intermediate, distinct from T4MO$^{\mathbf{P}}$. Of the three crystallized enzymatic μ-1,2-peroxo **P** species, only hDOHH$^{\mathbf{P}}$ is shown to be active in the native cycle. The high stability and low reactivity of many of the *cis*-μ-1,2 **P** species (synthetic and enzymatic), suggest that this geometry may not be the active species. However, the new evidence that enzymatic **P** species, like T4MO$^{\mathbf{P}\eta^2}$, are the active oxidant in some enzyme cycles implies that alternative types of peroxo intermediates exist.

In 2015, we published the first evidence for a distinct **P** species from CmlI.[15] Kinetic studies showed that **CmlI$^{\mathbf{P}}$** reacts rapidly with substrates to yield oxygenated products, but also that it is unusually stable in the absence of substrate, exhibiting a half-life of ~3 h at 4 ºC. This long lifetime allowed some of the spectroscopic features of **CmlI$^{\mathbf{P}}$** to be determined in detail, revealing that it is distinct from all but one of the previously reported peroxo intermediates. The *N*-oxygenase AurF was found to have a **P** species (AurF$^{\mathbf{P}}$) with similar electronic absorption maximum and Mössbauer parameters as **CmlI$^{\mathbf{P}}$**, however, the half-life of AurF$^{\mathbf{P}}$ is much shorter (~7 min at 4 ºC), and structural characterization is unavailable.[59] In contrast to the absorption of the typical *cis*-μ-1,2 **P** species at > 700 nm, **CmlI$^{\mathbf{P}}$** and AurF$^{\mathbf{P}}$ have significant absorption maxima at 500 nm. Resonance Raman (rR) experiments of **CmlI$^{\mathbf{P}}$** showed a ν(O–O) at 791 cm^{-1}, which is much lower than that of any known biological or synthetic diiron-cluster **P** species. The commonly observed (μ-1,2-peroxo)-diferric species generally has a ν(O–O) range of 840 – 925 cm^{-1}. Mössbauer analysis showed that **CmlI$^{\mathbf{P}}$** has two inequivalent Fe centers while (μ-1,2-peroxo)-diferric species generally have two similar iron(III) sites.[15]. Unfortunately, there were no diiron peroxo model complexes available to allow a definitive structural assignment based on this spectroscopic data. Consequently, the **CmlI$^{\mathbf{P}}$** peroxo structure was suggested to be μ-η^1:η^2 based on the similarity of its rR parameters to those of mixed-metal peroxo complexes that have comparably low ν(O–O) frequencies.[234-237]

In the current study, we have used X-ray absorption spectroscopy (XAS) and rR spectroscopy to structurally characterize three different states of CmlI, including **CmlI^{P}**. A new view of the structure is now presented based on this spectroscopic investigation. Our studies further refine the O_2 binding mode of **CmlI^{P}**, identifying a μ-1,1-peroxo species with a supporting μ-oxo bridge. This novel diiron core has consequences on the reactivity of the diiron cluster and supports the idea of that reactive peroxo intermediates can function within the canonical diiron framework.

4.2 – Experimental Procedures

4.2.1 – Overexpression and Purification of CmlI.

Expression of CmlI was performed in *E. coli* BL21(DE3) in M9 minimal medium in the presence of 100 μg/mL ampicillin. Cells were grown to an OD ~ 1.0 and induced with 150 μM IPTG and 50 μM $FeCl_3$ at which point the temperature was lowered to 20 °C and grown for an additional 15 h. Cells were harvested by centrifugation and stored at -80 °C until further use. Cells were resuspended in 50 mM potassium phosphate pH 7.4, 300 mM NaCl, 10 mM imidazole, lysed via sonication, and centrifuged. The resulting supernatant was loaded onto a Ni nitrilotriacetic acid column (Qiagen) equilibrated in the same buffer. After loading, the column was washed with the above buffer containing 20 mM imidazole, and protein was eluted in the same buffer containing 300 mM imidazole. Protein-containing fractions were pooled and dialyzed against 50 mM Bicine pH 9 and stored at -80 °C until further use. CmlI concentrations were determined by the calculated extinction coefficient (ε_{280} = 50 mM^{-1} cm^{-1}).

4.2.2 – CmlI^{Ox} Sample

As-isolated CmlI (**CmlI^{Ox}**) was thawed and concentrated to 3-4 mM by centrifugal filtration (Amicon Ultra-0.5 mL centrifugal filters, kDa 10 cutoff), and then mixed with glycerol to a final concentration of ~20% v/v. After loading into an XAS cup, the sample was flash frozen with LN_2. For the generation of D_2O samples (**CmlI^{Ox}-D_2O**),

a minimum of 5 concentration and re-dilution cycles was used to exchange into 50 mM Bicine pD 9 prepared with D_2O. No glycerol was used in D_2O-containing samples.

4.2.3 – Generation of CmlI^R and CmlI^P Samples for XAS

An aliquot of CmlI was degassed on an Ar Schlenk line and then brought into an anaerobic chamber where the reductant sodium hydrosulfite (10x molar excess) and the reduction mediator methyl viologen (20 µM final concentration) were added to the protein. The protein was stirred for 35 min to ensure the blue color from the methyl viologen remained, indicating complete reduction. The sodium hydrosulfite and methyl viologen were then removed by passing the CmlI through a PD-10 size exclusion column equilibrated with 50 mM Bicine, pH 9. Several fractions were collected and concentrated to 3-4 mM enzyme anaerobically using a centrifuge located within the anaerobic chamber and spin filters as described above.

Reduced: While in the anaerobic chamber, 400 µl of reduced enzyme was mixed with 100 µl glycerol and then loaded into an XAS cup (**CmlI^R**). The cup was then sealed in a large Reacti-Vial (Thermo Scientific). The vial was brought out of the chamber and submerged in LN_2. Only after the sample was frozen was the vial opened and the sample stored under LN_2.

Peroxo: A reduced sample was removed from the anaerobic chamber in a Reacti-Vial and then the peroxo intermediate was generated by blowing pure O_2 over the surface of the sample while stirring vigorously for 3 min. Glycerol was added to final concentration of ~20% by volume, and then the solution was placed in an XAS cup and frozen in LN_2. All work outside of the anaerobic chamber was done on ice and/or in a 4 °C cold room.

4.2.4 – Generation of CmlI^{ox} and CmlI^{P} Samples for rR.

CmlI^{Ox} and **CmlI^{P}** samples for rR were prepared in the same manner as the corresponding XAS samples, except that samples were loaded into flat-bottomed NMR tubes.

D_2O: **CmlI^{P}** in D_2O (**CmlI^{P}-D_2O**) was generated as described above, except that the enzyme was passed through a PD-10 size exclusion column equilibrated with buffer prepared with D_2O (50 mM Bicine, pD 9) after the reduction step. Concentration and re-dilution with D_2O buffer a minimum of two times ensured nearly complete isotope exchange. Samples prepared with D_2O did not contain glycerol.

$^{18}OH_2$: **CmlI^{P}** and **CmlI^{Ox}** in $^{18}OH_2$ were prepared in the same manner as their corresponding standard water samples, with the addition of several concentration and dilution cycles to exchange the $^{16}OH_2$-containing buffer with the $^{18}OH_2$-containing buffer. In the **CmlI^{P}** preparation, the exchange was performed on the diferrous enzyme in an anaerobic chamber. To prepare $^{18}OH_2$-containing buffer, 2 mL of standard buffer (50 mM Bicine, pH 9) was lyophilized for 24 h. The resulting salts were then dissolved in 2 mL $^{18}OH_2$ water, either anaerobically or on the bench top, as required by the sample.

4.2.5 – X-ray Absorption Spectroscopy

Iron K-edge X-ray absorption spectra were collected on SSRL beam line 7-3 and 9-3 using a 30 element and 100 element (respectively) solid state Ge detector (Canberra) with a SPEAR storage ring current of ~500 mA at a power of 3.0 GeV. The incoming X-rays were unfocused using a Si(220) double crystal monochromator, which was detuned to 40% of the maximal flux to attenuate harmonic X-rays. For **CmlI^{R}** and **CmlI^{Ox}**, 16 and 12 scans, respectively, were collected. For **CmlI^{P}**, two samples with 9 and 10 scans were collected and averaged. All scans were between 6882 eV and 8000 eV at ~10 K using an Oxford Instruments CF1208 continuous flow liquid helium cryostat. An iron foil was placed in the beam pathway prior to the ionization chamber I_0 and scanned concomitantly

for an energy calibration, with the first inflection point of the edge assigned to 7112.0 eV. A 3 μm Mn filter was used for the collection of **CmlI^{R}** and **CmlI^{Ox}**, and a "9" μm Mn filter (3 μm + 6 μm) and a Soller slit were used to increase the signal to noise ratio of the spectra for **CmlI^{P}**. Photoreduction was monitored by scanning the same spot on the sample twice and comparing the first derivative peaks associated with the edge energy during collection.

The detector channels from the scans were examined, calibrated, averaged, and processed for EXAFS analysis using EXAFSPAK [143] to extract χ(k). Theoretical phase and amplitude parameters for a given absorber-scatterer pair were calculated using FEFF 8.40 [144] and were utilized by the "opt" program of the EXAFSPAK package during curve fitting. Parameters for each species were calculated using a model derived from the crystal structure of analogous enzyme AurF (PDB code 3CHH). In all analyses, the coordination number of a given shell was a fixed parameter and was varied iteratively in integer steps, while the bond lengths (R) and mean-square deviation (σ^2) were allowed to freely float. The amplitude reduction factor S_0 was fixed at 0.9, while the edge-shift parameters E_0 was allowed to float as a single value for all shells. Thus, in any given fit, the number of floating parameters was typically equal to (2 x num shells) + 1. **CmlI^{R}** has a k range of 2 – 14 Å^{-1} and **CmlI^{Ox}** and **CmlI^{P}** have a range of 2 – 15 Å^{-1}.

Pre-edge analysis was performed on data normalized in the "process" program of the EXAFSPAK package, and pre-edge features were fit as described elsewhere [44] between 7108 eV to 7118 eV using the Fityk[145] program with pseudo-Voigt functions composed of 50:50 Gaussian/Lorentzian functions.

4.2.6 – Resonance Raman Spectroscopy

Resonance Raman spectra were obtained at ~4 ºC with excitation at 561 nm (100 mW at source, Cobolt Jive 04-01 series) through the sample in a flat bottom NMR tube using a 90^{o} backscattering arrangement (parallel to the slit direction). The collimated Raman scattering was collected using two Plano convex lenses (f = 12 cm, placed at an

appropriate distance) through the appropriate long pass edge filter (Semrock) into an Acton AM-506M3 monochromator equipped with a Princeton Instruments ACTON PyLON LN/CCD-1340x400 detector. The detector was cooled to -120 ^{o}C prior to the experiments. Spectral calibration was performed using the Raman spectrum of acetonitrile/toluene 50:50 (v:v). The spectra of **CmlI^{Ox}** were collected with 180, 450 and 225 scans with acquisition times of 5s, 2s and 4s for the ^{16}O, ^{18}O and D_2O samples, respectively, for a total of 15 min collections. The spectra of **CmlI^{P}** were collected with 180 scans with an acquisition time of 10s for the ^{18}O and D_2O samples for a total of 30 min collections, and 225 scans with an acquisition time of 4s for the ^{16}O samples for a total of 15 min. The collected data was processed using Spekwin32,[238] and a multipoint baseline correction was performed for all spectra.

4.3 – Results

4.3.1 – XAS Analysis of CmlI^{R}, CmlI^{Ox} and CmlI^{P}

X-ray absorption near edge structure (XANES) analysis was utilized to gain structural insight into the active sites of several CmlI species: **CmlI^{R}**, **CmlI^{Ox}**, **CmlI^{P}** (Figure 4.3). This analysis provides information about the oxidation state (from the Fe K-edge energy) and the symmetry of the target metal centers (from the pre-edge peak area). The K-edge energy for **CmlI^{R}** is 7122.1 eV, which falls in the range typical for diferrous species (7121 eV – 7123 eV).[13, 36-38] **CmlI^{Ox}** has a K-edge energy of 7124.1 eV, which is two electron volts higher than that of the reduced species. This difference in K-edge energy is consistent with the difference observed between diferrous and diferric states in other diiron enzyme systems.[36, 38, 139] The oxygenated **CmlI^{P}** has a K-edge of 7124.9 eV, suggesting that **CmlI^{Ox}** and **CmlI^{P}** have the same oxidation state with slightly different electronic environments. **CmlI^{P}** has an energy lower than that found for the μ-1,2-peroxo species of hDOHH (hDOHH^{P}, 7125.6 eV)[36] but one that falls in the range of synthetic

diferric μ-1,2-peroxo complexes with an additional single atom bridge (7123 eV to 7126 eV). [105, 110-112]

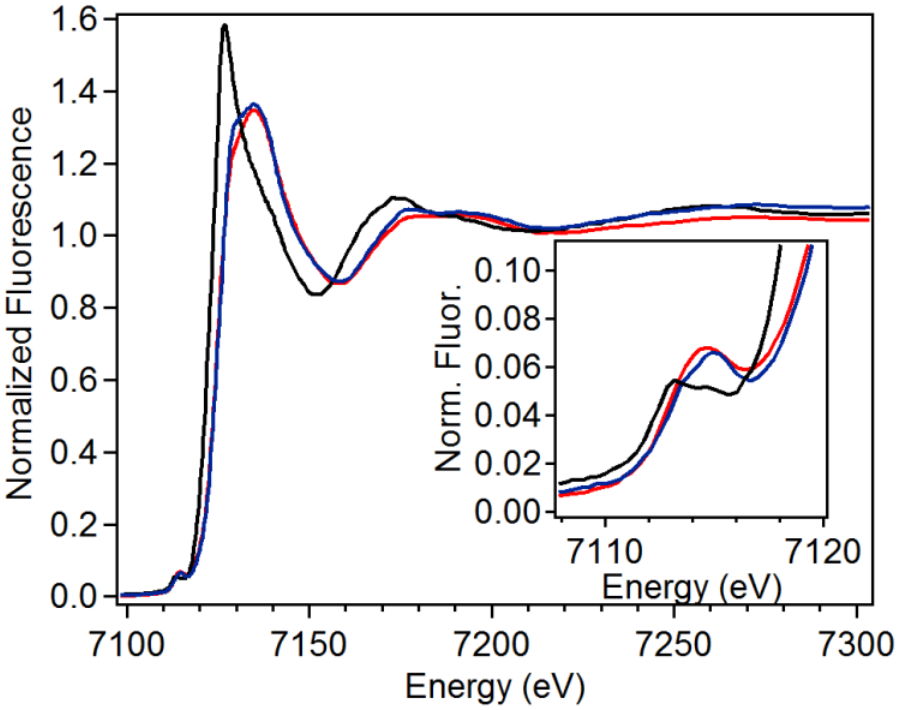

Figure 4.3. XANES region for **CmlI^{R}** (solid black), **CmlI^{Ox}** (solid blue) and **CmlI^{P}** (solid red). Inset: Magnification of the pre-edge region.

The pre-edge peak in the XANES region corresponds to a formally forbidden 1s →3d transition in first row transition metal complexes.[147] The intensity of the pre-edge peak increases as the metal center is distorted away from centrosymmetry, which is reflected in a larger pre-edge peak area.[186]. The fits of the pre-edge are summarized in Table 4.1 and individual fits of the pre-edge region are shown in Figure 4.13 – Figure 4.15. The pre-edge feature of **CmlI^{R}** is fit with pseudo-Voigt functions that yield an area of 8.4 units, which falls between values for five-coordinate (~11 units) and six-coordinate (~5 units) diferrous centers,[43] and is similar to the recently reported value for six-coordinate diferrous CmlA.[38] The pre-edge area of **CmlI^{Ox}** is 14.5 units, consistent with a six-coordinate (μ-oxo)diferric center (~14.5 units).[44, 85]Interestingly, **CmlI^{P}** has a pre-edge area of 19.2 units, which is significantly higher than that of hDOHH^{P} (12.4 units)[36]

and those found for synthetic six-coordinate diferric-peroxo complexes (13 – 16 units)[105, 110, 112] and close to the range found for mononuclear iron(IV)-oxo species (20 to 30 units). However Mössbauer spectroscopy has established **CmlI^{P}** to have an antiferromagnetically coupled high spin (S = 5/2) diferric cluster,[15]so that the last option can be discarded. As XAS measurements provide averaged information on all the Fe present in the sample, one way to interpret the **CmlI^{P}** pre-edge area is to consider its diferric active site as consisting of one five-coordinate Fe center (average of ~24 units) and one six-coordinate Fe center (average of ~14.5 units)., which would give rise a pre-edge area of 19.3 units, consistent with the value of 19.2 units obtained for **CmlI^{P}**.

Table 4.1. XANES analysis of CmlI Species.

Species	**K-edge (eV)**	**Pre-edge Area (units)**
CmlI^{R}	7122.1	8.4
CmlA^{R} [a]	7121.5	8.4
CmlI^{Ox}	7124.1	14.5
CmlA^{Ox} [b]	7126.8	13.4
CmlI^{P}	7124.9	19.2
hDOHH^{P}	7125.6	12.4

[a]Data from ref [38], [b]data from ref [139], [c]data from ref [36].

Extended X-ray absorption fine structure (EXAFS) analysis provides information about the identity of the atoms in close contact to the iron centers and their distance from the iron. The final fits of each species can be found in Table 4.2, and full fits for individual species can be found in the supplementary information (Figure 4.16 – Figure 4.18, Table 4.5 – Table 4.7). Presented below is the EXAFS analysis of **CmlI^{R}**, **CmlI^{Ox}**, and **CmlI^{P}**, which are used to generate a structural model of each species.

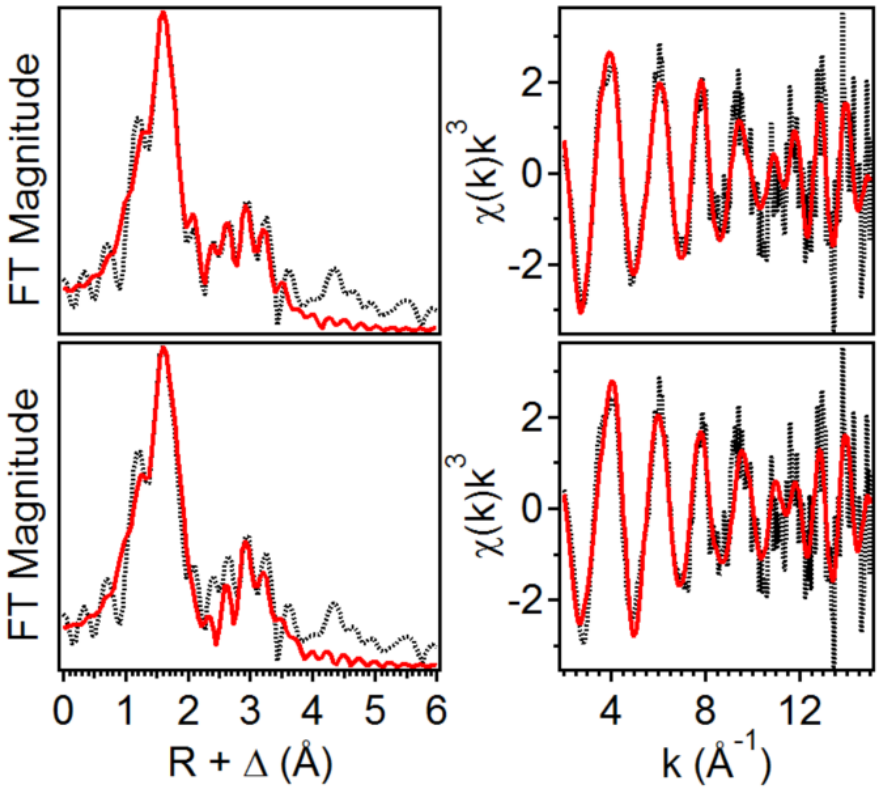

Figure 4.4. Left Column: Fourier transforms of the EXAFS data (black dotted) with best fit (solid red) for **CmlI^{P}** (top; Table 4.7, fit 23) and **CmlI^{P}** without an Fe•••O at 2.82 Å (bottom; Table 4.7, fit 26), k range = 2 – 15 Å^{-1}. Right column: unfiltered EXAFS data (black dotted) with best fit (red solid) for **CmlI^{P}** (top; Table 4.7, fit 23) and **CmlI^{P}** without an Fe–O at 2.82 Å (bottom; Table 4.7, fit 26).

The Fourier transformed (FT) EXAFS data of the various CmlI samples all show an intense feature at R + Δ < 2 Å that is assigned to the scattering atoms of the primary coordination sphere, while the weaker features observed at R + Δ > 2 Å are generally associated with second sphere interactions. In the final fit of **CmlI^{R}**, the prominent feature consists of 1 Fe–O/N at 1.94 Å and 5 Fe–N/O scatterers at 2.10 Å (Table 4.2). The distance at 2.10 Å is consistent with protein-derived carboxylate and histidine ligands, as we have established previously.[36, 38] These assignments are based on metal-ligand distances found in the crystal structures of nonheme diiron proteins,[14, 18, 31, 34, 53, 149-152] including the structure of diferrous CmlI.[35] The shorter Fe–N/O distance at 1.94 Å is assigned to a μ-OH bridge based on comparison to the Fe–O distances associated with

the μ-hydroxo ligand in the reduced clusters of CmlA[38] and synthetic (μ-hydroxo)diferrous complexes.[92, 159, 160]

Beyond the primary sphere ligands, there is a C scatterer at 2.58 Å, consistent with the carbon atom from a bidentately bound carboxylate ligand on each Fe. Such carbon scatterers have also been observed in the EXAFS analyses of both diferrous[38] and diferric[139] CmlA, in agreement with their crystal structures.[18, 38] The Fe•••Fe distance is found at 3.35 Å but has a mean squared deviation (σ^2) of 9.90×10^{-3} Å^2. This high value seems to suggest that the Fe is not rigidly fixed in the active site, a feature that may not be specific to CmlI. Similarly large σ^2 values have been reported in the EXAFS fits of other reduced diiron enzymes such as Fe(II)Fe(III) uteroferrin (12×10^{-3} Å^2) and Fe(II)Fe(II) MMOH (13.3×10^{-3} Å^2).[46, 164] The remaining Fe•••C shells at 3.14 Å and 3.99 Å are consistent with scattering derived from the outer shells of imidazole rings of the histidine ligands. The shell at 2.98 Å is consistent with the carbonyl carbon of carboxylate ligands bound to the diiron core, which are observed in the crystal structure of CmlI.[35] These carbon scatterers are also observed in the EXAFS analysis of sMMOH,[46] RNR,[57] and Δ^9D.[162]

The best fit to the EXAFS data for diferric **CmlI^{Ox}** yields three shells of scatterers, with one Fe–O/N at 1.83 Å, two Fe–O/N at 2.00 Å, and three Fe–N/O at 2.15 Å (Table 4.2). The longer 2.15 Å shell is consistent with histidine ligation and longer monodentate carboxylate interactions, and a shorter 2.00 Å distance shell is consistent with terminal aqua ligands and shorter carboxylate interactions, including those from μ-1,3 bridges. Additionally, **CmlI^{Ox}** has a much shorter Fe–O distance at 1.83 Å, which is consistent with a μ-oxo bridge. The assignment of an oxo bridge at 1.83 Å would also be consistent with the large pre-edge area associated with **CmlI^{Ox}** presented earlier. Unlike for **CmlI^{R}**, the fit for **CmlI^{Ox}** does not require a carbon scatterer at ~2.6 Å, suggesting that the bidentate carboxylate ligands found in **CmlI^{R}** have changed binding modes. Notably, the Fe•••Fe distance is the same as that found for the reduced state, at 3.32 Å, a phenomenon that has been observed in several systems.[36, 38] The carbon shells fit at 3.57

Å and 4.28 Å are derived from histidine ligands. The 4.28 Å distance is from a well-known multiple scattering interaction of the imidazole ring whereas the distance at 3.57 Å can be assigned to the C_β of an N_δ-bound histidine ligand. This scattering distance has also been observed in hDOHH and CmlA [36, 38] and is consistent with the histidine ligation observed in the crystal structure of CmlI.

Table 4.2. Fit parameters for CmlI species.

	Fe-N/O			Fe-O/N			Fe•••Fe			Fe•••C			GOF		
Fit	**N**	**R(Å)**	**$\sigma^2(10^{-3})$**	**N**	**R(Å)**	**$\sigma^2(10^{-3})$**	**N**	**R(Å)**	**$\sigma^2(10^{-3})$**	**N**	**R(Å)**	**$\sigma^2(10^{-3})$**	**E_o**	**F**	**F'**
CmlI^{R}	5	2.10	5.02	1	1.94	5.35	1	3.35	9.90	1	2.58	1.35	-12.0	206	470
										3	2.98	2.76			
										5	3.14	2.48			
										4	3.99	1.15			
CmlI^{Ox}	3	2.15	1.73	2	2.00	0.97	1	3.32	3.38	4	3.57	1.39	-3.79	196	488
				1	1.83	2.71				3	4.28	1.04			
CmlI^{P}	3	2.13	2.50	2	1.98	2.09	1	3.35	4.47	3	3.14	4.87	-1.86	111	456
				1	1.83	4.05				3	3.56	1.46			
				1	2.82	1.50				3	4.28	5.12			

The best fit for **CmlI^{P}** is similar to that of **CmlI^{Ox}** except for the inclusion of a scatterer at 2.8 Å (Table 4.2). The major FT peak at R + Δ ~ 1.7 Å (Figure 4.4, top left) consists of one Fe–O/N at 1.83 Å, two Fe–O/N at 1.98 Å, and three Fe–N/O at 2.13 Å. The assignments of these distances correspond to those for **CmlI^{Ox}**, including the 1.83-Å oxygen scatterer as a μ-oxo bridge. The only difference is that the proximal oxygen atom of the peroxo moiety would fall in the shell at 1.98 Å in a manner similar to what is observed for hDOHH^{P}.[36] The Fe•••Fe distance is 3.35 Å, very similar to those observed for **CmlI^{Ox}** and **CmlI^{R}**. Three shells of carbon scatterers found at 3.14 Å, 3.56 Å, and 4.28 Å are consistent with histidine ligands.

The most notable feature of the **CmlI^{P}** fit is the requirement for a Fe•••O scatterer at 2.82 Å, as demonstrated by the better fit of the FT peaks centered at ~ 2.5 Å (Figure 4.4, compare top to bottom) as well as the increase in the goodness-of-fit value upon deletion of this scatterer (see Table 4.7, fit 23 versus fit 26). This scatterer is not required in the fits for **CmlI^{Ox}**, **CmlI^{R}** or decayed **CmlI^{P}** samples and is therefore unique to, and diagnostic of, **CmlI^{P}**. Such a scatterer has also not been reported before in EXAFS analysis of any diferric-peroxo species. The 2.82-Å scatterer has a σ^2 value of 1.50×10^{-3} Å^2, which is remarkably low for a low-Z atom at such a long distance, implying that the O scatterer is held relatively well fixed in space. In addition, it must also be positioned equidistant to the two Fe centers; otherwise, the higher σ^2 value should be observed. Reducing N to 0.5 results in a σ^2 value of -1.50×10^{-3} Å^2 (Table 4.7, fit 29), which supports the assignment of a 2.82-Å scatterer that is equidistant from each Fe center. A logical assignment for this scatterer would be to the distal oxygen of peroxo bridge that is not bound in a μ-1,2- mode.

4.3.2 – Resonance Raman Characterization of CmlI^{Ox} and CmlI^{P}.

Resonance Raman experiments were performed to confirm the presence of a μ-oxo bridging ligand in **CmlI^{P}**, as suggested by the EXAFS analysis. The UV-vis and EXAFS data for **CmlI^{Ox}** point to the presence of a (μ-oxo)diferric cluster. To further verify this assignment, the rR spectrum of **CmlI^{Ox}** was obtained in $^{16}OH_2$ water and

showed a peak at 487 cm^{-1} (Figure 4.5, left panel). This feature downshifted 18 cm^{-1} to 469 cm^{-1} in a sample of **CmlI^{Ox}** prepared in $^{18}OH_2$ (Figure 4.5, middle panel). Both the location of the peak and the magnitude of the shift are consistent with an assignment to ν_s(Fe-O-Fe), the symmetric Fe–O–Fe stretch of a (μ-oxo)diferric center. For comparison, the ν_s(Fe–O–Fe) vibrational mode for the (μ-oxo)diferric center in CmlA was also observed at a similar value of 481 cm^{-1} with a ^{18}O shift of 17 cm^{-1}.[139]

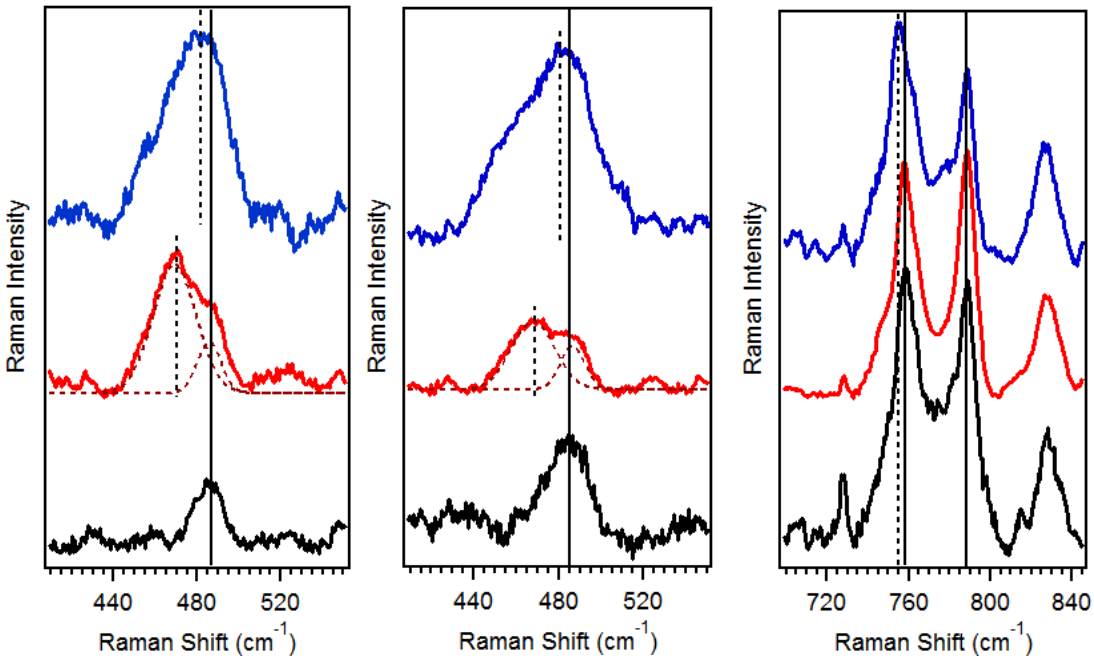

Figure 4.5. Resonance Raman spectra of **CmlI^{Ox}** (left), and **CmlI^{P}** (middle, right) in $^{16}OH_2$ (black), $^{18}OH_2$ (red) and $^{16}OD_2$ (blue). λ_{ex} = 561 nm, Power = ~100 mW. All spectra were collected in solution at ~4 ºC. Protein concentration ~1 mM for each sample, 50 mM Bicine pH/pD = 9. $^{18}OH_2$ enrichment of the samples was ~60%.

To put this vibration into a broader context, we compared its frequency with data originally collected by Sanders-Loehr and co-workers that established a correlation between ν(Fe–O–Fe) and ∠Fe–O–Fe for other Fe–O–Fe complexes.[239] Since the original 1989 study, examples of oxo-bridged diiron complexes with an additional μ-1,2-peroxo bridge (green squares) have been characterized,[102, 103, 105, 110, 111] as well as complexes with bis(μ-oxo)diiron diamond cores.[240-242] These new data have been included to the plot

shown in Figure 4.6 and extend the correlation to entries with ∠Fe–O–Fe approaching 90°. Based on Figure 4.6, the observed ν_s(Fe–O–Fe) frequency of 487 cm^{-1} would then correspond to an ∠Fe–O–Fe of ~134° for the Fe–O–Fe unit in **CmlI^{Ox}**, in good agreement with an angle of 130° that is calculated assuming Fe1–O and Fe2–O distances of 1.83 Å and an Fe•••Fe distance of 3.32 Å.

Close inspection of the 740-800-cm^{-1} region in the $^{16}OH_2$ and $^{18}OH_2$ samples shows the loss of signal intensity at ~780 cm^{-1} in the $^{18}OH_2$ sample relative to $^{16}OH_2$, revealing a peak at ~790 cm^{-1} (Figure 4.7, left top and left middle). Fitting the protein-related features with Gaussian functions did not sufficiently fit the peaks in the Raman spectrum. In the $^{16}OH_2$ sample an additional function centered at 780 cm^{-1} was required, while in the $^{18}OH_2$ sample, functions at 780 cm^{-1} and 750 cm^{-1} had to be included, which are consistent with ν_{as}(Fe-O-Fe) modes of the ^{16}O and ^{18}O isotopomers. On the Sanders-Loehr correlation in Figure 4.6, they correspond to an ∠Fe-O-Fe of 138º, which is in agreement with the EXAFS-derived angle of 135º for **CmlI^{Ox}**.

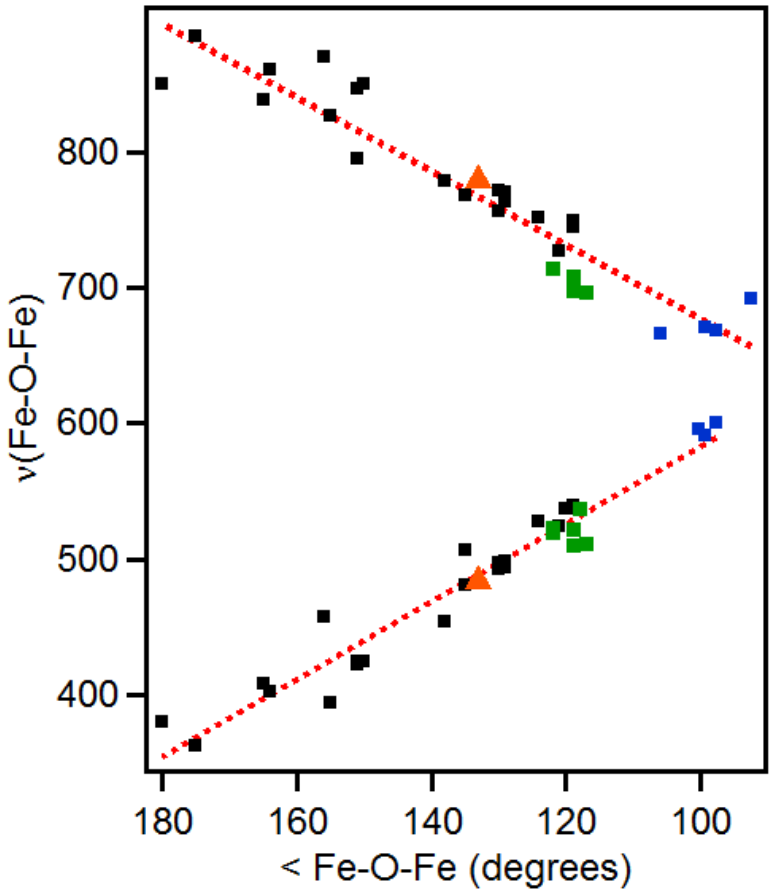

Figure 4.6. Extended data set for the Sanders-Loehr correlation of ∠Fe–O–Fe and ν(Fe–O–Fe) in oxo-bridged diiron complexes. Data from the original study (black),[239] augmented by data for species with (μ-oxo)(μ-1,2-peroxo)diiron cores (green)[102, 103, 105, 110, 111] and species with bis(μ-oxo)diiron diamond cores (blue).[240, 241] The data points corresponding to **CmlI^{P}** are shown as orange triangles. Red dotted lines represent the best linear fits of the data.

In the Raman spectrum of **CmlI^{P}**, we previously identified the ν(O–O) vibration at 791 cm^{-1}, which downshifted 43 cm^{-1} when **CmlI^{P}** was formed with $^{18}O_2$. In the experiments reported here, the ν(O-O) is observed at 789 cm^{-1} and does not shift in $^{18}OH_2$ buffer. This observation is consistent with recent mechanistic data that demonstrates that water is not incorporated into the products of *N*-oxygenation by CmlI and therefore does not exchange with the bound peroxo moiety.[124]

In the lower Raman shift range, a peak is observed at 485 cm^{-1}, which downshifts to 467 cm^{-1} in $^{18}OH_2$ buffer (Figure 4.5), thereby providing evidence for the persistence

of an oxo bridge in **CmlI^{P}**. This peak can be assigned to ν_s(Fe-O-Fe), and its slightly lower frequency than that of **CmlI^{Ox}** suggests a slight increase in the Fe–O–Fe angle. These results are in agreement with the EXAFS analysis.

Although the 789 cm^{-1} peak is not perturbed by $^{18}OH_2$ buffer, scrutiny of the 740-800-cm^{-1} region in $^{16}OH_2$ and $^{18}OH_2$ buffer reveals a peak that is in fact sensitive to the presence of $^{18}OH_2$ (Figure 4.7, right top and right middle). Fitting the 740-800 cm^{-1} region of the $^{16}OH_2$ sample only with Gaussian functions at 758 cm^{-1} (a protein-derived mode) and 789 cm^{-1} (ν(O–O)) is insufficient to match the observed peak shape and requires inclusion of another peak at 780 cm^{-1} (Figure 4.7, top right). Fitting the signals in this region of the 60% $^{18}OH_2$ sample (Figure 4.7, middle right) requires the inclusion of peaks at 780 cm^{-1} and 749 cm^{-1}. The peaks can be assigned respectively to the ν_{as}(Fe-O-Fe) modes of the ^{16}O and ^{18}O isotopomers and correspond to an ∠Fe-O-Fe of 138º on the Sanders-Loehr correlation, which is in reasonable agreement with the EXAFS-derived angle of 133º.

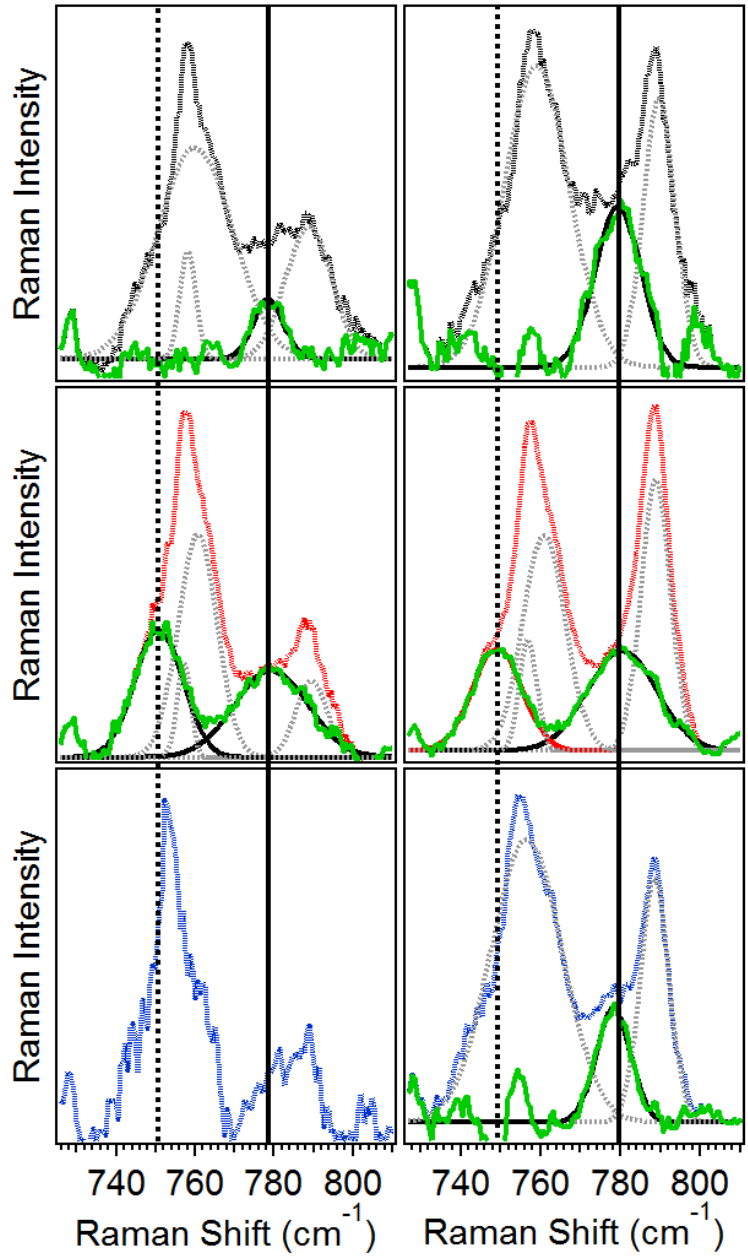

Figure 4.7. Resonance Raman spectra of **CmlI^{Ox}** (left) and **CmlI^{P}** (right) in the 740-800-cm^{-1} region in $^{16}OH_2$ (top), $^{18}OH_2$ (middle) and $^{16}OD_2$ buffer (bottom). λ_{ex} = 561 nm, Power = ~100 mW. The experimental data (solid black, red lines) are fit with Gaussian functions to model the protein feature at ~760 cm^{-1} and the peroxo/protein peak at 789 cm^{-1}. These peaks are then subtracted from the experimental data (resulting green solid line). All spectra were collected in solution at ~4 ºC. Protein concentration ~1 mM for each sample, pH/pD = 9. $^{18}OH_2$ enrichment of the samples was ~60%.

Table 4.3. Select data points from extended Sanders-Loehr correlation.

Species	∠Fe-O-Fe (°)[a]	ν_s(Fe-O-Fe) (cm^{-1})[b]	ν_{as}(Fe-O-Fe) (cm^{-1})[b]	Refs
CmlI^{P}	133	485 (-18) [-4]	780 (-31) [-2]	This work
CmlI^{Ox}	130	487 (-18) [-7]	780 (-30)	This work
1	122	523 (-16)	714 (-14)	*110*
2	117	511 (-12)	696 (-30)	*102*
3	119	522 (-13)	708 (-32)	*111*
4	*130*	497 (-17)	772 (-37)	*243*
5	*124*	528 (-17)	751 (-30)	*208*
CmlA	135	481 (-17)	-	*139*
OxyHr	*134*	486 (-14) [+4]	753 (-37)	*75*
metHrCN	137	512 (-14)	782 (-28)	*87*
6	*99*	591 (-27)	671 (-31)	*241*
7	*93*	-	692 (-32)	*240*
8	106	-	666 (-32)	*240*

[a] Angles in italics come from X-ray diffraction studies, the remaining angles are derived from EXAFS data. [b] Values in parenthesis come from ^{18}O isotope shifts, while those in brackets come from D_2O isotope shifts. **1** = $[(BnBQA)Fe^{III}_2(O)(O_2)(CH_3CN)_2]^{2+}$, BnBQA = *N*-benzyl-*N*,*N*-bis(2-quinolinylmethyl)amine; **2** = $[(6\text{-}Me_3TPA)_2Fe^{III}_2(O)(O_2)]^{2+}$, 6-$Me_3$TPA = tris(6-methyl-2-pyridylmethyl)amine; **3** = $[(BQPA)Fe^{III}_2(O)(O_2)]^{2+}$, BQPA = bis(2-quinolylmethyl)-2-pyridylmethylamine; **4** = $[(TPA)_2Fe^{III}_2(O)(OBz)]^{3+}$, TPA = tris(2-pyridylmethyl)amine, OBz = benzoate; **5** = $[(Tp)_2Fe^{III}_2(O)(OAc)_2]$, Tp = tris(1–pyrazolyl)borate; **6** = $[(6\text{-}Me_3TPA)_2Fe^{III}_2(O)(OH)]^{3+}$;**7** = $[(6\text{-}Me_3TPA)_2Fe^{III}_2(O)_2]^{2+}$;**8** = $[(5\text{-}Me_3TPA)_2Fe^{III}Fe^{IV}(O)_2]^{3+}$, 5-$Me_3$TPA = tris(5-methyl-2-pyridylmethyl)amine.

4.3.3 – Effect of D_2O on the Active Site

To interrogate the effect of water on the **CmlI** active site, we conducted rR experiments with **CmlI^{Ox}-D_2O** and **CmlI^{P}-D_2O**. The ν(O-O) in **CmlI^{P}** is unaffected by D_2O (Figure 4.5). This is in contrast to **OxyHr**, which has a ν(O-O) at 844 cm^{-1} that increases by 4 cm^{-1} in the presence of D_2O.[87] This result indicates that **CmlI^{P}** is unlikely to have a hydroperoxo ligand. D_2O-sensitive vibrations were observed for both **CmlI^{Ox}** and **CmlI^{P}**. The ν_s(Fe-O-Fe) peak (Table 4.3) assigned for **CmlI^{Ox}** downshifted by 7 cm^{-1} in **CmlI^{Ox}-D_2O** (Figure 4.5, left panel, blue trace), while the corresponding feature in **CmlI^{P}** downshifted by 4 cm^{-1} in **CmlI^{P}-D_2O** (Figure 4.5, center panel, blue trace). This isotope shift is of a similar magnitude to that observed for **OxyHr**, (+4 cm^{-1},Table 4.3)

but in the opposite direction.[75] The ν_{as}(Fe-O-Fe) downshifted by 2 cm^{-1} to 778 cm^{-1} in **CmlI^{P}-D$_2$O** relative to the $^{16}OH_2$ sample (Figure 4.7, right bottom); however **CmlI^{Ox}-D$_2$O** is unable to be fit in a similar manner (Figure 4.7, left bottom). Clearly, D_2O has some interaction with the μ-oxo moiety in CmlI, which we will explore in the Discussion.

4.4 – Discussion

In synthetic diiron chemistry, the stability of (μ-1,2-peroxo)diferric intermediates allows these species to be trapped[102, 105, 110-112] and in some instances crystallized[91, 94, 109, 244], but typically it results in low substrate oxidation reactivity. Recently, the first enzymatic diiron peroxo intermediate with a long lifetime, hDOHH^{P}, was structurally characterized[17, 36, 65]. Importantly, this intermediate decays concomitant with the formation of oxidized product. **CmlI^{P}** is another such example of a reactive peroxo-diferric intermediate and has been directly shown to be the active oxidant in the catalytic cycle.[124] Initial rR characterization of **CmlI^{P}** provided strong evidence for a peroxo binding mode that was distinct from the commonly found (μ-1,2-peroxo)diferric motif.[15] Here, further spectroscopic analysis by XAS and rR provides the necessary information to construct a better structural picture of a reactive diferric-peroxo species in solution. This improved model, presented in Figure 4.8, provides insight into how the reactive peroxo species from CmlI can catalyze the *N*-oxygenation reaction of the native substrate.

4.4.1 – Structural Models of CmlI^{R} and CmlI^{Ox} from XAS Analysis

The active sites of **CmlI^{R}** and **CmlI^{Ox}** have similar structural features to those found in CmlA by XRD and XAS studies,[18, 38, 139] and in the crystal structure of AurF.[14] In addition to a μ-1,3-glutamate bridge observed by XRD,[35] both **CmlI^{R}** and **CmlI^{Ox}** models have a solvent-derived single-atom bridge between the Fe centers, a feature which is further supported in the case of **CmlI^{Ox}** by its UV-vis and rR spectra.[64, 139] The assignment of a single atom bridge in **CmlI^{R}** distinguishes it from structures of diferrous

RNR [31, 151] and Δ^9D [53], which only use two μ-1,3-carboxylate bridges to connect the metal centers. sMMO also utilizes single atom bridges, in addition to a μ-1,3-carboxylate bridge, with a solvent derived oxygen ligand in the reduced form and a bis(μ-hydroxo) "diamond core" motif in the oxidized form.[47, 150]

EXAFS analysis of **CmlI^{R}** reveals a required ~2.6 Å scatterer per Fe, which could arise from the C atom of a bidentate carboxylate ligand. Based on the crystal structure of diferrous CmlI (PDB code 5HYH),[35] the C_δ (carbonyl carbon) of E205 on Fe1 is found at 2.6 Å, indicating that E205 could bind in a bidentate mode. However, in order to accommodate the N = 1 for this 2.6 Å scatterer, there either is one 2.6-Å interaction on both Fe centers or two interactions on only one Fe center. It is unclear which other residues would be chelated in a similar binding mode, but a conformational change of the active site ligands would be required to accommodate it. Alternatively, E236 on Fe1 could also bind in a bidentate mode to Fe1 while forming a μ-1,1-carboxylato bridging interaction between Fe1 and Fe2. E236 appears rather flexible and is bound in this configuration in the crystal structure of reduced CmlI.[35] In this interpretation, the bridging oxygen atom of the carboxylate would be assigned to the 1.94-Å scatterer instead of a μ-OH bridge to be consistent with N = 1 for the scatterer at 2.6 Å.

4.4.2 – The CmlI^{P} Model

The model for **CmlI^{P}** has very similar primary sphere ligands as **CmlI^{Ox}**, including a short Fe–O distance at 1.83 Å indicative of a μ-oxo bridge, identical Fe•••Fe distances and similar carbon scattering shells (Table 4.2). The unique component of **CmlI^{P}** is the requirement of a 2.82-Å scatterer that does not appear in the other CmlI samples, and we assign this feature to the distal O atom of the μ-1,1-peroxo ligand. **CmlI^{R}** does have a distance at ~2.6 Å, which is assigned to a bidentately bound carboxylate ligand. Precedent for a carbon atom at this distance can be found in the crystal structures of diferrous and diferric CmlA at 2.6 and 2.5 Å, respectively.[18, 38]The 2.8-Å scatterer is unlikely to be derived from a carboxylate ligand, as such scatterers have not been reported in EXAFS studies of diiron enzymes before. Additionally, in the XAS

data that was collected for **CmlI^{R}** and **CmlI^{P}** the resolution is such that 2.6 and 2.8 Å distances can be distinguished. Therefore, the source of the 2.6 and 2.8-Å scatterers is not the same.

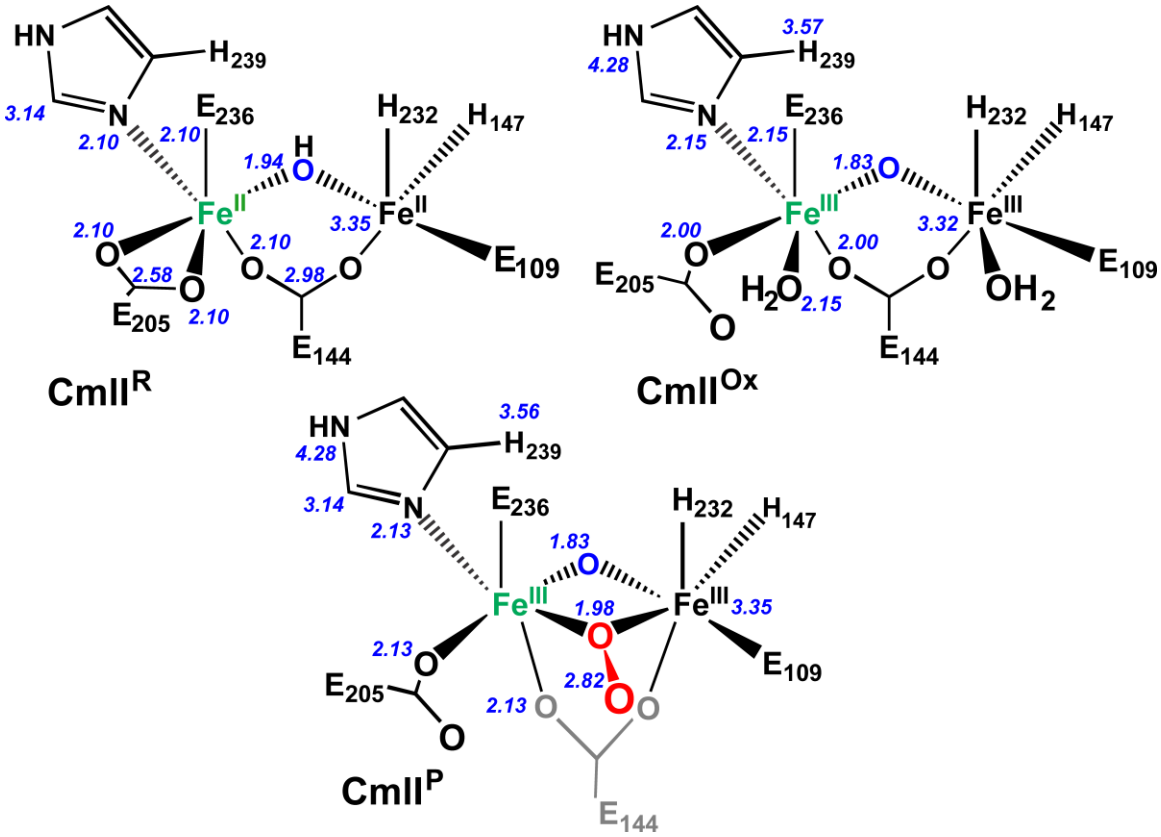

Figure 4.8. Structural models of **CmlI^{R}** (top left), **CmlI^{Ox}** (top right) and **CmlI^{P}** (bottom) as determined by EXAFS analysis. Numbers in italics represent the best fit scattering distances in angstroms. The Fe atoms colored in green are Fe1, in black is Fe2.

Table 4.4. Select structural metrics for **CmlI^P** and relevant synthetic peroxo complexes.

Species	Metal	Mode[a]	M•••M (Å)	M – O_p (Å)[b]	ν(O-O) (cm^{-1})
CmlI^P	Fe_2	C	3.35	1.98; 2.82	789
9	Fe_2	A	3.46	1.88; 2.91	900
10	Fe_2	A	3.40	1.88, 1.89; 2.86, 2.88	908
11	Fe_2	A	3.17	1.73; 2.97[c]	847
12	Fe, Cu	D	3.92	1.89, 1.92; 2.03, 2.66	790
13	Co_2	D	3.34	1.85, 1.92; 1.93, 2.76	839
14	Co_2	A	3.77	1.86; 2.70	866
15	Cu_2	E	3.53	1.99; 2.90, 3.00	860

[a] The mode in this column refers to the O_2 binding mode from Figure 4.9

[b] In this column, the M–O proximal distance is listed first, followed by the M–O distal distance.

[c] The μ-oxo and μ-1,2-peroxo atoms are disordered over two positions, each with 0.5 occupancy, so these values are not very reliable and represent the average from the crystal structure.

4.4.3 – Comparison of CmlI^P to Synthetic Diferric-Peroxo Intermediates

To better address the assignment of the 2.82-Å scatterer in **CmlI^P**, available structural data was used to parse the possibilities to arrive at a working model. As detailed in the introduction, O_2 binds in a *cis*-μ-1,2 mode (Figure 4.9, A) in all crystallographically characterized synthetic diferric-peroxo species, and all except one have an additional single-atom bridge, like $[Fe^{III}_2(N\text{-Et-HPTB})(O_2)(Ph_3PO)_2]^{3+}$ (**9**) (N-Et-HPTB = N,N,N',N'-tetrakis(2-benzimidazolylmethyl)-2-hydroxy-1,3-diaminopropane)[109] and the acid/base pair of $[Fe^{III}_2(6Me_2\text{-BPP})_2(OH)(O_2)]^+$ (**10**) and $[Fe^{III}_2(6Me_2\text{-BPP})_2(O)(O_2)]$ (**11**) ($6Me_2$-BPP = N,N-bis(6-methyl-2-pyridylmethyl)-3-amino-propionate).[244] In these species, the ∠Fe–O–O–Fe torsion angle is ~0°, meaning that the Fe1–O1–O2–Fe2 plane is flat, forcing the distal O (Fe1•••O2 and Fe2•••O1) of the peroxo moiety to a distance of ~2.9 Å in **9** and **10** and ~3 Å in **11** (Fe•••Fe: **9** = 3.46 Å, **10** = 3.40 Å, **11** = 3.17 Å). These distances are longer than the 2.82 Å distance observed in **CmlI^P**. The metal-metal separation for **9** and **10** is ~0.1 Å longer than **CmlI^P**, while the

oxo-bridged **11** has a metal-metal separation that is ~0.2 Å shorter than **CmlI^{P}**. Importantly, a ~2.8 Å O scatterer has not been reported in the EXAFS analyses for these synthetic peroxo species or related complexes[102, 105, 110-112] or for the enzymatic μ-1,2-peroxo species hDOHH^{P}.[36] This data is consistent with **CmlI^{P}** not having a μ-1,2-peroxo moiety, as corroborated by UV-vis, rR and Mössbauer experiments.[15]

4.4.4 – Comparison of CmlI^{P} to μ-η^2:η^1-Peroxo Intermediates

Although all crystallized synthetic diferric-peroxo species exhibit μ-1,2-peroxo binding modes, alternative O_2 binding modes exist in other dinuclear peroxo complexes. Naruta has reported the crystal structure of an Fe/Cu complex with an η^2:η^1-peroxo binding mode, where O_2 is bound η^2 to Fe and η^1 to Cu (Figure 4.9, D), namely $[(\text{TMP-5Me-TPA})Fe^{III}(O_2)Cu^{II}]^{1+}$ (**12**) (TMP-5Me-TPA = 10,15,20-tris(2,4,6-trimethylphenyl)-5-(2'-bis((5''-methyl-2''-pyridylmethyl)aminomethyl)pyridine-5'-carboxyamidophenyl)-porphyrin).[245] In this case, the Fe-O-O-Cu plane is flat with Fe–O_{peroxo} distances of 1.89 and 2.03 Å, Cu–O_{peroxo} distances of 1.92 and 2.66 Å, and an Fe•••Cu separation of 3.92 Å. The Fe(O_2)Cu core has a much longer metal-metal separation than for **CmlI^{P}** and additionally, there would be no way to accommodate a 2.82 Å scatterer with an η^2:η^1 configuration. The 2.66-Å distance comes only from one of the metal centers, the σ^2 value of such a scatterer in an EXAFS experiment should be higher than the 1.50×10^{-3} Å^2 value observed for **CmlI^{P}**. Complex **12** has a ν(O–O) of 790 cm^{-1}, very close to that for **CmlI^{P}**, however the ability of d^9 Cu^{II} to back-donate into the O–O bond weakens it relative to d^5 Fe^{III} analogs. Therefore, direct comparison of ν(O–O) from Cu-containing peroxo species to Fe based intermediates is not trivial.

Another example of a crystallized complex with a μ-η^2:η^1-peroxo ligand is $[(\text{oxapyme})Co^{III}_2(O_2)]^{2+}$ (**13**) (oxapyme = 2-(Bis-pyridin-2-ylmethyl-amino)-*N*-[2-(5-{2-[2-(methyl-pyridin- 2-ylmethyl-amino)-acetylamino]-phenyl}-[1,3,4]oxadiazol-2-yl)-phenyl]-acetamide) (Figure 4.9, D).[246] The Co•••Co separation is 3.34 Å, with Co1- η^2 -

O_{peroxo} bond lengths of 1.85 and 1.93 Å and Co2- η^1-O_{peroxo} distances of 1.92 and 2.76 Å. This complex initially appears to have distances similar to what is observed for **CmlI^P**, but the rR data collected for **CmlI^P** is consistent with an Fe–O–Fe vibration. This means that the short O distance (1.83 Å) in **CmlI^P** must belong to a μ-oxo ligand and cannot be assigned to the peroxo moiety, as in **13**. In addition, in **13** the 2.76 Å distance is only observed with respect to one of the Co centers, and similar to **12**, it would be inconsistent with the well behaved fit of the 2.8-Å scatterer (N = 1 with a σ^2 of 1.50×10^{-3} Å^2, see Table 4.2) which is interpreted as the 2.82-Å distance being equidistant with respect to both Fe centers.

The Co complex provides an additional point of comparison because both the η^2:η^1 binding mode (**13**), and the μ-1,2 peroxo binding mode (**14**) [(oxapyme)$Co^{III}(O_2)Co^{III}(NO_2)]^{1+}$ have been analyzed by FT-Raman. Complex **13** has a ν(O–O) = 839 cm^{-1}, with no ν(Co–O–Co) vibration reported, and **14** has a ν(O–O) of 866 cm^{-1}. In going from a μ-1,2-peroxo binding mode in **14** to an η^2:η^1 configuration in **13**, the change in the O–O stretching frequency is -27 cm^{-1}. The ν(O-O) for **CmlI^P** is at least 60 cm^{-1} lower in energy than other (μ-1,2-peroxo)diferric intermediates.[15] This structural and vibrational analysis argues against the η^2:η^1-O_2 assignment for **CmlI^P**.

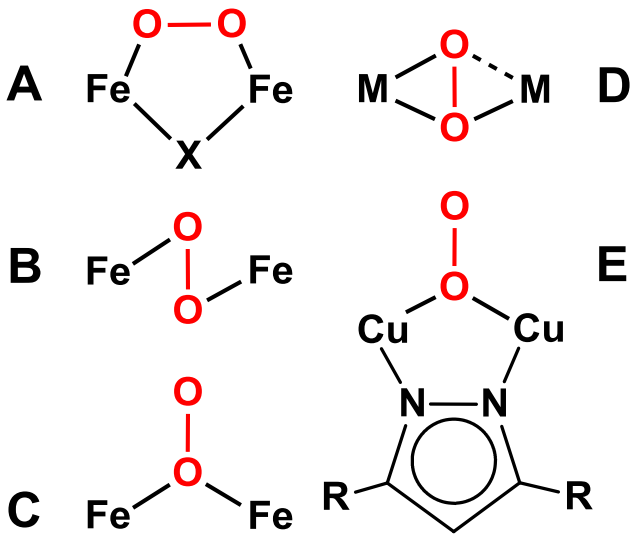

Figure 4.9. Possible O_2 binding modes for dimetal peroxide species. X represents an additional bridging ligand, M represents a transitional metal center, and R represents the remaining sections of the L^{et} ligand from **15**.

4.4.5 – Comparison of CmlI^P to μ-η^1:η^1-Peroxo Complexes

Synthetic copper-peroxo complexes provide examples of additional O_2 binding modes for comparison. In one example, Meyer and co-workers have isolated a dicopper-μ-1,1-hydroperoxo complex, $[Cu^{II}_2(L^{et})(OOH)](OTf)(BPh_4)$ (**15**) (L^{et} = 3,5-bis(1-ethyl-4,7-di-*iso*propyl-1,4,7-triazacyclononane)pyrazole),[247] which has a nearly planar Cu–O_2–Cu core with a metal-metal separation of 3.53 Å and Cu–O_{peroxo} distances of ~2 and 2.95 Å. The metal-metal distance is ~0.2 Å longer than in **CmlI^P** (the pyrazolate ligand of **15** prevents a closer interaction), but the Cu–O distances are comparable. The distances to the distal oxygen atom are ~2.95 Å, which is longer than the 2.82 Å distance for **CmlI^P**. However, a μ-1,1-peroxo binding geometry would rationalize the low σ^2 of the 2.82 Å shell, as the distal oxygen atom would be symmetrically positioned between both Fe centers. Additionally, the Cu–O_{peroxo} distances found for **15** suggests that the distal O-atom of a μ-1,1-peroxo bridge in **CmlI^P** cannot be coplanar with the Fe–O–Fe unit and must come out of that plane in order to be 2.8 Å from the Fe centers. The rR spectrum of

15 shows a ν(O-O) vibration at 860 cm^{-1}.[247] but the authors mention that there is significant mechanical coupling between the ν(O-O) and ν(Cu-O), which makes direct comparison to the ν(O-O) of **CmlI^{P}** challenging. Additionally, a ν(Cu-O-Cu) feature was not observed for **15**, which reinforces our assignment that **CmlI^{P}** has a distinct μ-oxo bridge unrelated to the peroxo moiety. This analysis is consistent with a model for **CmlI^{P}** that contains a μ-oxo-diferric core, with a μ-1,1-peroxo moiety that is not coplanar to the Fe-μ-O-Fe unit.

4.4.6 – Support for the Assignment of the 2.8-Å Scatterer from the Structure of Product-Bound AurF

Further support for the assignment of the 2.82 Å scatterer comes from the crystal structure of a homologous arylamine oxygenase, AurF with product bound (PDB code 3CHT).[14] The product of the AurF-catalyzed reaction is *para*-nitrobenzoic acid (pNBA), which is bound in the active site substrate channel in this structure, with one of the oxygen atoms of the nitro group oriented between the two Fe centers (Figure 4.10). If **CmlI^{P}** adopts the proposed μ-1,1-peroxo binding configuration, it would conveniently place the distal peroxo oxygen at 2.82 Å from the Fe centers, at a very similar location as the oxygen atom of pNBA, which presumably is derived from the peroxo ligand. This structure would place the distal peroxo oxygen in the substrate pocket, close to where an O-atom of the nitro group that is formed during the reaction. This juxtaposition should facilitate oxygen atom transfer from the diiron-bound μ-1,1-peroxo intermediate to the substrate. The product bound AurF crystal structure sheds possible light on the rigid positioning of the 2.82 Å scatterer, as reflected in its small σ^2 value (Table 4.2). Three of the monodentate carboxylate ligands of the AurF diiron center (Figure 4.10, labeled 1 – 3) have their distal oxygen atoms pointing into the substrate pocket within 2.8 to 3.1 Å of the oxygen atom of pNBA. This could point to potential interactions between the distal O atom of carboxylate ligands and the peroxo moiety.

The analysis of the pre-edge, in light of the product bound crystal structure of AurF, provides useful information for the structural assignments of **CmlI^{P}**. In the context of synthetic six-coordinate peroxo-diferric complexes, the pre-edge area of **CmlI^{P}** is unusually large, at a value of 19.2 units, compared with values between 12 and 16 units in the synthetic models. The presence of a μ-oxo bridge is not the sole contributor of intensity to the pre-edge peak, as **CmlI^{Ox}** also has a μ-oxo bridge and a pre-edge area of 14.5 units. Therefore, the introduction of the peroxo ligand in **CmlI^{P}** has resulted in the higher degree of distortion to the Fe centers and so an interaction between the peroxo ligand and something else is required to rationalize the value of the pre-edge area. A plausible candidate would be from the carboxylate ligands bound to the Fe centers. Based on the crystal structure of product bound AurF, the distal O atoms from three monodenate carboxylate ligands are within ~3 Å of the proposed position of the peroxo ligand (Figure 4.10). In the crystal structure of diferrous CmlI, the analogous carboxylate ligands E205 and E109 (labeled 1 and 3 from Figure 4.10) are also oriented in a similar way. These ligands could sterically/electrostatically interact with the peroxo ligand such that the distal peroxo oxygen is fixed to a point that is equidistant between both Fe centers. The subsequent perturbation of the Fe coordination geometry from the peroxo/carboxylate interactions would result in an increased pre-edge value, consistent with experimental observation.

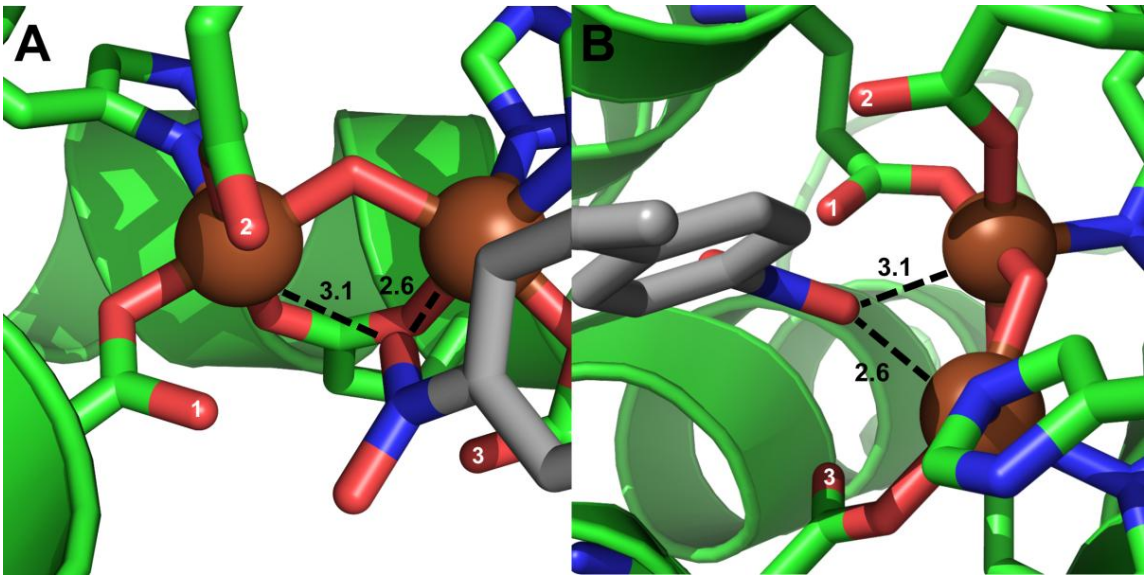

Figure 4.10. Crystal structure of product-bound AurF (PDB code: 3CHT). Distances shown are in angstroms. Panel B is a 90º rotation of panel A. Carboxylate ligands that have oxygen atoms pointed toward the substrate channel are labeled 1 to 3. Carbon atoms from AurF are shown in green, oxygen atoms are in red, nitrogen atoms are in dark blue, iron atoms are represented as brown spheres and the carbon atoms of *para*-nitrobenzoic acid are shown as gray

4.4.7 – Additional Structural Considerations for the CmlI^{P} Active Site

The rR analysis of **CmlI^{P}** and **CmlI^{Ox}** demonstrate that the ν(Fe–O–Fe) vibrations are affected by substitution with D_2O. The only other diiron system that has reported isotope shifts from D_2O is **OxyHr**. Sanders-Loehr and co-workers showed that the isotope shift from D_2O in OxyHr was the result of hydrogen bonding interactions between the end-on hydroperoxo ligand and the μ-oxo bridge.[75] Along similar lines, the D_2O isotope shift in CmlI could also be from hydrogen bonding interactions.

In **CmlI^{P}**, the source of the hydrogen bonding interactions are likely not from a hydroperoxo ligand, as the ν(O–O) is not affected by D_2O substitution. In contrast, the ν(O–O) of the hydroperoxo ligand of **OxyHr** is changed by such substitution.[87] Protonation of the μ-oxo ligand can also be ruled out based on precedent from synthetic complexes. Direct protonation of an oxo bridge substantially decreases the ν(Fe–O–Fe)

vibration. This is observed when the μ-oxo-μ-1,2-peroxo-diferric complex **1** is protonated to the μ-hydroxo conjugate acid. The energy of the ν(Fe–O–Fe) vibration in the μ-hydroxo complex decreases by ~100 cm^{-1}, from 523 cm^{-1} in **1** to 424 cm^{-1}, which is far from 485 cm^{-1} measured for **CmlI^{P}**.[110] One possibility is that a protonated protein ligand can interact with the Fe–O–Fe unit. E236 in the crystal structure of CmlI is able to move to the proposed position of the μ-oxo ligand, so if protonated, E236 could feasibly interact with the Fe–O–Fe unit in both **CmlI^{Ox}** and **CmlI^{P}**.[35] However, at pH = 9 for the CmlI samples, it is likely unfavorable for the carboxylate residues to be protonated. Alternatively, free water molecules could be present the active site. One of these water molecules could coordinate to the μ-oxo ligand and the proximal O atom of E236 in a bridging mode, forming a six-membered ring (Figure 4.11). This would rationalize the observed shift in the rR experiment.

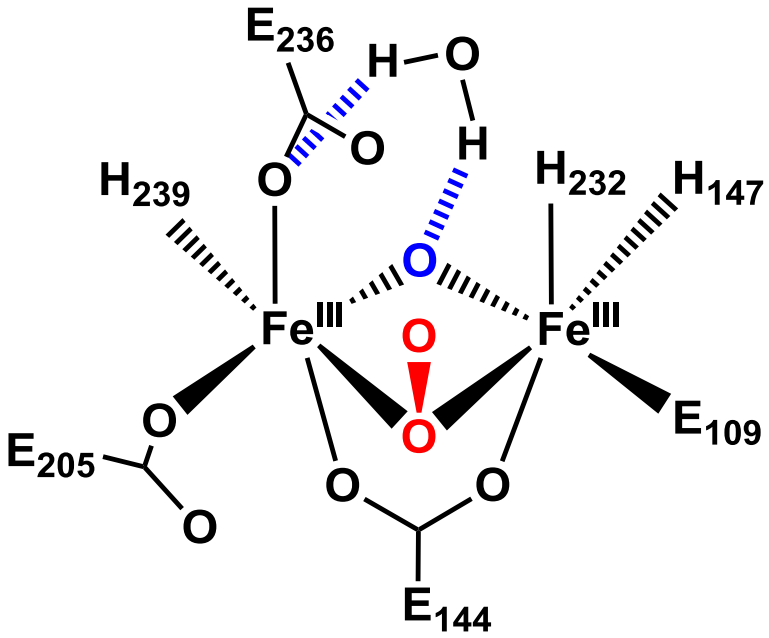

Figure 4.11. Proposed interactions of water with **CmlI^{P}**. The red atoms are from the O_2 derived peroxo ligand, blue atom is the μ-oxo bridge. Some ligands are omitted for clarity.

The **CmlI^{P}** structure also raises an interesting question about the charge accumulation on the diiron cluster. With μ-oxo and μ-1,1-peroxo ligands, the formal charge on the diferric cluster would be -2, compared to **CmlI^{R}** which would have a -1 or

neutral charge and **CmlI^{Ox}** which would have a neutral charge. However, if net charge accumulation in the active site is to be avoided, the charge on **CmlI^{P}** has to be carefully considered. The proposed interaction between water and the μ-oxo bridge could serve to partially neutralize the charge of the oxo ligand. This would serve to reduce the net charge on the cluster to somewhere between -2 and -1, closer to the other CmlI species.

4.4.8 – Disparity Between XAS and XRD – CmlI vs CmlIΔ33

The crystal structure of reduced CmlI (**CmlIΔ33^{R}**) featured five-coordinate Fe centers with a 3.6 Å separation, bridged by two glutamate residues.[35] This is in contrast to the XAS-derived **CmlI^{R}** model, which is consistent with six-coordinate centers having a metal-metal separation of 3.35 Å and a μ-OH bridge (Figure 4.8). A possible explanation for the difference is the manner by which **CmlI^{R}** and **CmlIΔ33^{R}** are obtained. **CmlI^{R}** is isolated in solution through the chemical reduction of the as-isolated form **CmlI^{Ox}**, whereas **CmlIΔ33^{R}** is generated by soaking crystals of the μ-1,2-peroxo crystal structure (**CmlIΔ33$^{P'}$**) in chemical reductant, which removes the peroxo moiety. The nature of the crystalline **CmlIΔ33^{R}** may simply prevent major rearrangement of the diiron cluster, and so it reflects a trapped intermediate that is not the same as in the solution state.

Aside from the difference in peroxo binding mode, the structure of **CmlI^{P}** determined here is distinct from crystal structure of **CmlIΔ33$^{P'}$** in that there is strong evidence for a μ-oxo bridge between the Fe centers in **CmlI^{P}** that is absent in the crystal. In addition, the crystal structure **CmlIΔ33$^{P'}$** has a single atom μ-1,1-carboxylate bridge that is inconsistent with the XAS and rR model of **CmlI^{P}** determined here. However, the single atom bridge in both forms likely helps to maintain the common Fe•••Fe distance of ~3.3 Å.[35]

4.4.9 – Possible Mechanism for O-O Bond Cleavage in CmlI^{P}

In light of the updated structure of **CmlI^{P}** as well as mechanistic work,[124] we can better assess how **CmlI^{P}** carries out reactions with the native substrate. During the course of the native reaction, **CmlI^{P}** is capable of oxidizing the more electron-rich aryl-amine substrate (Figure 4.1, left), as well as a less electron-rich aryl-nitroso substrate from later in the reaction pathway.[124] This means that **CmlI^{P}** is ambiphilic, or able to switch between being a nucleophilic and an electrophilic oxidant. There is currently no evidence to suggest that an intervening high-valent intermediate is generated to facilitate the *N*-oxygenation reactivity. Peroxo and superoxo diiron intermediates have been proposed to be active oxidants in some cases,[22, 23, 248] but most other nonheme diiron systems, particularly sMMOH, are proposed to function through high-valent intermediates, like **Q** (Figure 4.12, A).[83]

Unfortunately, there are no examples in the literature of μ-1,1-peroxo-diferric species to compare to, but there are mononuclear end-on hydroperoxo intermediates that approximate the proposed O_2 binding mode of **CmlI^{P}** (Figure 4.12, B and C). In synthetic mononuclear iron complexes, O–O bond cleavage is proposed to go through either a heterolytic water-assisted mechanism (Figure 4.12, B) or a homolytic mechanism (Figure 4.12, C) depending on the supporting ligand.[249, 250] In the heterolytic case, the Fe complex is supported by a tetradentate ligand, so a water ligand can be bound *cis* to the hydroperoxo moiety. The bound hydroperoxo and water ligands form a 5-membered ring and the proposed oxidant for the system is generated as an oxoiron(V) species. In the homolytic case, the iron complex is supported by a pentadentate ligand and is unlikely to bind additional ligands. When the O–O bond is cleaved, the resulting active oxidant is an oxoiron(IV) species with a hydroxyl radical. Based on these mechanisms, it is unlikely that the O–O bond in **CmlI^{P}** is cleaved homolytically (Figure 4.12, C), as this would generate a hydroxyl radical an $Fe^{III}Fe^{IV}$ intermediate, which would be inconsistent with the lack of an intervening oxidant species, as well as a lack of C–H bond activation by CmlI.[15, 124]

A heterolytic mechanism, however, could be viable. In the first step of the native reaction (Figure 4.12, D), the amine group could start as aryl-NH_3^+, and transfer a proton to generate a hydroperoxo, which would then undergo O–O cleavage and subsequently transfer a proton to the diferric cluster or a basic protein residue. Another possibility is that the electron rich aryl-NH_2 substrate could attack **CmlI^P** as a nucleophile, causing a heterolytic cleavage of the O–O bond to generate the hydroxylamine product and a diferric cluster. In the later step of the biosynthetic pathway, the nitroso would be susceptible to nucleophilic attack by the peroxo ligand (Figure 4.12, E), which would cleave the peroxo bond heterolytically to generate chloramphenicol and a diferric cluster. This reaction too, could vary depending on the exact location of the protons involved.

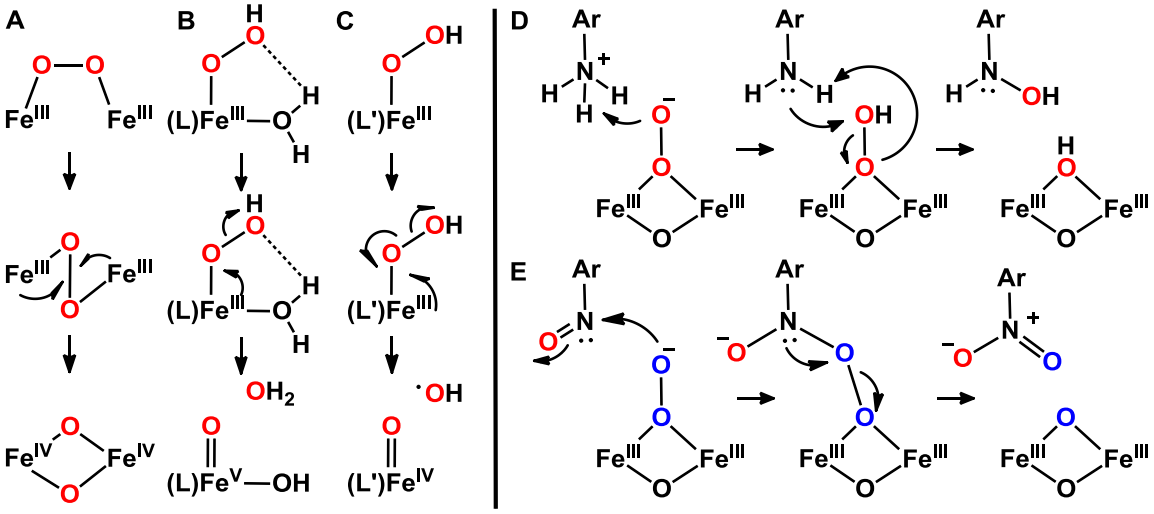

Figure 4.12. Left: O–O bond cleavage mechanisms for peroxo-diferric (A), and mononuclear end-on hydroperoxo (B, C) intermediates. L represents a tetradentate N-donor ligand, L' represents a pentadentate N-donor ligand. Right: possible electrophilic (D) and nucleophilic (E) oxidant mechanisms for **CmlI^P** along the native reaction pathway.

4.5 – Conclusion

Enzymatic peroxo-diferric intermediates have been known for several decades, but every structurally characterized example, until very recently, has contained a μ-1,2-peroxo binding mode. **CmlI^P** been demonstrated to have a μ-oxo bridge as well as a μ-1,1-peroxo ligand that interacts with protein derived ligands in the CmlI active site. It is

the only example of a reactive μ-1,1-peroxo species in diiron chemistry. Despite having the same 4α helix fold and a similar active site as C–H activating enzymes like sMMOH, CmlI is unable to facilitate C–H bond oxidation which expands the known capabilities of nonheme diiron enzymes. Studies with synthetic models would help to further characterize this intermediate and understand the effects of the μ-1,1-peroxo geometry on the reactivity of the diiron cluster.

4.6 – Acknowledgments

XAS data were collected on Beamlines 7-3 and 9-3 at the Stanford Synchrotron Radiation Lightsource, SLAC National Accelerator Laboratory. SLAC is supported by the U.S. Department of Energy (DOE), Office of Science, Office of Basic Energy Sciences under Contract No. DE-AC02-76SF00515. Use of Beamlines 7-3 and 9-3 is supported by the DOE Office of Biological and Environmental Research and the National Institutes of Health, National Institute of General Medical Sciences (including P41GM103393). Thanks go to Professors Lawrence Que, Jr. and John Lipscomb for helping to edit this chapter. Major thanks to Anna Komor, for contributing all of the samples and helping to write and edit. I would also like to thank Brent Rivard for assistance with protein growth and helpful discussions.

4.7 – Supplementary Information

General EXAFS considerations: In the fit tables of EXAFS data, N refers to the number of scatterers used for a particular shell, R is the distance of the scattering shell, σ^2 is the mean-squared deviation (or Debye-Waller factor), E_0 is the edge shift parameter, and the goodness of fit (GOF) parameters are calculated as $F = \sqrt{\sum k^6 \left(\chi_{\exp} - \chi_{calc}\right)^2}$,

$F' = \sqrt{\sum k^6 \left(\chi_{\exp} - \chi_{calc}\right)^2 / \sum k^6 \chi_{\exp}{}^2}$. For all fits, the amplitude reduction factor (S_0^2) was set to 0.9.

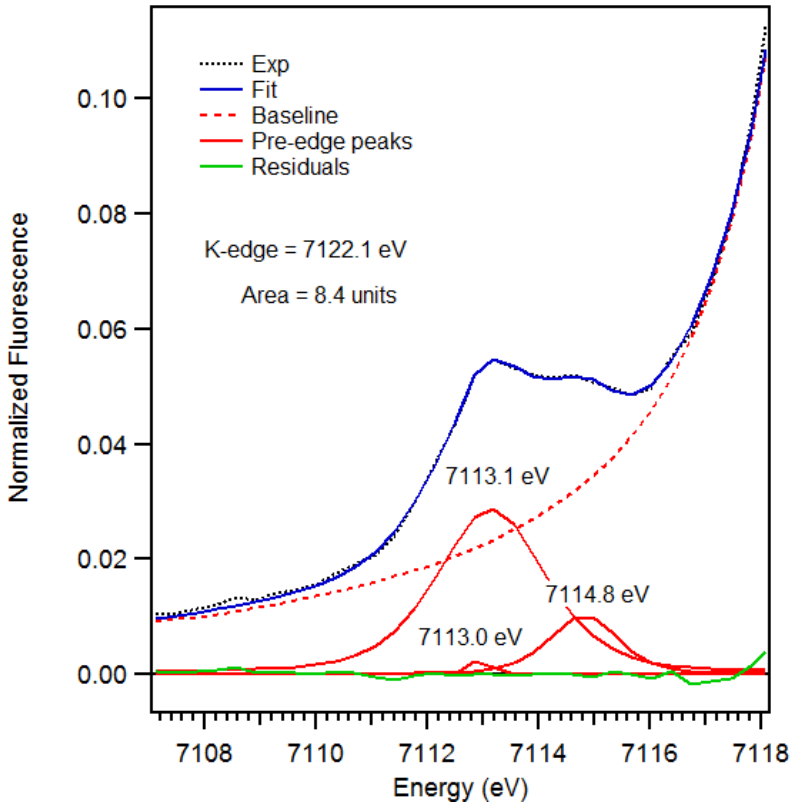

Figure 4.13. Pre-edge region analysis of **CmlI^R**. The experimental data (black dotted), baseline (red dashed), pre-edge peak components (red solid), residuals (green solid) and total fit (blue solid) are shown.

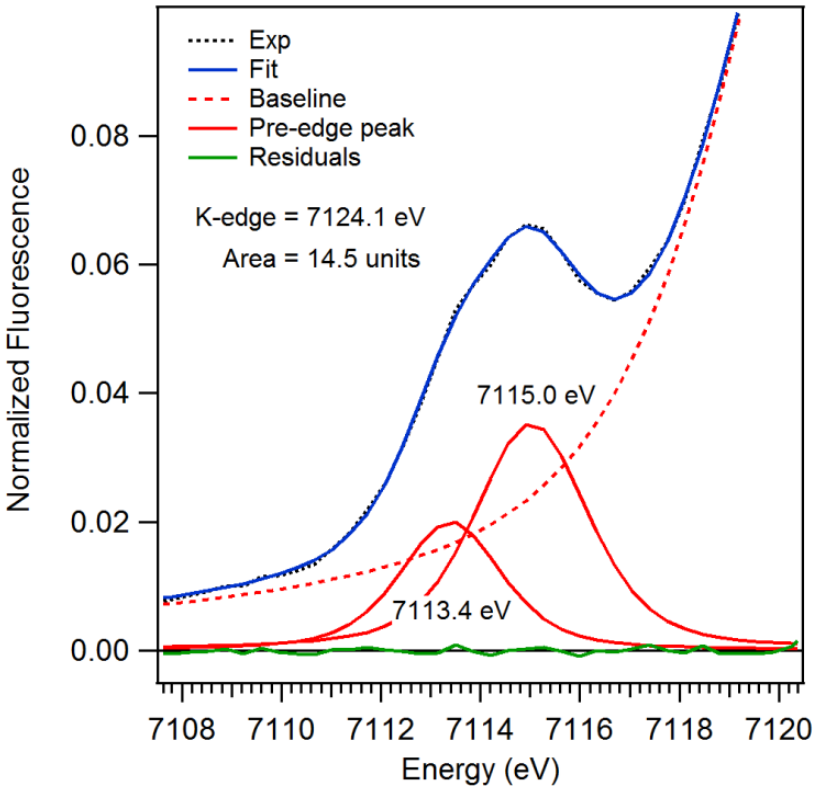

Figure 4.14. Pre-edge region analysis of **CmII^{Ox}**. The experimental data (black dotted), baseline (red dashed), pre-edge peak components (red solid), residuals (green solid) and total fit (blue solid) are shown.

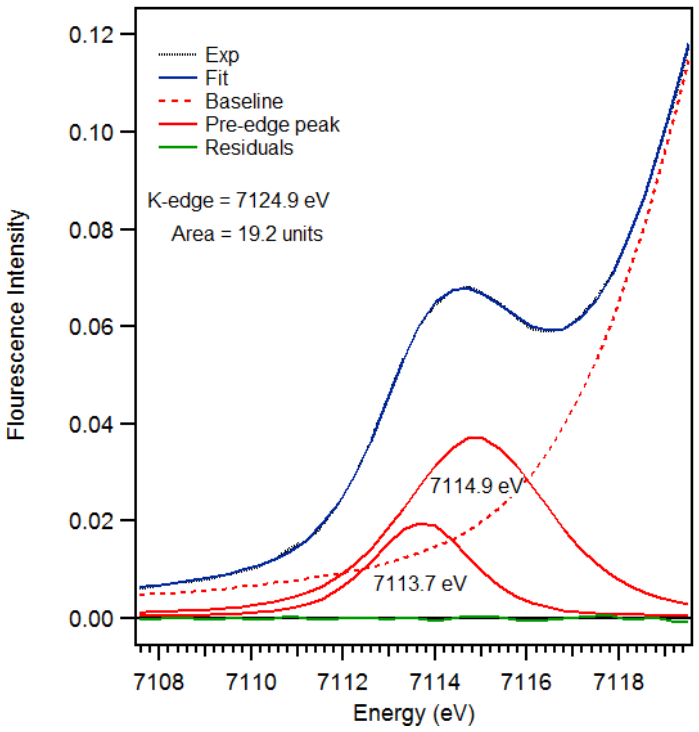

Figure 4.15. Pre-edge region analysis of **CmlI^{P}**. The experimental data (black dotted), baseline (red dashed), pre-edge peak components (red solid), residuals (green solid) and total fit (blue solid) are shown.

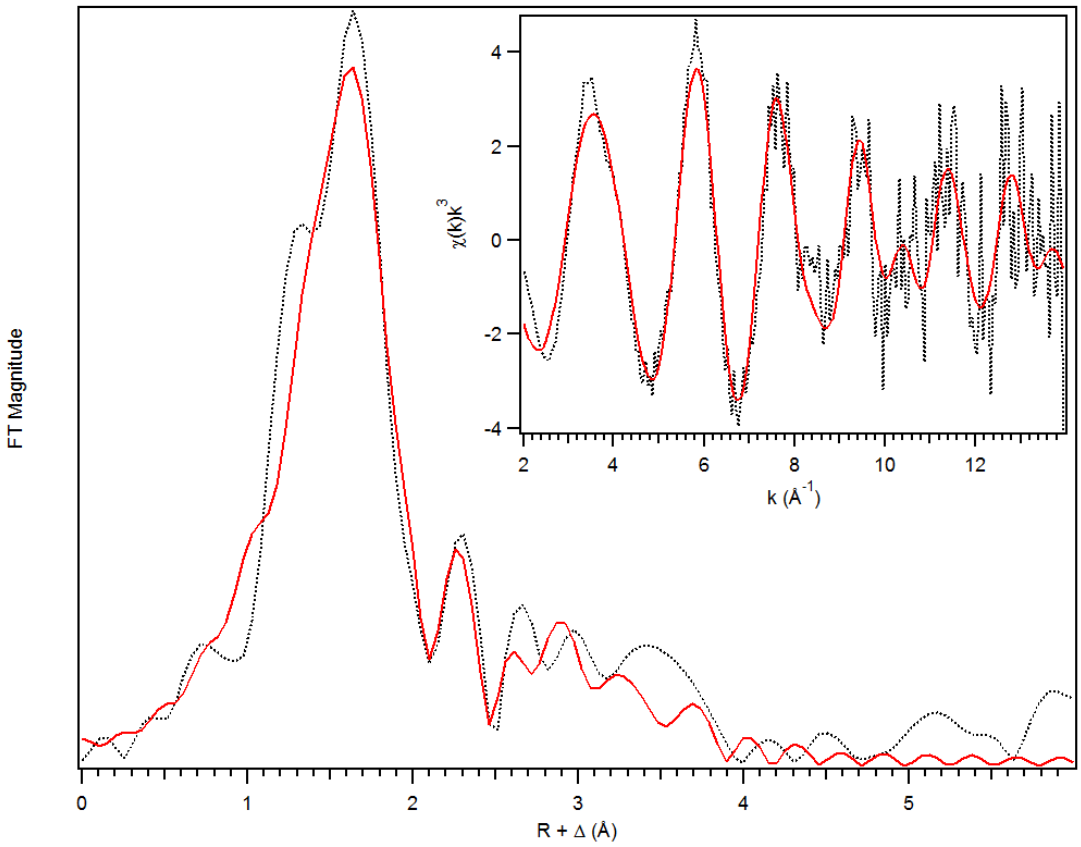

Figure 4.16. Fit (red solid line) of the unfiltered (black dotted) EXAFS data (inset) and corresponding Fourier transform of **CmII^{R}** (Table 4.5, Fit 17). Data was fit between k = 2 – 14 Å^{-1}.

Table 4.5. Fit parameters for the unfiltered EXAFS data of **CmlI^{R}**, between k = 2 – 14 Å^{-1}. Fit 17 gives the most reasonable fit of the experimental data.

	Fe-N			Fe-O			Fe•••Fe			Fe•••C				GOF	
Fit	N	R(Å)	$\sigma^2(10^{-3})$	N	R(Å)	$\sigma^2(10^{-3})$	N	R(Å)	$\sigma^2(10^{-3})$	N	R(Å)	$\sigma^2(10^{-3})$	E_o	F	F'
1	6	2.10	7.61										-10.3	300	568
2	5	2.10	6.23										-9.53	304	572
3	4	2.11	4.81										-8.82	323	590
4	3	2.11	3.31										-8.22	365	627
5	3	2.12	2.60	1	2.01	2.03							-9.71	304	572
6	4	2.11	4.06	1	1.98	4.40							-11.2	288	557
7	5	2.10	4.99	1	1.94	5.01							-12.8	281	550
8	4	2.11	4.03	2	1.97	7.33							-13.6	274	544
9	4	2.13	4.87	1	2.02	4.61				3	3.11	4.20	-8.72	257	527
10	4	2.12	4.83	1	2.01	6.35				3	3.14	0.93	-9.05	240	509
										3	2.99	3.97			
11	4	2.12	4.76	1	2.00	5.61				3	3.15	0.87	-9.66	226	493
										3	2.99	3.68			
										1	2.59	1.38			
12	4	2.12	4.76	1	2.01	4.90	1	3.34	9.20	3	2.99	2.77	-8.88	221	487
										5	3.15	2.08			
										1	2.60	0.85			
13	4	2.12	5.01	1	2.01	5.90	1	3.35	9.54	5	3.15	2.62	-9.10	210	475
										3	2.99	3.50			
										1	2.60	1.41			
										4	4.01	1.06			
14	4	2.12	4.80	1	2.00	5.54				5	3.13	3.88	-9.61	217	484
										3	2.96	4.31			
										1	2.60	2.07			
										4	4.02	1.30			

Table 4.5. (continued) Fit parameters for the unfiltered EXAFS data of **CmlI^{R}**, between k = 2 – 14 Å^{-1}. Fit 17 gives the most reasonable fit of the experimental data.

	Fe-N			Fe-O			Fe•••Fe			Fe•••C				GOF	
Fit	N	R(Å)	$\sigma^2(10^{-3})$	N	R(Å)	$\sigma^2(10^{-3})$	N	R(Å)	$\sigma^2(10^{-3})$	N	R(Å)	$\sigma^2(10^{-3})$	E_o	F	F'
15	4	2.12	4.91	1	2.01	6.72	1	3.34	9.73	5	3.15	2.23	-9.04	223	490
										3	2.99	3.16			
										4	4.00	1.49			
16	4	2.13	5.11	1	2.02	3.96	1	3.38	10.36	5	3.13	7.48	-8.09	227	495
										4	4.02	1.32			
										1	2.61	1.36			
17	**5**	**2.10**	**5.02**	**1**	**1.94**	**5.35**	**1**	**3.35**	**9.90**	**1**	**2.58**	**1.35**	**-12.0**	**206**	**470**
										3	**2.98**	**2.76**			
										5	**3.14**	**2.48**			
										4	**3.99**	**1.15**			
18	4	2.11	4.71				1	3.35	8.37	1	2.60	1.08	-7.27	233	501
										3	3.00	2.37			
										5	3.16	1.74			
										4	4.02	0.75			
19	5	2.11	4.75	1	1.94	4.36	1	3.34	8.55	0.5	2.58	-2.50	-11.7	198	462
										3	2.99	1.03			
										5	3.14	1.15			
										4	3.99	3.31			

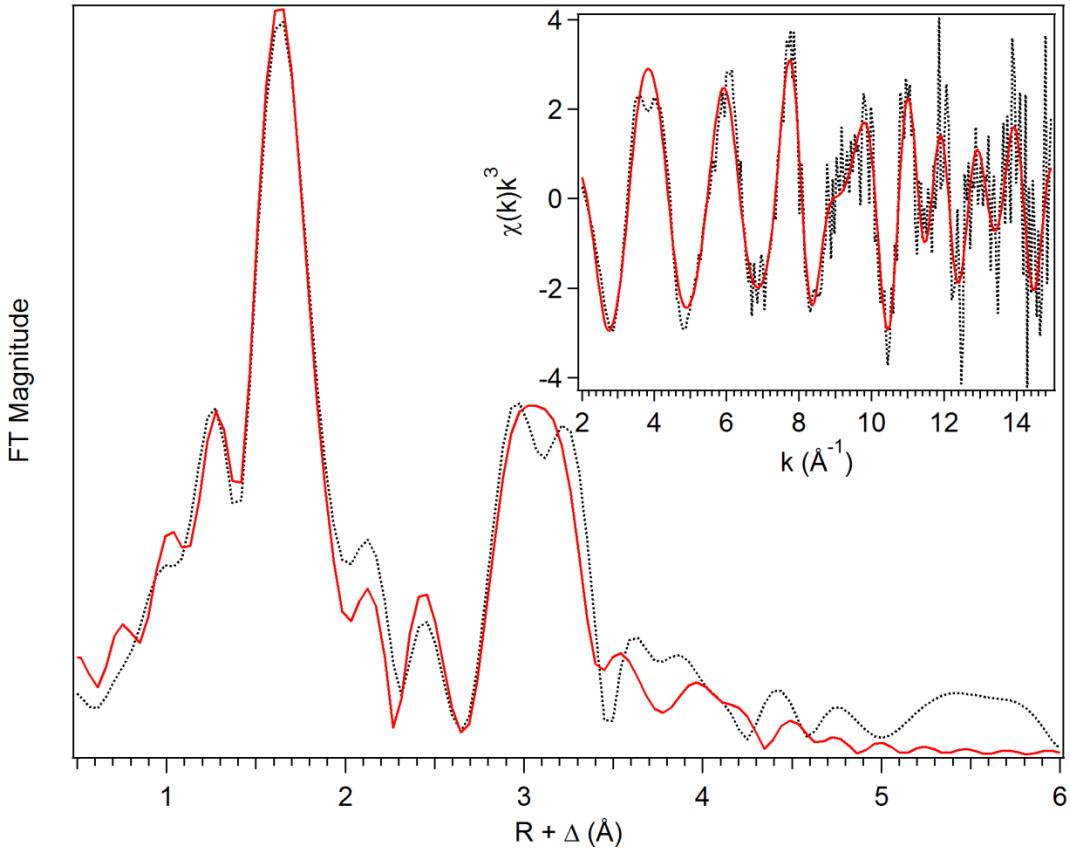

Figure 4.17. Fit (red solid line) of the unfiltered (black dotted) EXAFS data (inset) and corresponding Fourier transform of **CmlI^{Ox}** (Table 4.6, Fit 15). Data was fit between k = 2 – 15 Å^{-1}.

Table 4.6. Fit parameters for the unfiltered EXAFS data of **CmlI^{Ox}**, between k = 2 – 15 Å^{-1}. Fit 15 gives the most reasonable fit of the experimental data.

	Fe-N			Fe-O			Fe•••Fe			Fe•••C				GOF	
Fit	N	R(Å)	$\sigma^2(10^{-3})$	N	R(Å)	$\sigma^2(10^{-3})$	N	R(Å)	$\sigma^2(10^{-3})$	N	R(Å)	$\sigma^2(10^{-3})$	E_o	F	F'
1	6	2.11	10.64										0.50	408	704
2	5	2.11	8.68										1.22	388	687
3	4	2.12	6.92										1.88	383	682
4	3	2.12	5.26										2.46	404	701
5	4	2.11	6.58	1	1.95	18.06							-0.27	378	678
6	3	2.17	2.44	1	2.03	-0.50							2.26	3.57	659
7	3	2.18	4.56	2	2.04	3.92							1.33	388	687
8	3	2.16	1.74	2	2.02	0.74							-2.42	331	635
				1	1.84	3.15									
9	3	2.16	1.96	2	2.02	0.94	1	3.31	2.52				-1.78	248	550
				1	1.85	3.63									
10	3	2..17	2.19	2	2.03	1.16	1	3.31	2.35	2	3.12	3.67	-0.76	239	538
				1	1.85	4.45									
11	3	2.15	1.82	2	2.01	0.98	1	3.31	3.20	2	3.07	10.44	-2.85	209	504
				1	1.84	3.08				3	3.57	1.14			
12	3	2.16	1.77	2	2.01	0.99	1	3.32	3.53	2	3.06	9.28	-2.39	190	481
				1	1.84	3.22				3	3.58	0.55			
										3	4.29	1.07			
13	3	2.15	1.79	2	2.01	0.99	1	3.32	3.22	2	3.07	10.95	-2.65	191	481
				1	1.84	3.16				4	3.57	1.70			
										3	4.29	1.18			
14	3	2.17	2.10	2	2.03	1.11	1	3.31	2.40	2	3.12	3.36	-0.74	230	528
				1	1.85	4.28				3	4.31	3.17			
15	**3**	**2.15**	**1.73**	**2**	**2.00**	**0.97**	**1**	**3.32**	**3.38**	**4**	**3.57**	**1.39**	**-3.79**	**196**	**488**
				1	**1.83**	**2.71**				**3**	**4.28**	**1.04**			

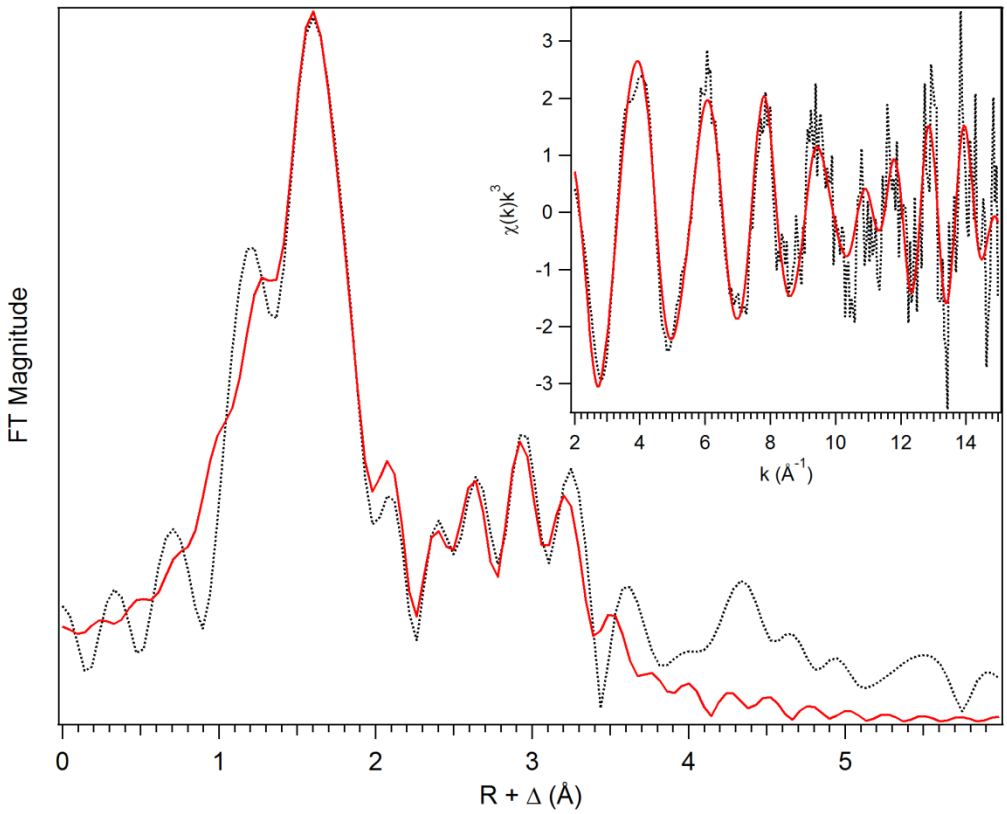

Figure 4.18. Fit (red solid line) of the unfiltered (black dotted) EXAFS data (inset) and corresponding Fourier transform of **CmlI^{P}** (Table 4.7, Fit 23). Data was fit between k = 2 – 15 Å^{-1}.

Table 4.7. Fit parameters for the unfiltered EXAFS data of **CmIII^{P}**, between k = 2 – 15 Å^{-1}. Fit 23 gives the most reasonable fit of the experimental data.

	Fe-N			Fe-O			Fe•••Fe			Fe•••C				GOF	
Fit	N	R(Å)	$\sigma^2(10^{-3})$	N	R(Å)	$\sigma^2(10^{-3})$	N	R(Å)	$\sigma^2(10^{-3})$	N	R(Å)	$\sigma^2(10^{-3})$	E_o	F	F'
1	5	2.08	12.13										1.63	202	615
2	4	2.09	9.45										2.62	199	610
3	3	2.10	6.99										3.64	211	629
4	5	2.08	9.28	1	1.86	9.72							-0.65	188	594
5	5	2.08	8.96	2	1.86	14.71							-2.53	190	599
6	4	2.10	7.67	1	1.91	9.84							0.24	187	593
7	4	2.10	7.77	2	1.91	15.33							-1.50	187	592
8	3	2.12	5.25	1	1.97	4.90							1.71	191	599
9	3	2011	6.41	2	1.96	13.93							-0.59	187	593
10	3	2.13	2.58	2	1.98	2.05							-3.21	175	573
				1	1.82	3.58									
11	3	2.12	2.10	1	1.99	-0.20							-3.64	176	574
				2	1.88	9.04									
12	3	2.12	2.54	2	1.97	1.97	1	2.83	17.88				-3.29	172	568
				1	1.82	3.39									
13	3	2.13	2.54	2	1.98	1.98	1	3.37	35.99				-3.14	175	572
				1	1.82	3.54									
14	3	2.13	3.32	2	1.99	2.76	1	3.11	21.89				-2.23	154	536
				1	1.83	4.53									
				1	2.83	0.21									

Table 4.7. (continued) Fit parameters for the unfiltered EXAFS data of **CmlI^{P}**, between k = 2 – 15 Å^{-1}. Fit 23 gives the most reasonable fit of the experimental data.

	Fe-N			Fe-O			Fe•••Fe			Fe•••C				GOF	
Fit	N	R(Å)	$\sigma^2(10^{-3})$	N	R(Å)	$\sigma^2(10^{-3})$	N	R(Å)	$\sigma^2(10^{-3})$	N	R(Å)	$\sigma^2(10^{-3})$	E_o	F	F'
15	3	2.13	2.72	2	1.98	2.53	1	3.29	10.99	1	3.11	-2.30	-2.29	124	483
				1	1.82	4.54									
				1	2.82	3.75									
16	3	2.14	3.22	2	1.99	3.02	1	3.30	6.34	3	3.12	1.69	-0.99	133	499
				1	1.83	5.44									
				1	2.84	1.50									
17	3	2.13	2.84	2	1.98	2.50	1	3.11	7.61	3	3.34	0.91	-2.36	122	478
				1	1.83	4.47									
				1	2.83	1.23									
18	3	2.13	2.41	2	1.98	1.98	1	3.34	4.23	3	3.14	4.38	-2.40	118	469
				1	1.82	3.80				3	3.55	1.85			
				1	2.82	1.81									
19	3	2.12	6.25	2	1.96	12.77	1	3.30	5.03	3	3.12	1.55	0.43	130	494
				1	2.85	1.14				3	3.49	9.49			
20	3	2.13	1.98	2	1.97	1.52	1	3.33	2.88	3	3.15	2.58			
				1	1.8	3.09									
21	3	2.13	2.81	2	1.98	2.45	1	3.1	7.66	3	3.34	0.90	-2.42	118	470
				1	1.82	4.36				3	3.78	23.62			
				1	2.83	1.22									

Table 4.7. (continued) Fit parameters for the unfiltered EXAFS data of **CmIII^{P}**, between k = 2 – 15 Å^{-1}. Fit 23 gives the most reasonable fit of the experimental data.

	Fe-N			Fe-O			Fe•••Fe			Fe•••C				GOF	
Fit	N	R(Å)	$\sigma^2(10^{-3})$	N	R(Å)	$\sigma^2(10^{-3})$	N	R(Å)	$\sigma^2(10^{-3})$	N	R(Å)	$\sigma^2(10^{-3})$	E_o	F	F'
22	3	2.13	2.47	2	1.98	2.03	1	3.34	4.44	3	3.14	4.84	-2.11	109	451
				1	1.83	3.93				3	3.56	1.65			
				1	2.82	1.54				3	4.39	4.64			
23	**3**	**2.13**	**2.50**	**2**	**1.98**	**2.09**	**1**	**3.35**	**4.47**	**3**	**3.14**	**4.87**	**-1.86**	**111**	**456**
				1	**1.83**	**4.05**				**3**	**3.56**	**1.46**			
				1	**2.82**	**1.50**				**3**	**4.28**	**5.12**			
24	3	2.13	2.43	2	1.97	1.95	1	3.12	8.77	3	3.34	0.43	-3.59	116	465
				1	1.82	3.50				3	3.54	8.78			
				1	2.82	1.47				3	4.08	14.75			
25	3	2.14	2.89	2	1.99	2.52	1	3.57	7.75	3	3.12	4.61	-177	113	459
				1	1.83	4.66				3	3.34	1.43			
				1	2.82	0.98				3	3.97	5.76			
26	3	2.13	2.05	2	1.98	1.66	1	3.33	3.03	3	3.15	2.90	-2.79	130	493
				1	1.82	3.51				3	3.54	1.85			
										3	4.25	4.99			
27	3	2.14	3.25	2	1.99	3.03	1	3.30	6.45	3	3.12	1.71	-0.87	131	496
				1	1.84	5.59				3	4.29	8.00			
				1	2.84	1.43									
28	3	2.14	3.38	2	1.99	2.97				3	3.09	3.59	-1.24	142	516
				1	1.84	5.24				3	3.60	2.10			
				1	2.83	0.17				3	4.30	5.64			
29	3	2.14	2.81	2	1.99	2.37	1	3.36	4.55	3	3.15	7.15	-1.70	111	456
				1	1.83	4.56				3	3.57	0.86			
				0.5	2.82	-1.50				3	4.28	4.91			

Chapter 5 : Spectroscopic Studies of Synthetic Nonheme Iron Complexes

5.1 – Introduction

Synthetic nonheme iron complexes have been synthesized, in part, as a means to study interesting enzymatic intermediate species. Model complexes have the benefit of being synthetically customizable to adjust properties like solubility, sterics, and electronics. Moreover, these complexes are tolerant to conditions that would simply not be possible to use in enzymatic systems, such as temperatures below 0 ºC, extremes of pH, and use of organic solvents. These conditions allow for synthetic intermediate species to be stabilized and ultimately trapped along a target reaction pathway. The trapped intermediates can then be spectroscopically probed to obtain parameters that can be used to compare to enzymatic intermediates. The development of a large library of well characterized model complexes helps to identify and understand the properties and the chemistry of fleeting enzymatic intermediates.

X-ray absorption spectroscopy (XAS) was used to characterize various synthetic nonheme iron intermediates, and the analyses are presented herein. The XAS data helps to construct a working structural model of transient iron containing species. This type of characterization adds to the growing library of nonheme iron intermediates, and may help in the characterization and understanding of new enzymatic intermediates.

XAS provides two different sets of information, one set is the X-ray absorption near edge structure (XANES) and the other set is the extended X-ray absorption fine structure (EXAFS). The XANES region for iron covers the energy range from ~7100 eV to 7160 eV and includes the rising edge as well as the pre-edge region. The rising edge is where the K-edge energy is extracted, which is the energy required to liberate a core 1s electron from the metal center. This energy provides information about the relative electronic environment of a transition metal center, including oxidation state. Although, oxidation state is not the only factor that will affect the K-edge energy, as ligand identity and hardness,[39] effective nuclear charge,[40] metal-ligand bond length,[41] and the spin state of the metal[42] all affect this parameter. Before the rising edge there is a formally forbidden 1s → 3d transition in transition metal complexes called the pre-edge peak.[147]

This pre-edge peak will increase in intensity the further the metal center is distorted from a centrosymmetric environment.[186] The K-edge energy and the area of the pre-edge peak are sensitive tools for the analysis of coordination environment of iron containing samples.

The EXAFS region, which for Fe includes the energy range from ~7160 eV up to and beyond 8000 eV, provides the scattering distances from ligands and close contacts near the metal center. These scattering distances are averaged across all Fe containing species within a particular sample, so the purity of a sample is critical for accurate interpretation of the XAS data. EXAFS distances are initially extracted from the collected data set and must be pieced together and placed into a structural context to generate a working model. This process can be complicated if you have multiple Fe centers, either from several different species in the sample, or from a single dinuclear intermediate. In the case of a dinuclear intermediate, an assumption is made that the two metal centers are identical with respect to the working model. In this chapter, the dinuclear models will therefore have one Fe center (shown on the left) with scattering atoms displayed as well as a naked Fe center (on the right) that is assumed to have the same scattering interactions as the first. Once this working model is generated, a 3-D version is made, which is usually derived from existing relevant crystal structures. The 3-D model is then used to calculate accurate phase and amplitude parameters for the specific sample, and these parameters are used to fit the experimental EXAFS data and acquire the best fit distances. The record of the fitting process, including the best fit distances, is summarized in tables throughout the chapter. The fitted parameters are the Fe-scattering atom distance (R), the mean squared deviation or Debye-Waller factor (σ^2), and the edge shift (E_0). The R parameter is the distance between the Fe center and the particular scattering atom and the σ^2 reflects the flexibility of a particular scattering distance with a small positive value (closer to 1.0×10^{-3} Å^2) being reflective of a well ordered scatterer. As the σ^2 value increases, this can be interpreted as a single type of scattering atom (e.g. 5 C scatterers at 3.00 Å) having an average of a wide range of values

(from 2.95 Å to 3.05 Å) or a single distance that is the average of several types of scatterers that cannot be resolved from each other (e.g. 2 O scatterers at 2.15 Å, 1 N at 2.10 Å and 2 O at 2.05 Å that fit as 5 N/O scatterers at 2.10 Å). The limit of resolution (ΔR) for distinguishing two scattering distances within a single fit is given by:

$$\Delta R = \frac{\pi}{2\Delta k}$$

where Δk is the difference in the k range used for data analysis. As the k range is increased (which corresponds to more collected data), two scattering distances become easier to distinguish and will not be averaged together. The E_0 value represents how much the fitting model needs to be shifted from the experimental data in order to acquire an adequate fit, and ideally this value should be close to zero. There are two goodness of fit (GOF) parameters *F* and *F*' that are minimized as part of the fitting protocol. *F* is a residual measurement that assesses difference between the experimental and fitted data, and *F*' additionally takes into account the number of parameters that are used to fit the experimental data. The best fit of the experimental data is determined by a reasonable chemical assessment of the R and σ^2 values for a fit; additionally, the change in the E_0, *F* and *F*' parameters is considered.

5.2 – Experimental

All chemicals were purchased from commercial vendors and used as received, unless noted otherwise. 2-(tertbutylsulfonyl)iodosylbenzene (sPhIO),[251] *N*-benzyl-*N*,*N*-bis(2-quinolinylmethyl)amine (BnBQA),[92] 2,6-bis[(2,6-dimethylphenyl)methyl]-4-*tert*-butylbenzoate ($dxlCO_2^-$),[93] 1,2-bis[2-{bis(2-pyridylmethyl)amino-methyl}-6-pyridyl]ethane (6-HPA),[252] 1-(2-pyridylmethyl)-4,7-dimethyl-1,4,7-triazacyclononane (Pytacn), [253] tris(pyridylmethyl)amine (TPA),[254] *N*,*N*'-bis(2-pyridylmethyl)-*N*,*N*'-dimethyl-*trans*-1,2-di-aminocyclohexane (BPMCN),[255] tris(4-methoxy-3,5-dimethylpyridyl-2-methyl)amine (TPA*),[242] *N*-benzyl-*N*,*N*′,*N*′-tris(2-pyridylmethyl)-1,2-

diaminoethane (Bn-TPEN),[256] and $[Fe^{II}(NCMe)_2(OTf)_2]$[257] were prepared following previously published procedures.

5.2.1 – Sample Preparation

$[(BnBQA)_2Fe^{III}_2(O)(O_2)(NCMe)_2](OTf)_2$ (1) and **$[(BnBQA)_2Fe^{III}_2(HO)(O_2)(NCMe)_2](OTf)_3$** (**2**) were prepared as reported by Cranswick, et al.[110]

$[(BnBQA)_2Fe^{III}_2(O)(O_2)(NCMe)_2](OTf)_2 + Cl^-$ (1-Cl) was prepared by generating **1** then adding 2 equivalents (eq.) of $(Bu)_4NCl$ to the solution in MeCN. The 4 mM $[Fe]_T$ sample (~80% yield) was prepared at -40 °C. The brown-red colored sample was transferred into an XAS cup with a chilled pipette and was frozen in liquid nitrogen. LQAJJ01

$[(BnBQA)_2Fe^{III}_2(HO)(O_2)(NCMe)_2](OTf)_3 + Cl^-$ (2-Cl) was prepared by generating **1** and adding 2 eq. of $HClO_4$ to generate **2**. Then 2 eq. of $(Bu)_4NCl$ were added to the solution in MeCN. The 4 mM $[Fe]_T$ sample (~80%) was prepared at -40 °C. The light green colored sample was transferred into an XAS cup with a chilled pipette and was frozen in liquid nitrogen. LQAJJ02

$[(BnBQA)_2Fe^{III}_2(O)(O_2)(NCMe)_2](OTf)_2 + Sc^{3+}$ (1-Sc) was prepared by first generating **1** then adding 1 eq. of $Sc(OTf)_3$, which caused a new species to form with clean isosbestic points in the UV-vis spectrum. The solution of $Sc(OTf)_3$ was prepared by dissolving the dry solid into anhydrous MeCN. The 5 mM $[Fe]_T$ sample (~70%) was prepared at -40 °C and a chilled pipette was used to transfer the brown-green colored sample into an XAS cup and was frozen with liquid nitrogen. LQAJJ16

$[Fe^{III}_2(O_2)(dxlCO_2^-)_4(THF)_2]$ (3) was prepared by Alireza Shokri using a published procedure.[93] The 16 mM $[Fe]_T$ sample was generated at -80 °C in anhydrous toluene with

quantitative yield. The brown-red colored sample was transferred into an XAS cup with a chilled pipette and was frozen in liquid nitrogen. LQAS04

$[Fe^{III}_2(O_2)(dxlCO_2^-)_4(Py)_2]$ (4) was prepared by Ferman Chavez using a published procedure.[93] The 30 mM $[Fe]_T$ sample was prepared at -80 °C in anhydrous toluene, transferred into an XAS cup and frozen with liquid nitrogen. FAC041

$[Fe^{III}_2(O)(6\text{-}HPA)(OH_2)](ClO_4)_4$ (5) was prepared by Jai Prakash using a published procedure.[252]The solid **5** was dissolved into MeCN at room temperature for a final $[Fe]_T$ of 5 mM. The solution was then transferred to an XAS cup and frozen in liquid N_2. LQJP-Kodera-2

$[Fe^{III}_2(O)(6\text{-}HPA)(OBz)](ClO_4)_3$ (6) was prepared by Jai Prakash using a modified synthesis based on a published procedure.[243] To a reaction flask 6-HPA and $Fe^{III}(ClO_4)_3$ were added to methanol in a 1:2 molar ratio. The solution was stirred for 15 min, then 1 equivalent (with respect to 6-HPA) of ammonium benzoate (NH_4OBz) was added. The resulting solution was allowed to slowly evaporate in air over a week, which yielded diffraction quality crystals. The crystal structure was solved by Greg Rohde. The XAS sample was prepared by grinding a 1:9 (10mg:90mg) mixture of solid **6** and boron nitride into a fine powder. The powder was then tightly packed into a solid sample cell, sealed with kapton tape, and frozen in liquid N_2. Fe2O6HPAOBz

$[Fe^{III}_2(O)(O_2)(6\text{-}HPA)](ClO_4)_2$ (7) was prepared by Jai Prakash using a published procedure.[89] (JACS 2012 134 13236} A 2 mM solution ($[Fe]_T$ = 4 mM) of **5** is prepared at -40 °C in MeCN. To that solution, 2 equivalents of triethylamine and 1.5 equivalents of 30% H_2O_2 are added to generate **7** in near quantitative yield. A chilled pipette was then used to transfer **7** to an XAS cup which was frozen with liquid N_2, making a dark green/blue color sample. Jai-Kodera-3

[Fe^{IV}(O)(L)(Pytacn)]$(OTf)_2$ (8) (L = MeCN or H_2O) was prepared using a published procedure[258] with [$Fe^{II}(OTf)_2$(Pytacn)] provided by the Miquel Costas lab. A 5 mM solution of [$Fe^{II}(OTf)_2$(Pytacn)] was prepared in MeCN at 15 °C and 2 eq of CH_3CO_3H was added to the solution to generate **8** in ~85% yield based on the molar extinction coefficient for the species. The greenish brown solution was then transferred to a XAS cup and frozen in LN_2, maintaining the green color. LQAJJ03

[Fe^{IV}(O)(L)(Pytacn)]$(NO_3)_2$ (9) (L = MeCN or H_2O) was prepared using [$Fe^{II}(NO_3)_2$(Pytacn)] provided by Zoel Codolà (Miquel Costas lab). A 8.7 mM solution of [$Fe^{II}(NO_3)_2$(Pytacn)] was prepared in 2 mL of a 1:1 MeCN:H_2O solvent mixture at 20 °C. A 0.2 M stock solution of $(Bu)_4N(IO_4)$ dissolved in 2.61 M, 70% HNO_3 was prepared, and 1.1 eq of $(Bu)_4N(IO_4)$ was added to the Fe^{II} complex to generate the oxoiron(IV) complex **9** in quantitative yield. Final solution concentrations: [Fe] = 0.0087 M, [HNO_3] = 0.124 M, [IO_4] = 0.0095 M, [H_2O] = 28.8 M. The blue-green solution was transferred to an XAS cup and frozen in LN_2. The frozen sample was a light white green color. LQAJJ05

[Fe^{II}(Pytacn)$(OTf)_2$] with 3 eq $(NH_4)_2Ce^{IV}(NO_3)_6$ (CAN) (10) was prepared by Julio Lloret-Fillol. [Fe^{II}(Pytacn)$(OTf)_2$] (7.45 mg) was dissolved into 1.6 mL of MeCN. CAN (25 mg) was dissolved into 600 μL of MeCN. Triflic acid (TfOH, 1.5 mL) was diluted into 5 mL of Milli-Q water. To a vial, 1.44 mL of the Fe solution, 550 μL of the CAN solution and then 375 μL of the TfOH solution were added to form an oxoiron(IV)-Ce adduct at 25 ºC, with an absorption feature at 755 nm. Final concentrations: [Fe] = 4.71 nm; [CAN] = 17.7 nm, 3.8 eq; [TfOH] = 1.02 M, 216 eq; [H_2O] = 6.8 M, 1440 eq. The purple-gray solution was then transferred to an XAS cup and frozen in LN_2. The color of the frozen solid was a lighter tan color. LQJLF02

[Fe^{II}(Pytacn)$(OTf)_2$] with 9 eq $(NH_4)_2Ce^{IV}(NO_3)_6$ (CAN) (11) was prepared similarly to **10**. [Pytacn Fe(II)$(OTf)_2$] (7.40 mg) was dissolved into 800 μL of Milli-Q water and 800 μL of MeCN. TfOH (3 mL) was diluted into 10 mL of Milli-Q water for a [TfOH] = 2.6 M. CAN (58.3 mg) was dissolved into 600 μL of 2.6 M TfOH solution. To a vial, 1.4 mL of the Fe solution, 550 μL of the CAN solution, and then 300 μL of the 2.6 M TfOH solution were added to generate the oxoiron(IV)-Ce adduct species at 20 ºC. Final concentrations: [Fe] = 4.8 mM; [CAN] = 43.3 mM, 9 eq; [TfOH] = 0.99 M, 206 eq; [H_2O] = 33.4 M, 6990 eq. The purple-gray solution was then transferred to an XAS cup and frozen in LN_2. The color of the frozen solid was a darker tan color. LQAJJ09

[Fe^{IV}(O)(Pytacn)(L)]$(OTf)_2$ with 1 eq $(NH_4)_2Ce^{IV}(NO_3)_6$ (CAN) (12) was prepared by first generating the oxoiron(IV) species with $(Bu_4)N(IO_4)$. [Fe^{II}(Pytacn)$(OTf)_2$] (6 mg) was dissolved into a solution of 1 mL of Milli-Q water and 1 mL MeCN. $(Bu_4)N(IO_4)$ (0.1730 g) was dissolved into 2 mL of 2.6 M TfOH. 60 μL (1.2 eq) of the periodate solution was added to the Fe solution to generate the oxoiron(IV) species in ~90% yield at 20 ºC. A CAN solution was prepared (274 mg dissolved into 2 mL of 2.6 M TfOH) and 40 μL (1 eq) was added to the Fe solution to generate the oxoiron(IV)-Ce adduct. Final concentrations: [Fe] = 4.74 mM; [IO_4] = 5.71 mM, 1.2 eq; [Ce] = 4.76 mM, 1 eq; [TfOH] = 0.12 M, 26 eq; [H_2O] = 28.5 mM, 6000 eq. The greenish-brown sample was transferred into an XAS cup and frozen with LN_2. Color changed to a light tan upon freezing. LQAJJ06

[$Fe^{II}(MeCN)_2$(TPA)]$(OTf)_2$ + 3 eq of $(NH_4)_2Ce^{IV}(NO_3)_6$ (13). A sample of **13** was prepared analogously to **10**, starting from the [$Fe^{II}(MeCN)_2$(TPA)]$(OTf)_2$ complex and adding CAN. [$Fe^{II}(MeCN)_2$(TPA)]$(OTf)_2$ (14.5 mg) was dissolved into 2 mL Milli-Q water and 2 mL MeCN. A CAN solution was prepared (98.7 mg dissolved into 300 μL of 2.6 M TfOH). To 2 mL of the Fe stock solution in a cuvette were added 60 μL of the CAN solution and 55 μL of 11.3 M TfOH at 20 ºC, generating an oxoiron(IV) species in

~70% yield. Final concentrations: [Fe] = 4.72 mM; [Ce] = 17.0 mM, 3.6 eq; [TfOH] = 0.37 M, 78 eq; [H_2O] = 27.4 mM, 5820 eq. The green solution sample labeled LQAJJ14 was transferred into an XAS cup and frozen with LN_2. Color changed to orange upon freezing.

[Fe^{II}(α-BPMCN)$(OTf)_2$] + 9 eq of $(NH_4)_2Ce^{IV}(NO_3)_6$ (14). A sample of **14** was prepared by Dr. Scott Kleepsies using a published procedure.[259] The [Fe^{II}(α-BPMCN)$(OTf)_2$] complex was synthesized using a published procedure. [255] The 5-mM sample of **14** was generated at 0 °C in a solvent mixture of 1:1 MeCN:H_2O and the solution sample labled LQSK11 was transferred to an XAS cup using a chilled pipette and frozen with LN_2.

[Fe^{IV}(O)(TPA*)(L)]$^{2+}$ (L = MeCN or OTf) (15) was prepared by Caleb Allpress by the reaction of [Fe^{II}(TPA*)$_2$(MeCN)$_2$](OTf)$_2$ in MeCN solution with 1.2 eq. of sArIO in trifluroethanol at -40 °C. A 4-mM XAS sample labeled LQCA06 was generated in ~85% yield in a 20:1 MeCN:trifluoroethanol solvent mixture. The green solution labeled LQCA06 was transferred via a chilled pipette into an XAS cup and frozen in LN_2. XANES data was collected by Dr. Erik Farquhar.

[Fe^{IV}(NTs)(TPA*)(MeCN)]$^{2+}$ (16) was prepared by Mayank Puri using a modification to a published procedure.[260] To a 4.7 mM solution of [Fe^{II}(TPA*)(MeCN)$_2$]$^{2+}$ at -40 °C, 2 eq mesityl-*N*-tosyl-imidoiodinane (MsINTs) dissolved in trifluoroethanol was added. This procedure generated **16** in ~70% yield with a final solution composition of 95% MeCN and 5% trifluoroethanol. The sample labeled LQMP-585-B was transferred using a chilled pipette to an XAS cup and frozen in LN_2.

[Fe^{IV}(NTs)(BnTPEN)]$^{2+}$ (17) was prepared by Mayank Puri using a modification to a published procedure.[260] To a 4.7 mM solution of [Fe^{II}(OTf)(Bn-TPEN)](OTf) at -40 °C

was added 2 eq. of MsINTs dissolved in trifluoroethanol, generating **17** in ~75% yield with a final solution composition of 95% MeCN and 5% trifluoroethanol. The sample labeled LQMP-585-A was transferred using a chilled pipette to an XAS cup and frozen in LN_2.

5.2.2 – Physical Methods

5.2.2.1 – Data collection. Iron K-edge X-ray absorption spectra were collected at Stanford synchrotron radiation lightsource (SSRL) beam lines 7-3 (**1-Sc**, **3**, **4**, **13**, **15** – **17**) using a 30 element and 9-3 (**1-Cl**, **2-Cl**, **7**, **9**, **10**, **12**, **14**) using a 100 element solid state Ge detector (Canberra) with a SPEAR storage ring current between 350 mA and 500 mA at a power of 3.0 GeV. The incoming X-rays were unfocused using a Si(220) double crystal monochromator, which was detuned by 40% of the maximal flux to attenuate harmonic X-rays. Scans were collected from 6882 eV to 8000 eV at a temperature (10 K) that was controlled by an Oxford Instruments CF1208 continuous flow liquid helium cryostat. An iron foil was placed in the beam pathway prior to the ionization chamber I_0 and scanned concomitantly for an energy calibration, with the first inflection point of the edge assigned to 7112.0 eV. A 3 to 6 μm Mn filter and a Soller slit were used to increase the signal to noise ratio of the spectra. Photoreduction was monitored by scanning the same spot on the sample twice and comparing the first derivative peaks associated with the edge energy during collection. The number of scans acquired for each sample are as follows: **1-Cl**, 7 scans; **2-Cl**, 6 scans; **1-Sc**, 9 scans; **3**, 6 scans; **4**, 5 scans; **7**, 4 scans; **9**, 4 scans; **10**, 5 scans; **12**, 5 scans; **13**, 8 scans; **14**, 5 scans; **15**, 8 scans; **16**, 8 scans; **17**, 6 scans.

Iron K-edge X-ray absorption spectra were collected on the national synchrotron lightsource (NSLS) beam line X3B (**5**, **6**, **8**, **11**) using a 31 element solid state Ge detector (Canberra) with a SPEAR storage ring current of ~100-300 mA at a power of 2.8 GeV. A sagittally focused Si (111) double crystal monochromator was used for energy selection,

with a downstream nickel-coated mirror providing vertical focusing and rejection of higher harmonics. Scans were collected from 6882 eV to 8000 eV at a temperature (18 – 23 K) that was controlled by closed-system liquid helium Displex cyrostat. An iron foil was placed in the beam pathway prior to I_0 and scanned concomitantly for an energy calibration, with the first inflection point of the edge assigned to 7112.0 eV. A 3 to 6 μm Mn filter was used to increase the signal to noise ratio of the spectra. Photoreduction was monitored by scanning the same spot on the sample twice and comparing the first derivative peaks associated with the edge energy during collection. The number of scans acquired for each sample are as follows: **5**, 9 scans; **6**, 4 scans; **8**, 5 scans; **11**, 5 scans.

5.2.2.2 – Data processing. The detector channels from the scans were examined, calibrated, averaged, and processed for EXAFS analysis using EXAFSPAK[143] to extract χ(k). Theoretical phase and amplitude parameters for a given absorber-scatterer pair were calculated using FEFF 8.40[144] and were utilized by the "opt" program of the EXAFSPAK package during curve fitting. In all analyses, the coordination number of a given shell was a fixed parameter and was varied iteratively in integer steps, while the bond lengths (R) and mean-square deviation (σ^2) were allowed to freely float. The amplitude reduction factor S_0 was fixed at 0.9, while the edge-shift parameter E_0 was allowed to float as a single value for all shells. Thus, in any given fit, the number of floating parameters was typically equal to (2 x num shells) + 1. The goodness of fit (GOF) parameter *F* is defined by the equation:

$$F = \sqrt{\sum k^6 \left(\chi_{\exp} - \chi_{calc}\right)^2}$$

and *F*' is defined by the equation:

$$F' = \sqrt{\sum k^6 \left(\chi_{\exp} - \chi_{calc}\right)^2 / \sum k^6 \chi_{\exp}{}^2}$$

where *k* is the X-ray energy converted to wavenumbers defined by the equation:

$$k = \sqrt{\frac{2m(E - E_{abs})}{\hbar^2}}$$

where m is the mass of the electron, E is the achieved X-ray energy, E_{abs} is the absorption edge energy (7112.0 eV for Fe) and $\hbar$ is Planck's constant divided by 2π.

Pre-edge analysis was performed on data normalized in the "process" program of the EXAFSPAK package, following the procedure described by Westre et al.[44] Most of the pre-edge features were fit between 7108 eV to 7118 eV, unless specified, using the Fityk[145] program with pseudo-Voigt functions composed of 50:50 Gaussian/Lorentzian functions. One function was fit as the baseline modeling the rising edge underneath the pre-edge peak and additional functions were used to fit the remaining pre-edge feature. The area was calculated by multiplying the height and the full width at half-maximum (FWHM) of each fitted function, adding these component functions together and multiplying by 100 to achieve convenient values.

5.3 – Results and Discussion

5.3.1 – XAS Analysis of μ-1,2-Peroxo Species Supported by the BnBQA Ligand

5.3.1.1 – XAS analysis of 1-Cl. The K-edge energy of **1-Cl** was found to be 7122.8 eV. This falls below the range for peroxo-diferric complexes, as other (μ-oxo)(μ-1,2-peroxo)diferric species have K-edge energies of about 7124 eV.[105, 110] However, Cl^- is interacting with the Fe in this sample (see below) and it is known that chloride and sulfide ligands will decrease the K-edge energies of transition metal complexes.[186]

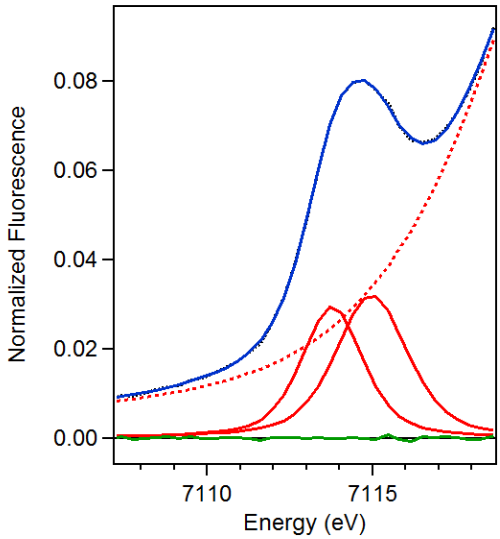

Figure 5.1. Pre-edge region analysis of **1-Cl**. The experimental data (black dotted), baseline (red dashed), pre-edge peak components (red solid), residuals (green solid) and total fit (blue solid) are shown.

The pre-edge peak has a maximum at 7114.6 eV and was fit with two functions to model the peak with a combined area of 14.9 units (Figure 5.1). This value is within the range for six-coordinate synthetic peroxo-diferric complexes, which have pre-edge areas between 13 and 15 units.[105, 110]

Table 5.1. Pre-edge peak component analysis of **1-Cl**.

Peak Position (eV)	Peak Area (units)	Relative Area
7113.8	6.66	1.00
7115.0	8.26	1.24

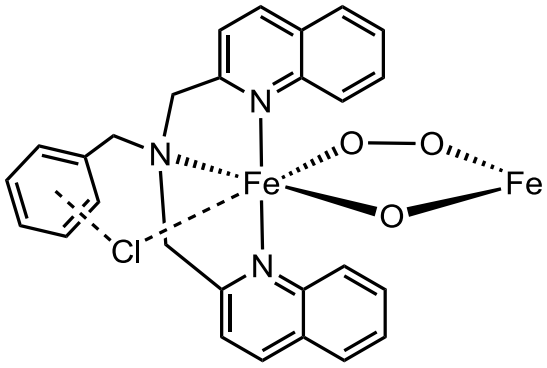

Figure 5.2. Working model of **1-Cl**.

The EXAFS analysis of **1-Cl** is summarized in Table 5.2 and Figure 5.3. The 3-D model used for FEFF calculation was modified from the crystal structure of the bis(μ-hydroxo)diferrous precursor complex.[92] The best fit of the sample (Table 5.2, fit 12) gives scattering pair distances that correspond to 4 Fe–N/O at 2.25 Å, 1 Fe–N/O at 1.86 Å, 1 Fe•••Cl at 2.74 Å, 2 Fe•••C at 2.85 Å, and 1 Fe•••Fe at 3.18 Å. This fit has similarities to the fit reported for the parent complex **1**, in that the Fe–N scatterers (2.25 Å vs 2.21 Å), Fe–O scatterers (1.86 Å vs 1.81 Å) and the Fe•••Fe distances (3.18 Å vs 3.16 Å) are nearly identical. However, the C shells for **1** and **1-Cl** decrease from 2.99 Å to 2.85 Å, respectively, and in addition a Fe•••Cl scatterer at 2.74 Å is also required for the best fit of **1-Cl**. The 2.85 Å and 2.74 Å scatterers ($\Delta R = 0.11$ Å) are just outside of the resolution of the EXAFS data (0.12 Å), but inclusion of the Cl gives a substantial improvement to the fit (fit 10 vs fit 12), and so was kept in the final fit.

Initial comparison looks like **1** and **1-Cl** have identical cores, but the contraction of the carbon shell in **1-Cl**, relative to **1** raises interesting questions. The Fe•••C scatterers of **1** at 2.99 Å correspond nicely to the aliphatic methylene linkers between the aromatic arms of the BnBQA ligand, based on comparison to the $[(BnBQA)_2Fe^{II}_2(OH)_2]^{2+}$ crystal structure (average 3.03 Å).[92] The other metrics between **1** and **1-Cl** are basically the same, so the ligand itself must be distorting in order to accommodate the 0.15 Å reduction in the Fe•••C distance of **1-Cl**. One reason for this distortion would be the introduction of the large Cl ion to the sterically crowded diiron center. The 2.74 Å Fe•••Cl distance is longer than other characterized terminally bound Fe–Cl species, as these distances tend to be between 2.3 and 2.5 Å.[261-264] Attempts to fit the Cl scatterer at ~2.3 Å were not successful, and would yield results that were unreasonable. Additionally, one might expect a larger change in the bond distances of the diiron core with anionic ligands, and no substantial changes are observed. Another possibility is that the Cl is bridging between the Fe centers. This is a common binding mode for Cl ligands, with Fe–Cl distances between 2.3 and 2.7 Å, Fe•••Fe distances between 3 and 3.7 Å and Fe–Cl–Fe angles between 70 and 100º.[265-268] Based on the EXAFS fit, a bridging Cl would have a ∠Fe–Cl–Fe in **1-Cl** of ~71º, which is on the short end of the range. Changes to the bonding distances in the diiron core would also be anticipated, as an additional bridging ligand should affect the Fe•••Fe distance, and this is not observed. A final type of interaction would be a π-interaction between the Cl and the benzyl group of the BnBQA ligand.[269] This interaction could sandwich the Cl ion between the Fe and the benzyl ring at a longer distance than would otherwise be found in a terminally bound Fe–Cl species (Figure 5.2). The rearrangement would involve a rotation of the benzyl group towards the Fe center, and could affect the position of the rest of the ligand, and in turn affect the Fe•••C distances. This type of interaction would be consistent with a change in the K-edge observed in the XANES analysis, while maintaining a similar diiron core to the parent complex.

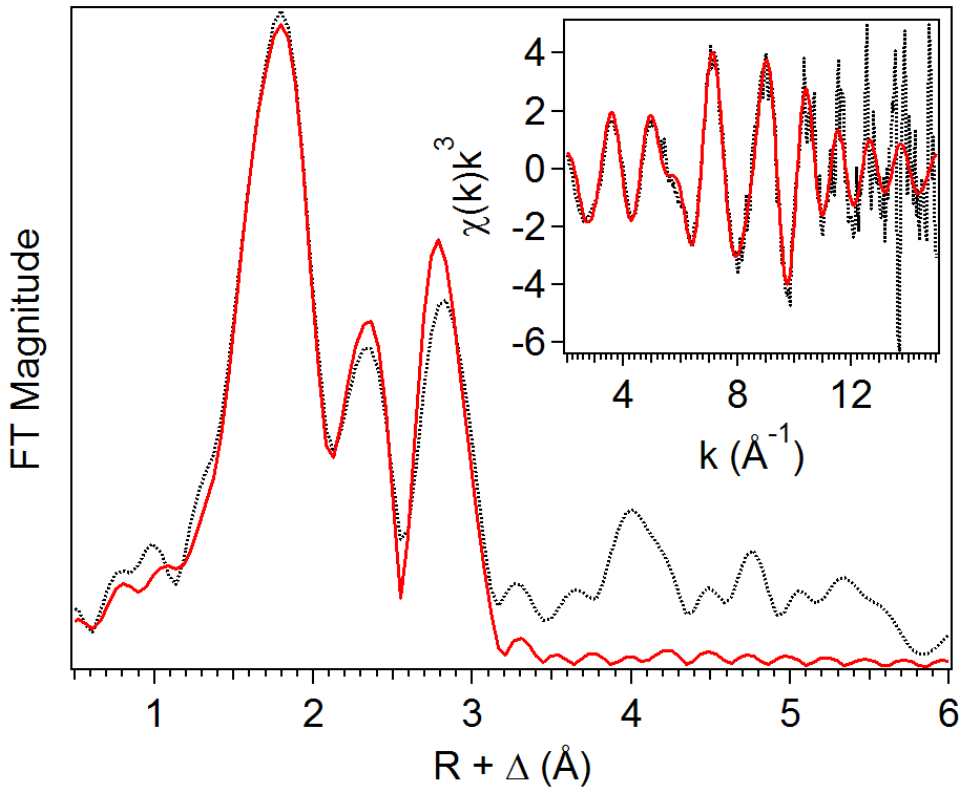

Figure 5.3. Fit (red solid line) of the unfiltered (black dotted) EXAFS data (inset) and corresponding Fourier transform (Fit 12). k = 2 – 15 $Å^{-1}$.

Overall, the EXAFS derived model is consistent with a (μ-oxo)(μ-peroxo)diferric core, with a long range Cl interaction, possibly between the Fe center and the benzyl group of the BnBQA ligand. This would fix the Cl distance so that the scatterer would still be observed without being tightly bound to the Fe center. The fit is consistent with both Fe centers having a similar interaction.

Table 5.2. EXAFS fit parameters for **1-Cl** between k = 2 – 15 $Å^{-1}$. Fit 12 gives the most reasonable fit of the data. Italicized components were fit as O atoms.

	Fe-N/*O*			**Fe-Cl**			**Fe•••Fe**			**Fe•••C**				**GOF**	
Fit	**N**	**R(Å)**	**$\sigma^2(10^{-3})$**	**N**	**R(Å)**	**$\sigma^2(10^{-3})$**	**N**	**R(Å)**	**$\sigma^2(10^{-3})$**	**N**	**R(Å)**	**$\sigma^2(10^{-3})$**	**E_o**	**F**	**F'**
1	6	2.24	7.39										-5.04	751	850
2	5	2.25	6.05										-3.06	700	820
3	4	2.25	4.75										-1.87	667	800
4	3	2.26	3.41										-1.07	661	797
5	4	2.26	5.01										0.13	525	710
	1	*1.86*	*3.79*												
6	4	2.24	4.92										-1.17	537	718
	2	*1.87*	*9.30*												
7	4	2.25	4.89										-1.00	524	709
	1	*1.86*	*3.97*												
	1	*1.93*	*49.14*												
8	4	2.26	4.87				1	3.18	3.46				0.60	435	646
	1	*1.87*	*3.91*												
9	4	2.25	4.71				1	3.15	4.39	3	2.93	2.27	-2.34	395	615
	1	*1.86*	*3.86*												
10	4	2.25	4.73				1	3.15	3.69	4	2.93	4.04	-3.01	403	622
	1	*1.86*	*3.92*												
11	4	2.25	4.52	1	2.73	2.37	1	3.17	3.58	4	2.81	12.77	-1.72	342	573
	1	*1.86*	*3.64*												
12	**4**	**2.25**	**4.47**	**1**	**2.74**	**2.48**	**1**	**3.18**	**3.68**	**2**	**2.85**	**4.48**	**-0.38**	**344**	**575**
	1	***1.86***	***3.56***												
13	4	2.26	4.70	1	2.74	3.11	1	3.18	3.39				0.96	362	589
	1	*1.87*	*3.68*												

Table 5.2 (continued). EXAFS fit parameters for **1-Cl** between k = 2 – 15 $Å^{-1}$. Fit 12 gives the most reasonable fit of the data. Italicized components were fit as O atoms.

	Fe-N/*O*			**Fe-Cl**			**Fe•••Fe**			**Fe•••C**					**GOF**
Fit	**N**	**R(Å)**	**$\sigma^2(10^{-3})$**	**N**	**R(Å)**	**$\sigma^2(10^{-3})$**	**N**	**R(Å)**	**$\sigma^2(10^{-3})$**	**N**	**R(Å)**	**$\sigma^2(10^{-3})$**	**E_o**	**F**	**F'**
14	4	2.25	4.31	2	2.76	5.83	1	3.18	3.87	4	2.86	3.58	-1.30	359	587
	1	*1.86*	*3.58*												
15	3	2.26	2.93	1	2.74	2.46	1	3.18	3.84	2	2.85	3.01	-0.05	360	587
	1	*1.86*	*3.22*												

5.3.1.2 – XAS analysis of 2-Cl. The K-edge energy of **2-Cl** was found at 7122.8 eV, which is the same as **1-Cl**. The pre-edge peak has a maximum at 7114.3 eV with an area of 14.1 units. This value, again, is close to **1-Cl** (14.9 units) and falls in the middle of the range for peroxo diferric complexes, which have pre-edge areas between 13 and 16 units. For comparison, **2** has an edge energy of 7123.3 eV with a pre edge area of 13.8 units.[110] It is interesting that **1-Cl**, **2**, and **2-Cl** all have similar XANES analysis, despite having different sample composition.

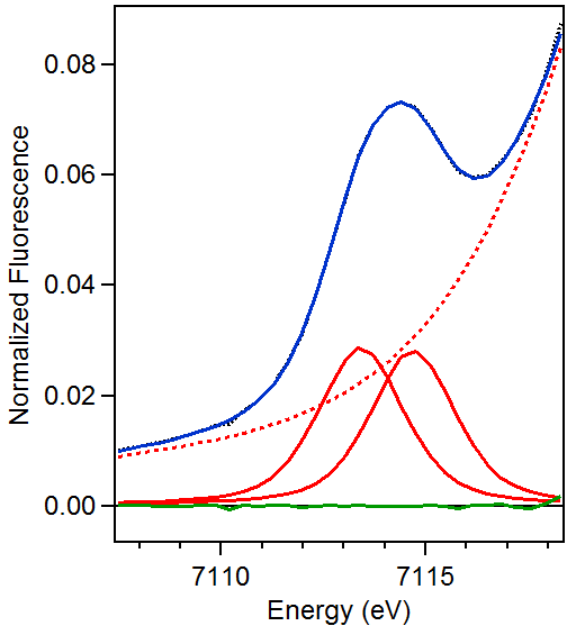

Figure 5.4. Pre-edge region analysis of **2-Cl**. The experimental data (black dotted), baseline (red dashed), pre-edge peak components (red solid), residuals (green solid) and total fit (blue solid) are shown.

Table 5.3. Pre-edge component analysis for **2-Cl**.

Peak Position (eV)	Peak Area (units)	Relative Area
7113.4	7.14	1.02
7115.0	6.95	1.00

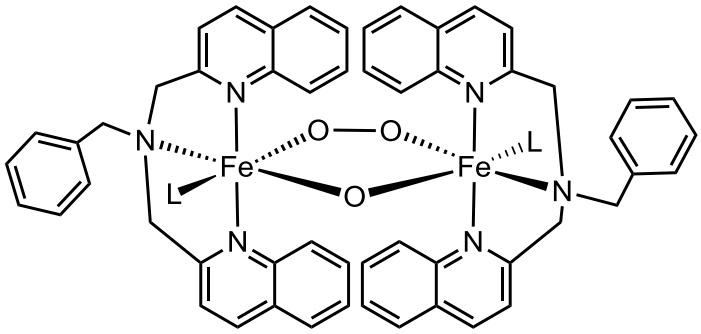

Figure 5.5. EXAFS derived model for **2-Cl**. L = solvent ligand.

The EXAFS analysis is summarized in Table 5.4 and Figure 5.5 and Figure 5.6. The 3-D model used for FEFF calculation was modified from the crystal structure of the bis(μ-hydroxo)diferrous precursor complex.[92] The FEFF analysis of the sample gives scattering pair distances that correspond to 3 Fe–N/O at 2.21 Å, 1 Fe–N/O at 1.82 Å, 2 Fe–O/N at 2.04 Å, 5 Fe•••C at 2.95 Å, and 1 Fe•••Fe at 3.12 Å. This fit has similarities to the best fit of **1**, as the Fe–N/O scatterers (2.21 Å vs 2.17 Å for **1**), the Fe–O/N scatterer (1.82 Å vs 1.81 Å for **1**), the Fe•••C scatterers (2.95 Å vs 2.94 Å for **1**) and the Fe•••Fe scatterer (3.12 Å vs 3.16 Å for **1**) are at identical within error.[110] **2-Cl** is different in that the primary Fe–N scatterers have separated into two shells, one shell at 2.21 Å and the other at 2.04 Å. Neither of these distances are consistent with Fe–Cl distances, in fact, Cl is not needed to fit the EXAFS data, or at least, is not distinct enough to be observed. Additionally, if negatively charged Cl were binding to the Fe centers, a change in the Fe•••Fe would be anticipated, and this is not observed in the experiment. The 2.21 Å distance would be consistent with the nitrogen donors of the BnBQA ligand, and the 2.04 Å distance could be consistent with a solvent ligand and the proximal peroxo oxygen atom. What is interesting is that **2-Cl** is generated by adding Cl^- to a solution of **2** and then freezing the sample, and **2** has an EXAFS fit with 2 Fe–O scatterers at 1.91 Å and a metal separation of 3.41 Å.[110] Attempts to fit **2-Cl** with an Fe•••Fe scatterer at 3.41 Å were unsuccessful.

The EXAFS derived model of **2-Cl** is consistent with, but not exactly identical to the (μ-oxo)(μ-1,2-peroxo)diferric core for **1**. While the μ-oxo bridge in **2-Cl** is the same as in **1**, the Fe–O scatterer consistent with the peroxo oxygen distance (1.91 Å for **1**) lengthens to 2.04 Å and the Fourier transform (Figure 5.6) is different from both **1**, **2**, and **1-Cl**. One possibility is that under the sample conditions, the Cl acted as a base to **2**, deprotonating the μ-hydroxo ligand to a μ-oxo ligand. **2-Cl** was generated using $HClO_4$ with a pK_a in MeCN near -1, whereas HCl has a pK_a of near 10.[270] This would be consistent with the observed scattering distances, but does not explain why **2-Cl** is fit differently than **1**. In addition, the UV-vis spectra of **2-Cl** at -40 ºC looks the same as **2**, so any change to the sample must happen during the freezing process.

Another possibility is the Cl facilitated decomposition of **2-Cl**. The bis(μ-hydroxo)diferrous starting material has bond lengths that are mostly consistent with **2-Cl**, with Fe-N distances ~2.25 Å, Fe•••Fe distance of 3.135 Å, but with Fe–OH distances of 2.090 and 1.985 Å,[92] so a diferric diamond-core species may be possible. The 1.82 Å and 2.04 Å distances would require a (μ-oxo)(μ-hydroxo/aqua)diferric core, but (μ-oxo)(μ-hydroxo) cores tend to have Fe•••Fe distances between 2.8 and 2.9 Å,[241]so this is less likely. What is clear is that this chemistry is complicated, and requires further investigation.

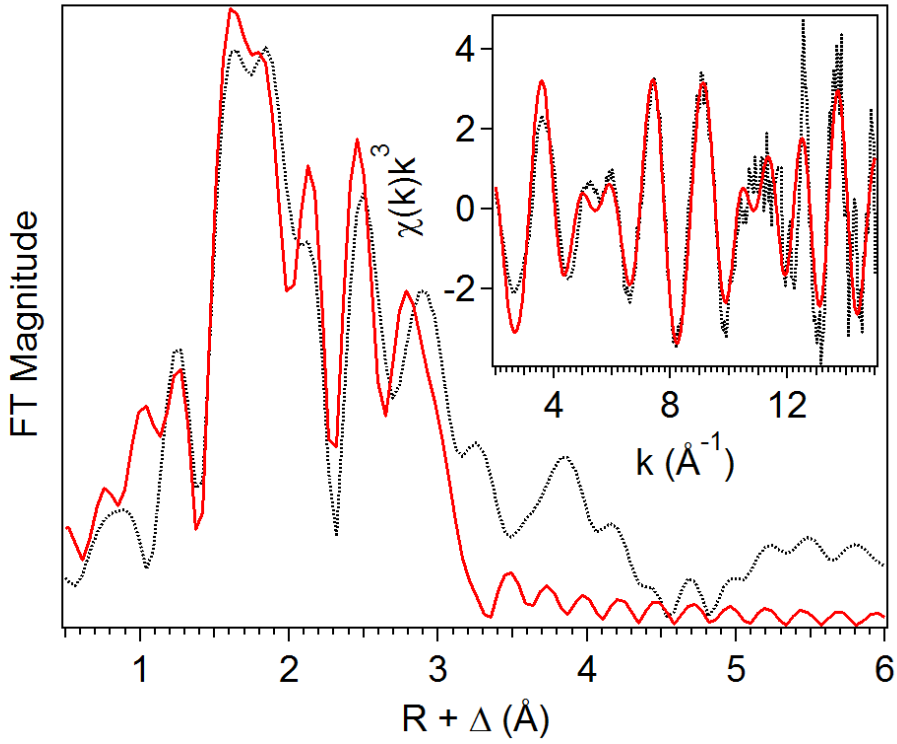

Figure 5.6. EXAFS fit of **2-Cl**. The best fit (red solid line) of the unfiltered (black dotted) EXAFS data (inset) and corresponding Fourier transform (Fit 9). k = 2 – 15 $Å^{-1}$.

Table 5.4. EXAFS fit parameters for **2-Cl** between k = 2 – 15 $Å^{-1}$. Fit 9 gives the most reasonable fit of the data.

	Fe-N			**Fe-O**			**Fe•••Fe**			**Fe•••C**				**GOF**	
Fit	**N**	**R(Å)**	**$\sigma^2(10^{-3})$**	**N**	**R(Å)**	**$\sigma^2(10^{-3})$**	**N**	**R(Å)**	**$\sigma^2(10^{-3})$**	**N**	**R(Å)**	**$\sigma^2(10^{-3})$**	**E_o**	**F**	**F'**
1	6	2.21	8.07										-0.64	522	790
2	5	2.21	6.11										0.067	467	746
3	4	2.22	4.40										0.92	423	710
4	3	2.22	2.76										1.89	403	693
5	3	2.21	2.91	1	1.84	4.91							1.61	406	696
6	3	2.20	0.04	1	1.86	2.44							-4.25	290	591
				1	2.05	-1.50									
7	3	2.21	0.70	1	1.83	0.99							-5.51	307	604
				2	2.05	3.16									
8	3	2.22	0.92	1	1.83	1.53	1	3.16	4.07				-3.19	318	616
				2	2.05	4.08									
9	**3**	**2.21**	**1.66**	**1**	**1.82**	**1.74**	**1**	**3.12**	**3.78**	**5**	**2.95**	**1.61**	**-5.62**	**180**	**465**
				2	**2.04**	**5.40**									
10	3	2.20	0.95	1	1.83	1.07				5	2.92	3.04	-7.01	257	553
				2	2.04	5.40									
11	4	2.19	2.94	1	1.83	1.49	1	3.13	3.59	5	2.95	1.87	-5.03	187	473
				1	2.01	0.66									
12	4	2.19	5.12	1	1.85	7.34	1	3.13	2.90	5	2.96	1.11	-3.05	246	542
13	3	2.20	3.10	2	1.91	25.17	1	3.12	2.93	5	2.96	1.07	-4.05	249	546

5.3.1.3 – XAS Analysis of 1-Sc. The K-edge energy of **1-Sc** was found at 7123.5 eV, which is slightly lower than the K-edge energies found for (μ-oxo)(μ-peroxo)-diferric species (7124 eV).[105, 110] Interestingly, the μ-hydroxo conjugate acid of **1** has a K-edge energy of 7123.3 eV, which is quite similar to **1-Sc**.[110] The pre-edge peak of **1-Sc** has a maximum at 7114.5 eV and was found to have an area of 13.7 units (Table 5.5). This value is within the range observed for six-coordinate diferric peroxo complexes (13 to 15 units). However, **2** has a pre edge area of 13.8 units, which again, is similar to **1-Sc**. This might suggest that the Sc^{3+} has a similar effect to the proton on **1**, possibly interacting with the μ-oxo unit.

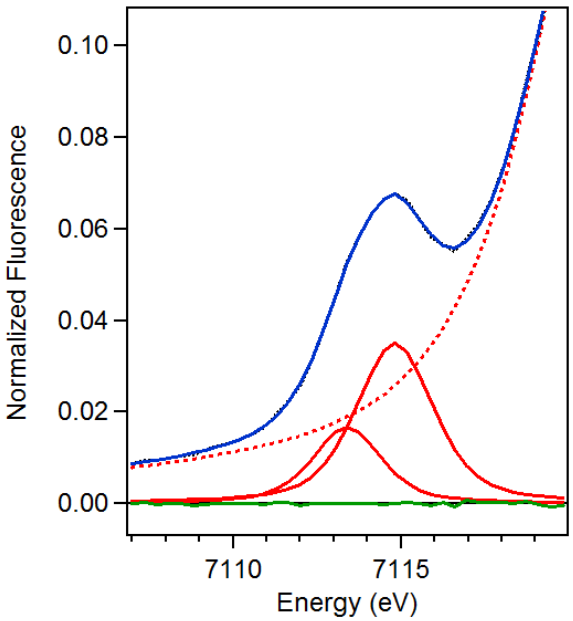

Figure 5.7. Pre-edge region analysis of **1-Sc**. The experimental data (black dotted), baseline (red dashed), pre-edge peak components (red solid), residuals (green solid) and total fit (blue solid) are shown.

Table 5.5. Pre-edge component analysis for **1-Sc**.

Peak Position (eV)	Peak Area (units)	Relative Area
7113.4	4.06	1.00
7114.8	9.61	2.37

Despite similarities in the XANES region, **1-Sc** and **2** have very different UV-vis features (Figure 5.8). **1** has λ_{max} at 505 nm and 650 nm, which have been assigned to the oxo-to-Fe and peroxo-to-Fe ligand to metal charge transfer (LMCT) transitions, respectively.[110] Upon addition of 1 equivalent of anhydrous $Sc(OTf)_3$, the intensity of the 505 nm feature decreases while a new feature at 563 nm appears, and the intensity of the 650 nm feature decreases while a less intense broad feature centered at ~770 nm appears. In contrast, **2** has a very intense chromophore centered at 735 nm, with an intense shoulder below 600 nm. This preliminarily shows that Sc^{3+} addition does not behave exactly like the addition of an acid, and affects both the oxo and peroxo LMCT transitions.

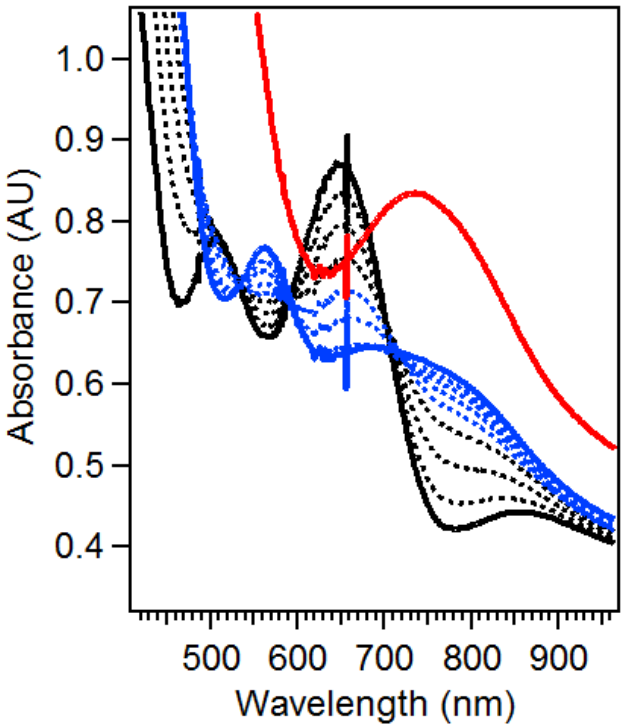

Figure 5.8. UV-vis spectrum of **1** (solid black), **1-Sc** (solid blue), and **2** (solid red). The dashes lines correspond to the conversion of **1** to **1-Sc** with 1 eq. of $Sc(OTf)_3$ added. Isosbestic points are observed at 534 and 591 nm with a pseudo-isosbestic point ~708 nm. Features: **1**, 505, 650, 860 nm; **1-Sc**, 563, 770 nm; **2**, 735 nm. The concentration of the diiron complex is 0.5 mM, in MeCN at -40 ºC.

The EXAFS analysis of **1-Sc** is summarized in Table 5.6 and Figure 5.9 and Figure 5.10. The 3-D model used for FEFF calculation was modified from the crystal structure of the bis(μ-hydroxo)diferrous precursor complex.[92] The best fit of the sample gives scattering pair distances that correspond to 4 Fe–N/O at 2.19 Å, 1 Fe–O/N at 1.85 Å, 1 Fe–O/N at 2.04 Å, 2 Fe•••Sc at 2.99 Å and 1 Fe•••Fe at 3.13 Å.

.

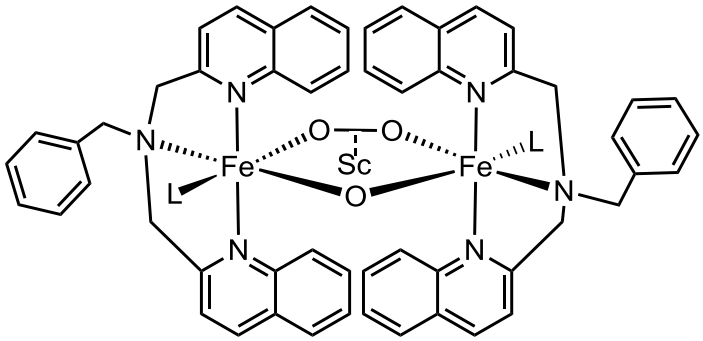

Figure 5.9. EXAFS derived model for **1-Sc**.

This fit has similarities to the fit reported for **1**. The distances for the Fe–N (**1**, 2.17 Å), short Fe–O (**1**, 1.81 Å) and Fe•••Fe (**1**, 3.16 Å) scatterers are nearly identical,[110] despite the differences in the UV-vis and XANES analysis. The short Fe-O distance is consistent with maintaining the μ-oxo bridge in **1-Sc**, and suggests that the Sc^{3+} is not behaving like a proton and interacting with the oxo unit. For comparison, the protonated **2** has the same Fe–N and Fe•••C scatterers as **1** but instead has 2 Fe–O/N at 1.91 Å and an Fe•••Fe at 3.41 Å.[110] The main differences between **1-Sc** and **1** are that **1-Sc** has a longer Fe–O scatterer (2.04 Å) assigned to the Fe–O_{peroxo}, compared to **1** (1.92 Å) and **1-Sc** has an Fe•••Sc shell where **1** has a carbon shell (2.99 Å). This elongation of the Fe–O distance might result from the Sc ion interacting with the peroxo ligand. The C/Sc scattering is a bit more complicated to understand.

In fitting **1-Sc**, different combinations of Sc and C scatterers were used. If Fe•••C scatterers were exclusively used, a large number (>4) of scatterers were needed in order to adequately fit the data with a σ^2 value < 1×10^{-3} $Å^{-2}$, indicating that more carbon scatterers may be required (Table 5.6, fit 9). As the ~3 Å C atoms are derived from the

methylene linker atoms, requiring more than 4 starts becoming chemically unreasonable. For comparison, **1** required 4 carbon scatterers at 2.99 Å and had a σ^2 value of 2.50×10^{-3} $Å^{-2}$. If both Sc and C scatterers are used (Table 5.6, fit 10), they fit to 2.99 and 2.91 Å respectively. The resolution of the experiment is 0.12 Å, so with a difference between the shells of 0.08 Å, it is not technically possible to distinguish the Sc from the C shell. This means that the two shells should instead be combined into one. The best fit instead uses 2 Fe•••Sc scatterers, and has goodness of fit parameters that are an improvement over C or C/Sc fits (Table 5.6, fit 12 vs fit 9, 10). The stoichiometry of **1-Sc** is only consistent with 1 eq. of Sc^{3+} per dimer, based on the clean isosbestic behavior observed in the UV-vis spectra. As observed in the EXAFS fits of **1** and **2**, the carbon shell fits at the same distance, so the interpretation of the best fit of **1-Sc** is that the 2 Fe•••Sc shell consists of Sc and C interactions at 2.99 Å. Sc is a much larger scatterer than C, so Sc will contribute more to the phase component of measured interference pattern than the C scatterers at the same distance. Thus, using Sc phase parameters results in a better fit compared to C.

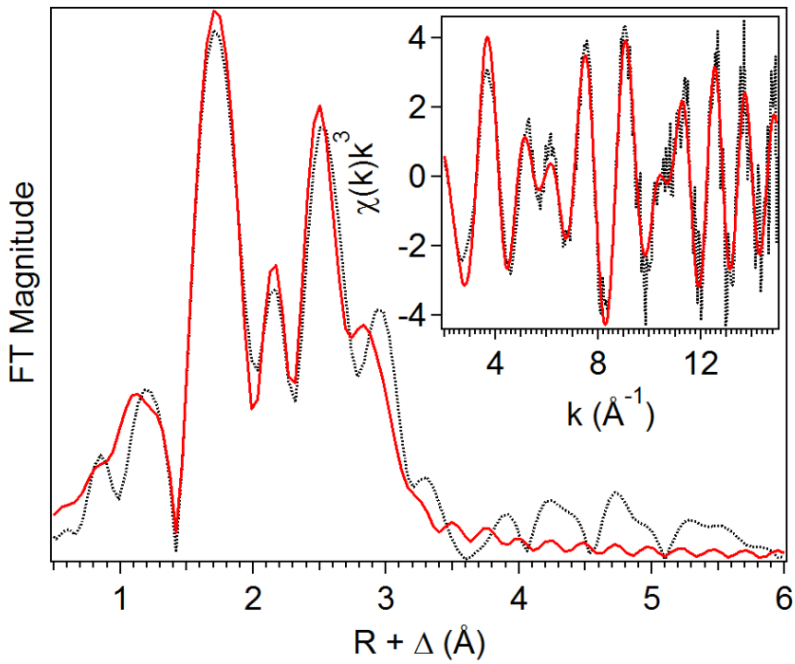

Figure 5.10. Fit (red solid line) of the unfiltered (black dotted) EXAFS data (inset) of **1-Sc** and corresponding Fourier transform (Fit 12). k = 2 – 15 $Å^{-1}$.

What can be definitively said is that there is at least one Sc scatterer at ~3 Å, and this has structural ramifications for the diferric core. However, the 2.99 Å distance raises questions about how the Sc atom is positioned with respect to the plane defined by the $Fe(O_2)(O)Fe$ core. We can first make several reasonable assumptions, 1) the $Fe(O_2)(O)Fe$ core is co-planar (flat), 2) we use a Sc-O bond length of 1.93 Å, as observed in the $[(TMC)Fe^{III}\text{-}O\text{-}Sc^{III}(OTf)_4]$ crystal structure,[271] 3) the O–O distance is 1.45 Å. If the Sc sits in the $Fe(O_2)(O)Fe$ plane, binding to the oxo moiety would result in an Fe•••Sc distance of ~3.3 Å (Figure 5.11, left) and binding side-on to the peroxo moiety results in an Fe•••Sc distance of ~4Å (Figure 5.11, left). In this case, neither configuration is consistent with the EXAFS data, but we can further rule out some possibilities. If the Sc atom interacts with the oxo ligand to make a "hydroxo-like" species similar to **2**, the Fe–O and Fe•••Fe distances should be elongated, but behavior is not observed in the experiment. Additionally, the Sc–O distance of 1.93 Å assumes a fairly strong interaction between the oxo ligand and scandium which is also inconsistent with the EXAFS data, especially considering the Sc–O distance is most likely longer than 1.93 Å. In order to accommodate a ~3 Å Sc distance, the scatterer must not be in the $Fe(O_2)(O)Fe$ plane. If a Sc binding angle perpendicular to the $Fe(O_2)(O)Fe$ plane ($\alpha = 90^{o}$) is considered the corresponding Fe•••Sc distance is ~3 Å (Figure 5.11, right), which agrees quite well with the experimental data. Several assumptions have been used, however, slight changes to the bond distances for the O–O and Sc–O bonds should only affect the α angle slightly, moving several degrees towards or away from the iron. Additionally, a Sc atom binding to the peroxo ligand would rationalize the elongation of the Fe–O distance assigned to the $Fe–O_{peroxo}$ bond, from 1.91 Å in **1** to 2.04 Å in **1-Sc**.

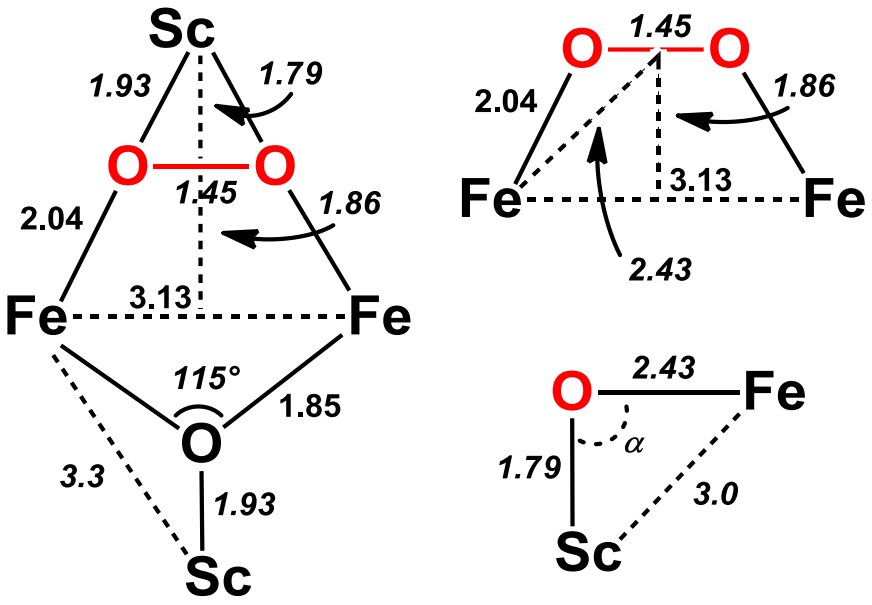

Figure 5.11. Bonding metrics for determining the relative position of Sc in **1-Sc**. Left: Top down view of **1-Sc** and metrics used to calculate the Fe•••Sc distance for binding to the oxo and peroxo ligands in the $Fe(O_2)(O)Fe$ plane. Right: Metrics used to calculate the Fe•••Sc distance for binding to the peroxo ligand at 90º to the $Fe(O_2)(O)Fe$ plane. Top: Top down view of **1-Sc** with relevant atoms, bottom: side view of **1-Sc** looking down the Fe•••Fe vector, calculations performed with $\alpha = 90º$. All bond distances are in angstroms. Oxygen atoms in red are from the peroxo ligand. Distances in italics are from assumptions or calculations.

Overall, the EXAFS data of **1-Sc** indicates that the Sc atom is likely binding to the peroxo moiety out of the $Fe(O_2)(O)Fe$ plane, close to a perpendicular angle ($\alpha \sim 90º$). This is favored over binding to the oxo moiety because **1-Sc** is fit with a 1.85 Å Fe–O distance consistent with an oxo bridge that is unchanged from **1**, whereas the 1.91 Å Fe–O distance which corresponds to the Fe–O peroxo in **1** elongates to 2.04 Å upon binding of Sc.

Table 5.6. EXAFS fit parameters for **1-Sc**. Italicized parameters were fit as O scatterers. Fit 12 corresponds to the most reasonable fit of the data between k = 2 – 15 $Å^{-1}$.

	Fe-N/*O*			**Fe•••Sc**			**Fe•••Fe**			**Fe•••C**				**GOF**	
Fit	**N**	**R(Å)**	**$\sigma^2(10^{-3})$**	**N**	**R(Å)**	**$\sigma^2(10^{-3})$**	**N**	**R(Å)**	**$\sigma^2(10^{-3})$**	**N**	**R(Å)**	**$\sigma^2(10^{-3})$**	**E_o**	**F**	**F'**
1	6	2.19	6.90										-2.28	636	760
2	5	2.19	5.38										-1.81	584	729
3	4	2.19	4.00										-1.33	553	709
4	3	2.20	2.66										-0.75	554	710
5	4	2.18	4.05										-2.95	501	675
	1	*1.86*	*4.50*												
6	4	2.18	1.10										-6.02	443	628
	1	*1.87*	*0.13*												
	1	*2.03*	*-1.70*												
7	4	2.19	1.20				1	3.19	3.75				-4.58	475	657
	1	*1.87*	*0.61*												
	1	*2.04*	*-1.40*												
8	4	2.19	3.92				1	3.06	11.61	3	2.93	-1.20	-5.00	173	398
	1	*1.85*	*2.67*												
	1	*2.04*	*4.85*												
9	4	2.18	3.56				1	3.12	4.92	6	2.94	0.95	-5.65	190	416
	1	*1.84*	*2.22*												
	1	*2.02*	*3.90*												
10	4	2.18	2.88	1	2.99	0.55	1	3.12	2.97	4	2.91	6.53	-5.90	164	387
	1	*1.84*	*1.95*												
	1	*2.02*	*2.59*												
11	4	2.18	4.19	2	2.99	2.90	1	3.14	1.83				-3.53	172	395
	1	*1.86*	*5.03*												
12	**4**	**2.19**	**2.80**	**2**	**2.99**	**3.21**	**1**	**3.13**	**2.36**				**-4.91**	**150**	**370**
	1	***1.85***	***2.12***												
	1	***2.04***	***2.01***												

5.3.2 – XAS Analysis of Peroxo-Diferric Species Supported by Bulky Carboxylate Ligands

5.3.2.1 – XAS Analysis of 3 and 4. The K-edge energy for **3** was found to be 7124.4 eV, and for **4** was found to be 7123.6 eV. These energies are close to those of (μ-oxo)(μ-peroxo)-diferric species (7124 eV).[105, 110] The pre-edge peak for **3** has a maximum at 7112.7 eV with a calculated area of 11.8 units and **4** has a pre-edge maximum at 7112.8 eV with a calculated peak area of 9.6 units (Table 5.7, Figure 5.12). These pre-edge values fall on the high end of six-coordinate ferric centers, which range from 4 to 10 units,[44, 85] but are lower than those of synthetic peroxo-diferric species (13 to 16 units),[105, 110, 112] and μ-oxo bridged diferric centers (average 14.5 units).[44, 85] The pre-edge analysis would be consistent with six-coordinate diferric centers without a bridging oxo unit.

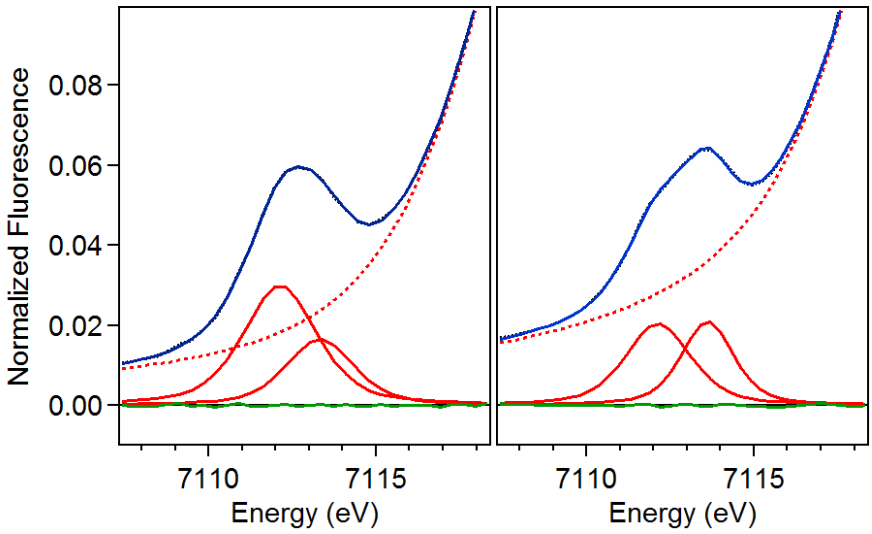

Figure 5.12. Pre-edge region analysis of **3** (left) and **4** (right). The experimental data (black dotted), baseline (red dashed), pre-edge peak components (red solid), residuals (green solid) and total fit (blue solid) are shown.

Table 5.7. XANES analysis for **3** and **4**.

Species	K-edge (eV)	Peak Position (eV)	Area (units)	Relative Area
3	7124.4	7112.1	7.87	1.99
		7113.3	3.96	1.00
			Total = 11.8	
4	7123.6	7112.1	5.75	1.48
		7113.6	3.88	1.00
			Total = 9.6	

The results of the EXAFS analysis for **3** and **4** are summarized in Figures 5.13 and 5.14 and Tables 5.8 and 5.9. The 3-D models used for the FEFF calculations were modified from the crystal structure of the diferrous starting materials for **3** and **4**.[93] The best fit of **3** gives scattering pair distances that correspond to 4 Fe–N/O at 2.05 Å, 1.5 Fe–O/N at 1.94 Å, 1.5 Fe•••C at 2.47 Å, 1 Fe•••Fe at 3.41 Å, and 2 Fe•••C at 2.99 Å. The 2.05 Å scatterers correspond to the carboxylate ligand oxygen atoms bound to the Fe centers. These carboxylate ligands are likely bound in several different configurations, but these cannot be determined from the 2.05 Å distance alone. The 1.94-Å scatterer likely corresponds to the O atoms of the peroxo unit. The scatterer is best fit with N = 1.5, which would correspond to one of the peroxo atoms bridging in a μ-1,1 mode between Fe centers, with the second O atom binding to only one Fe center, in an η^2 mode (Figure 5.13). This would be consistent with an overall η^2:η^1-peroxo binding geometry. The 1.94-Å scatterer in **3** does have a rather high σ^2 of 7.11×10^{-3} Å^2, which could suggest that the bridging O atom is not symmetric to both Fe centers (Fe1–O1 ≠ Fe2–O1). Additionally, the σ^2 may suggest that the two peroxo oxygen atoms may not be at exactly the same distance (Fe1–O1 ≠ Fe1–O2), but they cannot be distinguished from each other due to the resolution of the experiments (ΔR = 0.12 Å). The carbon shells provide information about some of the possible carboxylate binding modes. The Fe•••C distance at 2.47 Å is consistent with carbon atom of a carboxylate ligand bound bidentately to the metal.[38, 139] The best fit requires N = 1.5, which would be consistent with having two bidentate carboxylate interactions on one Fe center, and only one interaction on the second Fe. The 2.99 Å C scatterers correspond to the carbon atom of the carboxylate group of either μ-1,3-bridging or monodentate binding modes. The

Fe•••Fe distance of 3.41 Å is much longer than the crystallographically measured distance of 2.73 Å for the diferrous paddlewheel precursor, which is consistent with a rearrangement of the carboxylate ligands. A 3.4-Å metal separation is observed for **2** as well as the peroxo intermediate of hDOHH, both of which are μ-hydroxo bridged peroxo intermediates.[36, 110]

There are no synthetic examples of (μ-η^2:η^1-peroxo)diferric complexes to compare the structural parameters of **3** against, but several mononuclear and dinuclear peroxo complexes can shed light on the peroxo binding assignment. By XAS analaysis, there is an example of an η^2-peroxo in the [(TMC)Fe^{III}(η^2-O_2)Sc^{III}] (TMC = tetramethylcyclam) complex, with Fe–O_{peroxo} distances at 1.98 Å, which are similar to those assigned in **3**.[236] In addition, the pre-edge area of the TMC complex is 14.4 units, which is also close to the 11.8 units for **3**, supporting the assignment of the scatterer. Two μ-η^2:η^1-peroxo complexes have been characterized by X-ray crystallography, [(oxapyme)Co^{III}_2(η^2:η^1-O_2)]$^{2+}$ (**A**) (oxapyme = 2-(bis-pyridin-2-ylmethyl-amino)-*N*-[2-(5-{2-[2-(methyl-pyridin-2-ylmethyl-amino)-acetylamino]-phenyl}-[1,3,4]oxadiazol-2-yl)-phenyl]-acetamide),[246] and [(TMP-5Me-TPA)Fe^{III}(O_2)Cu^{II}]$^+$ (**B**) (TMP-5Me-TPA = 10,15,20-tris(2,4,6-trimethylphenyl)-5-(2'-bis((5''-methyl-2''-pyridylmethyl)aminomethyl)pyridine-5'-carboxyamidophenyl)-porphyrin).[245] In **A**, the Co1 center is bound to the peroxo ligand in an η^2 mode, with Co1–O1 and Co1–O2 distances of 1.926 and 1.846 Å, respectively. The Co2 center is bound to the peroxo in an η^1 mode and has Co2–O1 and Co2•••O2 distances of 1.922 and 2.763 Å, respectively, and the complex has a Co•••Co distance at 3.339 Å (Figure 5.13A). The dicobalt core of **A** has comparable structural metrics as **3**, with similar M–O distances (~1.92 Å for **A**, 1.94 Å for **3**) and metal-metal separations (3.339 Å for **A**, 3.41 Å for **3**). Interestingly, the Co1–O distances of 1.846 and ~1.92 Å (Δ ~ 0.7 Å) would not be resolvable in a hypothetical EXAFS experiment of **A** with the same resolution data as **3**. This would support the interpretation that the Fe–η^2-O_{peroxo} distances in **3** might not be identical, consistent with the increased σ^2 value for the 1.94-Å scatterer. The structural metrics for **B** are similar to those found for **A** and **3** (Figure 5.13B). The Fe center in **B** is bound in an η^2 mode to the peroxo ligand, with Fe–O1 and Fe–O2 distances of 2.030 and 1.891 Å, respectively, and the Cu center is bound in an η^1 mode with Cu–O1 and Cu•••O2

distances of 1.915 and 2.657 Å, respectively. These metrics are consistent with the assignments for **3**, with the notable difference in the metal-metal separation (3.916 Å for **B** and 3.41 Å for **3**). Both complexes **A** and **B** have long M•••O2 distances (2.763 and 2.657 Å, respectively) which are not observed in the EXAFS analysis of **3**. The only distance observed between ~2 and 3 Å for **3** is the 2.47-Å scatterer, but this distance is too short compared to **A** and **B** to be assigned as an Fe•••O_{peroxo} scatterer without substantial distortion of the diferric core. Overall, these crystallographically characterized models support the assignment of a μ-η^2:η^1-peroxo binding mode for **3**.

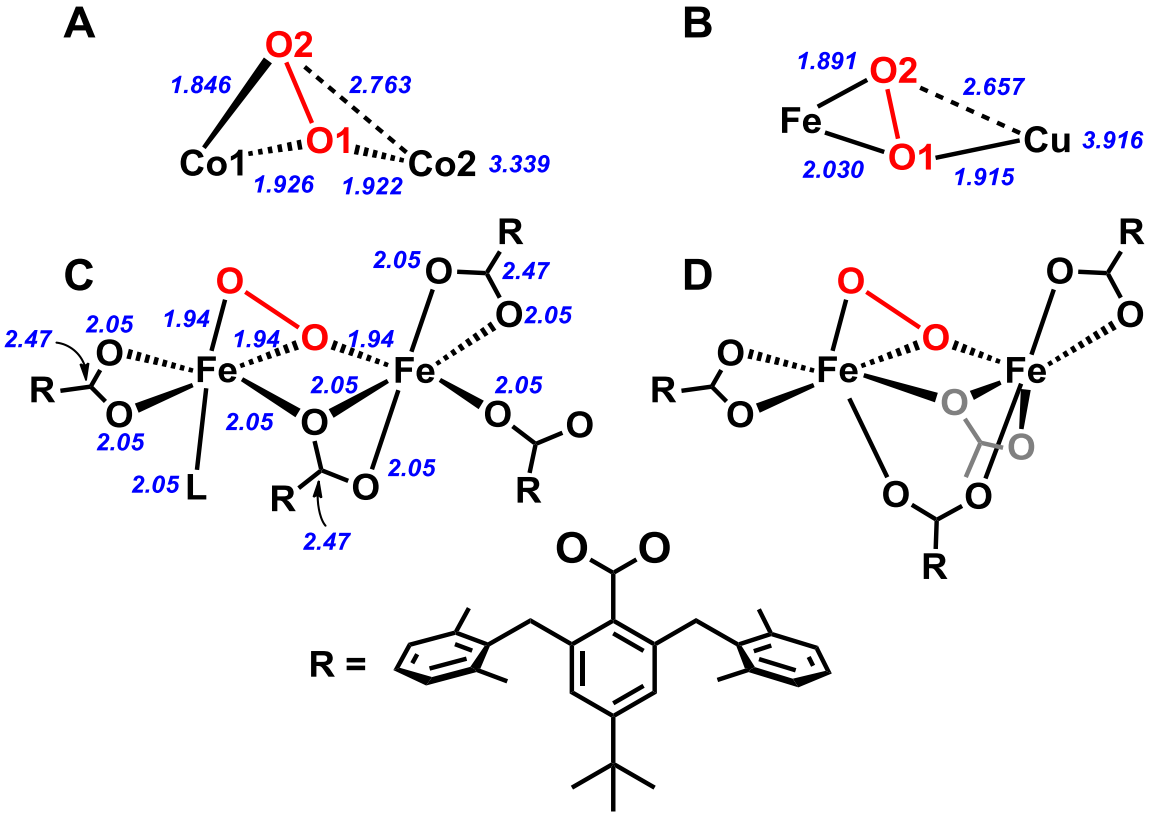

Figure 5.13. Summary of EXAFS derived models for **3** and **4**, and related structural models. A: the dicobalt core of complex **A** from ref [246]; B: the iron-copper core of complex **B** from ref [245]; C: the monodentate carboxylate model for **3** and **4**, with distances included from **3**; D: the bridging carboxylate model for **3** and **4**. L = THF (complex **3**) or pyridine (complex **4**). Oxygen atoms in red are derived from the peroxo ligand. All distances provided are in angstroms.

An overall model of **3** is tricky to determine, particularly because the only ligands in the solution are the dxlCO_2 ligand, THF and the O_2^{2-}. The N = 1.5 carbon scatterer at 2.47 Å is consistent with three of the carboxylate ligands having a bidentate mode. This leaves the remaining carboxylate ligand able to bind in a monodentate mode or a μ-1,3-bridging mode. If the η^2:η^1-peroxo binding mode is considered, there are two possible

models that would be consistent with the experimental data. The first model has a monodentate carboxylate ligand on Fe2 with a THF ligand bound to Fe1 (Figure 5.13, C), and the second model has a μ-1,3-carboxylate bridge and no THF ligand bound (Figure 5.13, D). Model 1 is favored, as **3** and **4** have similar, but not identical Fe•••Fe distances (see below) so the additional ligand binding site may be necessary to differentiate them. Another possibility would be that **3** may correspond to model 2 and **4** may correspond to model 1, or vice versa. Additional characterization would be required to further understand the structure.

The best fit of **4** gives scattering pair distances that correspond to 4 Fe–N/O at 2.09 Å, 1.5 Fe–O/N at 1.94 Å, 1.5 Fe•••C at 2.47 Å, 1 Fe•••Fe at 3.33 Å, 2 Fe•••C at 3.07 Å and 2 Fe•••C at 4.03 Å. The scatterers for **4** are assigned similarly to **3**, with several differences. The FT of **4** looks different than that for **3**; the peaks above R + Δ = 2 Å are more intense for **4** than for **3** (Figure 5.14). The large peak at R + Δ ~ 3 Å corresponds to the Fe•••Fe distance at 3.33 Å in **4**, which is 0.08 Å shorter than **3**. This difference is either the result of the different effects of the extra ligand (THF in **3**, pyridine in **4**) or from slightly different structures (Figure 5.13, C/D). Additionally, there is a sharp feature at R + Δ ~ 3.6 Å that requires carbon scatterers at 4.03 Å that is not straight forward to assign. With a μ-1,3-carboxylate bridge (like model 2), the two closest carbon atoms to the Fe center would be from the carboxylate at ~3 Å, and the C1 carbon of the central benzene ring sits at ~4.3 Å, so a 4 Å carbon is not feasible. However, with bidentate bound or monodentately bound carboxylate ligands, the C1 carbon can reach ~4Å depending on the orientation. This agrees with the assignment of the ~2.5 Å scatterer as belonging to a carboxylate ligand bound bidentate to Fe. Interestingly, there is some intensity in the FT of **3** at R + Δ ~ 3.6 Å, but adding a scatterer at ~4 Å did not result in sensible results. This might further support the notion that **3** and **4** may have slightly different carboxylate ligand configurations.

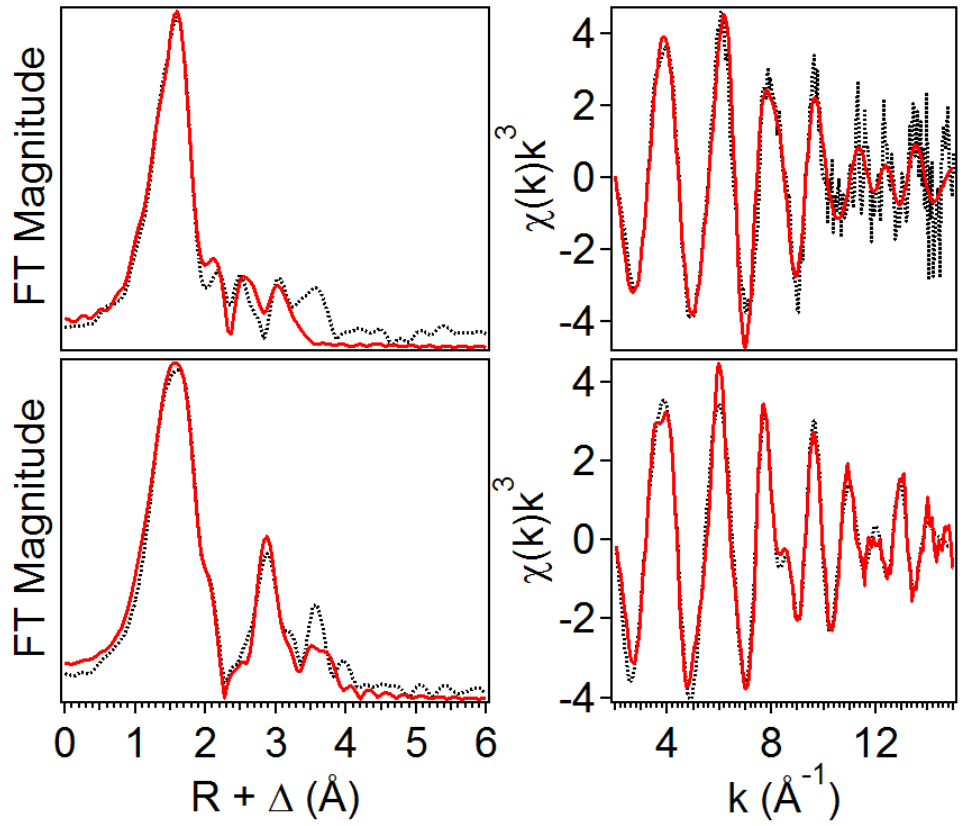

Figure 5.14. EXAFS analysis for **3** (top row) and **4** (bottom row). Left column: Fourier transform of the EXAFS data (black dotted) with best fit (red solid line). Right column: unfiltered EXAFS data (black dotted) with best fit (red solid line). **3**, Fit 13, k = 2 – 15 $Å^{-1}$; **4**, Fit 12, k = 2 – 15 $Å^{-1}$.

Table 5.8. EXAFS fit parameters for **3**. Fit 13 corresponds to the most reasonable fit of the data between k = 2 – 15 $Å^{-1}$.

	Fe-O/N			Fe-O			Fe•••Fe			Fe•••C				GOF	
Fit	N	R(Å)	$\sigma^2(10^{-3})$	N	R(Å)	$\sigma^2(10^{-3})$	N	R(Å)	$\sigma^2(10^{-3})$	N	R(Å)	$\sigma^2(10^{-3})$	E_o	F	F'
1	6	2.02	9.89										-0.63	224	452
2	5	2.03	7.99										-0.06	197	425
3	4	2.03	6.20										0.85	197	425
4	5	2.02	7.39	1	1.84	17.37							-2.14	199	426
5	4	2.04	5.06	1	1.91	4.23							-1.32	188	414
6	4	2.04	5.12	1	1.92	4.32	1	3.40	8.31				-1.23	181	407
7	4	2.04	4.47	1	1.91	2.43	1	3.40	7.59	1	2.47	0.00	-1.41	139	356
8	4	2.04	4.25	1	1.90	2.05	1	3.39	7.51	1.5	2.47	1.25	-1.92	145	363
9	4	2.05	5.11	1	1.93	3.62	1	3.41	7.92	1.5	2.47	1.76	-0.03	139	355
										2	3.00	3.54			
10	4.5	2.05	6.20	1	1.92	5.38	1	3.41	7.97	1.5	2.47	1.96	-0.41	139	357
										2	2.99	3.15			
11	4.5	2.04	7.24				1	3.42	7.72	1.5	2.47	2.16	1.68	144	363
										2	3.00	3.69			
12	5	2.04	7.12	1	1.89	7.57	1	3.40	7.92	1.5	2.46	2.11	-0.98	144	363
										2	2.99	2.85			
13	**4**	**2.05**	**5.96**	**1.5**	**1.94**	**7.11**	**1**	**3.41**	**7.96**	**1.5**	**2.47**	**2.01**	**-0.67**	**139**	**357**
										2	**2.99**	**2.94**			
14	4	2.05	5.61	1.5	1.93	6.67	1	3.40	8.40	1	2.47	0.48	-0.93	140	358
										2	3.00	3.77			
15	4	2.05	4.87	1.5	1.92	4.85				1	2.47	0.17	-1.36	143	362
										2	3.00	3.53			
16	4	2.04	5.56	1.5	1.92	7.50	1	3.39	8.50	2	3.09	20.26	-1.65	182	407
17	4	2.05	4.96	1.5	1.92	5.02	1	3.40	8.50	1	2.40	0.23	-1.20	140	357
										2	3.00	4.38			
18	4.5	2.05	6.23	1.5	1.92	7.25	1	3.40	8.04	1.5	2.47	2.03	-1.32	144	363
										2	2.99	4.56			
19	4	2.04	7.96	1	2.03	8.72	1	3.41	7.58	2	2.47	3.55	1.41	143	361
										2	3.00	2.97			

Table 5.9. EXAFS fit parameters for **4**. Fit 12 corresponds to the most reasonable fit of the data between k = 2 – 15 $Å^{-1}$.

	Fe-O/N			**Fe-O**			**Fe•••Fe**			**Fe•••C**				**GOF**	
Fit	**N**	**R(Å)**	**$\sigma^2(10^{-3})$**	**N**	**R(Å)**	**$\sigma^2(10^{-3})$**	**N**	**R(Å)**	**$\sigma^2(10^{-3})$**	**N**	**R(Å)**	**$\sigma^2(10^{-3})$**	**E_o**	**F**	**F'**
1	6	2.05	11.52										-0.22	202	477
2	5	2.06	9.37										0.49	183	454
3	4	2.07	7.30										1.69	182	454
4	4	2.08	4.79	1	1.93	2.06							-0.70	152	413
5	5	2.06	6.84	1	1.90	3.53							-1.85	168	436
6	4.5	2.08	5.71	1.5	1.92	4.61							-2.01	163	429
7	4.5	2.07	5.62	1.5	1.92	4.40	1	3.32	3.98				-2.38	110	352
8	4.5	2.08	5.60	1.5	1.92	4.32	1	3.32	3.87	1	2.45	1.97	-2.13	81	300
9	4.5	2.08	5.64	1.5	1.93	4.64	1	3.32	5.16	1	2.47	1.58	-1.04	54	247
										2	3.07	1.65			
10	4.5	2.08	5.66	1.5	1.93	4.74	1	3.32	5.29	1	2.47	1.55	-0.80	35	198
										2	3.07	1.50			
										2	4.02	1.93			
11	4.5	2.08	5.69	1.5	1.92	4.77	1	3.32	5.14	2	3.08	1.96	-1.30	67	275
										2	4.02	2.02			
12	**4**	**2.09**	**5.86**	**1.5**	**1.94**	**5.05**	**1**	**3.33**	**5.25**	**1.5**	**2.47**	**3.42**	**-0.19**	**33**	**191**
										2	**3.07**	**1.59**			
										2	**4.03**	**2.04**			

5.3.3 – XAS Analysis of Peroxo-Diferric Species Supported by the 6-HPA Ligand

5.3.3.1 – XAS Analysis of 5 – 7. The K-edge energy was found at 7124.3 eV for **5** and at 7124.5 eV for **6** (Table 5.10). These values are similar to those of other μ-oxo-diferric species. The (μ-oxo)(μ-peroxo)diferric **7** has a K-edge energy of 7123.2 eV, which is lower than for other reported peroxo-diferric complexes (7124 eV),[105, 110] as well as the (μ-oxo)diferric complexes **5** and **6**.

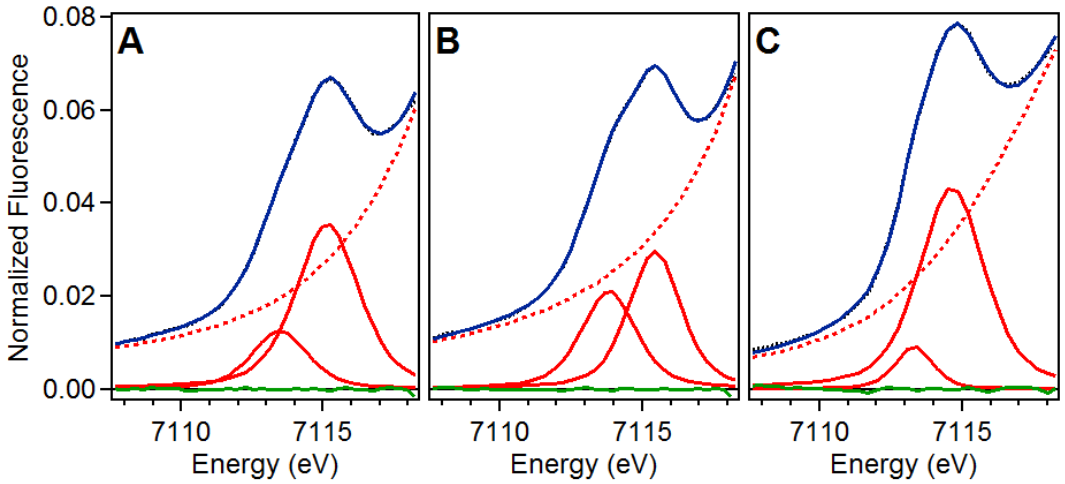

Figure 5.15. Pre-edge region analysis of **5** (A), **6** (B) and **7** (C). The experimental data (black dotted), baseline (red dashed), pre-edge peak components (red solid), residuals (green solid) and total fit (blue solid) are shown.

The pre-edge areas are 11.3 units for **5**, 12.4 units for **6** and 13.2 units for **7** (Table 5.10, Figure 5.15). All of these pre-edge values fall just at, or below, the range of values of μ-oxo bridged diferric centers (13 to 17 units)[44, 85] and **7** is just within the range for six-coordinate synthetic peroxo-diferric species (13 to 16 units).[105, 110, 112] The pre-edge analysis is therefore consistent with six-coordinate iron centers for **5 – 7**. Interestingly, the pre-edge areas increase with a decrease in the the Fe–O–Fe angle (see below).

Table 5.10. XANES analysis of **5** – **7**.

Species	K-edge (eV)	Peak Position (eV)	Area (units)	Relative Area
5	7124.3	7113.8	4.81	1.00
		7115.4	6.45	1.34
			Total = 11.3	
6	7124.5	7113.5	2.94	1.00
		7115.2	9.43	3.21
			Total = 12.4	
7	7123.2	7113.3	1.43	1.00
		7114.6	11.76	8.21
			Total = 13.2	

The results of the EXAFS analysis for **5 – 7** are summarized in Table 5.11 – Table 5.13 and Figure 5.15 – Figure 5.17. The 3-D model used for the FEFF calculation for **5** was modified from the crystal structure of **5**,[252] and the models for **6** and **7** were modified from the solved crystal structure for **6**. The best fit of **5** gives scattering pair distances that correspond to 5 Fe–N/O at 2.14 Å, 1 Fe–O/N at 1.79 Å, 5 Fe•••C at 3.03 Å and 1 Fe•••Fe at 3.57 Å. These distances compare quite well to the available crystal structure, assisting in the assignment of the scatterers. The 5 Fe-N/O scatterers at 2.14 Å arise from the 4 nitrogen interactions with the 6-HPA ligand, which range in the crystal structure from 2.113 Å to 2.244 Å (average = 2.175 Å), and the single aqua ligand on each Fe, which are 2.086 Å and 2.059 Å (average = 2.073 Å) in the crystal structure. When all these interactions are averaged into one shell, the result is 2.15 Å, which corresponds nicely to the EXAFS data. The μ-oxo ligand has an average distance in the crystals of 1.804 Å, which compares well to 1.79 Å for the EXAFS fit, though, the σ^2 value for this scatterer is low ($< 1 \times 10^{-3}$ Å^2). This low σ^2 is due in part to the Fe-O-Fe angle being nearly linear (179°). Use of a single Fe scatterer to model the Fe•••Fe was inadequate to fit the intense peak in the FT (Figure 5.17, top) at R + Δ ~3.3 Å, and resulted in a σ^2 with a negative value (Table 5.11 , fit 9 and fit 15). Inclusion of Fe-O-Fe multiple scattering pathways greatly improved the fit and resulted in an Fe•••Fe distance of 3.57 Å, which agrees with the crystallographically determined 3.608 Å. The remaining carbon shell is fit at 3.03 Å, which corresponds to the carbon atoms of the methylene linkers, as well as the C2 or C6 carbon atoms of the pyridine rings.

The best fit of **6** gives scattering pair distances that correspond to 3 Fe–N/O at 2.14 Å, 3 Fe–O/N at 1.99 Å, 1 Fe–O/N at 1.80 Å, 4 Fe•••C at 2.99 Å, and 1 Fe•••Fe at 3.29 Å (Figure 5.17, middle row). This complex is assigned similarly as **5**, though there are several important differences. The primary Fe–N/O interactions, if fit with 5 scatterers refines to 2.08 Å with a σ^2 value of 8×10^{-3} Å^2 (Table 5.12, fit 8). This distance is much shorter than for **5** at 2.14 Å, and doesn't agree with the crystal structure of **6**, which has an average Fe–N distance of 2.188 Å, and an average Fe-$O_{carboxylate}$ distance of 2.016 Å (average of Fe–N and Fe–O = 2.154 Å). As **6** is a powder sample of the crystalline material, this fit is unreasonable. Additionally, the distance consistent with the μ-oxo bridge has a high σ^2 value of 6.13×10^{-3} Å^2. When the primary scattering shell is further split into 3 Fe–N/O at 2.14 Å and 3 Fe–N/O 1.99 Å shells, within error, the distances fit much better to the crystal structure of **6** and the 1.80 Å scatterer has a much smaller σ^2 value (Table 5.12, fit 13) Fitting the ~2–Å scatterer with less than N = 3 results in unreasonable fits (Table 5.12, fits 12 and 14). The Fe•••Fe distance at 3.29 Å in **6** is contracted by ~0.3 Å relative to **5**, and is consistent with an Fe-O-Fe angle of ~132º, which agrees with the crystal structure of **6** (132.6º). The carbon shell at 2.99 Å identical, within error, to the carbon shell at 3.03 Å for **5**.

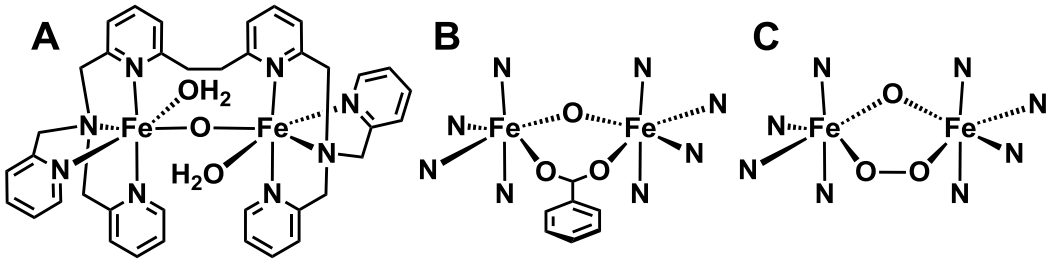

Figure 5.16. EXAFS derived models of **5** (A), **6** (B) and **7** (C). The 6-HPA ligand is shown in A, and removed for clarity in B and C.

The best fit of **7** gives scattering pair distances that correspond to 4 Fe–N/O at 2.20 Å, 2 Fe–O/N at 1.86 Å, 7 Fe•••C at 3.03 Å, and 1 Fe•••Fe at 3.15 Å (Figure 5.17, bottom row). This fit is nearly identical to that for the $[(6\text{-}Me_3\text{-}TPA)_2Fe^{III}{}_2(O)(O_2)]^{2+}$ (6-Me_3-TPA = tris(6-methyl-2-pyridylmethyl)amine, **C**) complex.[102] Additionally, the K-

edge energies (7123.2 eV for **7** and 7123.6 eV for **C**) and pre-edge areas (13.2 units for **7** and 12.5 units for **C**) are very close. The two Fe-O scatterers at 1.86 Å correspond to the μ-oxo ligand and the proximal peroxo oxygen atom, with the rather high σ^2 value of 7.08 $\times$ 10^{-3} $Å^2$, reflecting a significant difference between the two Fe–O distances. In the EXAFS analysis of **1**, 1 Fe–O_{oxo} at 1.81 Å and 1 Fe–O_{peroxo} at 1.92 Å are required for the best fit, but these scatterers are just outside of the resolution of the experiment (resolution = 0.12 Å, difference = 0.11 Å).[110] Attempts to fit **7** with two separate Fe–O shells resulted in unrealistic fit parameters. Overall, **7** has a structure very similar or identical to several other (μ-oxo)(μ-1,2-peroxo)diferric species.

Across this series of 6-HPA supported complexes, there are some interesting observations. Compared to **5** and **6**, the primary N scatterers in **7** have elongated from 2.14 Å to 2.20 Å, and the number of short Fe–O scatterers at ~1.8 Å has increased from 1 to 2 in **7**. Based on the crystallographic bond lengths, this elongation is due in part to a distribution of Fe–$N_{pyridine}$ distances which range from ~2.1 to 2.2 Å, as well as having a shorter Fe–O distance (OH_2 in **5**, OBz in **6**) that all average into the same EXAFS shell. The Fe•••Fe distance also changes, contracting by ~0.4 Å from **5** to **7**. The EXAFS derived Fe–O–Fe angle decreases as well, from 171º in **5** to 116º in **7**, consistent with a linear Fe–O–Fe unit in **5** converting to the bent Fe–O–Fe configuration in **7**. This movement suggests that the 6-HPA ligand is flexible enough to accommodate a wide range of metal-metal separations despite the presence of the ethylene linker. However, to date there have been no reported bis(μ-oxo)diferric or (μ-oxo)(μ-hydroxo)diferric diamond core species supported by 6-HPA, which are commonly found with the untethered TPA derivatives and related supporting ligands.[241] This could reflect the need for more work to synthesize and characterize these complexes, but also may suggest that the 6-HPA ligand is not flexible enough to accommodate the 2.7 to 2.9 Å Fe•••Fe distances required for these diamond core species.

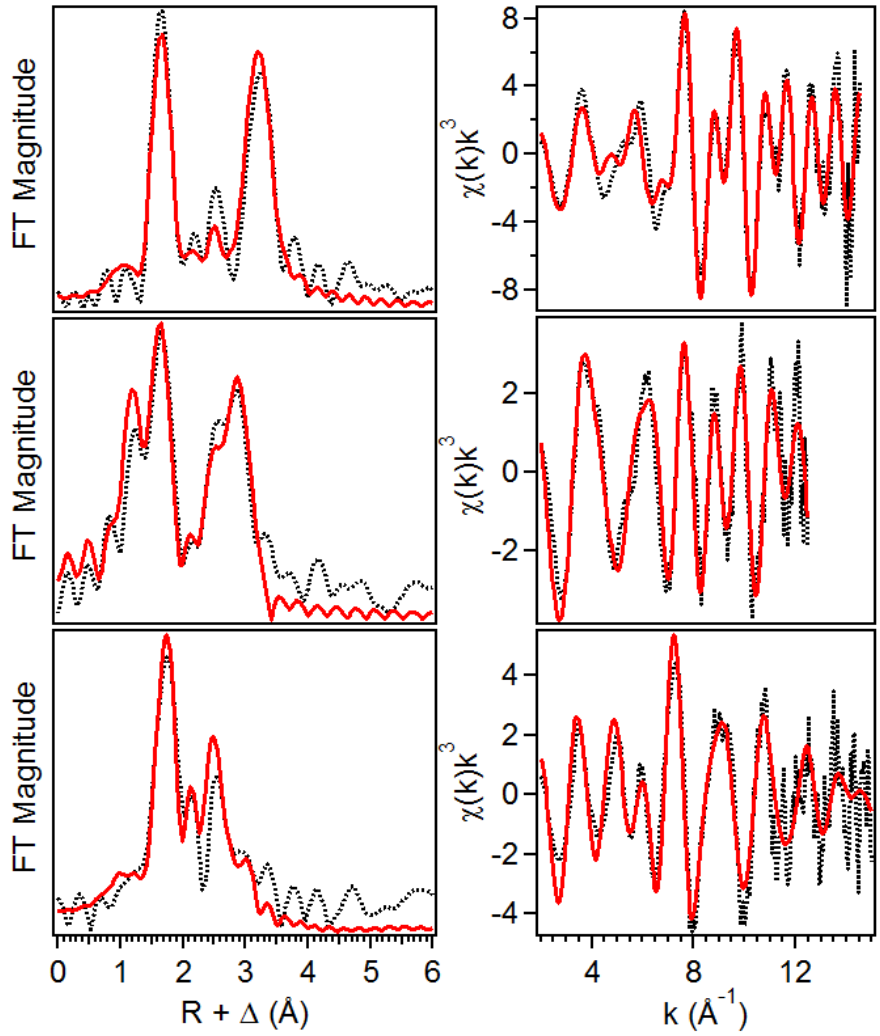

Figure 5.17. EXAFS analysis for **5** (top row), **6** (middle row) and **7** (bottom row). Left column: Fourier transform of the EXAFS data (black dotted) with best fit (red solid line). Right column: unfiltered EXAFS data (black dotted) with best fit (red solid line). **5**, Fit 20, k = 2 – 14.5 $Å^{-1}$; **6**, Fit 13, k = 2 – 12.5 $Å^{-1}$; **7**, Fit 9, k = 2 – 15 $Å^{-1}$.

Table 5.11. EXAFS fit parameters for **5**. Fit 17 corresponds to the most reasonable fit of the data between k = 2 – 14.5 $Å^{-1}$. Double scattering pathways are designated with /, triple scattering pathways are designated with //.

	Fe-O/N			Fe-O			Fe•••C			Fe•••Fe				GOF	
Fit	N	R(Å)	$\sigma^2(10^{-3})$	N	R(Å)	$\sigma^2(10^{-3})$	N	R(Å)	$\sigma^2(10^{-3})$	N	R(Å)	$\sigma^2(10^{-3})$	E_o	F	F'
1	6	2.12	4.46										-10.7	1793	802
2	5	2.11	3.49										-12.0	1798	803
3	4	2.11	2.50										-13.3	1834	811
4	5	2.13	3.92	1	1.79	0.55							-6.30	1584	754
5	5	2.11	3.70	2	1.78	5.30							-10.0	1673	775
6	4	2.10	2.62	2	1.78	6.11							-12.2	1758	794
7	4	2.13	2.88	1	1.79	0.36							-5.88	1639	767
8	5	2.13	3.98	1	1.79	0.44	5	3.02	4.12				-5.26	1449	721
9	5	2.12	3.81	1	1.78	0.55	5	3.00	3.87	1	3.63	-2.30	-9.72	472	411
10	5	2.13	3.81	1	1.78	0.29	5	3.02	3.04	1	3.60	-0.70	-6.49	340	350
										1	/3.60	-0.70			
11	5	2.14	3.97	1	1.79	0.25	5	3.03	3.30	1	3.60	2.87	-4.40	541	440
										3	/3.60	2.87			
12	5	2.16	4.23	1	1.80	0.26	5	3.08	5.32	1	3.53	4.04	-0.69	848	552
										3	//3.53	4.04			
13	5	2.14	3.99	1	1.79	0.26	5	3.03	3.36	1	3.58	2.79	-3.69	497	422
										3	/3.58	2.79			
										1	//3.58	2.79			

Table 5.11. (continued) EXAFS fit parameters for **5**. Fit 17 corresponds to the most reasonable fit of the data between k = 2 – 14.5 $Å^{-1}$. Double scattering pathways are designated with /, triple scattering pathways are designated with //.

	Fe-O/N			**Fe-O**			**Fe•••C**			**Fe•••Fe**				**GOF**	
Fit	**N**	**R(Å)**	**$\sigma^2(10^{-3})$**	**N**	**R(Å)**	**$\sigma^2(10^{-3})$**	**N**	**R(Å)**	**$\sigma^2(10^{-3})$**	**N**	**R(Å)**	**$\sigma^2(10^{-3})$**	**E_o**	**F**	**F'**
14	5	2.15	4.03	1	1.79	0.31	5	3.04	3.23	1	3.55	1.57	-2.20	498	422
										1	/3.55	1.57			
										2	//3.55	1.57			
15	5	2.12	4.02	1	1.79	0.21	7	2.93	6.33	1	3.64	-2.40	-7.75	511	428
							7	3.06	3.69						
16	5	2.14	3.66	1	1.79	0.62	7	3.02	0.29	1	3.51	1.36	-2.60	458	405
							7	3.18	0.66	2	//3.51	1.36			
17	**5**	**2.14**	**3.91**	**1**	**1.79**	**0.29**	**5**	**3.03**	**2.84**	**1**	**3.57**	**1.13**	**-4.05**	**358**	**359**
										2	**/3.57**	**1.13**			
										1	**//3.57**	**1.13**			

Table 5.12. EXAFS fit parameters for **6**. Fit 13 corresponds to the most reasonable fit of the data between k = 2 – 12.5 $Å^{-1}$

	Fe-O/N			Fe-O			Fe•••C			Fe•••Fe				GOF	
Fit	N	R(Å)	$\sigma^2(10^{-3})$	N	R(Å)	$\sigma^2(10^{-3})$	N	R(Å)	$\sigma^2(10^{-3})$	N	R(Å)	$\sigma^2(10^{-3})$	E_o	F	F'
1	4	2.08	11.81										-0.79	371	750
2	5	2.07	15.57										-1.37	380	759
3	5	2.05	10.55	1	1.82	4.92							-5.52	345	723
4	4	2.06	8.06	1	1.84	5.49							-4.8	344	722
5	5	2.08	8.66	1	1.83	6.73							-5.87	346	723
6	5	2.06	8.16	1	1.82	4.29				1	3.28	0.80	-9.91	158	492
7	5	2.08	8.13	1	1.83	5.74	5	2.99	4.37	1	3.29	2.31	-5.81	102	393
8	5	2.08	8.20	1	1.83	6.13	4	2.99	2.64	1	3.29	2.57	-5.43	98	386
9	5	2.08	8.25	1	1.83	5.95	4	2.99	2.60	1	3.31	2.48	-5.79	92	374
							1	3.55	-2.30						
10	5	2.08	8.22	1	1.83	5.78	4	2.99	2.70	1	3.30	2.08	-5.99	93	375
							2	3.54	2.70						
11	4	2.10	6.18	2	1.88	12.65	4	2.98	2.45	1	3.31	2.34	-6.53	91	372
							2	3.55	0.29						
12	4	2.11	3.53	1	1.98	-2.40	4	2.99	2.79	1	3.30	2.68	-5.32	95	379
				1	1.82	1.21									
13	**3**	**2.14**	**2.28**	**3**	**1.99**	**2.62**	**4**	**2.99**	**3.12**	**1**	**3.29**	**2.39**	**-6.73**	**99**	**387**
				1	**1.80**	**2.37**									
14	3	3.14	0.76	2	2.01	-1.40	4	2.99	2.57	1	3.3	2.84	-5.55	93	376
				1	1.83	0.79									

Table 5.13. EXAFS fit parameters for **7**. Fit 9 corresponds to the most reasonable fit of the data between k = 2 – 15 $Å^{-1}$.

	Fe-O/N			Fe-O			Fe•••C			Fe•••Fe				GOF	
Fit	**N**	**R(Å)**	**$\sigma^2(10^{-3})$**	**N**	**R(Å)**	**$\sigma^2(10^{-3})$**	**N**	**R(Å)**	**$\sigma^2(10^{-3})$**	**N**	**R(Å)**	**$\sigma^2(10^{-3})$**	**E_o**	**F**	**F'**
1	6	2.20	6.21										-1.26	767	874
2	5	2.19	4.84										-2.88	687	827
3	4	2.19	3.61										-4.23	632	793
4	3	2.18	2.40										-5.37	608	778
5	5	2.22	5.24	1	1.86	2.62							5.52	424	650
6	4	2.22	3.74	1	1.86	2.41							6.85	382	616
7	4	2.22	3.77	1	1.86	2.41				1	3.09	6.55	6.32	272	520
8	4	2.21	3.65	1	1.85	2.89	7	3.03	1.56	1	3.15	1.43	3.20	275	524
9	**4**	**2.20**	**3.74**	**2**	**1.86**	**7.08**	**7**	**3.03**	**2.03**	**1**	**3.15**	**1.74**	**3.52**	**241**	**491**
10	5	2.21	5.13	1	1.85	2.98	7	3.02	2.80	1	3.14	2.61	2.21	342	584
11	4	2.21	3.89	2	1.86	6.79	7	3.09	7.23				4.76	256	505
12	4	2.21	3.84	2	1.86	6.84				1	3.08	6.62	5.19	263	512
13	4	2.21	3.78	2	1.86	6.86	7	3.17	2.54	1	3.01	3.31	5.74	232	480

5.3.4 – XAS Analysis of Oxoiron(IV) Species Supported by the Pytacn Ligand

5.3.4.1 – XAS analysis of 8 and 9. The K-edge energy of **8** was found at 7125.0 eV and **9** was found at 7124.8 eV (Table 5.14). These values fall in the range of mononuclear oxoiron(IV) complexes which have K-edge energies from 7123 to 7126 eV.[272-274] The pre-edge peak for **8** is centered at 7114.0 eV has an area of 21.1 units (Figure 5.18). A pre-edge area of 21.1 units is at the lower end of the range for oxoiron(IV) species, with values from 20 to 38 units (average 27 units),[272-274] but is still consistent with the assignment. The pre-edge peak of **9** is centered at 7114.2 eV has an area of 17.4 units (Figure 5.18), which is lower than that for **8** and falls below the range for oxoiron(IV) species. The main difference between **8** and **9**, aside from the counter-ion is that **9** was prepared in an acetonitrile and water mixture in the presence of nitric acid. The water molecules or nitrate could be interacting with the ferryl unit in **9**, which would result in a more centrosymmetric Fe center and a lower pre-edge area.

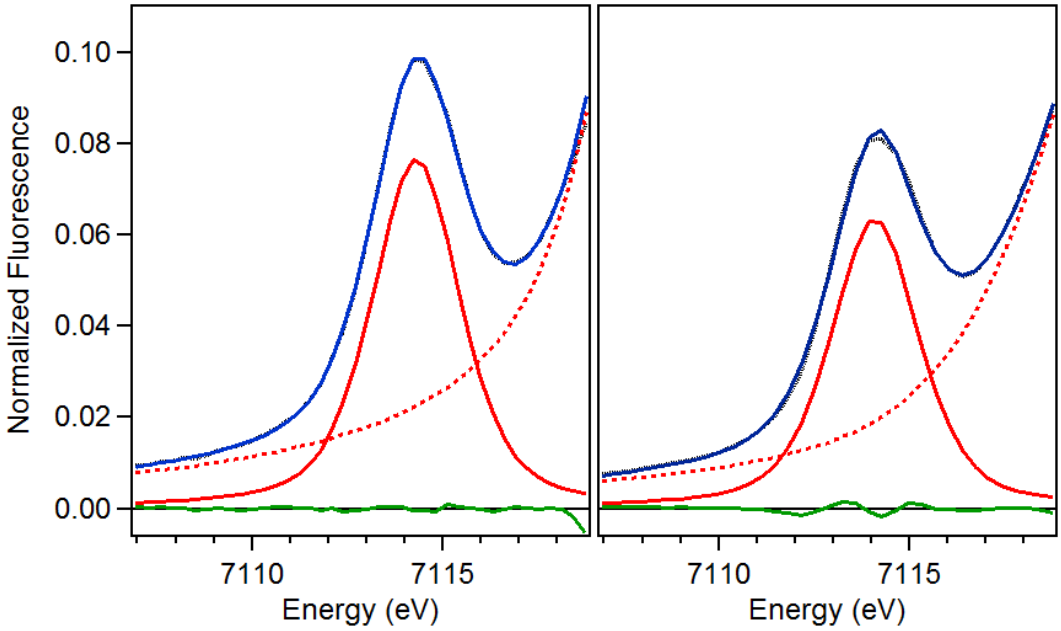

Figure 5.18. Pre-edge region analysis of **8** (left) and **9** (right). The experimental data (black dotted), baseline (red dashed), pre-edge peak components (red solid), residuals (green solid) and total fit (blue solid) are shown.

Table 5.14. XANES analysis of **8** and **9**.

Species	K-edge (eV)	Peak Position (eV)	Area (units)
8	7125.0	7114.0	21.1
9	7124.8	7114.2	17.4

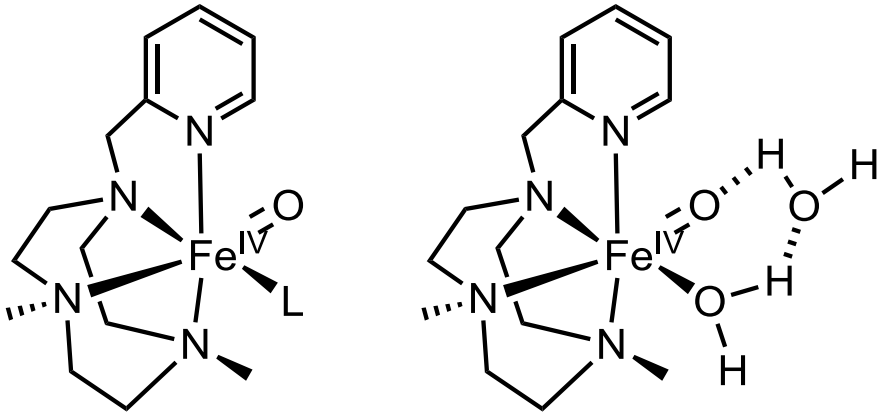

Figure 5.19. The EXAFS derived models for **8** (left) and **9** (right), where L is likely a solvent ligand, either OH_2 or MeCN.

The results of the EXAFS analysis for **8** and **9** are summarized in Tables 5.15 and Table 5.16 and Figures 5.19 – Figure 5.21. The 3-D models used for the FEFF calculations for **8** and **9** were modified from the crystal structure of ferrous starting material.[253] The best fit of **8** gives scattering pair distances that correspond to 5 Fe–N/O at 1.99 Å, 1 Fe–O/N at 1.65 Å, 5 Fe•••C at 2.82 Å and 5 Fe•••C at 2.96 Å. The shell at 1.99 Å is consistent with the nitrogen donors of the Pytacn ligand, as well as a solvent derived ligand. The short Fe–O distance of 1.65 Å is very similar to other synthetic oxoiron(IV) complexes, which have Fe=O distances between 1.64 and 1.70 Å.[275] The intense FT feature at R + Δ ~2.3 Å (Figure 5.20) required two carbon shells to properly fit the peak, which correspond to all of the carbon atoms in the macrocyclic ligand and the 2 and 6 positions of the pyridyl arm. Overall, **8** has a structure consistent with an oxoiron(IV) species.

The best fit of **9** gives scattering pair distances that correspond to 5 Fe–N/O at 1.98 Å, 1 Fe–O/N at 1.67 Å, 5 Fe•••C at 2.81 Å and 5 Fe•••C at 2.97 Å. This set of fitted parameters is identical to the oxoiron(IV) complex of **8**, within the error of the XAS

measurement. The only notable difference between **8** and **9** is the slight elongation of the Fe=O scatterer from 1.65 Å in **8** to 1.67 Å in **9**. However, these seemingly identical structures raise an interesting question of why the pre-edge area of **9** is smaller than that for **8**. As discussed above, one rationale is that the high concentration of water in the presence of acid allows for some interaction with the Fe=O unit. It is unlikely to be protonated to an Fe^{IV}-OH unit, as the hydroxo bond is ~1.8 Å, which is inconsistent with the EXAFS fit for **9**.[276, 277] An alternative explanation would involve some hydrogen bonding interaction between the solvent ligand *cis* to the oxo ligand and the bulk solvent (Figure 5.19). This could potentially form a 6-membered ring that may affect the Fe=O bond length and the *cis* ligand. These effects ultimately could change the centrosymmetry of the Fe center such that the pre-edge area decreases. More work would be required to demonstrate this effect.

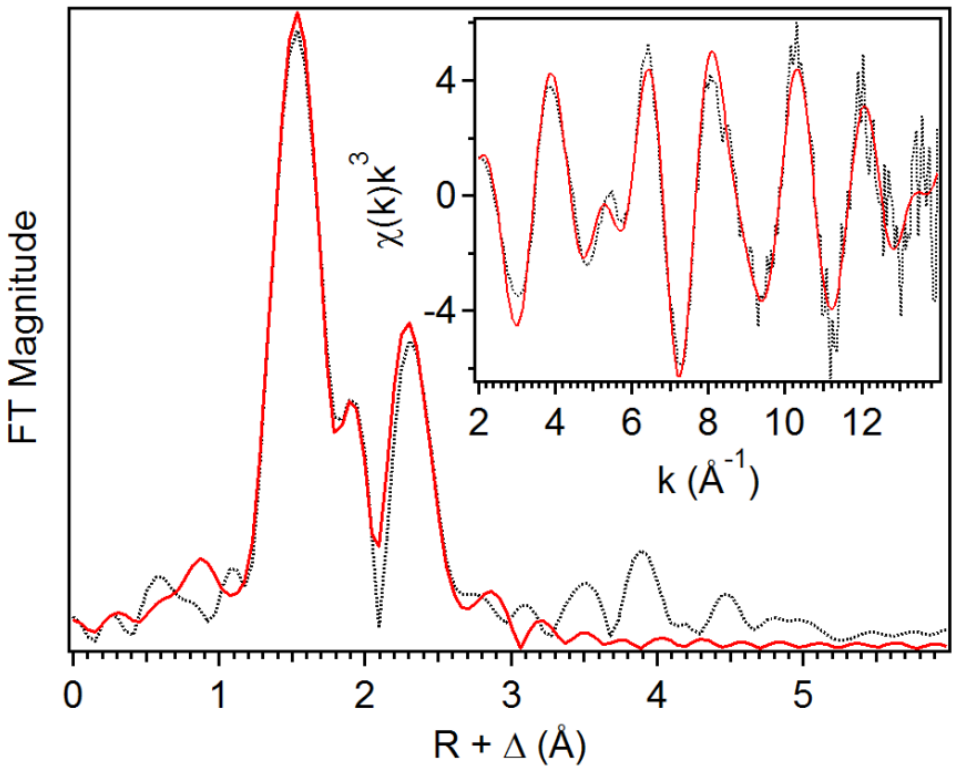

Figure 5.20. EXAFS analysis of **8**. The best fit (red solid line) of the unfiltered (black dotted) EXAFS data (inset) with corresponding Fourier transform (Fit 10). k = 2 – 14 $Å^{-1}$.

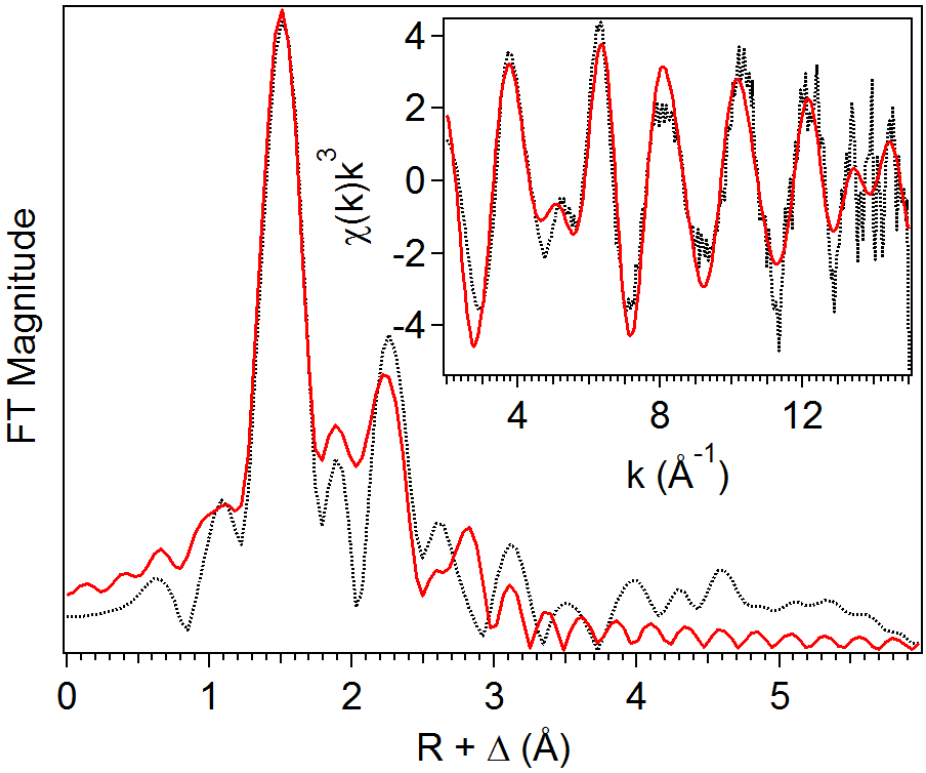

Figure 5.21. EXAFS analysis of **9**. The best fit (red solid line) of the unfiltered (black dotted) EXAFS data (inset) with corresponding Fourier transform (Fit 8). k = 2 – 15 $Å^{-1}$.

Table 5.15. EXAFS fit parameters for **8**. Fit 10 corresponds to the most reasonable fit of the data between k = 2 – 14 $Å^{-1}$.

	Fe-N/O			Fe-O/N			Fe•••C				GOF	
Fit	N	R(Å)	$\sigma^2(10^{-3})$	N	R(Å)	$\sigma^2(10^{-3})$	N	R(Å)	$\sigma^2(10^{-3})$	E_0	F	F'
1	6	1.98	4.07							-9.52	529	558
2	5	1.98	3.05							-9.30	474	529
3	4	1.98	1.99							-9.02	456	518
4	3	1.98	0.82							-9.05	491	538
5	5	1.98	3.25	1	1.65	3.88				-7.69	358	459
6	4	1.99	2.16	1	1.64	3.81				-6.52	384	476
7	3	1.99	0.89	1	1.64	2.99				-5.25	455	517
8	5	1.98	3.34	1	1.65	3.83	5	2.85	5.04	-7.15	228	366
9	5	1.98	3.38	1	1.65	3.68	10	2.86	10.26	-6.88	233	371
10	**5**	**1.99**	**3.39**	**1**	**1.65**	**3.61**	**5**	**2.82**	**1.52**	**-6.09**	**218**	**359**
							5	**2.96**	**2.45**			

Table 5.16. EXAFS fit parameters for **9**. Fit 8 corresponds to the most reasonable fit of the data between k = 2 – 15 $Å^{-1}$.

	Fe-N/O			Fe-O			Fe•••C				GOF	
Fit	**N**	**R (Å)**	**σ^2 (x10^{-3})**	**N**	**R (Å)**	**σ^2 (x10^{-3})**	**N**	**R (Å)**	**σ^2 (x10^{-3})**	**E_0**	**F**	**F'**
1	6	1.99	7.86							-3.31	505	687
2	5	1.99	5.85							-3.62	436	637
3	4	1.99	4.24							-3.56	386	600
4	4	1.98	4.18	1	1.67	5.29				-3.43	323	548
5	5	1.98	5.64	1	1.67	4.29				-3.60	311	539
6	5	1.98	5.73	1	1.67	4.47	5	2.88	10.31	-2.86	232	465
7	5	1.98	5.71	1	1.67	4.45	10	2.89	16.03	-3.06	232	466
8	**5**	**1.98**	**5.49**	**1**	**1.67**	**4.71**	**5**	**2.81**	**3.08**	**-3.33**	**209**	**442**
							5	**2.97**	**2.77**			

5.3.5 – XAS Analysis of Fe–Ce Adducts Supported by the Pytacn, TPA and α-BPMCN Ligands

5.3.5.1 – XAS analysis of 10 and 11. The K-edge energy for **10** was found at 7124.9 eV, and for **11** was found at 7125.4 eV. These K-edge energies fall in the range of oxoiron(IV) species, which have a range from 7123 to 7126 eV.[272-274] However, this range also overlaps with K-edge energies of (μ-1,2-peroxo)diferric species (7123 to 7126 eV).[105, 110, 112] The pre-edge peak of **10** has a maximum at 7114.1 eV with an area of 13.8 units, and the pre-edge peak of **11** has a maximum at7114.5 eV with an area of 12.3 units. These values are very low for an oxoiron(IV) species, which have a range of pre-edge areas from 20 to 38 units.[272-274] **10** and **11** also require two pre-edge component peaks to fit the pre-edge feature, whereas most oxoiron(IV) species only require one component peak. Peroxo-diferric species, however, have a range of pre-edge values from 12 to 16 units,[36, 105, 110, 112] consistent with **10** and **11**. The XANES parameters for **10** and **11** are also similar to the [(TMC)Fe^{III}(η^2-O_2)Sc^{III}] complex, that has a K-edge energy of 7125.3 eV and a pre-edge area of 14.4 units.[236] Overall, the XANES data for **10** and **11** are inconsistent with an oxoiron(IV) species, but are more similar to peroxo-diferric intermediates.

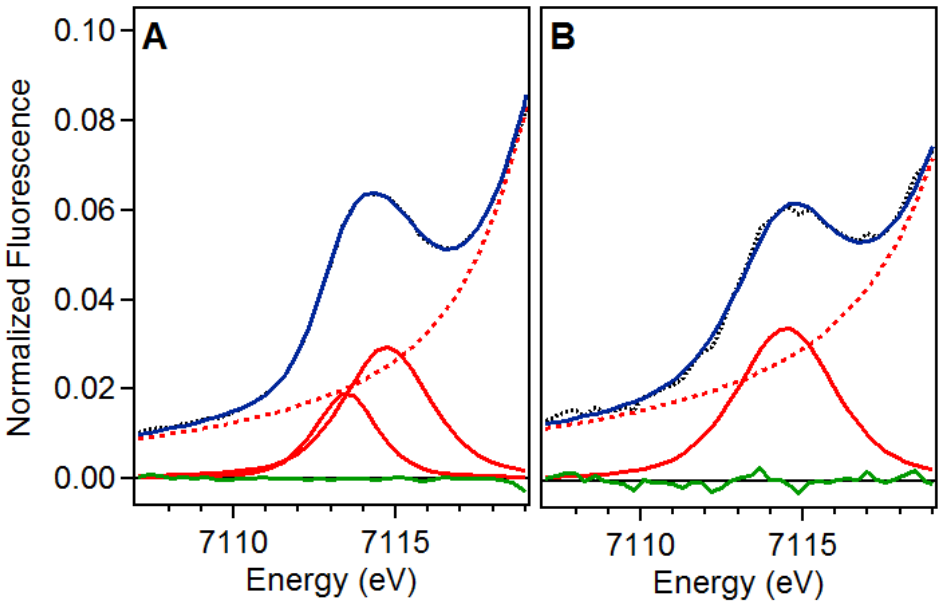

Figure 5.22. Pre-edge analysis for **10** (A) and **11** (B). The experimental data (black dotted), baseline (red dashed), pre-edge peak components (red solid), residuals (green solid) and total fit (blue solid) are shown.

Table 5.17. Pre-edge analysis for **10** and **11**.

Species	K-edge (eV)	Peak Position (eV)	Area (units)	Relative Area
10	7124.8	7113.5	4.36	1.00
		7114.7	9.42	2.16
			Total = 13.8	
11	7125.4	7114.5	**Total = 12.3**	1.00

The results of the EXAFS analysis for **10** and **11** are summarized in Table 5.18 and Table 5.19 and Figure 5.23 and Figure 5.24. The 3-D model used for the FEFF calculation for **10** and **11** was modified from the crystal structure of ferrous starting material.[253] The best fit of **10** gives scattering pair distances that correspond to 3 Fe–N/O at 2.23 Å, 2 Fe–N/O at 2.09 Å, 1 Fe–O/N at 1.94 Å, 1 Fe•••O at 2.47 Å, 5 Fe•••C at 3.01 Å and 1 Fe•••Ce at 3.67 Å. Compared to the oxoiron(IV) complexes of **8** and **9**, the primary sphere looks very different. **10** is generated by first forming the oxoiron(IV) species with CAN at room temperature in near quantitative yield, and as the sample is frozen the color changes indicating some different species is formed. The Fe–N/O distances at 2.23 Å and 2.09 Å in **10** are much longer than the ~2.0 Å scatterers for the

Fe^{IV} species. Additionally, there is no evidence for a short Fe–O length at ~1.6 Å for **10**, or even a μ-oxo ligand (~1.8 Å). Because of the absence of these thumbprint features, assignment as an Fe^{III} species would be consistent with the XANES data. The macrocyclic tertiary amine donors of the Pytacn ligand likely all maintain similar distances and thus are assigned to the 2.23 Å shell. The pyridine ligand, and the solvent derived ligand (water or acetonitrile) fit reasonably in the 2.09 Å shell, but it is also possible to have a mixture of all five N/O donors between these two shells. This leaves the Fe–O at 1.94 Å, which is consistent with either a μ-hydroxo ligand or proximal oxygen of a peroxo ligand. All of these shells are required for the best fit, as removal of one substantially increases the σ^2 values for the other shells (See Table 5.18). A carbon shell is needed at 3.01 Å, consistent with the C scatters in **8** and **9**.

In order to narrow down the possibilities we look at the Fe•••Ce distance at 3.67 Å, which fits in the very intense FT peak at R + Δ ~3.5 Å (Figure 5.24). If the 1.94 Å was assigned to a linear Fe–OH–Ce complex, assuming the Fe–O = Ce–O = 1.94 Å, the metal separation would need to be at ~3.9 Å. This indicates that the ∠ Fe–OH–Ce must not be linear (180º), and maintaining the same bonding metrics, the ∠ Fe–OH–Ce would be ~ 140º. This configuration is plausible, as there are examples of (μ-OH)differric complexes with Fe–OH distances between 1.96 and 2.01 Å, Fe•••Fe distances ~3.7 Å with ∠ Fe–OH–Fe of ~140º.[197, 198]

There is another O scatterer, with a small σ^2 value at 2.47 Å, meaning that this scatterer is well positioned. There is no clear source of a ~2.5 Å scatterer from a Fe–μ-OH–Ce complex, so the O scatterer likely comes from something else. One possibility would be that one of the Ce ligands (possibly NO_3) interacts with the μ-OH bridge in a hydrogen bond, which could rigidly fix the scatterer at ~2.5 Å (Figure 5.23, left). Another possibility would be to assign the 1.94-Å scatterer as the proximal oxygen atom of a peroxo ligand, then the ~2.5-Å scatterer would come from the distal oxygen atom. There are two types of peroxo binding configurations that could accommodate the 2.5 Å distance, a distorted μ-1,2-peroxo (Figure 5.23, middle) and η^1:η^2-peroxo (Figure 5.23, right) modes. The distorted μ-1,2-peroxo is less favored, as μ-1,2-peroxo-diferric species generally have a single atom bridge in addition to the peroxo ligand and have much shorter Fe•••Fe distances between 3.1 and 3.4 Å. These complexes tend to be blue or

green, whereas **10** is tan/brown. In addition, the distal peroxo oxygen in μ-1,2-peroxo-diferric complexes are not reported in EXAFS, and based on crystallography, are found between 2.9 and 3.0 Å. A substantial distortion in the ∠ Fe–O–O–Ce would therefore be required to accommodate a ~2.5 Å distal oxygen atom, and there is no clear reason why such a distortion should occur. The favored peroxo structure is the η^1:η^2-peroxo (Figure 5.23, right), with the proximal peroxo oxygen acting as a bridge between the Fe and Ce centers. The peroxo ligand would be bound side-on to the Ce center, which should rigidly fix the O positions. This would rationalize why the σ^2 for the 2.47-Å scatterer is 1.76 × 10^{-3} Å^2, much better than the distorted μ-1,2-peroxo and μ-OH models. This η^1:η^2-peroxo geometry would also be similar to that proposed for **3** and **4**. Resonance Raman experiments would ultimately help determine if a peroxo moiety was present, and could distinguish between all three possibilities.

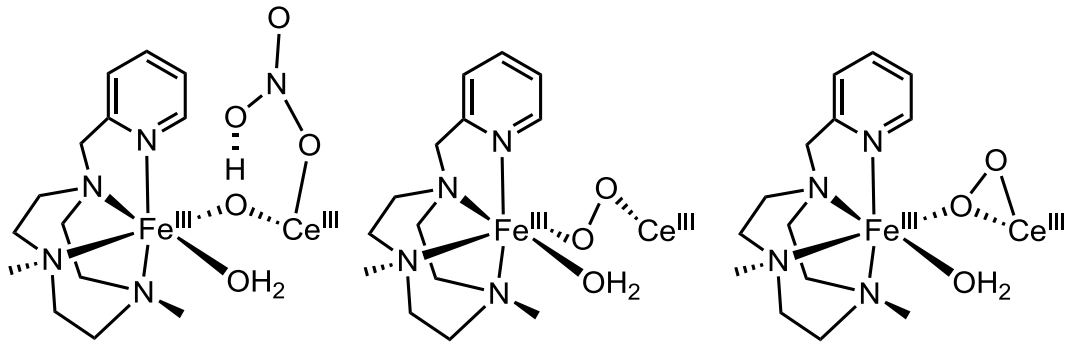

Figure 5.23. Possible EXAFS derived models for **10** and **11**. Left: μ-OH model with hydrogen bonding; Middle: distorted μ-1,2-peroxo model; Right: η^1:η^2-peroxo model.

The best fit of **11** gives scattering pair distances that correspond to 4 Fe–N/O at 2.17 Å, 2 Fe–O/N at 1.97 Å, 1 Fe•••O at 2.40 Å, 5 Fe•••C at 3.03 Å, and 1 Fe•••Ce at 3.63 Å. This fit is very similar to that for **10** but there are some subtle differences. The primary sphere scatterers were not able to be split into three shells like **10**, but instead we have a shorter shell of 4 Fe-N scatterers at 2.17 Å, compared to 2.23 and 2.09 Å for **10**, and 2 Fe–O scatterers at 1.97 Å, versus one scatterer at 1.94 Å for **10**. This is also visually apparent in the FT peak at R + Δ ~ 1.5 Å of both samples (Figure 5.24). Interestingly, the two longer shells from **10** are averaged, it results in a distance at ~2.16 Å, which is consistent with **11**. The reason for this change could be due in part to the increased amount of Ce added to **11**, which reduced the signal to noise for the sample and

decreased the usable k range for that experiment (k = 2 – 15 Å^{-1} for **10**, 2 – 13.75 Å^{-1} for **11**). Aside from the O scatterer at 2.40 Å, the remaining scatterers are identical to **10** within error. The 2.40-Å scatterer in **11** is slightly shorter than **10**, but the overall model is still consistent with the favored η^1:η^2-peroxo model (Figure 5.23, right).

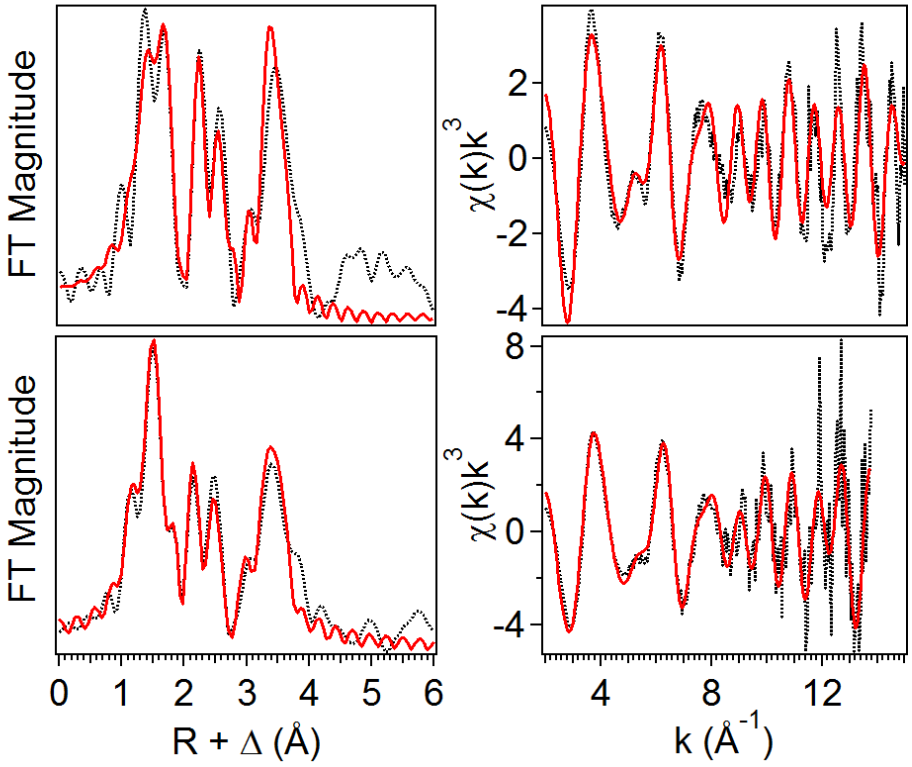

Figure 5.24. EXAFS analysis for **10** (top row) and **11** (bottom row). Left column: Fourier transform of the EXAFS data (black dotted) with best fit (red solid line). Right column: unfiltered EXAFS data (black dotted) with best fit (red solid line). **10**, Fit 12, k = 2 – 15 Å^{-1}; **11**, Fit 12, k = 2 – 13.75 Å^{-1}.

Table 5.18. EXAFS fit parameters for **10**. Fit 12 corresponds to the most reasonable fit of the data between k = 2 – 15 $Å^{-1}$.

	Fe-N			Fe-O			Fe•••C			Fe•••Ce				GOF	
Fit	**N**	**R(Å)**	**$\sigma^2(10^{-3})$**	**N**	**R(Å)**	**$\sigma^2(10^{-3})$**	**N**	**R(Å)**	**$\sigma^2(10^{-3})$**	**N**	**R(Å)**	**$\sigma^2(10^{-3})$**	**E_0**	**F**	**F'**
1	6	2.38	8.77										-30.6	561	847
2	4	2.29	6.91										-44.6	622	891
3	3	2.27	34.15	3	2.11	9.76							7.47	440	750
4	2	2.23	2.02	1	1.90	3.06							3.50	441	751
	3	2.08	2.51												
5	2	2.22	1.74	1	1.89	3.23				1	3.66	3.02	3.70	283	602
	3	2.08	2.42												
6	2	2.22	1.49	1	1.89	2.86	5	2.99	8.08	1	3.66	3.08	3.35	198	503
	3	2.08	2.26												
7	2	2.21	1.64	1	1.88	2.47	10	2.98	16.44	1	3.65	3.06	2.26	223	534
	3	2.07	2.20												
8	2	2.22	1.20	1	1.89	2.34	2	2.91	4.27	1	3.66	3.00	2.84	195	499
	3	2.07	1.95				3	3.03	3.27						
9	2	2.26	1.16	1	1.93	3.80	2	2.94	3.34	1	3.66	2.95	5.19	159	451
	3	2.11	2.43	1	2.45	1.55	3	3.06	3.29						
10	2	2.27	1.83	1	1.94	4.47	5	3.01	8.61	1	3.66	3.07	5.38	163	456
	3	2.11	2.97	1	2.46	1.52									
11	2	2.27	1.26	2	1.99	9.03	5	3.01	8.07	1	3.66	3.07	5.22	165	460
	2	2.13	1.52	1	2.45	1.37									
12	**3**	**2.23**	**4.96**	**1**	**1.94**	**4.00**	**5**	**3.01**	**8.78**	**1**	**3.67**	**3.05**	**5.82**	**160**	**452**
	2	**2.09**	**1.39**	**1**	**2.47**	**1.76**									

Table 5.18. (continued) EXAFS fit parameters for **10.** Fit 12 corresponds to the most reasonable fit of the data between k = 2 – 15 $Å^{-1}$.

	Fe-N			Fe-O			Fe•••C			Fe•••Ce				GOF	
Fit	N	R(Å)	$\sigma^2(10^{-3})$	N	R(Å)	$\sigma^2(10^{-3})$	N	R(Å)	$\sigma^2(10^{-3})$	N	R(Å)	$\sigma^2(10^{-3})$	E_0	F	F'
13	5	2.16	25.34	1	2.06	7.41	5	3.02	8.54	1	3.67	3.15	6.89	166	460
				1	2.50	1.13									
14	3	2.20	15.05	1	2.49	1.24	5	3.02	8.82	1	3.67	3.15	6.76	167	462
	2	2.07	8.45												
15	3	2.19	3.98	1	1.89	2.41	5	3.00	8.20	1	3.66	3.09	3.83	196	500
	2	2.06	0.75												
16	3	2.23	4.12	1	1.93	3.32	2	2.94	3.93	1	3.67	2.96	5.67	156	446
	2	2.09	0.83	1	2.46	1.91	3	3.06	3.91						

Table 5.19. EXAFS fit parameters for **11**. Fit 12 corresponds to the most reasonable fit of the data between k = 2 – 13.75 $Å^{-1}$.

	Fe-N			Fe-O			Fe•••C			Fe•••Ce				GOF	
Fit	**N**	**R(Å)**	**$\sigma^2(10^{-3})$**	**N**	**R(Å)**	**$\sigma^2(10^{-3})$**	**N**	**R(Å)**	**$\sigma^2(10^{-3})$**	**N**	**R(Å)**	**$\sigma^2(10^{-3})$**	**E_0**	**F**	**F'**
1	6	2.05	14.08										-5.51	738	803
2	5	2.05	12.31										-5.15	747	808
3	4	2.06	10.61										-4.54	770	820
4	3	2.06	8.87										-4.09	810	842
5	5	2.12	8.17	1	1.95	0							-3.24	663	761
6	4	2.13	5.72	1	1.95	-0.50							-2.69	651	755
7	3	2.14	3.17	1	1.96	-1.10							-2.27	650	753
8	5	2.12	8.55	1	1.94	0.54				1	3.63	1.95	-3.50	438	619
9	4	2.12	6.26	1	1.95	0.04				1	3.63	1.94	-3.16	431	614
10	4	2.14	5.57	2	1.96	2.98				1	3.63	1.99	-4.08	429	612
11	4	2.13	5.54	2	1.95	3.02	5	3.00	6.32	1	3.63	1.80	-3.99	347	551
12	**4**	**2.17**	**5.17**	**2**	**1.97**	**2.72**	**5**	**3.03**	**7.41**	**1**	**3.64**	**2.05**	**-1.71**	**312**	**522**
				1	**2.40**	**1.12**									
13	5	2.14	8.44	1	1.96	0.39	5	3.02	6.78	1	3.63	1.92	-1.81	319	528
				1	2.41	2.34									
14	5	2.10	8.73	1	1.93	1.12	5	3.11	5.18	1	3.64	2.05	-3.92	352	555
							5	2.96	3.01						
15	4	2.13	6.02	2	1.95	3.45	5	3.11	6.00	1	3.62	1.90	-4.06	355	557
							5	2.96	3.70						
16	4	2.16	5.50	2	1.97	2.88	5	2.98	6.15	1	3.63	2.08	-2.43	317	527
				1	2.40	2.14	3	3.11	4.73						

5.3.5.2 – XAS analysis of 12. The K-edge energy was found at 7125.2 eV, which is close to those for **10** (7124.8 eV) and **11** (7125.4 eV). Similarly, the K-edge of **12** falls in the range of mononuclear Fe^{IV}, but could also be in the range for diferric complexes. The pre-edge peak has a maximum at 7114.1 eV with an area of 12.5 units. This value compares well to both **10** and **11**, with pre-edge areas of 13.8 and 12.3 units respectively. Based on the XANES analysis, **12** has too low of a pre-edge area to be consistent with and oxoiron(IV) intermediate, but falls in the range of six-coordinate diferric species, including peroxo-diferric intermediates. Based on comparison to **10** and **11**, **12** can be similarly assigned to an Fe^{III} intermediate, and is not consistent with an oxoiron(IV) intermediate.

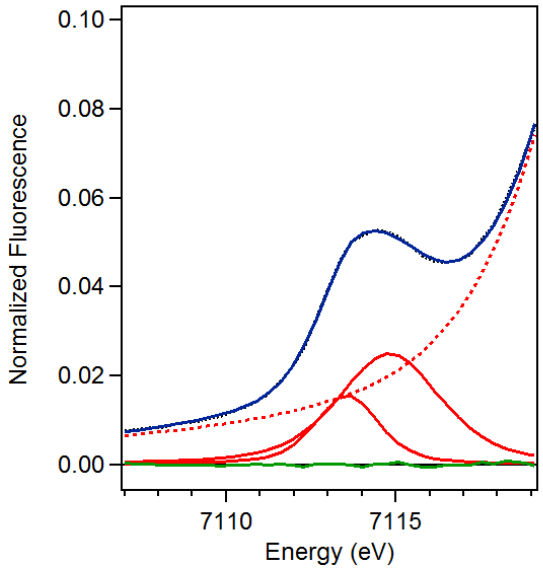

Figure 5.25. Pre-edge analysis for **12**. The experimental data (black dotted), baseline (red dashed), pre-edge peak components (red solid), residuals (green solid) and total fit (blue solid) are shown.

Table 5.20. Pre-edge analysis of **12**.

Species	K-edge (eV)	Peak Position (eV)	Area (units)	Relative Area
12	7125.2	7113.6	3.48	1.00
		7114.8	8.98	2.58
			Total = 12.5	

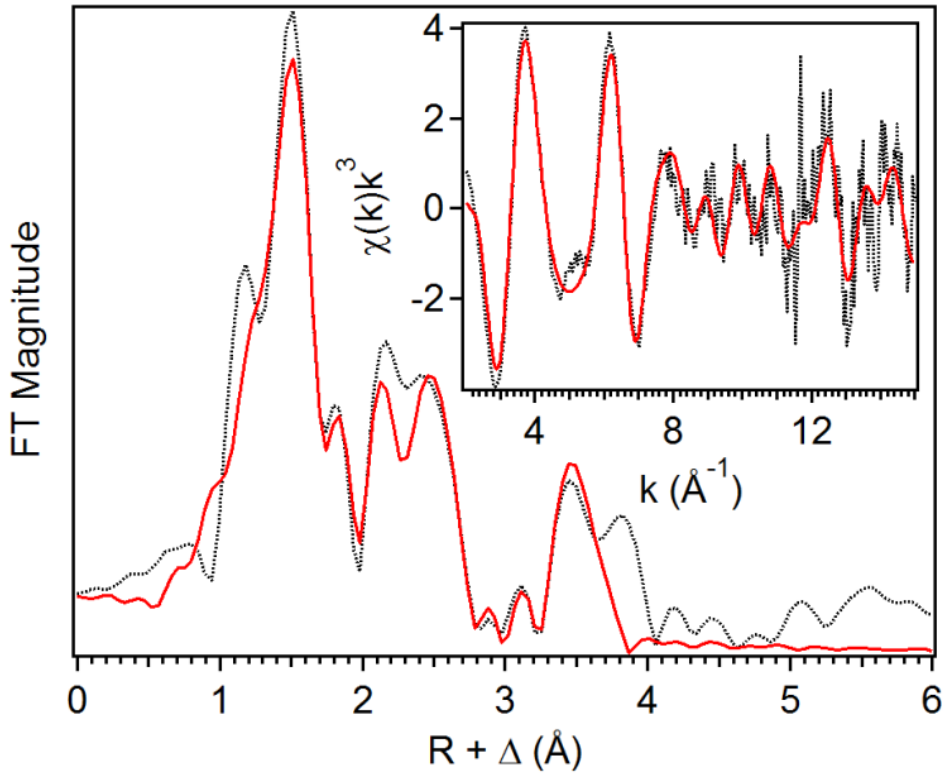

Figure 5.26. Fe K-edge EXAFS analysis for **12**. Fourier transform of the EXAFS data (black dotted) with best fit (red solid line). inset: unfiltered EXAFS data (black dotted) with best fit (red solid line). **12**, Fit 10, k = 2 – 15 $Å^{-1}$.

The results of the EXAFS analysis for **12** are summarized in Table 5.21 and Figure 5.26. The 3-D model used for the FEFF calculation for **12** was modified from the crystal structure of ferrous starting material.[253] The best fit of **12** gives scattering pair distances that correspond to 4 Fe–N/O at 2.16 Å, 2 Fe–N/O at 1.97 Å, 1 Fe•••O at 2.41 Å, 5 Fe•••C at 2.99 Å and 1 Fe•••Ce at 3.67 Å. This fit is nearly identical to **11** and quite similar to **10**, both of which are most consistent with a η^1:η^2-peroxo model (Figure 5.23, right). The main difference in the sample composition is that an oxoiron(IV) intermediate was formed using periodate in high yield for **12**, then only one equivalent of CAN was added to the solution to generate the Fe-Ce adduct. This is in contrast to exclusive use of CAN as an oxidant in **10** and **11**. While the distances fit are similar, the σ^2 values are larger for **12** compared to the other two samples (Table 5.21). Additionally, in the FT of **12**, the peak at R + Δ ~ 3.5 Å is much less intense than for **10** or **11** (Figure 5.26). These observations combined may suggest that less of the Fe^{III}–Ce adduct is generated in **12**.

Mössbauer experiments would help determine if the observed change is related to Fe speciation, if there were some equilibrium between the Fe-Ce adduct an something else. Another possibility is that the additional equivalents of Ce in the solution for **10** and **11** may interact with the intermediate and affect the scattering. For instance, if the Ce^{III} or additional Ce^{IV} atoms bind to or interact with the 3.67 Å Ce scatterer of the Fe-Ce adduct, it may help to increase the intensity of the FT peak. This phenomenon would not necessarily be observed in the Fe K-edge EXAFS.

To further study the properties of **12**, Ce L_3 edge XAS was collected, along with the spectra for CAN in a 1:1 MeCN:H_2O mixture in the presence (**CAN-H**) and absence (**CAN**) of acid, as a control. The results are summarized in Table 5.22 – Table 5.24 and Figure 5.27 – Figure 5.29. The Ce L_3-edge for **12** was found at 5729.1 eV, **CAN** was found at 5730.9 eV and **CAN-H** was found at 5731.3 eV. As there are not many studies that directly report or compare L_3-edge energies, the absolute values for these samples are not informative, however, the XANES region is. Generally, in the Ce L_3-edge XANES region, Ce^{IV} has two strong characteristic peaks of equal intensity, whereas Ce^{III} has only one red shifted peak with higher intensity.[278, 279] Both **CAN** and **CAN-H** should have Ce in the +4 oxidation state, as these samples are made by dissolving the CAN solid into the solvent. Two strong peaks are observed in the XANES region (Figure 5.27) for both **CAN** and **CAN-H** at 5733 and 5741 eV, consistent with assignment as Ce^{IV} species. **12** has a different XANES spectrum, where the peak at 5733 eV has been shifted to 5731 eV with much higher intensity, and the peak at 5741 eV has decreased in intensity. The presence of the peak at 5741 eV indicates that there may be some amount of Ce^{IV} in **12**, but the new feature at 5731 eV paired with a L_3-edge energy that is ~2 eV lower than those for the Ce^{IV} samples suggests that the majority species in **12** is consistent with Ce^{III}. Any remaining Ce^{IV} would be consistent with incomplete formation of **12** starting from the Fe^{IV}-Ce^{IV} species at higher temperatures. This suggests a possible with a thermal equilibrium, which would be consistent with the observation that the Fe^{IV}-Ce^{IV} to Fe^{III}-Ce conversion is reversible. The change in Ce oxidation state in **12** must be related to the Fe complex in solution, as the sample is prepared by first generating an oxoiron(IV) species with periodate then adding 1 equivalent of Ce^{IV} such that excess Ce^{III} is not present.

Based on the combined Fe K-edge and Ce L_3-edge XANES for **12**, the oxidation state of the sample is consistent with Fe^{III} and Ce^{III}.

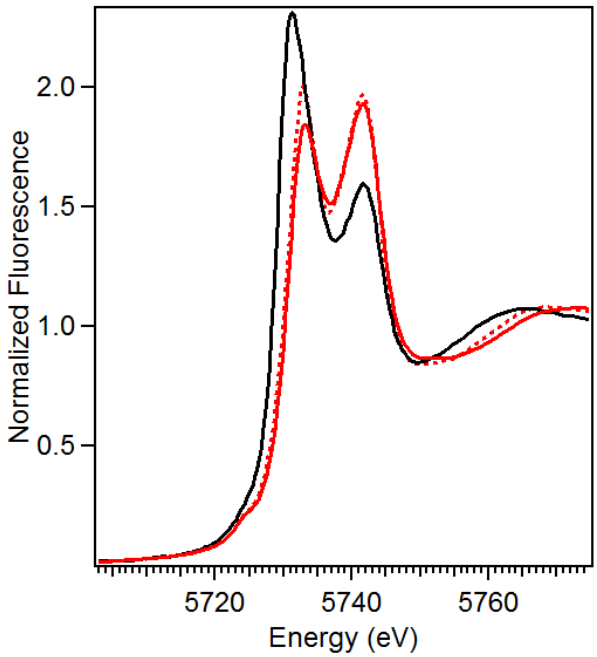

Figure 5.27. Normalized Ce L_3-edge XAS fluorescence data for **12** (solid black), **CAN** (solid red), and **CAN-H** (dashed red). L_3-edge energies: **12** = 5729.1 eV, **CAN** = 5730.9 eV, **CAN-H** = 5731.3 eV.

Ce L_3-edge EXAFS analysis is also useful for assessing the structures of the Ce containing samples. The k range for the Ce XAS is limited to 2 – 10.3 $Å^{-1}$ due to the Ce L_2 transition, so unfortunately the resolution for these experiments is not great (0.19 Å) and interpretation of long range interactions is limited. In the FT of each sample, there is a very intense peak at R + Δ ~ 2.1 Å that is from the primary coordination sphere and in **12** and **CAN-H**, there is an additional feature at ~ 3.5 Å that is consistent with intense multiple scattering effects from nitrate ligands bound in a bidentate fashion (Figure 5.28).[279] **CAN** lacks this feature, indicating that there is a change in the coordination of the nitrate ligands relative to **12** and **CAN-H**. The best fit of **CAN-H** has 10 Ce–O/N scatterers at 2.54 Å, 2 Ce–O/N at 2.07 Å, 4 Ce•••N/O at 2.95 Å, and Ce•••N/O multiple scattering pathways at 4.12 Å. The 2.54 Å distances are consistent with Ce–O interactions from nitrate ligand bound bidentate to the Ce, consistent with the crystal structure of CAN.[280] The scatterers at 2.95 Å are consistent with the N atoms of the nitrate ligands, and the multiple scattering effects at 4.12 Å are consistent with the distal O atom on the nitrate ligands. These multiple scattering effects help to fit the FT peak at

3.5 Å reasonably well (Figure 5.29). The identity of the 2 scatterers at 2.07 Å are not clear, but could be from monodentate bound nitrate ligands or solvent derived ligands. Overall, the EXAFS derived structure and distances agree well with the crystal structure of CAN, having primarily bidentate nitrate ligands.

The best fits of both **12** and **CAN** only include the primary coordination sphere, as attempts to fit the longer distance features were unsatisfactory (Table 5.23 and Table 5.24). For **12**, 7 Ce–O/N at 2.57 Å, 1 Ce–O/N at 2.09 Å and for **CAN**, 6 Ce–O/N at 2.55 Å, 1 Ce–O/N at 2.12 Å. The distances at ~2.5 Å are assigned to the Ce–O distances from bound nitrate ligands, consistent with the crystal structure of CAN.[280] In **CAN**, the assignment of the Ce–O distance at 2.12 Å, similar to **CAN-H**, is not clear. This distance could be assigned to the Ce–O distance of a Ce–μ-O–Ce species, which would be consistent with the lack of a peak at ~3.5 Å in the FT (Figure 5.28).[279] However, due to the solvent mixture used for **CAN**, this short distance could be also be from solvent derived ligands. What is clear is that the presence of acid appears to change the coordination environment of the Ce atoms under these experimental conditions. The assignment of the 2.09 Å scatterer for **12** is aided by the Fe K-edge EXAFS for the same sample. A shorter Fe–O distance at 1.97 Å for **12** (Table 5.21) was assigned to the proximal peroxo oxygen atom of a peroxo ligand (see Figure 5.23). Based on this, the Ce–O distance at 2.09 Å likely corresponds to an oxygen atom of the putative peroxo ligand. Increasing the N of this scatterer to 2 resulted in higher σ^2 values, which is why N = 1 was used in the best fit, but overall goodness of fit values for N = 2 fits were not very different (Table 5.24). Based on these results and the errors associated with the N value, it is possible that **12** has 2 scatterers at 2.09 Å. While there is a FT peak at 3.5 Å for **12**, it was not well fit by the same nitrate ligand multiple scatterering effects required for **CAN-H**. Attempts to fit scatterers at ~3 and ~4.1 Å (consistent with nitrate ligands) resulted in a substantial decrease in the primary sphere Ce–O distance between 2.3 and 2.45 Å. These shorter Ce–O distances are more consistent with Ce–OH_2 ligand binding,[279] which would be inconsistent with the bidentate nitrate ligand features at 3 and 4.1 Å. Fitting the FT peak at 3.5 Å with an Fe scatterer resulted in a Ce•••Fe distance at ~3.7 Å, consistent with the Fe K-edge EXAFS, but with a negative σ^2 value. Unfortunately, no combination of Fe or nitrate scatterers at longer distances resulted in a satisfactory fit, however, so

were not included in the best fit. **12** is not fit the same as **CAN-H** despite having a similar long range feature in the FT, and **12** has a similar fit as **CAN** but has a FT distinct that is distinct. These results are not inconsistent with the Fe K-edge data, but the limited k range of the Ce data ultimately prevents extracting additional information.

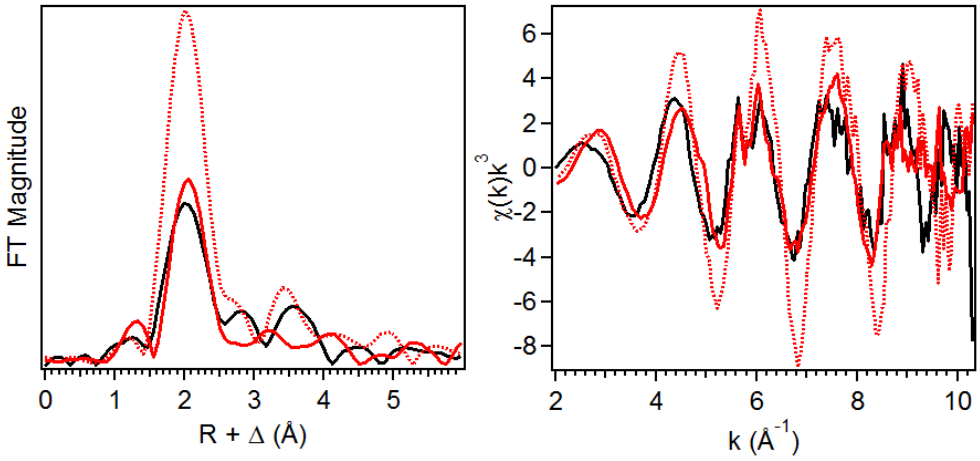

Figure 5.28. EXAFS analysis for **12** (black), **CAN** (solid red) and **CAN-H** (dashed red). Left column: Fourier transform of the EXAFS data. Right column: unfiltered EXAFS data between k = 2 – 10.3 $Å^{-1}$.

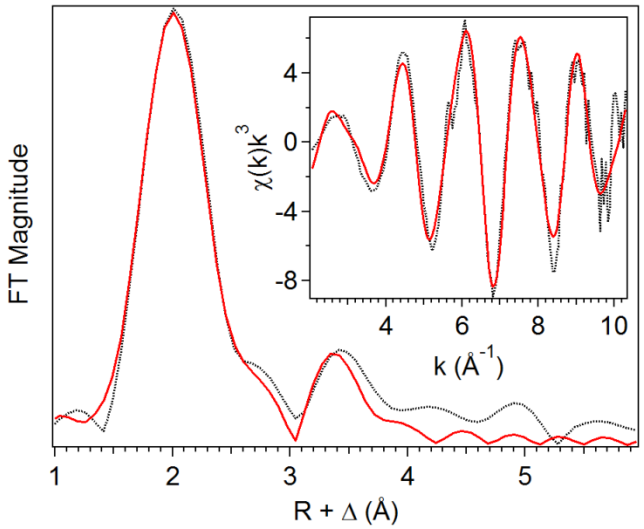

Figure 5.29. Ce L_3-edge EXAFS analysis for **CAN-H**. Fourier transform of the EXAFS data (black dotted) with best fit (red solid line). inset: unfiltered EXAFS data (black dotted) with best fit (red solid line). Fit 7, k = 2 – 10.3 $Å^{-1}$.

Table 5.21. Fe K-edge EXAFS fit parameters for **12**. Fit 10 corresponds to the most reasonable fit of the data between k = 2 – 15 $Å^{-1}$.

	Fe-N			**Fe-O**			**Fe•••Ce**			**Fe•••C**				**GOF**	
Fit	**N**	**R(Å)**	**$\sigma^2(10^{-3})$**	**N**	**R(Å)**	**$\sigma^2(10^{-3})$**	**N**	**R(Å)**	**$\sigma^2(10^{-3})$**	**N**	**R(Å)**	**$\sigma^2(10^{-3})$**	**E_o**	**F**	**F'**
1	6	2.05	14.55										-7.11	267	605
2	5	2.05	12.51										-6.93	276	615
3	4	2.05	10.50										-6.93	300	640
4	3	2.04	8.32										-7.87	344	686
5	3	2.15	5.31										-5.59	245	579
	2	1.96	3.90												
6	3	2.15	5.43				1	3.66	7.18				-5.57	234	566
	2	1.96	3.97												
7	3	2.14	5.92				1	3.66	6.96	5	2.98	7.74	-5.98	149	452
	2	1.96	4.14												
8	3	2.16	5.37	1	2.41	6.88	1	3.67	6.91	5	2.99	8.11	-4.78	135	431
	2	1.97	4.11												
9	3	2.15	6.14	1	2.43	5.64	1	3.66	6.97	5	2.90	31.53	-6.21	132	425
	2	1.96	4.27							5	2.99	8.90			
10	**4**	**2.16**	**8.35**	**1**	**2.42**	**4.24**	**1**	**3.67**	**6.76**	**5**	**2.99**	**8.22**	**-4.74**	**136**	**431**
	2	**1.97**	**4.65**												

Table 5.22. Ce L_3-edge EXAFS fit parameters for **CAN-H**. Fit 7 corresponds to the most reasonable fit of the data between k = 2 – 10.3 $Å^{-1}$. Scatterers in italics are multiple scattering pathways linked to the single scattering shell.

	Ce-O/N			**Ce-O**			**Ce•••N/O**				**GOF**	
Fit	**N**	**R(Å)**	**$\sigma^2(10^{-3})$**	**N**	**R(Å)**	**$\sigma^2(10^{-3})$**	**N**	**R(Å)**	**$\sigma^2(10^{-3})$**	**E_o**	**F**	**F'**
1	12	2.51	3.39							5.85	360	413
2	8	2.51	0.37							5.88	388	430
3	12	2.50	3.90				6	2.95	4.72	3.11	300	378
4	10	2.54	1.97	2	2.07	2.24				9.61	252	347
5	10	2.54	2.23	2	2.07	2.14	4	2.94	9.39	9.78	231	331
6	10	2.54	1.94	2	2.06	2.20	4	2.95	10.26	8.93	193	303
							4	4.26	2.51			
							4	*4.26*	*2.51*			
7	**10**	**2.54**	**1.96**	**2**	**2.07**	**2.56**	**4**	**2.95**	**11.94**	**9.32**	**162**	**278**
							4	**4.12**	**2.59**			
							8	***4.12***	***2.59***			
8	12	2.50	3.72				6	2.95	5.78	3.42	234	333
							4	4.06	2.05			
							8	*4.06*	*2.05*			

Table 5.23. Ce L_3-edge EXAFS fit parameters for **CAN**. Fit 4 corresponds to the most reasonable fit of the data between k = 2 – 10.3 $Å^{-1}$.

	Ce-O/N			**Ce-O**			**Ce•••N/O**				**GOF**	
Fit	**N**	**R(Å)**	**$\sigma^2(10^{-3})$**	**N**	**R(Å)**	**$\sigma^2(10^{-3})$**	**N**	**R(Å)**	**$\sigma^2(10^{-3})$**	**E_o**	**F**	**F'**
1	12	2.54	11.73							8.09	240	638
2	8	2.53	6.60							7.77	162	524
3	6	2.54	4.02							8.34	147	501
4	**6**	**2.55**	**4.69**	**1**	**2.12**	**3.68**				**9.99**	**130**	**470**
5	6	2.55	4.79	1	2.13	3.42	3	3.04	4.54	10.13	120	450
6	6	2.54	0.42	1	2.15	-1.20				7.81	115	441
				1	2.37	-7.20						
7	6	2.53	3.80	2	2.29	37.22				7.51	145	496

Table 5.24. Ce L_3-edge EXAFS fit parameters for **12**. Fit 6 corresponds to the most reasonable fit of the data between k = 2 – 10.3 $Å^{-1}$. Scatterers in italics are multiple scattering pathways linked to the single scattering shell.

	Ce-O/N			Ce-O			Ce•••N/O				GOF	
Fit	**N**	**R(Å)**	**$\sigma^2(10^{-3})$**	**N**	**R(Å)**	**$\sigma^2(10^{-3})$**	**N**	**R(Å)**	**$\sigma^2(10^{-3})$**	**E_o**	**F**	**F'**
1	12	2.54	12.22							3.72	304	682
2	10	2.53	10.06							2.86	281	657
3	8	2.54	7.65							4.31	265	638
4	7	2.55	6.47							5.49	264	636
5	6	2.55	5.24							5.21	270	643
6	**7**	**2.57**	**6.52**	**1**	**2.09**	**1.53**				**7.96**	**247**	**615**
7	7	2.55	6.47	2	1.97	78.83				5.72	261	632
8	6	2.57	5.72	2	2.09	11.75				8.93	269	642
9	6	2.58	4.77	1	2.09	-0.01				8.60	246	613
10	7	2.57	6.62	1	2.11	2.97				7.88	193	543
11	7	2.57	-0.09	1	2.40	-1.06				4.18	202	557
12	12	2.52	13.85				6	2.96	3.76	0.02	238	603
13	7	2.34	7.35	2	2.09	1.95	6	2.88	-1.50	-17.8	194	547
14	7	2.45	8.09				6	2.93	1.75	-7.94	184	531
							6	4.14	2.53			
							6	*4.14*	*2.53*			
15	7	2.39	7.84	2	2.12	6.90	7	2.90	1.05	14.4	162	497
							6	4.10	2.91			
							6	*4.10*	*2.91*			

5.3.5.3 – XAS analysis of 13. The K-edge energy was found at 7124.9 eV. This value is close to those for diferric peroxo complexes like **6** and **10-12** at ~7125 eV. The pre-edge peak for **13** has a maximum centered at 7114.2 eV with an area of 8.6 units. This value is lower than the Fe-Ce adducts **10-12**, and falls in the range of six-coordinate ferric centers, between 4 and 9 units.[44, 85]

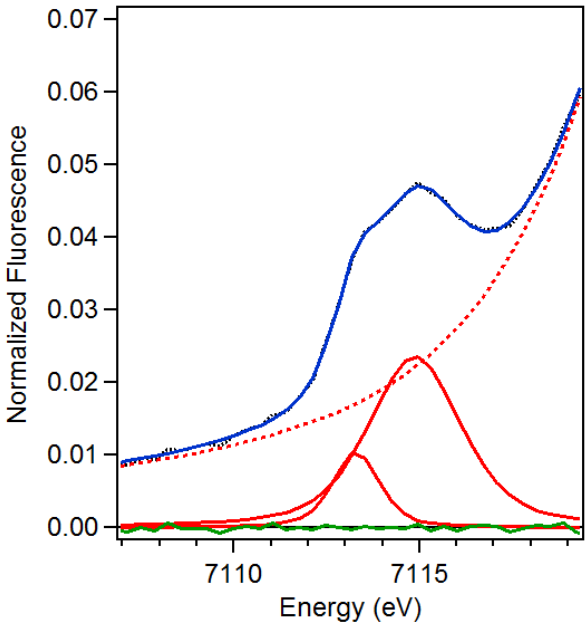

Figure 5.30. Pre-edge analysis for **13**. The experimental data (black dotted), baseline (red dashed), pre-edge peak components (red solid), residuals (green solid) and total fit (blue solid) are shown.

Table 5.25. Pre-edge analysis for **13**.

Peak Position (eV)	Peak Area (units)	Relative Area
7113.3	1.55	1.00
7114.9	7.02	4.53

The results of the EXAFS analysis for **13** are summarized in Table 5.26 and Figure 5.31 and Figure 5.32. The 3-D model used for the FEFF calculation for **13** was modified from the crystal structure of the $[Fe^{II}_2(OH)_2(TPA)_2]^{2+}$ complex.[92] The best fit of **13** gives scattering pair distances that correspond to 1 Fe–N/O at 1.87 Å, 5 Fe–N/O at 2.05 Å, 1 Fe•••O/N at 2.54 Å, 5 Fe•••C at 2.98 Å, and 1 Fe•••Ce at 3.62 Å. This fit is quite similar to the final fits of **10** – **12**, which were proposed to be Fe^{III}–(O_2)–Ce^{III} adducts, though there are some slight differences. The primary FT peak at R + Δ ~ 1.7 Å

for **13** (Figure 5.32) is assigned to the 2.05 Å and 1.87 Å scatterers, and the overall FT is more similar to that of **11** with two shells for the primary sphere (4 Fe–N at 2.17 Å, 2 Fe–O at 1.97 Å) compared to three shells for **10** (3 Fe–N at 2.23 Å, 2 Fe–N at 2.09 Å, 1 Fe–O at 1.94 Å) (see Figure 5.24). The tripodal ligand framework of the TPA ligand in **13** likely allows for all of the N-donor ligands to bind at 2.05 Å and therefore these atoms easily fit into one scattering shell, compared to the fits with the Pytacn ligand for **10** and **11**. The 1.87 Å scatterer in **13** is shorter than in **10** (1.94 Å) or **11** (1.97 Å), and could be consistent with a longer μ-oxo ligand, a shorter μ-hydroxo ligand or the proximal oxygen atom of a peroxo ligand. An Fe•••O distance at 2.54 Å is required to fit the FT peak at ~2.2 Å, but this scatterer has a σ^2 value (4.54×10^{-3} Å^2) higher than for **10** and **11**, but similar to that for **12**. This may indicate that the 2.5-Å oxygen atom in **13** may be less rigidly positioned, or there is a mixture of species in the sample. This scatterer would be consistent with the distal peroxo oxygen of an Fe-Ce η^1:η^2-peroxo species (Figure 5.31, left), in agreement with **10** – **12**. Similar to other pyridine containing complexes, Fe•••C scatterers at ~3 Å are also required to fit the sharp FT peak centered at 2.5 Å. The best fit of **13** also requires one Ce scatterer at 3.62 Å, consistent with the Pytacn based samples. However, the FT peak at ~3.4 Å that is fit with Ce has a smaller but distinct peak next to it at 3.7 Å. Attempts to fit a 2nd Ce scatterer at 3.81 Å for the sample resulted in lower GOF values (Table 5.26, fit 10), but the FT peaks at 3.4 and 3.7 Å could not be adequately fit. This might indicate that **13** has some amount of an Fe-Ce adduct with a ~3.8 Å distance, as well as the peroxo adduct with a Ce distance of 3.6 Å. A 3.8 Å distance could correspond to a linear Fe–O–Ce species with Fe–O = Ce–O = 1.9 Å (Figure 5.31, right). Quantification of the species in the sample would require Mössbauer experiments.

Overall, the EXAFS data for **13** is consistent with an η^1:η^2-peroxo species similar to that assigned for **10** – **12**, due to the Fe–O scatter at ~2.5 Å and Fe•••Ce distance at 3.6 Å. The pre-edge are of **13** is several units lower than the Pytacn supported intermediates, but the primary sphere ligation in **13** seems to be closer to a centrosymmetric configuration, consistent with a lower value. However, some quantity of a linear Fe–O–Ce intermediate with a Ce distance at 3.8 Å (Figure 5.31, right) could contribute to the shorter 1.87-Å O scatterer and the increased σ^2 value in **13**, compared to **10** and **11**.

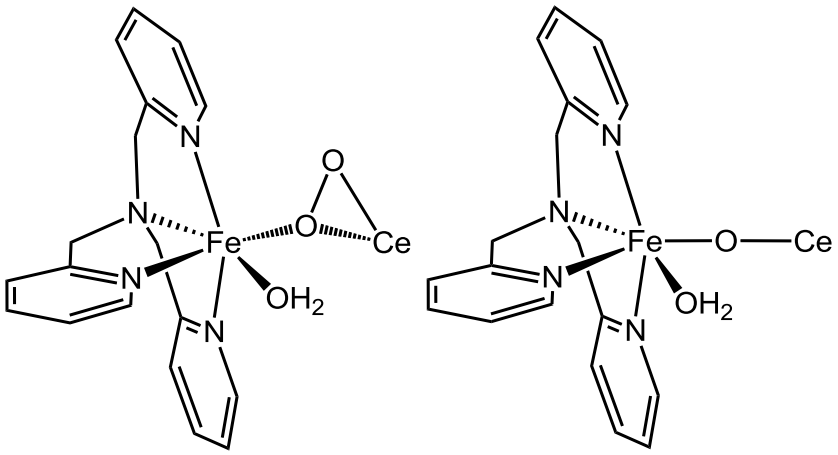

Figure 5.31. Possible EXAFS derived model for **13**. Left: η^1:η^2-peroxo model with Ce at ~3.6 Å, Right: linear Fe–O–Ce model with Ce at ~3.8 Å.

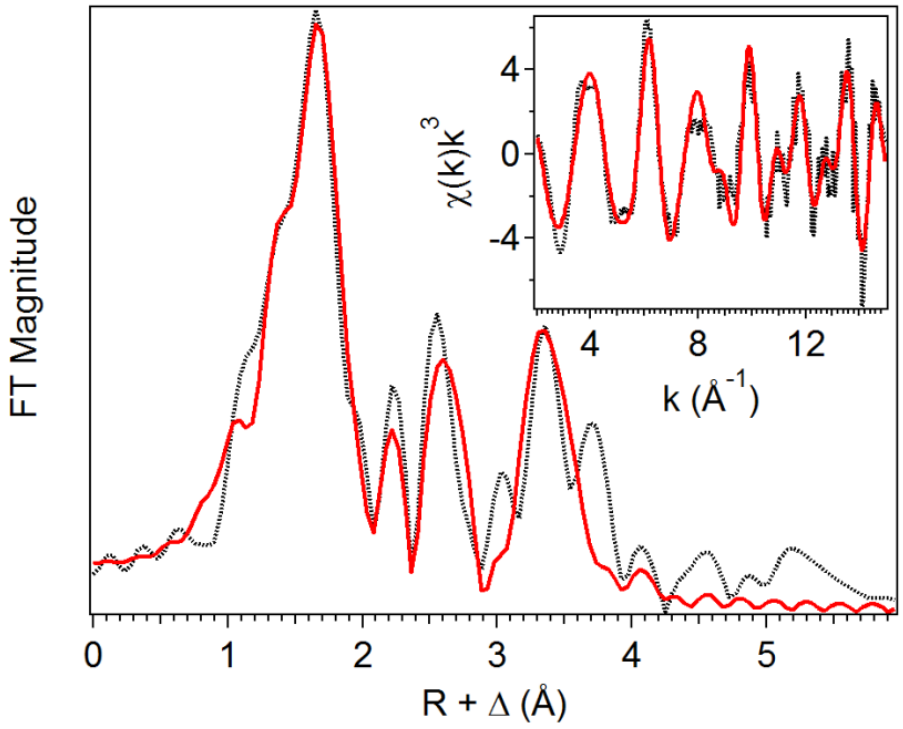

Figure 5.32. EXAFS analysis for **13**. Fourier transform of the EXAFS data (black dotted) with best fit (red solid line). inset: unfiltered EXAFS data (black dotted) with best fit (red solid line). Fit 9, k = 2 – 15 Å^{-1}.

Table 5.26. EXAFS fit parameters for **13**. Fit 9 corresponds to the most reasonable fit of the data between k = 2 – 15 $Å^{-1}$.

	Fe-N			Fe-O			Fe•••C			Fe•••Ce				GOF	
Fit	N	R(Å)	$\sigma^2(10^{-3})$	N	R(Å)	$\sigma^2(10^{-3})$	N	R(Å)	$\sigma^2(10^{-3})$	N	R(Å)	$\sigma^2(10^{-3})$	E_o	F	F'
1	6	2.05	5.17										-5.85	652	612
2	5	2.05	3.89										-5.33	636	605
3	4	2.05	2.63										-4.66	643	608
4	3	2.05	1.33										-4.26	688	629
5	5	2.04	2.77	1	1.87	2.59							-8.89	584	579
6	5	2.05	2.92	1	1.88	3.69	5	2.98	2.03				-7.57	425	494
7	5	2.05	3.02	1	1.88	4.34	5	2.99	2.37	1	3.63	2.60	-7.23	247	377
8	5	2.06	3.40	1	1.90	6.58	5	3.12	5.21	1	3.63	2.85	-5.5	246	376
							5	2.98	1.17						
9	**5**	**2.05**	**2.96**	**1**	**1.87**	**3.78**	**5**	**2.98**	**2.38**	**1**	**3.62**	**2.60**	**-7.92**	**234**	**367**
				1	**2.54**	**4.54**									
10	5	2.05	2.92	1	1.87	3.72	5	2.98	2.67	1	3.64	2.31	-7.85	207	345
				1	2.55	5.40				1	3.81	4.85			
11	5	2.05	3.38	1	1.90	6.20	5	2.98	0.64	1	3.63	2.97	-6.07	226	361
				1	2.70	17.46	3	3.13	1.68						
12	5	2.06	3.30	1	1.90	6.25	5	2.97	1.61	1	3.64	2.56	-5.53	219	355
							5	3.11	5.86	1	3.82	5.18			
13	5	2.05	3.97	1	2.53	2.94	5	2.99	2.46	1	3.63	2.51	-5.13	269	393

5.3.5.4 – XAS analysis of 14. The K-edge energy for **14** was found at 7125.2 eV (Table 5.27). This falls in the range of mononuclear oxoiron(IV) complexes, which have a range from 7123 to 7126 eV.[272-274] Coincidentally, like for **10 – 13**, this range also overlaps with K-edge energies of diferric species (7123 to 7126 eV). The solution structure of **14** as determined by resonance Raman spectroscopy and mass spectrometry is an oxoiron(IV) unit with a μ-oxo bridge between the Fe^{IV} and Ce^{IV} centers. The K-edge alone is not able to distinguish between Fe^{III} and Fe^{IV}. The pre-edge peak for **14** is centered at 7114.7 eV has an area of 11.5 units (Figure 5.33). This pre-edge value is very low for an oxoiron(IV) species, that normally have a range of pre-edge areas from 20 to 38 units.[272-274] Based on this, **14** is inconsistent with an oxoiron(IV) adduct. However, the pre-edge area is close to those for **10** – **12** which are proposed to be $Fe^{III}(O_2)Ce^{III}$ adducts. Overall, the XANES analysis is more consistent with an Fe^{III} center for **14**.

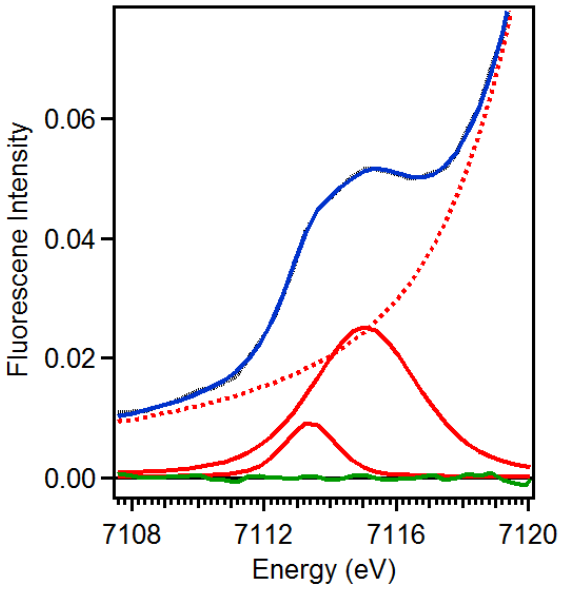

Figure 5.33. Pre-edge analysis for **14**. The experimental data (black dotted), baseline (red dashed), pre-edge peak components (red solid), residuals (green solid) and total fit (blue solid) are shown.

Table 5.27. Pre-edge analysis for **14**.

Species	K-edge (eV)	Peak Position (eV)	Area (units)	Relative Area
14	7125.2	7113.4	1.72	1.00
		7115.0	9.75	5.66
			Total = 11.5	

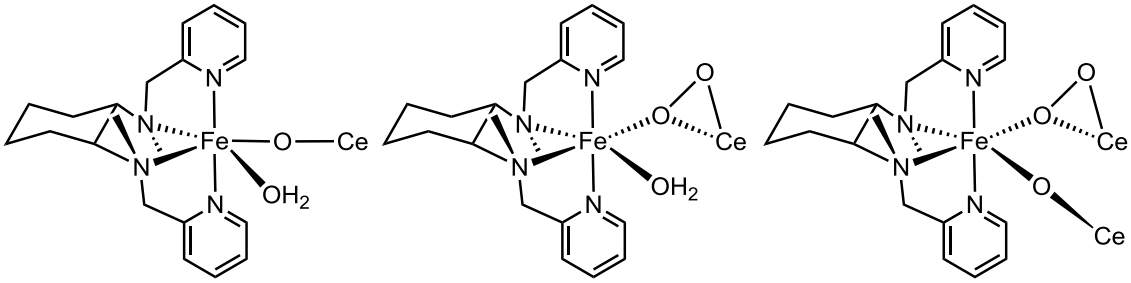

Figure 5.34. Possible EXAFS derived models for **14**. Left: linear Fe–O–Ce species; middle: $Fe(O_2)Ce$ model; right: combination model.

The results of the EXAFS analysis for **14** are summarized in Table 5.28 and Figure 5.34 and Figure 5.35. The 3-D model used for the FEFF calculation for **14** was modified from the crystal structure of the $[Fe^{II}_2(OTF)_2(\alpha\text{-BPMCN})_2]$ starting material.[281] The best fit of **14** gives scattering pair distances that correspond to 1 Fe–O/N at 1.89 Å, 5 Fe–N/O at 2.14 Å, 0.5 Fe•••O at 2.47 Å, 5 Fe•••C at 2.99 Å , 3 Fe•••C at 3.13 Å, 1 Fe•••Ce at 3.69 Å and 1 Fe•••Ce at 3.87 Å. The FT has a sharp feature at R + Δ ~1.7 Å that is fit with the primary sphere scatterers at 2.14 Å and 1.89 Å (Figure 5.35). Attempts to add a third shell at ~2 Å were unsuccessful (Table 5.28, fit 7). The 2.14-Å scatterers are assigned to the amine and pyridine donors from the BPMCN ligand based on similarity to the crystal structure of the starting material,[281] as well as an additional solvent derived ligand. The shorter 1.89-Å scatterer is consistent with a long μ-oxo ligand, a shorter μ-hydroxo ligand or the proximal oxygen atom of a peroxo ligand, similar to **13**. Unlike **10** – **13**, two shells of carbon scatterers are required for the best fit of **14**, with the 2.99-Å shell being assigned to a combination of aliphatic carbon atoms from the BPMCN ligand, as well as carbon atoms in the 2 position of the pyridine rings, and the 3.13-Å shell is consistent with the carbon atoms in the 6 position of the pyridine rings.

The remaining shells at 2.47, 3.69 and 3.87 Å raise interesting questions about the structure of **14**. The fit of **14** is modestly improved by the inclusion of an Fe•••O scatterer at 2.47 Å (Table 5.28, fit 15 vs fit 16), but needs an N value < 1 to obtain a reasonable σ^2 value (Table 5.28, fit 16 vs fit 17). In **10** – **13**, a scatterer at ~2.5 Å is paired with a Ce distance at ~3.7 Å, and these are signature features of a proposed Fe(η^1:η^2-peroxo)Ce species (Figure 5.34, middle). Indeed, the best fit for **14** includes a Ce scatterer at 3.69 Å that could pair with the 2.47-Å scatterer, but an additional Ce interaction is needed at 3.87 Å. A ~3.9 Å Ce distance would be consistent with a linear Fe-O-Ce model (Figure 5.34, left). The FT feature centered at ~3.6 Å is split into two peaks with equal intensity at 3.4 and 3.8 Å (Figure 5.35). If only a Ce scatterer at 3.67 Å is used, the 3.4-Å peak is fit, and if only a Ce at 3.87 Å is used, the 3.8-Å peak is fit. Adjusting the N values for both of these Ce scatterers to 0.5 produces a fit with too small of a σ^2 value for the 3.87-Å scatterer (Table 5.28, fit 12). Adjusting the N values for the 3.67-Å Ce to 0.4 and 0.6 for the 3.87-Å Ce produces a fit with too small of a σ^2 value for the 3.67-Å Ce (Table 5.28, fit 13). These fits indicate that either there are two separate species in the sample with roughly equal amounts, or there is one species with two separate Fe•••Ce interactions. In the first scenario, the two species would be consistent with a Fe(O_2)Ce model – with a Ce at ~3.7 Å and an O scatterer at ~2.5 Å (Figure 5.34, middle), and a linear Fe–O–Ce model with a μ-oxo interaction at 1.89 Å and a Ce distance at ~3.9 Å (Figure 5.34, left). In support of this scenario is the requirement of N = 0.5 for the ~2.5 scatterer, which would indicate that roughly half of the sample is consistent with the peroxo assignment, and would imply that the other portion is consistent with the linear model. The second scenario, is that **14** is one intermediate that has both a linear Fe-O-Ce unit, as well as a Fe(O_2)Ce unit (Figure 5.34, right). Mössbauer and resonance Raman experiments are needed to distinguish between these two possibilities, however the present data is more consistent with a mixture of species in the sample.

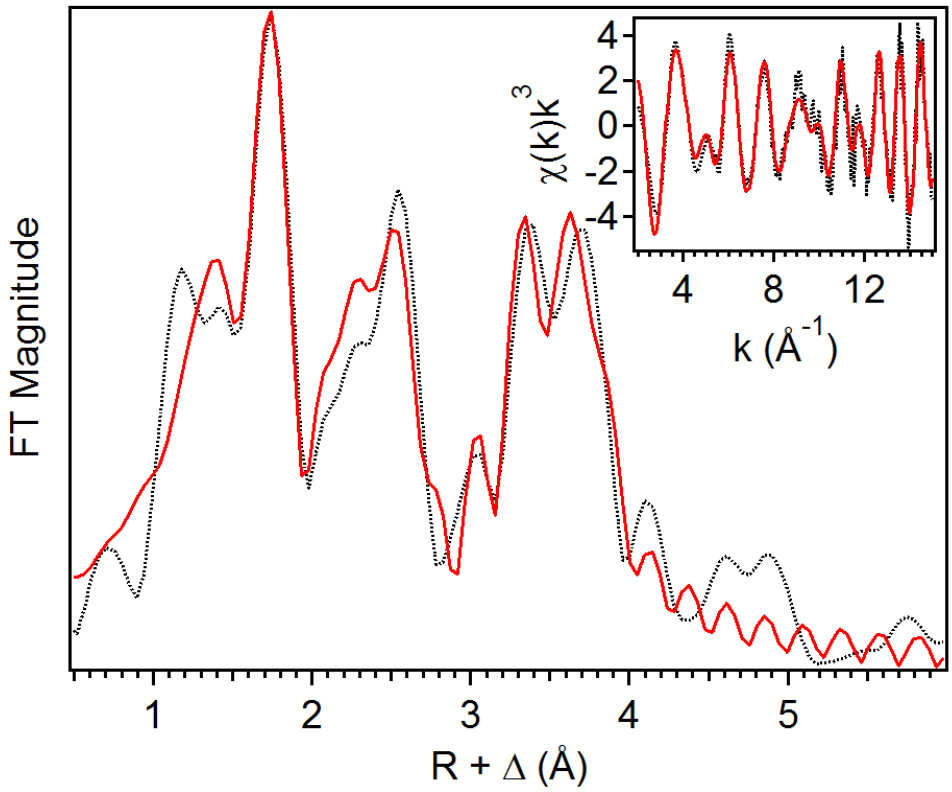

Figure 5.35. EXAFS analysis for **14**. Fourier transform of the EXAFS data (black dotted) with best fit (red solid line). inset: unfiltered EXAFS data (black dotted) with best fit (red solid line). Fit 16, k = 2 – 15 $Å^{-1}$.

Table 5.28. EXAFS fit parameters for **14**. Fit 16 corresponds to the most reasonable fit of the data between k = 2 – 15 $Å^{-1}$.

	Fe-N/O			Fe-O			Fe•••C			Fe•••Ce					
Fit	**N**	**R (Å)**	**σ^2 (x10^{-3})**	**N**	**R (Å)**	**σ^2 (x10^{-3})**	**N**	**R (Å)**	**σ^2 (x10^{-3})**	**N**	**R (Å)**	**σ^2 (x10^{-3})**	**E_0**	**F**	**F'**
1	6	2.14	14.19										5.17	704	796
2	5	2.14	10.24										5.67	688	786
3	4	2.15	6.97										6.31	674	779
4	3	2.15	4.40										6.87	675	779
5	4	2.14	4.61	2	1.91	9.38							1.46	612	742
6	5	2.13	6.98	1	1.89	3.60							2.94	610	741
7	4	2.14	4.63	1	1.96	7.61							1.37	612	742
				1	1.88	7.09									
8	5	2.13	7.45	1	1.89	3.71	5	2.99	2.14				2.43	446	634
9	5	2.13	7.55	1	1.89	3.94	5	3.00	3.21	1	3.65	2.32	2.72	267	490
10	5	2.13	7.57	1	1.88	3.64	5	2.99	3.51	1	3.89	1.73	2.52	231	456
11	5	2.13	7.68	1	1.88	3.72	5	3.00	2.87	1	3.69	2.87	2.47	147	363
										1	3.86	1.86			
12	5	2.13	7.69	1	1.88	3.73	5	3.00	4.00	0.5	3.68	1.39	2.45	152	370
										0.5	3.87	0.30			
13	5	2.13	7.66	1	1.88	3.78	5	3.00	4.05	0.4	3.67	0.17	2.53	151	369
										0.6	3.86	1.42			
14	5	2.13	7.77	1	1.88	3.88	5	3.00	4.08	1	3.69	2.85	2.72	137	350
				0.5	2.46	2.01				1	3.86	1.78			

Table 5.28. (continued) EXAFS fit parameters for **14**. Fit 16 corresponds to the most reasonable fit of the data between k = 2 – 15 $Å^{-1}$.

	Fe-N/O			Fe-O			Fe•••C			Fe•••Ce					
Fit	**N**	**R (Å)**	**σ^2 (x10^{-3})**	**N**	**R (Å)**	**σ^2 (x10^{-3})**	**N**	**R (Å)**	**σ^2 (x10^{-3})**	**N**	**R (Å)**	**σ^2 (x10^{-3})**	**E_0**	**F**	**F'**
15	5	2.13	7.68	1	1.88	3.77	5	2.98	2.44	1	3.69	3.31	3.02	144	360
							3	3.12	3.86	1	3.87	1.70			
16	**5**	**2.14**	**7.68**	**1**	**1.89**	**4.12**	**5**	**2.99**	**2.22**	**1**	**3.69**	**3.25**	**3.53**	**135**	**348**
				0.5	**2.47**	**3.84**	**3**	**3.13**	**3.48**	**1**	**3.87**	**1.77**			
17	5	2.14	7.46	1	1.89	4.22	5	2.98	2.10	1	3.69	3.23	3.67	135	348
				1	2.49	17.49	3	3.13	3.27	1	3.87	1.81			
18	5	2.14	7.38	1	1.90	4.58	5	3.00	1.61	1	3.65	2.64	4.17	249	473
				0.5	2.44	5.86	3	3.18	1.98						
19	5	2.14	7.36	1	1.90	4.37	5	3.00	0.90	1	3.89	1.94	4.19	203	427
				0.5	2.45	6.54	3	3.16	0.29						

5.3.6 – XAS Analysis of Oxoiron(IV) and Imidoiron(IV) Species Supported by the TPA* and BnTPEN Ligands.

5. 3.6.1 – XAS Analysis of 15. The K-edge energy for **15** was found at 7124.9 eV. This value is close to that of the parent $[Fe^{IV}(O)(MeCN)TPA]^{2+}$ complex at 7124.5 eV,[282] but much lower than the $[Fe^{IV}_2(O)_2(TPA^*)_2]^{4+}$ diamond core complex at 7130 eV.[242] The pre-edge peak for **15** has a maximum at 7114.4 eV and an area of 24.3 units (Figure 5.36). This value is close to that reported for parent complex at 25.4 units,[282] consistent with an assignment as an oxoiron(IV) species.

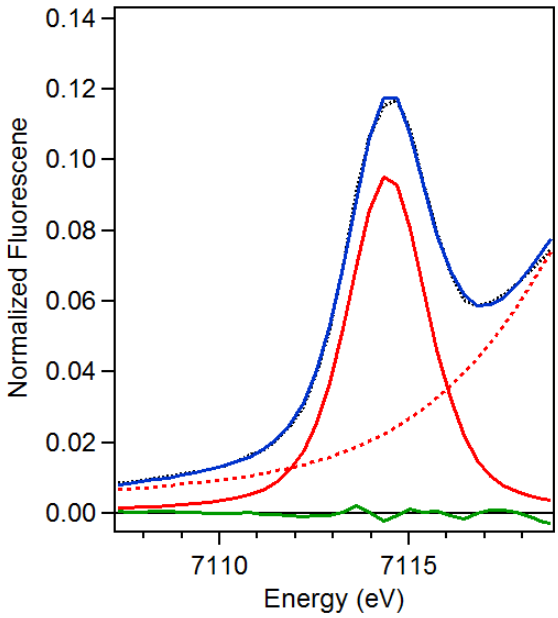

Figure 5.36. Pre-edge analysis of **15**. The experimental data (black dotted), baseline (red dashed), pre-edge peak components (red solid), residuals (green solid) and total fit (blue solid) are shown. Pre-edge energy 7114.4 eV with an area of 24.3 units (not normalized for concentration).

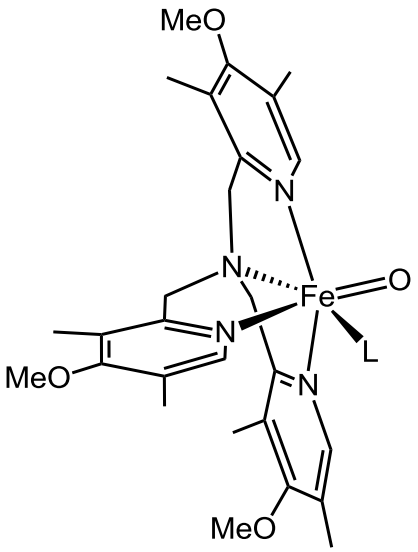

Figure 5.37. EXAFS derived model for **15**. L = MeCN or OTf.

The results of the EXAFS analysis for **15** are summarized in Table 5.29 and Figure 5.37 and Figure 5.38. The 3-D model used for the FEFF calculation for **15** was modified from the crystal structure of the $[Fe^{III}_2(O)(OH)(TPA^*)_2]^{3+}$ complex.[283] The best fit of **15** gives scattering pair distances that correspond to 1 Fe-O/N at 1.66 Å, 5 Fe-N/O at 1.95 Å, and 5 Fe•••C at 2.85 Å. The EXAFS fit for **15** is quite similar to that of the parent $[Fe^{IV}(O)TPA(MeCN)]^{2+}$ complex, which consists of 1 Fe–O at 1.67 Å, 4 Fe–N at 1.99 Å, 1 Fe–N at 2.20 Å, and several carbon scatterers at 2.89 Å. The fit of **15** can be assigned analogously, with the difference being that **15** does not require a scatterer at 2.20 Å. Overall, the fit of **15** is consistent with an oxoiron(IV) complex.

.

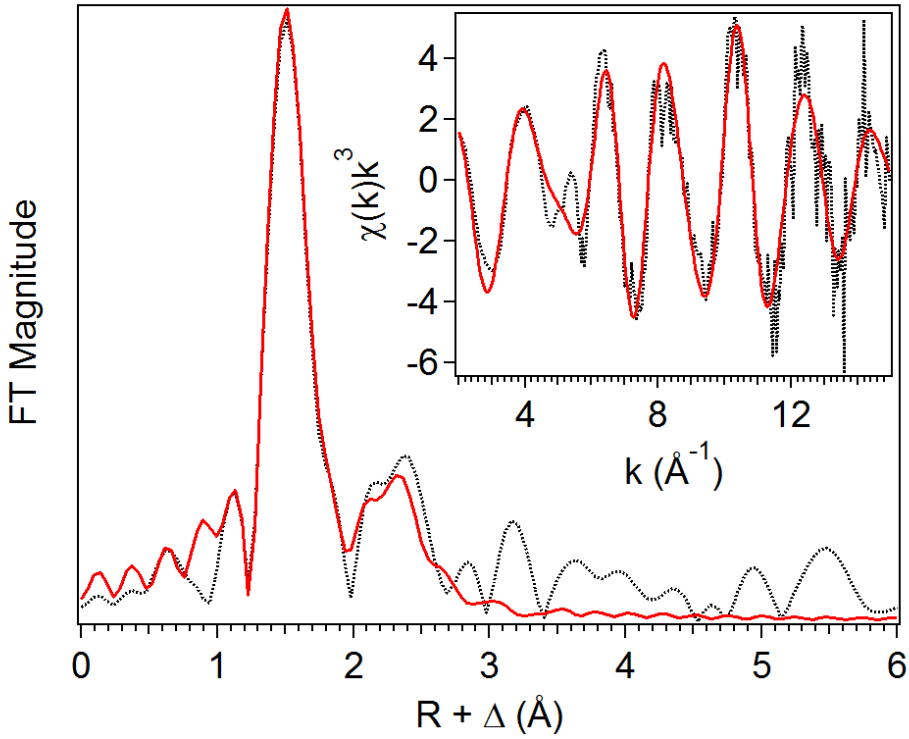

Figure 5.38. EXAFS analysis for **15**. Fourier transform of the EXAFS data (black dotted) with best fit (red solid line). inset: unfiltered EXAFS data (black dotted) with best fit (red solid line). Fit 7, k = 2 – 15 $Å^{-1}$.

Table 5.29. EXAFS fit parameters for **15**. Fit 7 corresponds to the most reasonable fit of the data between k = 2 – 15 $Å^{-1}$.

	Fe-N			Fe-O			Fe•••C				GOF	
Fit	**N**	**R(Å)**	**$\sigma^2(10^{-3})$**	**N**	**R(Å)**	**$\sigma^2(10^{-3})$**	**N**	**R(Å)**	**$\sigma^2(10^{-3})$**	**E_o**	**F**	**F'**
1	6	1.95	4.52							-7.73	840	722
2	5	1.95	3.35							-7.57	717	667
3	4	1.94	2.21							-7.61	625	622
4	5	1.95	4.12	1	1.66	0.93				-3.79	352	467
5	4	1.95	2.88	1	1.66	1.19				-3.38	352	467
6	5	1.95	4.28	1	1.66	0.83	3	2.84	3.21	-3.24	271	410
7	**5**	**1.95**	**4.23**	**1**	**1.66**	**0.85**	**5**	**2.85**	**6.28**	**-3.04**	**267**	**406**
8	5	1.96	4.31	1	1.66	0.82	3	2.82	3.23	-2.40	270	409
							3	2.92	5.43			
9	4	1.95	2.90	1	1.66	1.17	5	2.86	6.37	-1.80	252	394
				1	2.08	8.37						

5.3.6.2 – XAS Analysis of 16. The K-edge energy for **16** was found at 7126 eV. This falls on the high end of the range for oxoiron(IV) complexes, which have values between 7123 and 7126 eV.[272-274] However, the K-edge for **16** is ~1 eV higher than the oxoiron(IV) complex supported by the TPA* ligand (**15**). This suggests that the NTs imido unit has a different effect on the Fe nucleus than the oxo unit, despite having the same oxidation state. Unfortunately, there are not many examples to compare to. An analogous set of complexes supported by the N4Py ligand (N4Py = *N*,*N*-bis(2-pyridylmethyl)bis(2-pyridyl)methylamine)) has been reported. The oxoiron(IV) complex had a K-edge energy of 7123.7 eV,[282] while the imidoiron(IV) complex (**N-N4Py**) had essentially the same K-edge energy of 7123.8 eV.[260] The K-edge in the TPA* system appears to be more sensitive to the ligand identity than the N4Py systems. The pre-edge peak for **16** has a maximum at 7114.3 eV and an area of 11.8 units (Table 5.30, Figure 5.39). This value is lower than that for **15** at 24.3 units, and lower than the reported oxoiron(IV) and imidoiron(IV) complexes supported by N4Py with areas of 25.2 and 18 units respectively.[260, 282] However, the pre-edge area for the N4Py complex was obtained using a now outdated protocol that tends to overestimate pre-edge values for Fe(III) complexes. Using the same fitting protocol as **16** on **N-N4Py** gives a pre-edge area of 10.5 units (Table 5.30, Figure 5.39), which is much closer to that for **16**.

Table 5.30. Pre-edge analysis for **16** and the reanalyzed imidoiron(IV) N4Py complex (**N-N4Py**).[260]

Species	Peak Position (eV)	Area (units)	Relative Area
16	7113.9	6.26	3.2
	7115.5	3.56	1.8
	7117.5	1.99	1.0
		Total = 11.8	
N-N4Py	7113.9	**10.5**	1.0

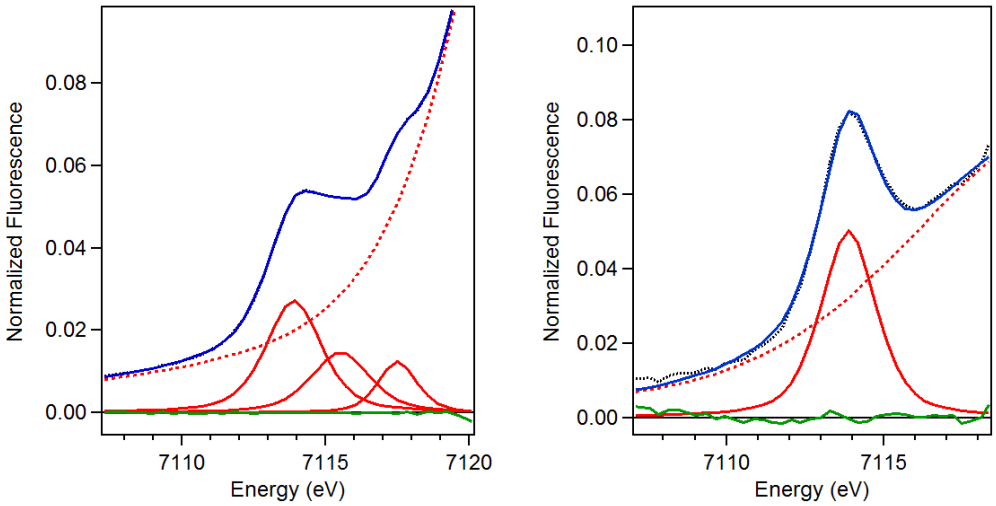

Figure 5.39. Pre-edge analysis of **16** (left) and **N-N4Py** (right). The experimental data (black dotted), baseline (red dashed), pre-edge peak components (red solid), residuals (green solid) and total fit (blue solid) are shown. Fitting range: **16** = 7108 to 7119 eV; **N-N4Py** = 7108 to 7118 eV.

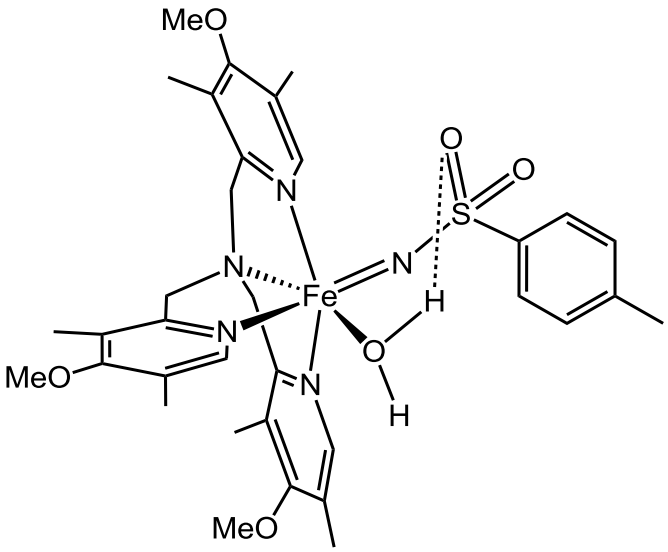

Figure 5.40. EXAFS derived model for **16**. The identity of the sixth ligand (drawn as water) is unknown, and could be substituted by a triflate anion or acetonitrile molecule.

The results of the EXAFS analysis for **16** are summarized in Table 5.31 and Figure 5.40 and Figure 5.41. The 3-D model used for the FEFF calculation for **16** was modified from the crystal structure of the $[Fe^{III}_2(O)(OH)(TPA^*)_2]^{3+}$ complex.[283] The best fit of **16** gives scattering pair distances that correspond to 5 Fe–N/O at 1.94 Å, 0.7 Fe–

N/O at 1.71 Å, 4 Fe•••C at 2.78 Å, and 2 Fe•••C at 2.91 Å. The fit of **16** is close to the fit for the oxoiron(IV) complex **15**, as the primary coordination sphere for **15** consists of 5 Fe–N/O scatterers at 1.95 Å and 1 Fe–O at 1.66 Å. One thing to note is that the Fe=N distance is associated with a scatterer with N = 0.7, consistent with the yield determined from Mössbauer analysis. Increasing the N value to 1 results in a very large σ^2 value for the scatterer (Table 5.31, fit 12). The 0.05 Å difference in the Fe=N versus the Fe=O distance contributes to the large change in the pre-edge areas for the two species. The carbon shell is split into two sets of scatterers for **16**, one set at ~2.78 Å, consistent with C2 carbons of pyridine rings and aliphatic carbon atoms and one set at 2.91 Å, consistent with the C6 position on the pyridine rings. Consistent with the pre-edge analysis, **N-N4Py** compares reasonably well to **16**, where the Fe=N distance was found to be 1.73 Å, with 5 Fe–N ligands at 1.97 Å and carbon scatterers at 2.88 Å.[260]

An interesting observation is that the FT peak at R + Δ ~ 3.1 Å could be fit with an Fe•••S scatterer at 3.53 Å with a reasonably small Debye-Waller factor for a scatterer at such long distance (Table 5.31, fit 11). This S atom would presumably be derived from the MsINTs oxidant; however this S is expected to be ~3.3 Å from the Fe atom, based on DFT calculations on the corresponding N4Py complex that assumed formation of a four-membered Fe–N–S–O chelate ring.[260] The crystal structure of the oxidant showed that an N–S bond length of 1.604 Å,[284] which is reproduced reasonably in the DFT calculation for **N-N4Py**. If similar bond distances and angles are maintained from the crystal structure of the oxidant, the only way to obtain an Fe•••S distance at 3.5 Å would be to elongate the N–S bond to ~1.9 Å. It is for this reason that fit 11 is disfavored despite the lower GOF values relative to the best fit.

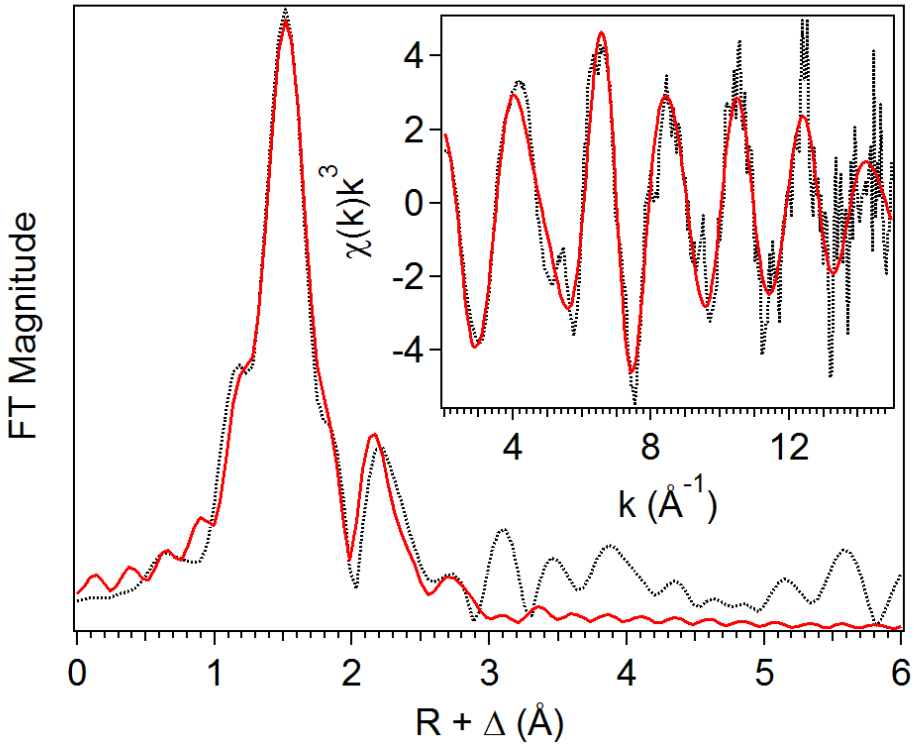

Figure 5.41. EXAFS analysis for **16**. Fourier transform of the EXAFS data (black dotted) with best fit (red solid line). inset: unfiltered EXAFS data (black dotted) with best fit (red solid line). Fit 10, k = 2 – 15 $Å^{-1}$.

Table 5.31. EXAFS fit parameters for **16**. Fit 10 corresponds to the most reasonable fit of the data between k = 2 – 15 $Å^{-1}$.

	Fe-N			Fe-N			Fe•••C			Fe•••S				GOF	
Fit	N	R(Å)	$\sigma^2(10^{-3})$	N	R(Å)	$\sigma^2(10^{-3})$	N	R(Å)	$\sigma^2(10^{-3})$	N	R(Å)	$\sigma^2(10^{-3})$	E_o	F	F'
1	6	1.94	5.23										-7.63	335	488
2	5	1.94	4.05										-7.52	303	464
3	4	1.94	2.90										-7.13	301	463
4	3	1.94	1.69										-6.70	347	496
5	5	1.94	3.60	1	1.74	9.46							-9.45	290	455
6	4	1.94	2.96	1	2.07	19.31							-6.45	294	457
7	5	1.94	3.88	0.5	1.71	4.66							-8.29	291	454
8	5	1.94	4.02	0.5	1.70	4.06	3	2.83	5.46				-7.02	240	413
9	5	1.94	4.01	0.5	1.70	3.86	3	2.77	1.93				-6.57	228	403
							3	2.90	2.66						
10	**5**	**1.94**	**3.85**	**0.7**	**1.71**	**6.86**	**4**	**2.78**	**4.39**				**-6.68**	**232**	**406**
							2	**2.91**	**1.10**						
11	5	1.94	3.87	0.7	1.70	6.58	4	2.78	4.40	1	3.53	3.70	-6.72	220	395
							2	2.91	1.10						
12	5	1.94	3.77	1	1.72	11.47	4	2.88	3.88				-7.21	237	410
							3	2.75	3.78						

5.3.6.3 – XAS Analysis of 17. The K-edge energy for **17** was found at 7123.4 eV. This value is close to that of the oxoiron(IV) BnTPEN complex with a K-edge energy of 7123.7 eV.[273] However, the BnTPEN-supported complexes are on the low end of the K-edge range for Fe^{IV} complexes, from 7123 and 7126 eV.[272-274] The pre-edge peak for **17** has a maximum at 7113.1 eV with an area of 15.3 units (Figure 5.42). This value is lower than that of the related oxoiron(IV) species at 32 units,[273] consistent with the observed changes in **15** and **16**, as well as the related N4Py supported complexes.[260, 282] **17** has a higher pre-edge area than **16** and **N-N4Py**, but the oxoiron(IV) BnTPEN complex has a higher pre-edge than the analogous N4Py complex or **15**. This difference may reflect a greater inherent distortion from a centrosymmetric Fe in BnTPEN compared to those with other ligands.

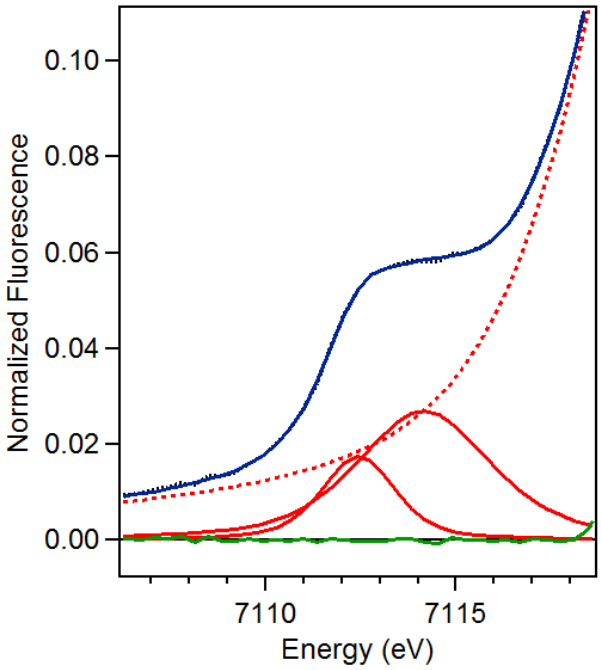

Figure 5.42. Pre-edge analysis for **17**. The experimental data (black dotted), baseline (red dashed), pre-edge peak components (red solid), residuals (green solid) and total fit (blue solid) are shown.

Table 5.32. Pre-edge analysis for **17**.

K-edge (eV)	Peak Position (eV)	Area (units)	Relative Area
7123.4	7112.4	4.01	1.00
	7114.2	11.3	2.82
		Total = 15.3	

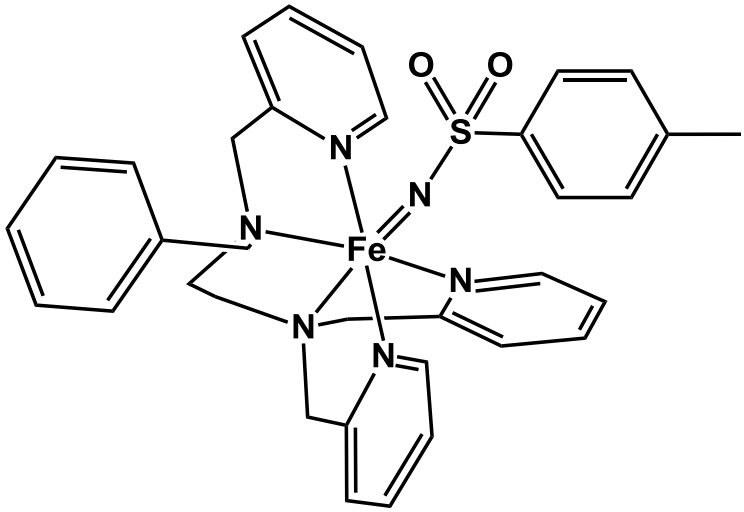

Figure 5.43. EXAFS derived model for **17**.

The results of the EXAFS analysis for **17** are summarized in Table 5.33 and Figure 5.43 and Figure 5.44. The 3-D model used for the FEFF calculation for **17** was modified from the unpublished crystal structure of $[Fe^{IV}(O)(BnTPEN)]^{2+}$ solved by Waqas Rasheed. The best fit of **17** gives scattering pair distances that correspond to 0.7 Fe–O/N at 1.72 Å, 5 Fe–N/O at 1.98 Å, 5 Fe•••C at 2.84 Å, and 3 Fe•••C at 2.99 Å. The EXAFS fit of **17** is similar to those of **16** and **N-N4Py**. The first coordination sphere in all three examples is comprised of a shorter Fe-N distance from the imido unit at ~1.7 Å and a longer distance for a set of Fe-N scatterers between 1.9 and 2.0 Å, consistent with the N donors of the respective supporting ligands. The N value for the 1.72-Å scatterer is best fit at 0.7, consistent with the yield of the imido species determined for **17**. Increasing this scatterer to N = 1 resulted in a much higher σ^2 value (Table 5.33, fit 9). Overall, there are slight differences in the scattering distances across all of these complexes, but for the

most part, the structure remains relatively unchanged. In **16** and **N-N4Py**, only one carbon shell at ~2.9 Å is required for the best fit, whereas **17** requires two shells of carbon scatterers, one at 2.84 Å and the other at 2.99 Å.

One of the fits involves one carbon shell and a Fe•••S scatterer (Table 5.33, fit 12). A S distance at 3.32 Å is derived from the MsINTs oxidant, as predicted by DFT calculations on the **N-N4Py** complex.[260] However, the σ^2 value for this S is somewhat high (7.43×10^{-3} Å^2) for an N = 0.7 scatterer, and the data is equally fit with more well behaved carbon shells in the best fit of the data (Table 5.33, fit 13). While both of these fits have similar GOF values, the fit with the two-carbon shell is favored.

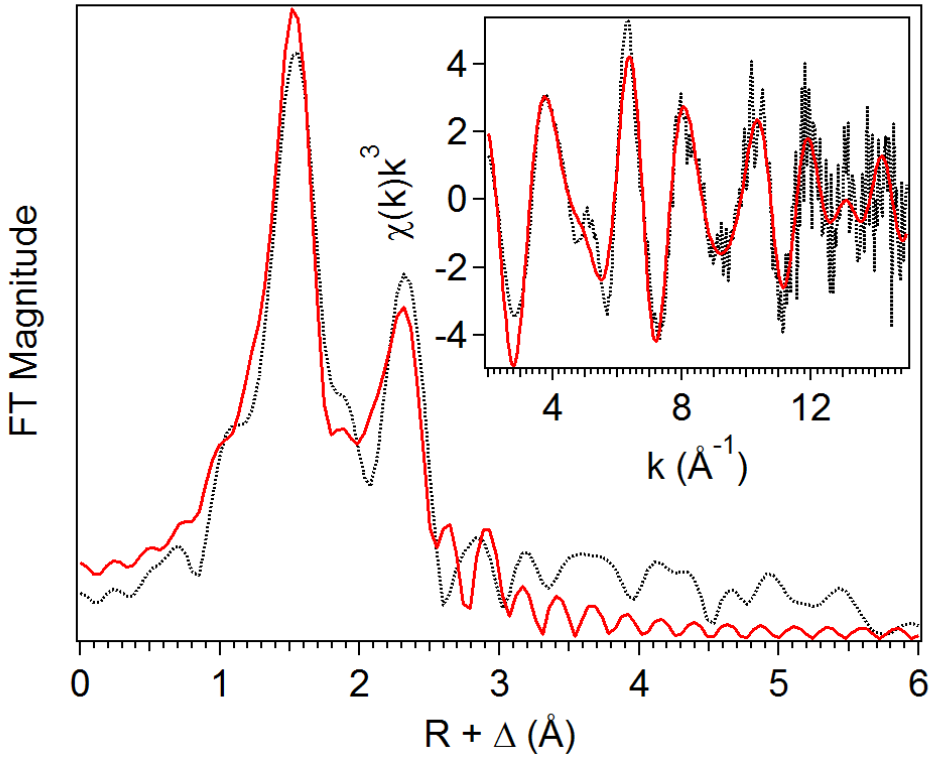

Figure 5.44. EXAFS analysis for **17**. Fourier transform of the EXAFS data (black dotted) with best fit (red solid line). inset: unfiltered EXAFS data (black dotted) with best fit (red solid line). Fit 13, k = 2 – 15 Å^{-1}.

Table 5.33. EXAFS fit parameters for **17**. Fit 13 corresponds to the most reasonable fit of the data between k = 2 – 15 $Å^{-1}$.

	Fe-N			Fe-N			Fe•••C			Fe•••S				GOF	
Fit	N	R(Å)	$\sigma^2(10^{-3})$	N	R(Å)	$\sigma^2(10^{-3})$	N	R(Å)	$\sigma^2(10^{-3})$	N	R(Å)	$\sigma^2(10^{-3})$	E_o	F	F'
1	6	1.99	8.12										-0.56	508	678
2	5	1.99	6.39										0.19	460	644
3	4	1.99	4.84										0.83	433	625
4	3	1.99	3.35										1.44	443	633
5	5	1.98	5.74	1	1.73	8.26							-1.63	426	620
6	4	1.99	4.49	1	1.79	16.77							-1.24	429	622
7	5	1.98	5.88	1	1.73	7.98	3	2.84	1.34				-1.85	277	501
8	5	1.98	5.95	1	1.73	8.46	3	2.82	0.13				-0.30	243	468
							3	2.94	2.90						
9	5	1.98	6.00	1	1.72	8.32	5	2.84	1.97				-0.17	240	466
							3	2.99	2.87						
10	5	1.98	5.94	1	1.73	7.88	5	2.84	2.53	1	3.30	14.90	-0.92	228	454
							3	3.01	4.96						
11	5	1.98	6.27	0.7	1.72	5.35	5	2.84	2.53	0.7	3.31	12.04	-0.51	233	458
							3	3.00	5.04						
12	**5**	**1.98**	**6.19**	**0.7**	**1.72**	**4.93**	**5**	**2.84**	**3.49**	**0.7**	**3.32**	**7.43**	**-1.89**	**242**	**467**
13	**5**	**1.98**	**6.30**	**0.7**	**1.72**	**5.52**	**5**	**2.84**	**2.00**				**0.05**	**243**	**468**
							3	**2.99**	**2.89**						

5.4 – Summary

In this chapter, the XAS analyses for a variety of different iron containing complexes were presented. While there are no direct ties between all of the complexes, there are some interesting generalizations that can be made by considering all of the information. For the complexes presented, the K-edge energies of Fe^{III} complexes were found between 7122.8 and 7125.4 eV, a 2.6 eV range despite having the same assigned oxidation state. Similarly, the Fe^{IV} complexes had K-edge energies that were found between 7123.4 and 7126 eV, coincidentally with a 2.6 eV range. There also is a great deal of overlap in the K-edge energies between Fe^{III} and Fe^{IV} complexes, reinforcing that oxidation state cannot and should not be assigned based on the value of one sample. A summary of all K-edge values can be found in Table 5.34.

The pre-edge areas for all of the presented complexes can be taken into account as well but it is more useful to subdivide into different categories of complexes. Of the Fe^{III} complexes analyzed, almost all of them were proposed to be consistent with a peroxo species with different binding modes and bridging ligands. The pre-edge areas ranged from 8.6 to 14.9 units (Table 5.34), with the higher end of the range being populated by peroxo complexes containing a μ-oxo bridge. This extends the range of pre-edge areas of all known dinuclear peroxo species from 9 to 16 units. The remaining two complexes (**5** and **6**) are μ-oxo bridged dimers with pre-edge areas of 11.3 and 12.4 units. Across all of the Fe^{III} complexes, almost all required two functions to fit the pre-edge feature, the positions of which changed based on the identity of the supporting ligands. The two complexes that were supported by carboxylate ligands (**3** and **4**) had functions fit at ~7112 and 7113.5 eV, whereas the remaining complexes with N-donor supporting ligands required functions at ~7113.5 and 7115 eV. Of the Fe^{IV} complexes analyzed, there were two classes of compounds, oxoiron(IV) (**8**, **9**, **15**) and imidoiron(IV) (**16**, **N-N4Py**, **17**). The oxoiron(IV) complexes had pre-edge areas of 17.3, 21.1 and 24.3 units and the imidoiron(IV) complexes had values of 10.5, 11.8, and 15.3 units. It is interesting how the ligand (oxo or imido) affects the pre-edge area and that the imido complexes are much lower, on average, than the oxo complexes. There are also differences in the

functions that are required to fit the Fe^{IV} complexes. The oxoiron(IV) species all require one function to fit the pre-edge feature centered around 7114 eV. The imidoiron(IV) complexes each needed a different number of functions to properly fit the pre-edge feature, so generalization is not clear.

The best fits of the EXAFS data for each of the analyzed complexes can be found summarized in Table 5.35. It is difficult to compare the EXAFS results across each of the complexes directly, but there are some generalizations that are apparent. In the Fe^{III} complexes, the primary sphere Fe-N/O distances are found between 2.05 and 2.25 Å, with the complexes supported by carboxylate ligands being on the shorter side of the range. Removing the carboxylate supported complexes reduces the range from 2.15 to 2.25 Å. The proximal oxygen atom of a peroxo ligand has an Fe-O distance between 1.86 and ~2 Å depending on the supporting ligands and in some cases fall into the same scattering shell as μ-oxo ligands. In the Fe^{IV} complexes, the primary Fe-N distances are found between 1.94 and 1.99 Å, with oxoiron(IV) complexes having a shorter Fe–O distance between 1.65 and 1.67 Å, and the imidoiron(IV) complexes have Fe–N distances at 1.71 and 1.72 Å.

Table 5.34. Summary of Fe K-edge XANES analysis presented in this chapter. Area values in bold are the sum of the component parts.

Species	K-edge (eV)	Peak Position (eV)	Area (units)	Relative Area
1-Cl	7122.8	7113.8	6.66	1.00
		7115.0	8.26	1.24
			14.9	
2-Cl	7122.8	7113.4	7.14	1.02
		7115.0	6.95	1.00
			14.1	
1-Sc	7123.5	7113.4	4.06	1.00
		7114.8	9.61	2.37
			13.7	
3	7124.4	7112.1	7.87	1.99
		7113.3	3.96	1.00
			11.8	
4	7123.6	7112.1	5.75	1.48
		7113.6	3.88	1.00
			9.6	
5	7124.3	7113.8	4.81	1.00
		7115.4	6.45	1.34
			11.3	
6	7124.5	7113.5	2.94	1.00
		7115.2	9.43	3.21
			12.4	
7	7123.2	7113.3	1.43	1.00
		7114.6	11.76	8.21
			13.2	
8	7125.0	7114.0	**21.1**	1.00
9	7124.8	7114.2	**17.3**	1.00
10	7124.8	7113.5	4.36	1.00
		7114.7	9.42	2.16
			13.8	
11	7125.4	7114.5	**12.3**	1.00
12	7125.2	7113.6	3.48	1.00
		7114.8	8.98	2.58
			12.5	

Table 5.34. (continued) Summary of Fe K-edge XANES analysis presented in this chapter. Area values in bold are the sum of the component parts.

Species	K-edge (eV)	Peak Position (eV)	Area (units)	Relative Area
13	7124.9	7113.3	1.55	1.00
		7114.9	7.02	4.53
			8.6	
14	7125.2	7113.4	1.72	1.00
		7115.0	9.75	5.66
			11.5	
15	7124.9	7114.4	**24.3**	1.00
16	7126.0	7113.9	6.26	3.20
		7115.5	3.56	1.80
		7117.5	1.99	1.00
			11.8	
N-N4Py	7123.8	7113.9	**10.5**	1.00
17	7123.4	7112.4	4.01	1.00
		7114.2	11.3	2.82
			15.3	

Table 5.35. Summary of Fe K-edge EXAFS analyses presented in this chapter. σ^2 columns have units of $\times 10^{-3}$ Å^2. Double scattering pathways are designated with /, triple scattering pathways are designated with //.

	Fe-N/O			Fe-O/N			Fe•••C			Fe•••Fe/Ce			Fe•••Cl/Sc		
Complex	**N**	**R (Å)**	**σ^2**	**N**	**R (Å)**	**σ^2**	**N**	**R (Å)**	**σ^2**	**N**	**R (Å)**	**σ^2**	**N**	**R (Å)**	**σ^2**
1-Cl	4	2.25	4.47	1	1.86	3.56	2	2.85	4.48	1	3.18	3.68	Cl	2.74	2.48
2-Cl	3	2.21	1.66	1	1.82	1.74	5	2.95	1.61	1	3.12	3.78			
				2	2.04	5.40									
1-Sc	4	2.19	2.80	1	1.85	2.12				1	3.13	2.36	2Sc	2.99	3.21
				1	2.04	2.01									
3	4	2.05	5.96	1.5	1.94	7.11	1.5	2.47	2.01	1	3.41	7.96			
							2	2.99	2.94						
4	4	2.09	5.86	1.5	1.94	5.05	1.5	2.47	3.42	1	3.33	5.25			
							2	3.07	1.59						
							2	4.03	2.04						
5	5	2.14	3.91	1	1.79	0.29	5	3.03	2.84	1	3.57	1.13			
										2	/3.57	1.13			
										1	//3.57	1.13			
6	3	2.14	2.28	3	1.99	2.62	4	2.99	3.12	1	3.29	2.39			
				1	1.80	2.37									
7	4	2.20	3.74	2	1.86	7.08	7	3.03	2.03	1	3.15	1.74			
8	5	1.99	3.39	1	1.65	3.61	5	2.82	1.52						
							5	2.96	2.45						
9	5	1.98	5.49	1	1.67	4.71	5	2.81	3.08						
							5	2.97	2.77						

Table 5.34. (continued) Summary of Fe K-edge EXAFS analyses presented in this chapter. σ^2 columns have units of $\times 10^{-3}$ Å^2. Double scattering pathways are designated with /, triple scattering pathways are designated with //.

	Fe-N/O			Fe-O/N			Fe•••C			Fe•••Fe/Ce			Fe•••Cl/Sc		
Complex	**N**	**R (Å)**	**σ^2**	**N**	**R (Å)**	**σ^2**	**N**	**R (Å)**	**σ^2**	**N**	**R (Å)**	**σ^2**	**N**	**R (Å)**	**σ^2**
10	3	2.23	4.96	1	1.94	4.00	5	3.01	8.78	Ce	3.67	3.05			
	2	2.09	1.39	1	2.47	1.76									
11	4	2.17	5.17	2	1.97	2.72	5	3.03	7.41	Ce	3.64	2.05			
				1	2.40	1.12									
12	4	2.16	8.35	1	2.42	4.24	5	2.99	8.22	Ce	3.67	6.76			
	2	1.97	4.65												
13	5	2.05	2.96	1	1.87	3.78	5	2.98	2.38	Ce	3.62	2.60			
				1	2.54	4.54									
14	5	2.14	7.68	1	1.89	4.12	5	2.99	2.22	Ce	3.69	3.25			
				0.5	2.47	3.84	3	3.13	3.48	Ce	3.87	1.77			
15	5	1.95	4.23	1	1.66	0.85	5	2.85	6.28						
16	5	1.94	3.85	0.7	1.71	6.86	4	2.78	4.39						
							2	2.91	1.10						
17	5	1.98	6.30	0.7	1.72	5.52	5	2.84	2.00						
							3	2.99	2.89						

Bibliography

[1] Lundin, D., Poole, A. M., Sjöberg, B.-M., and Högbom, M. (2012) Use of structural phylogenetic networks for classification of the ferritin-like superfamily, *J. Biol. Chem. 287*, 20565-20575.

[2] Nordlund, P., and Ecklund, H. (1995) Di-iron-carboxylate proteins, *Curr. Opin. Struct. Biol. 5*, 758-766.

[3] Liu, X., and Theil, E. C. (2005) Ferritins: dynamic management of biological iron and oxygen chemistry, *Acc. Chem. Res. 38*, 167-175.

[4] Wallar, B. J., and Lipscomb, J. D. (1996) Dioxygen activation by enzymes containing binuclear non-heme iron clusters, *Chem. Rev. 96*, 2625-2657.

[5] Tinberg, C. E., and Lippard, S. J. (2011) Dioxygen activation in soluble methane monooxygenase, *Acc. Chem. Res. 44*, 280-288.

[6] Bochevarov, A. D., Li, J., Song, W. J., Friesner, R. A., and Lippard, S. J. (2011) Insights into the different dioxygen activation pathways of methane and toluene monooxygenase hydroxylases, *J. Am. Chem. Soc. 133*, 7384-7397.

[7] Pikus, J. D., Studts, J. M., Achim, C., Kauffmann, K. E., Münck, E., Steffan, R. J., McClay, K., and Fox, B. G. (1996) Recombinant toluene-4-monooxygenase: Catalytic and Mössbauer studies of the purified diiron and Rieske components of a four-protein complex, *Biochemistry 35*, 9106-9119.

[8] Nordlund, P., and Reichard, P. (2006) Ribonucleotide reductases, *Annu. Rev. Biochem. 75*, 681-706.

[9] Krebs, C., Bollinger, J. M., Jr., and Booker, S. J. (2011) Cyanobacterial alkane biosynthesis further expands the catalytic repertoire of the ferritin-like di-iron-carboxylate' proteins, *Curr. Opin. Chem. Biol. 15*, 291-303.

[10] Das, D., Eser, B. E., Han, J., Sciore, A., and Marsh, E. N. G. (2011) Oxygen-independent decarbonylation of aldehydes by cyanobacterial aldehyde decarbonylase: a new reaction of diiron enzymes, *Angew. Chem. Int. Ed. 50*, 7148-7152.

[11] Fox, B. G., Lyle, K. S., and Rogge, C. E. (2004) Reactions of the diiron enzyme stearoyl-acyl carrier protein desaturase, *Acc. Chem. Res. 37*, 421-429.

[12] Griese, J. J., Roos, K., Cox, N., Shafaat, H. S., Branca, R. M. M., Lehtiö, J., Gräslund, A., Lubitz, W., Siegbahn, P. E. M., and Högbom, M. (2013) Direct observation of structurally encoded metal discrimination and ether bond formation in a heterodinuclear metalloprotein, *Proc. Natl. Acad. Sci. USA 110*, 17189-17194.

[13] Griese, J. J., Kositzki, R., Schrapers, P., Branca, R. M. M., Nordström, A., Lehtiö, J., Haumann, M., and Högbom, M. (2015) Structural basis for oxygen activation at a heterodinuclear manganese/iron cofactor, *J. Biol. Chem. 290*, 25254-25272.

[14] Choi, Y. S., Zhang, H., Brunzelle, J. S., Nair, S. K., and Zhao, H. (2008) In vitro reconstitution and crystal structure of p-aminobenzoate N-oxygenase (AurF) involved in aureothin biosynthesis, *Proc. Natl. Acad. Sci. USA. 105*, 6858-6863.
[15] Makris, T. M., Vu, V. V., Meier, K. K., Komor, A. J., Rivard, B. S., Münck, E., Que, L., Jr., and Lipscomb, J. D. (2015) An unusual peroxo intermediate of the arylamine oxygenase of the chloramphenicol biosynthetic pathway, *J. Am. Chem. Soc. 137*, 1608-1617.
[16] Stenkamp, R. E. (1994) Dioxygen and hemerythrin, *Chem. Rev. 94*, 715-726.
[17] Han, Z., Sakai, N., Boettger, L. H., Klinke, S., Hauber, J., Trautwein, A. X., and Hilgenfeld, R. (2015) Crystal structure of the peroxo-diiron(III) intermediate of deoxyhypusine hydroxylase, an oxygenase involved in hypusination, *Structure 23*, 882-892.
[18] Makris, T. M., Knoot, C. J., Wilmot, C. M., and Lipscomb, J. D. (2013) Structure of a dinuclear iron cluster-containing β-hydroxylase active in antibiotic biosynthesis, *Biochemistry 52*, 6662-6671.
[19] Thorsell, A. G., Persson, C., Voevodskaya, N., Busam, R. D., Hammarstrom, M., Gräslund, S., Gräslund, A., and Hallberg, B. M. (2008) Structural and biophysical characterization of human myo-inositol oxygenase, *J. Biol. Chem. 283*, 15209-15216.
[20] Riggs-Gelasco, P. J., Stemmler, T. L., and Penner-Hahn, J. E. (1995) XAFS of dinuclear metal sites in proteins and model compounds, *Coord. Chem. Rev. 144*, 245-286.
[21] Cramer, S. P., Hodgson, K. O., Stiefel, E. I., and Newton, W. E. (1978) A systematic X-ray absorption study of molybdenum complexes. The accuracy of structural information from extended x-ray absorption fine structure, *J. Am. Chem. Soc. 100*, 2748-2761.
[22] Beauvais, L. G., and Lippard, S. J. (2005) Reactions of the peroxo intermediate of soluble methane monooxygenase hydroxylase with ethers, *J. Am. Chem. Soc. 127*, 7370-7378.
[23] Tinberg, C. E., and Lippard, S. J. (2010) Oxidation reactions performed by soluble methane monooxygenase hydroxylase intermediates H_{peroxo} and Q proceed by distinct mechanisms, *Biochemistry 49*, 7902-7912.
[24] Murray, L. J., Naik, S. G., Ortillo, D. O., Garcia-Serres, R., Lee, J. K., Huynh, B. H., and Lippard, S. J. (2007) Characterization of the arene-oxidizing intermediate in ToMOH as a diiron(III) species, *J. Am. Chem. Soc. 129*, 14500-14510.
[25] Pandelia, M. E., Li, N., Noergaard, H., Warui, D. M., Rajakovich, L. J., Chang, W.-c., Booker, S. J., Krebs, C., and Bollinger, J. M., Jr. (2013) Substrate-triggered addition of dioxygen to the diferrous cofactor of aldehyde-deformylating oxygenase to form a diferric-peroxide intermediate, *J. Am. Chem. Soc. 135*, 15801-15812.

[26] Bollinger, J. M., Jr., Edmondson, D. E., Huynh, B. H., Filley, J., Norton, J. R., and Stubbe, J. (1991) Mechanism of assembly of the tyrosyl radical-dinuclear iron cluster cofactor of ribonucleotide reductase, *Science 253*, 292-298.
[27] Bollinger, J. M., Jr., Stubbe, J., Huynh, B. H., and Edmondson, D. E. (1991) Novel diferric radical intermediate responsible for tyrosyl radical formation in assembly of the cofactor of ribonucleotide reductase, *J. Am. Chem. Soc. 113*, 6289-6291.
[28] Acheson, J. F., Bailey, L. J., Brunold, T. C., and Fox, B. G. (2017) In-crystal reaction cycle of a toluene-bound diiron hydroxylase, *Nature advance online publication*.
[29] Xing, G., Diao, Y., Hoffart, L. M., Barr, E. W., Prabhu, K. S., Arner, R. J., Reddy, C. C., Krebs, C., and Bollinger, J. M., Jr. (2006) Evidence for C-H cleavage by an iron-superoxide complex in the glycol cleavage reaction catalyzed by myo-inositol oxygenase, *Proc. Natl. Acad. Sci. USA. 103*, 6130-6135.
[30] Snyder, R. A., Bell, C. B., Diao, Y., Krebs, C., Bollinger, J. M., and Solomon, E. I. (2013) Circular dichroism, magnetic circular dichroism, and variable temperature variable field magnetic circular dichroism studies of biferrous and mixed-valent myo-inositol oxygenase: Insights into substrate activation of O_2 reactivity, *J. Am. Chem. Soc. 135*, 15851-15863.
[31] Logan, D. T., Su, X. D., Aberg, A., Regnstrom, K., Hajdu, J., Eklund, H., and Nordlund, P. (1996) Crystal structure of reduced protein R2 of ribonucleotide reductase - the structural basis for oxygen activation at a dinuclear iron site, *Structure 4*, 1053-1064.
[32] Baldwin, J., Krebs, C., Saleh, L., Stelling, M., Huynh, B. H., Bollinger, J. M., Jr., and Riggs-Gelasco, P. (2003) Structural characterization of the peroxodiiron(III) intermediate generated during oxygen activation by the W48A/D84E variant of ribonucleotide reductase protein R2 from *Escherichia coli*, *Biochemistry 42*, 13269-13279.
[33] Zhang, K., Stern, E. A., Ellis, F., Sanders-Loehr, J., and Shiemke, A. K. (1988) The active site of hemerythrin as determined by X-ray absorption fine structure, *Biochemistry 27*, 7470-7479.
[34] Holmes, M. A., Le Trong, I., Turley, S., Sieker, L. C., and Stenkamp, R. E. (1991) Structures of deoxy and oxy hemerythrin at 2.0 Å resolution, *J. Mol. Biol. 218*, 583-593.
[35] Knoot, C. J., Kovaleva, E. G., and Lipscomb, J. D. (2016) Crystal structure of CmlI, the arylamine oxygenase from the chloramphenicol biosynthetic pathway, *J. Biol. Inorg. Chem. 21*, 589-603.
[36] Jasniewski, A. J., Engstrom, L. M., Vu, V. V., Park, M. H., and Que, L. (2016) X-ray absorption spectroscopic characterization of the diferric-peroxo intermediate of human deoxyhypusine hydroxylase in the presence of its substrate eIF5a, *J. Biol. Inorg. Chem. 21*, 605-618.

[37] Hwang, J., Krebs, C., Huynh, B. H., Edmondson, D. E., Theil, E. C., and Penner-Hahn, J. E. (2000) A short Fe-Fe distance in peroxodiferric ferritin: control of Fe substrate versus cofactor decay?, *Science 287*, 122-125.

[38] Jasniewski, A. J., Knoot, C. J., Lipscomb, J. D., and Que, L., Jr. (2016) A carboxylate shift regulates dioxygen activation by the diiron nonheme β-hydroxylase CmlA upon binding of a substrate-loaded nonribosomal peptide synthetase, *Biochemistry 55*, 5818-5831.

[39] Colpas, G. J., Maroney, M. J., Bagyinka, C., Kumar, M., Willis, W. S., Suib, S. L., Mascharak, P. K., and Baidya, N. (1991) X-ray spectroscopic studies of nickel complexes, with application to the structure of nickel sites in hydrogenases, *Inorg. Chem. 30*, 920-928.

[40] Wirt, M. D., Sagi, I., Chen, E., Frisbie, S. M., Lee, R., and Chance, M. R. (1991) Geometric conformations of intermediates of B12 catalysis by X-ray edge spectroscopy: Cobalt(I) B12, cobalt(II) B12, and base-off adenosylcobalamin, *J. Am. Chem. Soc. 113*, 5299-5304.

[41] Penner-Hahn, J. E., Fronko, R. M., Pecoraro, V. L., Yocum, C. F., Betts, S. D., and Bowlby, N. R. (1990) Structural characterization of the manganese sites in the photosynthetic oxygen-evolving complex using x-ray absorption spectroscopy, *J. Am. Chem. Soc. 112*, 2549-2557.

[42] Rudd, D. J., Goldsmith, C. R., Cole, A. P., Stack, T. D. P., Hodgson, K. O., and Hedman, B. (2005) X-ray absorption spectroscopic investigation of the spin-transition character in a series of single-site perturbed iron(II) complexes, *Inorg. Chem. 44*, 1221-1229.

[43] Randall, C. R., Shu, L., Chiou, Y.-M., Hagen, K. S., Ito, M., Kitajima, N., Lachicotte, R. J., Zang, Y., and Que, L., Jr. (1995) X-ray absorption pre-edge studies of high spin iron(II) complexes, *Inorg. Chem. 34*, 1036-1039.

[44] Westre, T. E., Kennepohl, P., DeWitt, J. G., Hedman, B., Hodgson, K. O., and Solomon, E. I. (1997) A multiplet analysis of Fe K-edge 1s → 3d pre-edge features of iron complexes, *J. Am. Chem. Soc. 119*, 6297-6314.

[45] Shu, L., Nesheim, J. C., Kauffmann, K., Münck, E., Lipscomb, J. D., and Que, L., Jr. (1997) An $Fe^{IV}_2O_2$ diamond core structure for the key intermediate Q of methane monooxygenase, *Science 275*, 515-518.

[46] Rudd, D. J., Sazinsky, M. H., Lippard, S. J., Hedman, B., and Hodgson, K. O. (2005) X-ray absorption spectroscopic study of the reduced hydroxylases of methane monooxygenase and toluene/o-xylene monooxygenase: differences in active site structure and effects of the coupling proteins MMOB and ToMOD, *Inorg. Chem. 44*, 4546-4554.

[47] Rosenzweig, A. C., Nordlund, P., Takahara, P. M., Frederick, C. A., and Lippard, S. J. (1995) Geometry of the soluble methane monooxygenase catalytic diiron center in two oxidation states, *Chem. Biol. 2*, 409-418.

[48] McCormick, M. S., Sazinsky, M. H., Condon, K. L., and Lippard, S. J. (2006) X-ray crystal structures of manganese(II)-reconstituted and native toluene/o-xylene

monooxygenase hydroxylase reveal rotamer shifts in conserved residues and an enhanced view of the protein interior., *J. Am. Chem. Soc. 128*, 15108-15110.

[49] Pulver, S. C., Froland, W. A., Lipscomb, J. D., and Solomon, E. I. (1997) Ligand field circular dichroism and magnetic circular dichroism studies of component B and substrate binding to the hydroxylase component of methane monooxygenase, *J. Am. Chem. Soc. 119*, 387-395.

[50] Pozzi, C., Di Pisa, F., Lalli, D., Rosa, C., Theil, E., Turano, P., Mangani, S., Iucr, A, V. A., S, V. J., I, S. E., and W, N. (2015) Time-lapse anomalous X-ray diffraction shows how Fe^{2+} substrate ions move through ferritin protein nanocages to oxidoreductase sites, *Acta Crystallogr. D Biol. Crystallogr. 71*, 941-953.

[51] Münck, E. (2000) Aspects of ^{57}Fe Mössbauer spectroscopy, In *Physical Methods in Bioinorganic Chemistry* (Que, L., Jr, Ed.), pp 287-319, University Science Books, Sausalito, CA.

[52] Solomon, E. I., and Park, K. (2016) Structure/function correlations over binuclear non-heme iron active sites, *JBIC, J. Biol. Inorg. Chem. 21*, Ahead of Print.

[53] Lindqvist, Y., Huang, W. J., Schneider, G., and Shanklin, J. (1996) Crystal structure of Δ^9 stearoyl-acyl carrier protein desaturase from castor seed and its relationship to other diiron proteins, *EMBO 15*, 4081-4092.

[54] Jia, C., Li, M., Li, J., Zhang, J., Zhang, H., Cao, P., Pan, X., Lu, X., and Chang, W. (2015) Structural insights into the catalytic mechanism of aldehyde-deformylating oxygenases, *Protein & Cell 6*, 55-67.

[55] Zocher, G., Winkler, R., Hertweck, C., and Schulz, G. E. (2007) Structure and action of the N-oxygenase AurF from *Streptomyces thioluteus*, *J. Mol. Biol. 373*, 65-74.

[56] Bailey, L. J., McCoy, J. G., Phillips, G. N., Jr., and Fox, B. G. (2008) Structural consequences of effector protein complex formation in a diiron hydroxylase, *Proc. Natl. Acad. Sci. USA 105*, 19194-19198.

[57] Dassama, L. M. K., Silakov, A., Krest, C. M., Calixto, J. C., Krebs, C., Bollinger, J. M., Jr., and Green, M. T. (2013) A 2.8 Å Fe-Fe separation in the Fe2III/IV intermediate (X) from *Escherichia coli* ribonucleotide reductase, *J. Am. Chem. Soc.*

[58] Fox, B. G., Shanklin, J., Somerville, C., and Münck, E. (1993) Stearoyl-acyl carrier protein Δ^9 desaturase from *Ricinus communis* is a diiron-oxo protein, *Proc. Natl. Acad. Sci. USA 90*, 2486-2490.

[59] Korboukh, V. K., Li, N., Barr, E. W., Bollinger, J. M., Jr., and Krebs, C. (2009) A long-lived, substrate-hydroxylating peroxodiiron(III/III) intermediate in the amine oxygenase, AurF, from *Streptomyces thioluteus*, *J. Am. Chem. Soc. 131*, 13608-13609.

[60] DeWitt, J. G., Bentsen, J. G., Rosenzweig, A. C., Hedman, B., Green, J., Pilkington, S., Papaefthymiou, G. C., Dalton, H., Hodgson, K. O., and Lippard, S. J. (1991) X-ray absorption, Mössbauer, and EPR studies of the dinuclear iron center in the hydroxylase component of methane monooxygenase, *J. Am. Chem. Soc. 113*, 9219-9235.

[61] Pereira, A. S., Small, W., Krebs, C., Tavares, P., Edmondson, D. E., Theil, E. C., and Huynh, B. H. (1998) Direct spectroscopic and kinetic evidence for the involvement of a peroxodiferric intermediate during the ferroxidase reaction in fast ferritin mineralization, *Biochemistry 37*, 9871-9876.

[62] Kutin, Y., Srinivas, V., Fritz, M., Kositzki, R., Shafaat, H. S., Birrell, J., Bill, E., Haumann, M., Lubitz, W., Högbom, M., Griese, J. J., and Cox, N. (2016) Divergent assembly mechanisms of the manganese/iron cofactors in R2lox and R2c proteins, *J. Inorg. Biochem. 162*, 164-177.

[63] Okamura, M. Y., Klotz, I. M., Johnson, C. E., Winter, M. R., and Williams, R. J. (1969) The state of iron in hemerythrin. A Mössbauer study, *Biochemistry 8*, 1951-1958.

[64] Makris, T. M., Chakrabarti, M., Münck, E., and Lipscomb, J. D. (2010) A family of diiron monooxygenases catalyzing amino acid beta-hydroxylation in antibiotic biosynthesis, *Proc. Natl. Acad. Sci. USA 107*, 15391-15396.

[65] Vu, V. V., Emerson, J. P., Martinho, M., Kim, Y. S., Münck, E., Park, M. H., and Que, L., Jr. (2009) Human deoxyhypusine hydroxylase, an enzyme involved in regulating cell growth, activates O_2 with a nonheme diiron center, *Proc. Natl. Acad. Sci. USA 106*, 14814-14819.

[66] Armstrong, G. D., and Sykes, A. G. (1986) Reactions of O_2 with hemerythrin, myoglobin, and hemocyanin: Effects of D_2O on equilibration rate constants and evidence for H-bonding, *Inorg. Chem. 25*, 3135-3139.

[67] Broadwater, J. A., Achim, C., Münck, E., and Fox, B. G. (1999) Mössbauer studies of the formation and reactivity of a quasi-stable peroxo intermediate of stearoyl-acyl carrier protein Δ(9)-desaturase, *Biochemistry. 38*, 12197-12204.

[68] Moenne-Loccoz, P., Baldwin, J., Ley, B. A., Loehr, T. M., and Bollinger, J. M., Jr. (1998) O_2 activation by non-heme diiron proteins: identification of a symmetric μ-1,2-peroxide in a mutant of ribonucleotide reductase, *Biochemistry 37*, 14659-14663.

[69] Lee, S. K., and Lipscomb, J. D. (1999) Oxygen activation catalyzed by methane monooxygenase hydroxylase component: Proton delivery during the O-O bond cleavage steps, *Biochemistry. 38*, 4423-4432.

[70] Liu, K. E., Wang, D., Huynh, B. H., Edmondson, D. E., Salifoglou, A., and Lippard, S. J. (1994) Spectroscopic detection of intermediates in the reaction of dioxygen with the reduced methane monooxygenase hydroxylase from *Methylococcus capsulatus* (Bath), *J. Am. Chem. Soc. 116*, 7465-7466.

[71] Spiro, T. G., and Czernuszewicz, R. S. (2003) Resonance Raman Spectroscopy, In *Physical Methods in Bioinorganic Chemistry* (Que Jr., L., Ed.), pp 59-120, University Science Books, Sausalito, CA.

[72] Liu, K. E., Valentine, A. M., Wang, D. L., Huynh, B. H., Edmondson, D. E., Salifoglou, A., and Lippard, S. J. (1995) Kinetic and spectroscopic characterization of intermediates and component interactions in reactions of

methane monooxygenase from *Methylococcus capsulatus* (Bath), *J. Am. Chem. Soc. 117*, 10174-10185.
[73] Dunn, J. B. R., Shriver, D. F., and Klotz, I. M. (1973) Resonance Raman studies of the electronic state of oxygen in hemerythrin, *Proc. Natl. Acad. Sci. USA 70*, 2582-2584.
[74] Song, W. J., and Lippard, S. J. (2011) Mechanistic studies of reactions of peroxodiiron(III) intermediates in T201 variants of toluene/o-xylene monooxygenase hydroxylase, *Biochemistry 50*, 5391-5399.
[75] Shiemke, A. K., Loehr, T. M., and Sanders-Loehr, J. (1986) Resonance Raman study of oxyhemerythrin and hydroxhemerythrin: Evidence for hydrogen bonding of ligands to the Fe-O-Fe center, *J. Am. Chem. Soc. 108*, 2437-2443.
[76] Sousa, C. M., Carpentier, P., Matias, P. M., Testa, F., Pinho, F., Sarti, P., Giuffrè, A., Bandeiras, T. M., and Romão, C. V. (2015) Superoxide reductase from *Giardia intestinalis*: structural characterization of the first SOR from a eukaryotic organism shows an iron centre that is highly sensitive to photoreduction, *Acta Crystallogr. D Biol. Crystallogr. 71*, 2236-2247.
[77] Gudmundsson, M., Kim, S., Wu, M., Ishida, T., Momeni, M. H., Vaaje-Kolstad, G., Lundberg, D., Royant, A., Ståhlberg, J., Eijsink, V. G. H., Beckham, G. T., and Sandgren, M. (2014) Structural and electronic snapshots during the transition from a Cu(II) to Cu(I) metal center of a lytic polysaccharide monooxygenase by X-ray photoreduction, *J. Biol. Chem. 289*, 18782-18792.
[78] Sigfridsson, K. G. V., Chernev, P., Leidel, N., Popovic-Bijelic, A., Gräslund, A., and Haumann, M. (2013) Rapid X-ray photoreduction of dimetal-oxygen cofactors in ribonucleotide reductase, *J. Biol. Chem. 288*, 9648-9661.
[79] Bailey, L. J., and Fox, B. G. (2009) Crystallographic and catalytic studies of the peroxide-shunt reaction in a diiron hydroxylase, *Biochemistry 48*, 8932-8939.
[80] Pozzi, C., Ciambellotti, S., Bernacchioni, C., Di Pisa, F., Mangani, S., and Turano, P. (2017) Chemistry at the protein–mineral interface in L-ferritin assists the assembly of a functional (μ^3-oxo)tris[(μ^2-peroxo)] triiron(III) cluster, *Proc. Natl. Acad. Sci. USA 114*, 2580-2585.
[81] Kovaleva, E. G., and Lipscomb, J. D. (2007) Crystal structures of Fe^{2+} dioxygenase superoxo, alkylperoxo, and bound product intermediates, *Science 316*, 453-457.
[82] Andersson, K. K., Froland, W. A., Lee, S.-K., and Lipscomb, J. D. (1991) Dioxygen independent oxygenation of hydrocarbons by methane monooxygenase hydroxylase component, *New J. Chem. 15*, 411-415.
[83] Banerjee, R., Proshlyakov, Y., Lipscomb, J. D., and Proshlyakov, D. A. (2015) Structure of the key species in the enzymatic oxidation of methane to methanol, *Nature 518*, 431-434.
[84] Moenne-Loccoz, P., Krebs, C., Herlihy, K., Edmondson, D. E., Theil, E. C., Huynh, B. H., and Loehr, T. (1999) The ferroxidase reaction of ferritin reveals a diferric μ-1,2 bridging peroxide intermediate in common with other O_2-activating non-heme diiron proteins, *Biochemistry 38*, 5290-5295.

[85] Roe, A. L., Schneider, D. J., Mayer, R. J., Pyrz, J. W., Widom, J., and Que, L., Jr. (1984) X-ray absorption spectroscopy of iron-tyrosinate proteins, *J. Am. Chem. Soc. 106*, 1676-1681.

[86] Broadwater, J. A., Ai, J., Loehr, T. M., Sanders-Loehr, J., and Fox, B. G. (1998) Peroxodiferric Intermediate of stearoyl-acyl carrier protein Δ^9 desaturase: Oxidase reactivity during single turnover and implications for the mechanism of desaturation, *Biochemistry 37*, 14664-14671.

[87] Shiemke, A. K., Loehr, T. M., and Sanders-Loehr, J. (1984) Resonance Raman study of the μ-oxo-bridged binuclear iron center in oxyhemerythrin, *J. Am. Chem. Soc. 106*, 4951-4956.

[88] Zang, Y., Kim, J., Dong, Y. H., Wilkinson, E. C., Appelman, E. H., and Que, L., Jr. (1997) Models for nonheme iron intermediates: Structural basis for tuning the spin states of Fe(TPA) complexes, *J. Am. Chem. Soc. 119*, 4197-4205.

[89] Kodera, M., Kawahara, Y., Hitomi, Y., Nomura, T., Ogura, T., and Kobayashi, Y. (2012) Reversible O–O bond scission of peroxodiiron(III) to high-spin oxodiiron(IV) in dioxygen activation of a diiron center with a bis-tpa dinucleating ligand as a soluble methane monooxygenase model, *J. Am. Chem. Soc. 134*, 13236-13239.

[90] Brunold, T. C., Tamura, N., Kitajima, N., Moro-Oka, Y., and Solomon, E. I. (1998) Spectroscopic study of $[Fe_2(O_2)(OBz)_2\{HB(pz')_3\}_2]$: Nature of the μ-1,2 peroxide-Fe(III) bond and Its possible relevance to O_2 activation by non-heme iron enzymes, *J. Am. Chem. Soc. 120*, 5674-5690.

[91] Kim, K., and Lippard, S. J. (1996) Structure and Mössbauer spectrum of a (μ-1,2-peroxo)bis(μ-carboxylato)diiron(III) model for the peroxo intermediate in the methane monooxygenase hydroxylase reaction cycle, *J. Am. Chem. Soc. 118*, 4914-4915.

[92] Kryatov, S., V., Taktak, S., Korendovych, I., V., Rybak-Akimova, E., V., Kaizer, J., Torelli, S., Shan, X., Mandal, S., MacMurdo, V., L., Mairata i Payeras, A., and Que, L., Jr. (2005) Dioxygen binding to complexes with $Fe(II)_2(\mu\text{-}OH)_2$ cores: Steric control of activation barriers and O_2-adduct formation, *Inorg. Chem. 44*, 85-99.

[93] Chavez, F., A., Ho, R., Y. N., Pink, M., Young, V., G., Jr., Kryatov, S., V., Rybak-Akimova, E., V., Andres, H., Münck, E., Que, L., Jr., and Tolman, W., B. (2002) Unusual peroxo intermediates in the reaction of dioxygen with carboxylate-bridged diiron(II,II) paddlewheel complexes, *Angew. Chem. 41*, 149-152.

[94] Ookubo, T., Sugimoto, H., Nagayama, T., Masuda, H., Sato, T., Tanaka, K., Maeda, Y., Okawa, H., Hayashi, Y., Uehara, A., and Suzuki, M. (1996) *cis*-μ-1,2-peroxo diiron complex: Structure and reversible oxygenation, *J. Am. Chem. Soc. 118*, 701-702.

[95] Dong, Y., Menage, S., Brennan, B. A., Elgren, T. E., Jang, H. G., Pearce, L. L., and Que, L., Jr. (1993) Dioxygen binding to diferrous centers. Models for diiron-oxo proteins, *J. Am. Chem. Soc. 115*, 1851-1859.

[96] Mizoguchi, T. J., Kuzelka, J., Spingler, B., DuBois, J. L., Davydov, R. M., Hedman, B., Hodgson, K. O., and Lippard, S. J. (2001) Synthesis and Spectroscopic Studies of Non-Heme Diiron(III) Species with a Terminal Hydroperoxide Ligand: Models for Hemerythrin, *Inorg. Chem. 40*, 4662-4673.

[97] Hayashi, Y., Kayatani, T., Sugimoto, H., Suzuki, M., Inomata, K., Uehara, A., Mizutani, Y., Kitagawa, T., and Maeda, Y. (1995) Synthesis, characterization, and reversible oxygenation of μ-alkoxo diiron(II) complexes with the dinucleating ligand *N*,*N*,*N*',*N*'-tetrakis{(6-methyl-2-pyridyl)methyl}-1,3-diamino-propan-2-olate, *J. Am. Chem. Soc. 117*, 11220-11229.

[98] Arii, H., Nagatomo, S., Kitagawa, T., Miwa, T., Jitsukawa, K., Einaga, H., and Masuda, H. (2000) A novel diiron complex as a functional model for hemerythrin, *J. Inorg. Biochem. 82*, 153-162.

[99] LeCloux, D. D., Barrios, A. M., Mizoguchi, T. J., and Lippard, S. J. (1998) Modeling the diiron centers of non-heme iron enzymes. Preparation of sterically hindered diiron(II) tetracarboxylate complexes and their reactions with dioxygen, *J. Am. Chem. Soc. 120*, 9001-9014.

[100] Zhao, M., Helms, B., Slonkina, E., Friedle, S., Lee, D., DuBois, J., Hedman, B., Hodgson, K. O., Frechet, J. M. J., and Lippard, S. J. (2008) Iron complexes of dendrimer-appended carboxylates for activating dioxygen and oxidizing hydrocarbons, *J. Am. Chem. Soc. 130*, 4352-4363.

[101] Shan, X., and Que, L., Jr. (2005) Intermediates in the oxygenation of a nonheme diiron(II) complex, including the first evidence for a bound superoxo species, *Proc. Natl. Acad. Sci. USA. 102*, 5340-5345.

[102] Dong, Y., Zang, Y., Kauffmann, K., Shu, L., Wilkinson, E. C., Münck, E., and Que, L., Jr. (1997) Models for nonheme diiron enzymes. Assembly of a high-valent $Fe_2(\mu\text{-}O)_2$ diamond core from its peroxo precursor, *J. Am. Chem. Soc. 119*, 12683-12684.

[103] Zhang, X., Furutachi, H., Fujinami, S., Nagatomo, S., Maeda, Y., Watanabe, Y., Kitagawa, T., and Suzuki, M. (2005) Structural and spectroscopic characterization of (μ-hydroxo or μ-oxo)(μ-peroxo)diiron(III) complexes: Models for peroxo intermediates of non-heme diiron proteins, *J. Am. Chem. Soc. 127*, 826-827.

[104] Kodera, M., Taniike, Y., Itoh, M., Tanahashi, Y., Shimakoshi, H., Kano, K., Hirota, S., Iijima, S., Ohba, M., and Okawa, H. (2001) Synthesis, characterization, and activation of thermally stable μ-1,2-peroxodiiron(III) complex, *Inorg. Chem. 40*, 4821-4822.

[105] Pap, J. S., Cranswick, M. A., Balogh-Hergovich, E., Barath, G., Giorgi, M., Rohde, G. T., Kaizer, J., Speier, G., and Que, L., Jr. (2013) An Iron(II)[1,3-bis(2'-pyridylimino)isoindoline] complex as a catalyst for substrate oxidation with H_2O_2 - Evidence for a transient peroxidodiiron(III) species, *Eur. J. Inorg. Chem. 2013*, 3858-3866.

[106] Murch, B. P., Bradley, F. C., and Que, L., Jr. (1986) A binuclear iron peroxide complex capable of olefin epoxidation, *J. Am. Chem. Soc. 108*, 5027-5028.

[107] Pap, J. S., Draksharapu, A., Giorgi, M., Browne, W. R., Kaizer, J., and Speier, G. (2014) Stabilisation of μ-peroxido-bridged Fe(III) intermediates with non-symmetric bidentate N-donor ligands, *Chem. Commun. 50*, 1326-1329.

[108] Duboc-Toia, C., Ménage, S., Ho, R. Y. N., Que, L., Lambeaux, C., and Fontecave, M. (1999) Enantioselective sulfoxidation as a probe for a metal-based mechanism in H_2O_2-dependent oxidations catalyzed by a diiron complex, *Inorg. Chem. 38*, 1261-1268.

[109] Dong, Y., Yan, S., Young, V. G., Jr., and Que, L., Jr. (1996) The crystal structure of a synthetic nonheme diiron-O_2 adduct: Insight into oxygen activation, *Angew. Chem. Int. Ed. 35*, 618-620.

[110] Cranswick, M. A., Meier, K. K., Shan, X., Stubna, A., Kaizer, J., Mehn, M. P., Münck, E., and Que, L., Jr. (2012) Protonation of a peroxodiiron(III) complex and conversion to a diiron(III/IV) intermediate: Implications for proton-assisted O-O bond cleavage in nonheme diiron enzymes, *Inorg. Chem. 51*, 10417-10426.

[111] Fiedler, A. T., Shan, X., Mehn, M. P., Kaizer, J., Torelli, S., Frisch, J. R., Kodera, M., and Que, L., Jr. (2008) Spectroscopic and computational studies of (μ -Oxo)(μ -1,2-peroxo)diiron(III) complexes of relevance to nonheme diiron oxygenase intermediates, *J. Phys. Chem. A 112*, 13037-13044.

[112] Frisch, J., R., Vu, V., V., Martinho, M., Münck, E., and Que, L., Jr. (2009) Characterization of two distinct adducts in the reaction of a nonheme diiron(II) complex with O_2, *Inorg. Chem. 48*, 8325-8336.

[113] Kodera, M., Tsuji, T., Yasunaga, T., Kawahara, Y., Hirano, T., Hitomi, Y., Nomura, T., Ogura, T., Kobayashi, Y., Sajith, P. K., Shiota, Y., and Yoshizawa, K. (2014) Roles of carboxylate donors in O-O bond scission of peroxodi-iron(III) to high-spin oxodi-iron(IV) with a new carboxylate-containing dinucleating ligand, *Chemical Science 5*, 2282-2292.

[114] Hummel, H., Mekmouche, Y., Duboc-Toia, C., Ho, R. Y. N., Que, L., Jr., Schunemann, V., Thomas, F., Trautwein, A. X., Lebrun, C., Fontecave, M., and Menage, S. (2002) A diferric peroxo complex with an unprecedented spin configuration: an S = 2 system arising from an S = 5/2, 1/2 pair, *Angew. Chem. Int. Ed. 41*, 617-620.

[115] Kodera, M., Ishiga, S., Tsuji, T., Sakurai, K., Hitomi, Y., Shiota, Y., Sajith, P. K., Yoshizawa, K., Mieda, K., and Ogura, T. (2016) Formation and high reactivity of the anti-dioxo form of high-spin μ-oxodioxodiiron(IV) as the active species that cleaves strong C−H bonds, *Chem.- Eur. J. 22*, 5924-5936.

[116] Bollinger, J. M., Jr., Krebs, C., Vicol, A., Chen, S., Ley, B. A., Edmondson, D. E., and Huynh, B. H. (1998) Engineering the diiron site of *Escherichia coli* ribonucleotide reductase protein R2 to accumulate an intermediate similar to H_{peroxo}, the putative peroxodiiron(III) complex from the methane monooxygenase catalytic cycle, *J. Am. Chem. Soc. 120*, 1094-1095.

[117] Jameson, G. N. L., Jin, W., Krebs, C., Perreira, A. S., Tavares, P., Liu, X., Theil, E. C., and Huynh, B. H. (2002) Stoichiometric production of hydrogen peroxide and

parallel formation of ferric multimers through decay of the diferric−peroxo complex, the first detectable intermediate in ferritin mineralization, *Biochemistry 41*, 13435-13443.

[118] MacMurdo, V. L., Zheng, H., and Que, L., Jr. (2000) Model for the Cofactor Formation Reaction of *E. coli* Ribonucleotide Reductase. From a Diiron(II) Precursor to an FeIIIFeIV Species via a Peroxo Intermediate, *Inorg. Chem. 39*, 2254-2255.

[119] Costas, M., Cady, C. W., Kryatov, S. V., Ray, M., Ryan, M. J., Rybak-Akimova, E. V., and Que, L., Jr. (2003) Role of carboxylate bridges in modulating nonheme diiron(II)/O2 reactivity, *Inorg. Chem. 42*, 7519-7530.

[120] LeCloux, D. D., Barrios, A. M., and Lippard, S. J. (1999) The reactivity of well defined diiron(III) peroxo complexes toward substrates: addition to electrophiles and hydrocarbon oxidation, *Bioorg. Med. Chem. 7*, 763-772.

[121] Worsdorfer, B., Lingaraju, M., Yennawar, N. H., Boal, A. K., Krebs, C., Bollinger, J. M., Jr., and Pandelia, M. E. (2013) Organophosphonate-degrading PhnZ reveals an emerging family of HD domain mixed-valent diiron oxygenases, *Proc. Natl. Acad. Sci. USA. 110*, 18874-18879.

[122] Rivard, B. S., Rogers, M. S., Marell, D. J., Neibergall, M. B., Chakrabarty, S., Cramer, C. J., and Lipscomb, J. D. (2015) Rate-determining attack on substrate precedes Rieske cluster oxidation during cis-dihydroxylation by benzoate dioxygenase, *Biochemistry 54*, 4652-4664.

[123] Capece, L., Lewis-Ballester, A., Yeh, S.-R., Estrin, D. A., and Marti, M. A. (2012) Complete reaction mechanism of indoleamine 2,3-dioxygenase as revealed by QM/MM simulations, *J. Phys. Chem. B 116*, 1401-1413.

[124] Komor, A. J., Rivard, B. S., Fan, R., Guo, Y., Que, L., Jr., and Lipscomb, J. D. (2016) Mechanism for six-electron aryl-N-oxygenation by the non-heme diiron enzyme CmlI, *J. Am. Chem. Soc. 138*, 7411-7421.

[125] He, J., Yao, X., and Vining, L. C. (2006) Cloning of the chloramphenicol biosynthesis genes of *Streptomyces venezuelae*-5230, *Shenyang Yaoke Daxue Xuebao 23*, 731-734.

[126] Vining, L. C., and Stuttard, C. (1995) Chloramphenicol, In *Biotechnology Series* (Vining, L. C., and Stuttard, C., Eds.), pp 505-530, Butterworth-Heinemann, Boston.

[127] Pacholec, M., Sello, J. K., Walsh, C. T., and Thomas, M. G. (2007) Formation of an aminoacyl-S-enzyme intermediate is a key step in the biosynthesis of chloramphenicol, *Org. Biomol. Chem. 5*, 1692-1694.

[128] Zhou, J., Gunsior, M., Bachmann, B. O., Townsend, C. A., and Solomon, E. I. (1998) Substrate binding to the alpha-ketoglutarate-dependent non-heme iron enzyme clavaminate synthase 2: coupling mechanism of oxidative decarboxylation and hydroxylation, *J. Am. Chem. Soc. 120*, 13539-13540.

[129] Ryle, M. J., Padmakumar, R., and Hausinger, R. P. (1999) Stopped-flow kinetic analysis of *Escherichia coli* taurine/alpha-ketoglutarate dioxygenase: Interactions with alpha-ketoglutarate, taurine, and oxygen, *Biochemistry 38*, 15278-15286.
[130] Hausinger, R. P. (2004) Fe(II)/alpha -ketoglutarate-dependent hydroxylases and related enzymes, *Crit. Rev. Biochem. Mol. Biol. 39*, 21-68.
[131] Bollinger, J. M., Jr., Price, J. C., Hoffart, L. M., Barr, E. W., and Krebs, C. (2005) Mechanism of taurine: alpha-ketoglutarate dioxygenase (TauD) from *Escherichia coli*, *Eur. J. Inorg. Chem. 2005*, 4245-4254.
[132] Wallar, B. J., and Lipscomb, J. D. (2001) Methane monooxygenase component B mutants alter the kinetics of steps throughout the catalytic cycle, *Biochemistry 40*, 2220-2233.
[133] Brazeau, B. J., and Lipscomb, J. D. (2003) Key amino acid residues in the regulation of soluble methane monooxygenase catalysis by component B, *Biochemistry 42*, 5618-5631.
[134] Zheng, H., and Lipscomb, J. D. (2006) Regulation of methane monooxygenase catalysis based on size exclusion and quantum tunneling, *Biochemistry 45*, 1685-1692.
[135] Davydov, R., Behrouzian, B., Smoukov, S., Stubbe, J., Hoffman, B. M., and Shanklin, J. (2005) Effect of substrate on the diiron(III) site in stearoyl acyl carrier protein Δ^9-desaturase as disclosed by cryoreduction electron paramagnetic resonance/electron nuclear double resonance spectroscopy., *Biochemistry 44*, 1309-1315.
[136] Yang, Y.-S., Baldwin, J., Ley, B. A., Bollinger, J. M., Jr., and Solomon, E. I. (2000) Spectroscopic and electronic structure description of the reduced binuclear non-heme iron active site in ribonucleotide reductase from *E. coli:* comparison to reduced Δ^9 desaturase and electronic structure contributions to differences in O_2 reactivity, *J. Am. Chem. Soc. 122*, 8495-8510.
[137] Solomon, E. I. (2001) Geometric and electronic structure contributions to function in bioinorganic chemistry: Active sites in non-heme iron enzymes, *Inorg. Chem. 40*, 3656-3669.
[138] Mitić, N., Schwartz, J. K., Brazeau, B. J., Lipscomb, J. D., and Solomon, E. I. (2008) CD and MCD studies of the effects of component B variant binding on the biferrous active site of methane monooxygenase, *Biochemistry 47*, 8386-8397.
[139] Vu, V. V., Makris, T. M., Lipscomb, J. D., and Que, L., Jr. (2011) Active-site structure of a β-hydroxylase in antibiotic biosynthesis, *J. Am. Chem. Soc. 133*, 6938-6941.
[140] Otwinowski, Z., and Minor, W. (1997) Processing of X-ray diffraction data collected in oscillation mode, *Methods Enzymol. 276*, 307-326.
[141] Murshudov, G. N., Skubak, P., Lebedev, A. A., Pannu, N. S., Steiner, R. A., Nicholls, R. A., Winn, M. D., Longa, F., and Vagin, A. A. (2011) REFMAC5 for the refinement of macromolecular crystal structures, *Acta Cryst. D67* 355-367.

[142] Emsley, P., Lohkamp, B., Scott, W. G., and Cowtan, K. (2010) Features and development of Coot, *Acta Cryst. D66*, 486-501.
[143] George, G. N. (1990) A suite of computer programs for analysis of X-ray absorption spectra, In *EXAFSPAK: A suite of computer programs for analysis of X-ray absorption spectra*.
[144] Ankudinov, A. L., Ravel, B., Rehr, J. J., and Conradson, S. D. (1998) Real-space multiple-scattering calculation and interpretation of x-ray-absorption near-edge structure, *Phys. Rev. B 58*, 7565-7576.
[145] Wojdyr, M. (2010) Fityk : a general-purpose peak fitting program, *J. Appl. Crystallogr. 43*, 1126-1128.
[146] Vergé, D., and Arrio-Dupont, M. (1981) Interactions between apoaspartate aminotransferase and pyridoxal 5'-phosphate. A stopped-flow study, *Biochemistry 20*, 1210-1216.
[147] de Groot, F. (2001) High-resolution X-ray emission and X-ray absorption spectroscopy, *Chem. Rev. 101*, 1779-1808.
[148] Scott, R. A. (2003) X-Ray Absorption Spectroscopy, In *Physical Methods in Bioinorganic Chemistry: Spectroscopy and Magnetism* (Que, L., Jr., Ed.), pp 465-503, University Science Books, Sausalito, CA.
[149] Whittington, D. A., and Lippard, S. J. (2001) Crystal structures of the soluble methane monooxygenase hydroxylase from *Methylococcus capsulatus* (Bath) demonstrating geometrical variability at the dinuclear iron active site, *J. Am. Chem. Soc. 123*, 827-838.
[150] Elango, N., Radhakrishnan, R., Froland, W. A., Wallar, B. J., Earhart, C. A., Lipscomb, J. D., and Ohlendorf, D. H. (1997) Crystal structure of the hydroxylase component of methane monooxygenase from *Methylosinus trichosporium* OB3b, *Protein Sci. 6*, 556-568.
[151] Eriksson, M., Jordan, A., and Eklund, H. (1998) Structure of *Salmonella typhimurium* nrdF ribonucleotide reductase in its oxidized and reduced forms, *Biochemistry 37*, 13359-13369.
[152] Holmes, M. A., and Stenkamp, R. E. (1991) Structures of met and azidomet hemerythrin at 1.66 Å resolution, *J. Mol. Biol. 220*, 723-737.
[153] Yoon, S., and Lippard, S. J. (2004) Water-dependent reactions of diiron(II) carboxylate complexes, *J. Am. Chem. Soc. 126*, 16692-16693.
[154] Mitra, M., Lloret-Fillol, J., Haukka, M., Costas, M., and Nordlander, E. (2014) Evidence that steric factors modulate reactivity of tautomeric iron-oxo species in stereospecific alkane C-H hydroxylation, *Chem. Commun. 50*, 1408-1410.
[155] Widger, L. R., Siegler, M. A., and Goldberg, D. P. (2013) Sulfide oxidation by O_2: Synthesis, structure and reactivity of novel sulfide-incorporated Fe(II) bis(imino)pyridine complexes, *Polyhedron 58*, 179-189.
[156] Zhang, Z.-T., and Cheng, X.-L. (2005) Hydrogen bonding and pi-pi stacking in hexaaquairon(II) bis(4',7-dimethoxyisoflavone-3'-sulfonate) octahydrate, *Acta cryst. C61*, m529-m531.

[157] Liang, Y., Li, W., and Guo, B.-J. (2005) Tetraaquabis(pyridine-3-carboxylato-κ N)iron(II), *Acta Cryst. E61*, m1782-m1784.
[158] Galet, A., Muñoz, M. C., Agustí, G., Martínez, V., Gaspar, A. B., and Real, J. A. (2005) Synthesis, crystal structure and magnetic properties of $[Fe(bpe)_4(H_2O)_2](TCNQ)_2$ (bpe = trans-1,2-bis(4-pyridyl)ethane and TCNQ = tetracyanoquinodimethane), *Z. Anorg. Allg. Chem. 631*, 2092-2095.
[159] Korendovych, I. V., Kryatov, S. V., Reiff, W. M., and Rybak-Akimova, E. V. (2005) Diiron(II) μ-aqua-μ-hydroxo model for non-heme iron sites in proteins, *Inorg. Chem. 44*, 8656-8658.
[160] Chaudhury, P., Wieghardt, K., Nuber, B., and Weiss, J. (1985) $[L_2Fe_2^{II}(\mu\text{-}OH)(\mu\text{-}CH_3CO_2)_2](ClO_4).H_2O$, a model compound for the diiron centers in deoxyhemerythrin, *Angew. Chem. Int. Ed. 24*, 778-779.
[161] Reem, R. C., and Solomon, E. I. (1984) MCD-EPR studies of deoxy[FeII,FeII]hemerythrin: probes of endogenous bridging ligands and exogenous ligand binding, *J. Am. Chem. Soc. 106*, 8323-8325.
[162] Shu, L., Broadwater, J. A., Achim, C., Fox, B. G., Münck, E., and Que, L., Jr. (1998) EXAFS and Mössbauer characterization of the diiron(III) site in stearyl-acyl carrier protein Δ^9-desaturase, *J. Biol. Inorg. Chem. 3*, 392-400.
[163] Rudd, D. J., Sazinsky, M. H., Merkx, M., Lippard, S. J., Hedman, B., and Hodgson, K. O. (2004) Determination by X-ray absorption spectroscopy of the Fe-Fe separation in the oxidized form of the hydroxylase of methane monooxygenase alone and in the presence of MMOD, *Inorg. Chem. 43*, 4579-4589.
[164] True, A. E., Scarrow, R. C., Randall, C. R., Holz, R. C., and Que, L., Jr. (1993) EXAFS studies of uteroferrin and its anion complexes, *J. Am. Chem. Soc. 115*, 4246-4255.
[165] Kovaleva, E. G., Neibergall, M. B., Chakrabarty, S., and Lipscomb, J. D. (2007) Finding intermediates in the O_2 activation pathways of non-heme iron oxygenases, *Acc. Chem. Res. 40*, 475-483.
[166] Wang, W., Liang, A. D., and Lippard, S. J. (2015) Coupling oxygen consumption with hydrocarbon oxidation in bacterial multicomponent monooxygenases, *Acc. Chem. Res. 48*, 2632-2639.
[167] Rosenzweig, A. C., Frederick, C. A., Lippard, S. J., and Nordlund, P. (1993) Crystal structure of a bacterial non-haem iron hydroxylase that catalyses the biological oxidation of methane, *Nature 366*, 537-543.
[168] Banerjee, R., Meier, K. K., Münck, E., and Lipscomb, J. D. (2013) Intermediate P* from soluble methane monooxygenase contains a diferrous cluster, *Biochemistry 52*, 4331-4342.
[169] Trehoux, A., Mahy, J.-P., and Avenier, F. (2016) A growing family of O_2 activating dinuclear iron enzymes with key catalytic diiron(III)-peroxo intermediates: Biological systems and chemical models, *Coord. Chem. Rev. 322*, 142-158.
[170] Lee, S. K., Nesheim, J. C., and Lipscomb, J. D. (1993) Transient intermediates of the methane monooxygenase catalytic cycle, *J. Biol. Chem. 268*, 21569-21577.

[171] Liu, Y., Nesheim, J. C., Lee, S.-K., and Lipscomb, J. D. (1995) Gating effects of component B on oxygen activation by the methane monooxygenase hydroxylase component, *J. Biol. Chem. 270*, 24662-246625.
[172] Brazeau, B. J., and Lipscomb, J. D. (2000) Kinetics and activation thermodynamics of methane monooxygenase compound Q formation and reaction with substrates, *Biochemistry 39*, 13503-13515.
[173] Yang, Y.-S., Broadwater, J. A., Pulver, S. C., Fox, B. G., and Solomon, E. I. (1999) Circular dichroism and magnetic circular dichroism studies of the reduced binuclear non-heme iron site of stearoyl-ACP Δ^9-desaturase: substrate binding and comparison to ribonucleotide reductase, *J. Am. Chem. Soc. 121*, 2770-2783.
[174] Schwartz, J. K., Wei, P.-p., Mitchell, K. H., Fox, B. G., and Solomon, E. I. (2008) Geometric and electronic structure studies of the binuclear nonheme ferrous active site of toluene-4-monooxygenase: Parallels with methane monooxygenase and insight into the role of the effector proteins in O_2 activation, *J. Am. Chem. Soc. 130*, 7098-7109.
[175] Kim, Y. S., Kang, K. R., Wolff, E. C., Bell, J. K., McPhie, P., and Park, M. H. (2006) Deoxyhypusine hydroxylase is a Fe(II)-dependent, HEAT-repeat enzyme. Identification of amino acid residues critical for Fe(II) binding and catalysis [corrected], *J. Biol. Chem. 281*, 13217-13225.
[176] Park, M. H. (2006) The post-translational synthesis of a polyamine-derived amino acid, hypusine, in the eukaryotic translation initiation factor 5A (eIF5A), *Biochem. J. 139*, 161-169.
[177] Saini, P., Eyler, D. E., Green, R., and Dever, T. E. (2009) Hypusine-containing protein eIF5A promotes translation elongation, *Nature 459*, 118-121.
[178] Gutierrez, E., Shin, B.-S., Woolstenhulme, C. J., Kim, J.-R., Saini, P., Buskirk, A. R., and Dever, T. E. (2013) eIF5A promotes translation of polyproline motifs, *Mol. Cell 51*, 35-45.
[179] Park, M. H., Nishimura, K., Zanelli, C. F., and Valentini, S. R. (2010) Functional significance of eIF5A and its hypusine modification in eukaryotes, *Amino Acids 38*, 491-500.
[180] Kaiser, A. (2012) Translational control of eIF5A in various diseases, *Amino Acids 42*, 679-684.
[181] Greganova, E., Altmann, M., and Bütikofer, P. (2011) Unique modifications of translation elongation factors, *FEBS J. 278*, 2613-2624.
[182] Skulan, A., J., Brunold, T., C., Baldwin, J., Saleh, L., Bollinger, J. M., Jr., and Solomon, E., I. (2004) Nature of the peroxo intermediate of the W48F/D84E ribonucleotide reductase variant: implications for O_2 activation by binuclear non-heme iron enzymes, *J. Am. Chem. Soc. 126*, 8842-8855.
[183] Krebs, C., Bollinger, J. M., Jr., Theil, E. C., and Huynh, B. H. (2002) Exchange coupling constant J of peroxodiferric reaction intermediates determined by Mössbauer spectroscopy, *J. Biol. Inorg. Chem. 7*, 863-869.

[184] Solomon, E. I., Brunold, T. C., Davis, M. I., Kemsley, J. N., Lee, S. K., Lehnert, N., Neese, F., Skulan, A. J., Yang, Y. S., and Zhou, J. (2000) Geometric and electronic structure/function correlations in non-heme iron enzymes, *Chem. Rev. 100*, 235-349.

[185] Shu, L. J., Liu, Y., Lipscomb, J. D., and Que, L., Jr. (1996) X-ray absorption spectroscopic studies of the methane monooxygenase hydroxylase component from *Methylosinus trichosporium* OB3b, *J. Biol. Inorg. Chem. 1*, 297-304.

[186] Sarangi, R. (2013) X-ray absorption near-edge spectroscopy in bioinorganic chemistry: Application to M-O_2 systems, *Coord. Chem. Rev. 257*, 459-472.

[187] Carson, E., C., and Lippard, S., J. (2006) Dioxygen-initiated oxidation of heteroatomic substrates incorporated into ancillary pyridine ligands of carboxylate-rich diiron(II) complexes, *Inorg. Chem. 45*, 837-848.

[188] Ou, C.-C., Lalancette, R. A., Potenza, J. A., and Schugar, H. J. (1978) Molecular structure and magnetic properties of μ-dihydroxo-bis[4-dimethylamino-2,6-pyridinedicarboxylatoaquoiron(III)]dihydrate, $[(CH_3)_2NC_7H_2NO_4(H_2O)FeOH]_2.2H_2O$, *J. Am. Chem. Soc. 100*, 2053-2057.

[189] Schmitt, W., Murugesu, M., Goodwin, J. C., Hill, J. P., Mandel, A., Bhalla, R., Anson, C. E., Heath, S. L., and Powell, A. K. (2001) Strategies for producing cluster-based magnetic arrays, *Polyhedron 20*, 1687-1697.

[190] Thich, J. A., Ou, C. C., Powers, D., Vasiliou, B., Mastropaolo, D., Potenza, J. A., and Schugar, H. J. (1976) Molecular structure and magnetic properties of μ-dihydroxo-bis[2,6-pyridinedicarboxylatoaquoiron(III)] and μ-dihydroxo-bis[4-hydroxo-2,6-pyridinedicarboxylatoaquoiron(III)] tetrahydrate, *J. Am. Chem. Soc. 98*, 1425-1433.

[191] Yoon, S., and Lippard Stephen, J. (2004) Synthesis and characterization of carboxylate-rich complexes having the [Fe2(mu-OH)2(mu-O2CR)]3+ and [Fe2(mu-O)(mu-O2CR)]3+ cores of O2-dependent diiron enzymes, *J. Am. Chem. Soc. 126*, 2666-2667.

[192] Makhlynets, O. V., Oloo, W. N., Moroz, Y. S., Belaya, I. G., Palluccio, T. D., Filatov, A. S., Müller, P., Cranswick, M. A., Que, L., and Rybak-Akimova, E. V. (2014) H_2O_2 activation with biomimetic non-haem iron complexes and AcOH: connecting the g = 2.7 EPR signal with a visible chromophore, *Chem. Commun. 50*, 645-648.

[193] Yoon, S., and Lippard, S. J. (2005) Water affects the stereochemistry and dioxygen reactivity of carboxylate-rich diiron(II) models for the diiron centers in dioxygen-dependent non-heme enzymes, *J. Am. Chem. Soc. 127*, 8386-8397.

[194] Riggs-Gelasco, P. J., Shu, L., Chen, S., Burdi, D., Huynh, B. H., Que, L., Jr., and Stubbe, J. (1998) EXAFS Characterization of the Intermediate X Generated During the Assembly of the Escherichia coli Ribonucleotide Reductase R2 Diferric Tyrosyl Radical Cofactor, *J. Am. Chem. Soc. 120*, 849-860.

[195] Yoon, S., Kelly, A. E., and Lippard, S. J. (2004) Di- and tetra-bridged diiron(II) complexes with four terphenyl-derived carboxylates and two water molecules, *Polyhedron 23*, 2805-2812.

[196] Turowski, P. N., Armstrong, W. H., Liu, S., Brown, S. N., and Lippard, S. J. (1994) Synthesis and characterization of a hydroxo-bridged diiron(III) complexes containing carboxylate or phosphate ester bridges: comparisons to diiron(III) proteins, *Inorg. Chem. 33*, 636-645.

[197] Shakya, R., Powell, D. R., and Houser, R. P. (2009) Unsupported μ-oxo- and μ-hydroxo-iron(III) dimers and mononuclear iron(III) complexes with pyridylbis(aminophenol) ligands, *Eur. J. Inorg. Chem. 2009*, 5319-5327.

[198] Jozwiuk, A., Ingram, A. L., Powell, D. R., Moubaraki, B., Chilton, N. F., Murray, K. S., and Houser, R. P. (2014) Redox and acid-base properties of asymmetric non-heme (hydr)oxo-bridged diiron complexes, *Dalton Trans. 43*, 9740-9753.

[199] Hazell, A., Jensen, K. B., McKenzie, C. J., and Toftlund, H. (1994) Synthesis and reactivity of (μ-oxo)diiron(III) complexes of tris(2-pyridylmethyl)amine. X-ray crystal structures of $[tpa(OH)FeOFe(H_2O)tpa](ClO_4)_3$ and $[tpa(Cl)FeOFe(Cl)tpa](ClO_4)_2$, *Inorg. Chem. 33*, 3127-3134.

[200] Dong, Y., Fujii, H., Hendrich, M. P., Leising, R. A., Pan, G., Randall, C. R., Wilkinson, E. C., Zang, Y., Que, L., Jr., Fox, B. G., Kauffmann, K., and Münck, E. (1995) A high-valent nonheme iron intermediate. Structure and properties of [Fe2(m-O)2(5-Me-TPA)2](ClO4)3, *J. Am. Chem. Soc. 117*, 2778-2792.

[201] Ogo, S., Wada, S., Watanabe, Y., Iwase, M., Wada, A., Harata, M., Jitsukawa, K., Masuda, H., and Einaga, H. (1998) Synthesis, structure, and spectroscopic properties of $[FeIII(tnpa)(OH)(PhCOO)]ClO_4$: A model complex for an active form of soybean lipoxygenase-1, *Angew. Chem. Int. Ed. 37*, 2102-2104.

[202] MacBeth, C. E., Gupta, R., Mitchell-Koch, K. R., Young, V. G., Lushington, G. H., Thompson, W. H., Hendrich, M. P., and Borovik, A. S. (2004) Utilization of hydrogen bonds to stabilize M-O(H) units: synthesis and properties of monomeric iron and manganese complexes with terminal oxo and hydroxo ligands, *J. Am. Chem. Soc. 126*, 2556-2567.

[203] Yamashita, M., Furutachi, H., Tosha, T., Fujinami, S., Saito, W., Maeda, Y., Takahashi, K., Tanaka, K., Kitagawa, T., and Suzuki, M. (2007) Regioselective arene hydroxylation mediated by a (μ-peroxo)diiron(III) complex: A functional model for toluene monooxygenase, *J. Am. Chem. Soc. 129*, 2-3.

[204] Celenligil-Cetin, R., Paraskevopoulou, P., Dinda, R., Staples, R. J., Sinn, E., Rath, N. P., and Stavropoulos, P. (2008) Synthesis, characterization, and reactivity of iron trisamidoamine complexes that undergo both metal- and ligand-centered oxidative transformations, *Inorg. Chem. 47*, 1165-1172.

[205] Mukherjee, J., Lucas, R. L., Zart, M. K., Powell, D. R., Day, V. W., and Borovik, A. S. (2008) Synthesis, structure, and physical properties for a series of monomeric iron(III) hydroxo complexes with varying hydrogen-bond networks, *Inorg. Chem. 47*, 5780-5786.

[206] Majumdar, A., and Lippard, S. J. (2013) Non-heme mononitrosyldiiron complexes: importance of iron oxidation state in controlling the nature of the nitrosylated products, *Inorg. Chem. 52*, 13292-13294.

[207] Majumdar, A., Apfel, U.-P., Jiang, Y., Moenne-Loccoz, P., and Lippard, S. J. (2014) Versatile reactivity of a solvent-coordinated diiron(II) compound: Synthesis and dioxygen reactivity of a mixed-valent FeIIFeIII species, *Inorg. Chem. 53*, 167-181.

[208] Armstrong, W. H., and Lippard, S. J. (1984) Reversible protonation of the oxo bridge in a hemerythrin model compound. Synthesis, structure, and properties of (μ-hydroxo)bis(μ-acetato)bis[hydrotris(1-pyrazolyl)borato]diiron(III) $[(HB(pz)_3)Fe(OH)(O_2CCH_3)_2Fe(HB(pz)_3)_2]^+$, *J. Am. Chem. Soc. 106*, 4632-4633.

[209] Scarrow, R. C., Maroney, M. J., Palmer, S. M., Que, L., Jr., Roe, A. L., Salowe, S. P., and Stubbe, J. (1987) EXAFS studies of binuclear iron proteins: Hemerythrin and ribonucleotide reductase, *J. Am. Chem. Soc. 109*, 7857-7864.

[210] Bai, Y., McCoy, J. G., Levin, E. J., Sobrado, P., Rajashankar, K. R., Fox, B. G., and Zhou, M. (2015) X-ray structure of a mammalian stearoyl-CoA desaturase, *Nature (London, U. K.) 524*, 252-256.

[211] Nordlund, P., and Eklund, H. (1993) Structure and function of the *Escherichia coli* ribonucleotide reductase protein R2, *J. Mol. Biol. 232*, 123-164.

[212] Guy, J. E., Whittle, E., Kumaran, D., Lindqvist, Y., and Shanklin, J. (2007) The crystal structure of the ivy Delta4-16:0-ACP desaturase reveals structural details of the oxidized active site and potential determinants of regioselectivity., *J. Biol. Chem. 282*, 19863-19871.

[213] Rardin, R. L., Tolman, W. B., and Lippard, S. J. (1991) Monodentate carboxylate complexes and the carboxylate shift: implications for polymetalloprotein structure and function, *New J. Chem. 15*, 417-430.

[214] Magnus, K. A., Hazes, B., Ton-That, H., Bonaventura, C., Bonaventura, J., and Hol, W. G. (1994) Crystallographic analysis of oxygenated and deoxygenated states of arthropod hemocyanin shows unusual differences, *Proteins 19*, 302-309.

[215] Kitajima, N., Fujisawa, K., Fujimoto, C., Morooka, Y., Hashimoto, S., Kitagawa, T., Toriumi, K., Tatsumi, K., and Nakamura, A. (1992) A new model for dioxygen binding in hemocyanin. Synthesis, characterization, and molecular structure of the μ–η^2:η^2 peroxo dinuclear copper(II) complexes, $[Cu(HB(3,5\text{-}R_2pz_3)]_2(O_2)$ (R = isopropyl and Ph)

J. Am. Chem. Soc. 114, 1277-1291.

[216] Lewis, E. A., and Tolman, W. B. (2004) Reactivity of dioxygen-copper systems, *Chem. Rev. 104*, 1047-1076.

[217] Funahashi, Y., Nishikawa, T., Wasada-Tsutsui, Y., Kajita, Y., Yamaguchi, S., Arii, H., Ozawa, T., Jitsukawa, K., Tosha, T., Hirota, S., Kitagawa, T., and Masuda, H. (2008) Formation of a bridged butterfly-type μ-η^2 :η^2 -peroxo dicopper core structure with a carboxylate group, *J. Am. Chem. Soc. 130*, 16444-16445.

[218] Xue, G., Fiedler, A. T., Martinho, M., Münck, E., and Que, L., Jr. (2008) Insights into the P-to-Q conversion in the catalytic cycle of methane monooxygenase from a synthetic model system, *Proc. Natl. Acad. Sci. USA 105*, 20615-20620.
[219] Xue, G., Geng, C., Ye, S., Fiedler, A. T., Neese, F., and Que, L., Jr. (2013) Hydrogen-bonding effects on the reactivity of [X-FeIII-O-FeIV=O (X = OH, F) complexes toward C-H bond cleavage, *Inorg. Chem. 52*, 3976-3984.
[220] Xue, G., De Hont, R., Münck, E., and Que, L., Jr. (2010) Million-fold activation of the [$Fe_2(\mu\text{-}O)_2$] diamond core for C-H bond cleavage, *Nat. Chem. 2*, 400-405.
[221] Siegbahn, P. E. M., and Crabtree, R. H. (1997) Mechanism of C-H activation by diiron methane monooxygenases: Quantum chemical studies, *J. Am. Chem. Soc. 119*, 3103-3113.
[222] Rinaldo, D., Philipp, D. M., Lippard, S. J., and Friesner, R. A. (2007) Intermediates in dioxygen activation by methane monooxygenase: A QM/MM study, *J. Am. Chem. Soc. 129*, 3135-3147.
[223] Murray, L. J., Garcia-Serres, R., Naik, S., Huynh, B. H., and Lippard, S. J. (2006) Dioxygen activation at non-heme diiron centers: characterization of intermediates in a mutant form of toluene/o-xylene monooxygenase hydroxylase, *J. Am. Chem. Soc. 128*, 7458-7459.
[224] Park, J. H., Dias, C. A. O., Lee, S. B., Valentini, S. R., Sokabe, M., Fraser, C. S., and Park, M. H. (2011) Production of active recombinant eIF5A: reconstitution in *E. coli* of eukaryotic hypusine modification of eIF5A by its coexpression with modifying enzymes, *Protein engineering, design & selection : PEDS 24*, 301-309.
[225] Lu, H. G., Chanco, E., and Zhao, H. M. (2012) CmlI is an N-oxygenase in the biosynthesis of chloramphenicol, *Tetrahedron 68*, 7651-7654.
[226] Fischbach, M. A., and Walsh, C. T. (2006) Assembly-line enzymology for polyketide and nonribosomal peptide antibiotics: Logic, machinery, and mechanisms, *Chem. Rev. 106*, 3468-3496.
[227] Walsh, C. T., Chen, H., Keating, T. A., Hubbard, B. K., Losey, H. C., Luo, L., Marshall, C. G., Miller, D. A., and Patel, H. M. (2001) Tailoring enzymes that modify nonribosomal peptides during and after chain elongation on NRPS assembly lines, *Curr. Opin. Chem. Biol. 5*, 525-534.
[228] Piraee, M., White, R. L., and Vining, L. C. (2004) Biosynthesis of the dichloroacetyl component of chloramphenicol in *Streptomyces venezuelae* ISP5230: Genes required for halogenation, *Microbiology 150*, 85-94.
[229] Sturgeon, B. E., Burdi, D., Chen, S., Huynh, B.-H., Edmondson, D. E., Stubbe, J., and Hoffman, B. M. (1996) Reconsideration of **X**, the diiron intermediate formed during cofactor assembly in *E. coli* ribonucleotide reductase, *J. Am. Chem. Soc. 118*, 7551-7557.
[230] Doan, P. E., Shanmugam, M., Stubbe, J., and Hoffman, B. M. (2015) Composition and structure of the inorganic core of relaxed intermediate X(Y122F) of *Escherichia coli ribonucleotide* reductase, *J. Am. Chem. Soc. 137*, 15558-15566.

[231] Han, W. G., and Noodleman, L. (2008) Structural model studies for the peroxo intermediate P and the reaction pathway from P-->Q of methane monooxygenase using broken-symmetry density functional calculations, *Inorg. Chem. 47*, 2975-2986.

[232] Menage, S., Brennan, B. A., Juarez-Garcia, C., Münck, E., and Que, L., Jr. (1990) Models for iron-oxo proteins: Dioxygen binding to a diferrous complex, *J. Am. Chem. Soc. 112*, 6423-6425.

[233] Song, W. J., Behan, R. K., Naik, S. G., Huynh, B. H., and Lippard, S. J. (2009) Characterization of a peroxodiiron(III) intermediate in the T201S Variant of toluene/o-xylene monooxygenase hydroxylase from *Pseudomonas sp.* OX1, *J. Am. Chem. Soc. 131*, 6074-6075.

[234] Chufan, E. E., Puiu, S. C., and Karlin, K. D. (2007) Heme-copper/dioxygen adduct formation, properties, and reactivity, *Acc. Chem. Res. 40*, 563-572.

[235] Naruta, Y., Sasaki, T., Tani, F., Tachi, Y., Kawato, N., and Nakamura, N. (2001) Heme-Cu complexes as oxygen-activating functional models for the active site of cytochrome c oxidase, *J. Inorg. Biochem. 83*, 239-246.

[236] Li, F., Van, H. K. M., Meier, K. K., Münck, E., and Que, L., Jr. (2013) Sc^{3+}-triggered oxoiron(IV) formation from O_2 and its non-heme iron(II) precursor via a Sc^{3+}-peroxo-Fe^{3+} intermediate, *J. Am. Chem. Soc. 135*, 10198-10201.

[237] Lee, Y.-M., Bang, S., Kim, Y. M., Cho, J., Hong, S., Nomura, T., Ogura, T., Troeppner, O., Ivanovic-Burmazovic, I., Sarangi, R., Fukuzumi, S., and Nam, W. (2013) A mononuclear nonheme iron(III)-peroxo complex binding redox-inactive metal ions, *Chem. Sci. 4*, 3917-3923.

[238] Menges, F. (2015) Spekwin32 - optical spectroscopy software, 1.72.0 ed.

[239] Sanders-Loehr, J., Wheeler, W. D., Shiemke, A. K., Averill, B. A., and Loehr, T. M. (1989) Electronic and Raman spectroscopic properties of oxo-bridge dinuclear iron centers in proteins and model compounds, *J. Am. Chem. Soc. 111*, 8084-8093.

[240] Wilkinson, E. C., Dong, Y. H., Zang, Y., Fujii, H., Fraczkiewicz, R., Fraczkiewicz, G., Czernuszewicz, R. S., and Que, L., Jr. (1998) Raman signature of the Fe_2O_2 "diamond" core, *J. Am. Chem. Soc. 120*, 955-962.

[241] Zheng, H., Zang, Y., Dong, Y., Young, V. G., Jr., and Que, L., Jr. (1999) Complexes with $Fe^{III}_2(\mu\text{-}O)(\mu\text{-}OH)$, $Fe^{III}_2(\mu\text{-}O)_2$, and $[Fe^{III}_3(\mu_2\text{-}O)_3]$ cores: Structures, spectroscopy, and core interconversions, *J. Am. Chem. Soc. 121*, 2226-2235.

[242] Xue, G., Wang, D., De Hont, R., Fiedler, A. T., Shan, X., Münck, E., and Que, L., Jr. (2007) A synthetic precedent for the $[Fe^{IV}_2(\mu\text{-}O)_2]$ diamond core proposed for methane monooxygenase intermediate Q, *Proc. Natl. Acad. Sci. USA 104*, 20713-20718.

[243] Norman, R. E., Yan, S., Que, L., Backes, G., Ling, J., Sanders-Loehr, J., Zhang, J. H., and O'Connor, C. J. (1990) (μ-Oxo)(μ-carboxylato)diiron(III) complexes with

distinct iron sites. Consequences of the inequivalence and its relevance to dinuclear iron-oxo proteins, *J. Am. Chem. Soc. 112*, 1554-1562.
[244] Zhang, X., Furutachi, H., Fujinami, S., Nagatomo, S., Maeda, Y., Watanabe, Y., Kitagawa, T., and Suzuki, M. (2005) Structural and spectroscopic characterization of (mu-hydroxo or mu-oxo)(mu-peroxo)diiron(III) complexes: models for peroxo intermediates of non-heme diiron proteins, *J. Am. Chem. Soc. 127*, 826-827.
[245] Chishiro, T., Shimazaki, Y., Tani, F., Tachi, Y., Naruta, Y., Karasawa, S., Hayami, S., and Maeda, Y. (2003) Isolation and crystal structure of a peroxo-bridged heme-copper complex, *Angew. Chem. Int. Ed. 42*, 2788-2791.
[246] Gavrilova, A. L., Qin, C. J., Sommer, R. D., Rheingold, A. L., and Bosnich, B. (2002) Bimetallic reactivity. One-site addition two-metal oxidation reaction of dioxygen with a bimetallic dicobalt(II) complex bearing five- and six-coordinate sites, *J. Am. Chem. Soc. 124*, 1714-1722.
[247] Kindermann, N., Dechert, S., Demeshko, S., and Meyer, F. (2015) Proton-induced, reversible interconversion of a μ-1,2-peroxo and a μ-1,1-hydroperoxo dicopper(II) complex, *J. Am. Chem. Soc. 137*, 8002-8005.
[248] Xing, G., Barr, E. W., Diao, Y., Hoffart, L. M., Prabhu, K. S., Arner, R. J., Reddy, C. C., Krebs, C., and Bollinger, J. M., Jr. (2006) Oxygen activation by a mixed-valent, diiron(II/III) cluster in the glycol cleavage reaction catalyzed by myo-inositol oxygenase, *Biochemistry 45*, 5402-5412.
[249] Oloo, W. N., Fielding, A. J., and Que, L., Jr. (2013) Rate-determining water-assisted O-O bond cleavage of an Fe(III)-OOH intermediate in a bio-inspired nonheme iron-catalyzed oxidation, *J. Am. Chem. Soc. 135*, 6438-6441.
[250] Liu, L. V., Hong, S., Cho, J., Nam, W., and Solomon, E. I. (2013) Comparison of high-spin and low-spin nonheme Fe(III)-OOH complexes in O-O bond homolysis and H-atom abstraction reactivities., *J. Am. Chem. Soc. 135*, 3286-3299.
[251] Biswas, A. N., Puri, M., Meier, K. K., Oloo, W. N., Rohde, G. T., Bominaar, E. L., Münck, E., and Que, L. (2015) Modeling TauD-J: A high-spin nonheme oxoiron(IV) complex with high reactivity toward C–H bonds, *J. Am. Chem. Soc. 137*, 2428-2431.
[252] Kodera, M., Itoh, M., Kano, K., Funabiki, T., and Reglier, M. (2005) A diiron center stabilized by a bis-TPA ligand as a model of soluble methane monooxygenase: Predominant alkene epoxidation with H_2O_2, *Angew. Chem. Int. Ed. 44*, 7104-7106.
[253] Company, A., Gómez, L., Fontrodona, X., Ribas, X., and Costas, M. (2008) A novel platform for modeling oxidative catalysis in non-heme iron oxygenases with unprecedented efficiency, *Chem.- Eur. J. 14*, 5727-5731.
[254] Lim, M. H., Rohde, J.-U., Stubna, A., Bukowski, M. R., Costas, M., Ho, R. Y. N., Münck, E., Nam, W., and Que, L., Jr. (2003) An FeIV=O complex of a tetradentate tripodal nonheme ligand, *Proc. Natl. Acad. Sci. USA. 100*, 3665-3670.

[255] Costas, M., and Que, L., Jr. (2002) Ligand topology tuning of iron-catalyzed hydrocarbon oxidations, *Angew. Chem. Int. Ed. 41*, 2179-2181.
[256] Kaizer, J., Klinker, E. J., Oh, N. Y., Rohde, J.-U., Song, W. J., Stubna, A., Kim, J., Münck, E., Nam, W., and Que, L., Jr. (2004) Nonheme FeIVO complexes that can oxidize the C-H bonds of cyclohexane at room temperature, *J. Am. Chem. Soc. 126*, 472-473.
[257] Hagen, K. S. (2000) Iron(II) triflate salts as convenient substitutes for perchlorate salts: Crystal structures of $[Fe(H_2O)_6](CF_3SO_3)_2$ and $Fe(MeCN)_4(CF_3SO_3)_2$, *Inorg. Chem. 39*, 5867-5869.
[258] Company, A., Prat, I., Frisch, J. R., Mas-Ballesté, D. R., Güell, M., Juhász, G., Ribas, X., Münck, D. E., Luis, J. M., Que, L., and Costas, M. (2011) Modeling the cis-oxo-labile binding site motif of non-heme iron oxygenases: Water exchange and oxidation reactivity of a non-heme iron(IV)-oxo compound bearing a tripodal tetradentate ligand, *Chem.- Eur. J. 17*, 1622-1634.
[259] Codolà, Z., Gómez, L., Kleespies, S. T., Que Jr, L., Costas, M., and Lloret-Fillol, J. (2015) Evidence for an oxygen evolving iron–oxo–cerium intermediate in iron-catalysed water oxidation, *Nat. Commun. 6*, 5865.
[260] Klinker, E. J., Jackson, T. A., Jensen, M. P., Stubna, A., Juhasz, G., Bominaar, E. L., Münck, E., and Que, L., Jr. (2006) A tosylimido analogue of a nonheme oxoiron(IV) complex, *Angew. Chem. Int. Ed. 45*, 7394-7397.
[261] Matthews, M. L., Krest, C. M., Barr, E. W., Vaillancourt, F. H., Walsh, C. T., Green, M. T., Krebs, C., and Bollinger, J. M., Jr. (2009) Substrate-triggered formation and remarkable stability of the C-H bond-cleaving chloroferryl intermediate in the aliphatic halogenase, SyrB2, *Biochemistry 48*, 4331-4343.
[262] Seth, S. K., Mandal, P. C., Kar, T., and Mukhopadhyay, S. (2011) A dinuclear oxo-bridged Fe(III) complex with tris(2-pyridylmethyl) amine: Structure and Hirshfeld surface analysis, *J. Mol. Struct. 994*, 109-116.
[263] Mandon, D., Machkour, A., Goetz, S., and Welter, R. (2002) Trigonal bipyramidal geometry and tridentate coordination mode of the tripod in $FeCl_2$ complexes with tris(2-pyridylmethyl)amine derivatives bis-α-substituted with bulky groups. Structures and spectroscopic comparative studies, *Inorg. Chem. 41*, 5364-5372.
[264] Sheng, X., Qiao, L., Qin, Y., Wang, X., and Wang, F. (2014) Highly efficient and quantitative synthesis of a cyclic carbonate by iron complex catalysts, *Polyhedron 74*, 129-133.
[265] Moreland, A. C., and Rauchfuss, T. B. (2000) Binding of π-acceptor ligands to (triamine)iron(II) complexes, *Inorg. Chem. 39*, 3029-3036.
[266] Benhamou, L., Machkour, A., Rotthaus, O., Lachkar, M., Welter, R., and Mandon, D. (2009) Regiospecific intramolecular O-demethylation of the ligand by action of molecular dioxygen on a ferrous complex: Versatile coordination chemistry of dioxygen in $FeCl_2$ complexes with (2,3-dimethoxyphenyl) α-substituted tripods in the tris(2-pyridylmethyl)amine series, *Inorg. Chem. 48*, 4777-4786.

[267] Thomas, C. M., Mankad, N. P., and Peters, J. C. (2006) Characterization of the terminal iron(IV) imides {[PhBP^{tBu2}(pz‘)]Fe^{IV}:NAd}$^{+}$, *J. Am. Chem. Soc. 128*, 4956-4957.

[268] Machkour, A., Mandon, D., Lachkar, M., and Welter, R. (2004) Easy preparation of the tris(2-fluoro-6-pyridylmethyl)amine ligand and instantaneous reaction of the corresponding dichloroferrous complex with molecular dioxygen: New access to dinuclear species, *Inorg. Chem. 43*, 1545-1550.

[269] Hay, B. P., and Custelcean, R. (2009) Anion−π interactions in crystal structures: Commonplace or extraordinary?, *Crystal Growth & Design 9*, 2539-2545.

[270] Kütt, A., Rodima, T., Saame, J., Raamat, E., Mäemets, V., Kaljurand, I., Koppel, I. A., Garlyauskayte, R. Y., Yagupolskii, Y. L., Yagupolskii, L. M., Bernhardt, E., Willner, H., and Leito, I. (2011) Equilibrium acidities of superacids, *J. Org. Chem. 76*, 391-395.

[271] Prakash, J., Rohde, G. T., Meier, K. K., Jasniewski, A. J., Van Heuvelen, K. M., Munck, E., and Que, L., Jr. (2015) Spectroscopic identification of an FeIII center, not FeIV, in the crystalline Sc-O-Fe adduct derived from [FeIV(O)(TMC)]$^{2+}$, *J. Am. Chem. Soc. 137*, 3478-3481.

[272] Jackson, T., A., Rohde, J.-U., Seo Mi, S., Sastri, C., V., DeHont, R., Stubna, A., Ohta, T., Kitagawa, T., Münck, E., Nam, W., and Que, L., Jr. (2008) Axial ligand effects on the geometric and electronic structures of nonheme oxoiron(IV) complexes, *J. Am. Chem. Soc. 130*, 12394-12407.

[273] Wang, D., Ray, K., Collins, M. J., Farquhar, E. R., Frisch, J. R., Gomez, L., Jackson, T. A., Kerscher, M., Waleska, A., Comba, P., Costas, M., and Que, L. (2013) Nonheme oxoiron(IV) complexes of pentadentate N5 ligands: spectroscopy, electrochemistry, and oxidative reactivity, *Chemical Science 4*, 282-291.

[274] England, J., Bigelow, J. O., Van Heuvelen, K. M., Farquhar, E. R., Martinho, M., Meier, K. K., Frisch, J. R., Munck, E., and Que, L. (2014) An ultra-stable oxoiron(IV) complex and its blue conjugate base, *Chemical Science 5*, 1204-1215.

[275] McDonald, A. R., and Que Jr, L. (2013) High-valent nonheme iron-oxo complexes: Synthesis, structure, and spectroscopy, *Coord. Chem. Rev. 257*, 414-428.

[276] Yosca, T. H., Rittle, J., Krest, C. M., Onderko, E. L., Silakov, A., Calixto, J. C., Behan, R. K., and Green, M. T. (2013) Iron(IV)hydroxide pK_a and the role of thiolate ligation in C–H bond activation by cytochrome P450, *Science 342*, 825-829.

[277] Hill, E. A., Weitz, A. C., Onderko, E., Romero-Rivera, A., Guo, Y., Swart, M., Bominaar, E. L., Green, M. T., Hendrich, M. P., Lacy, D. C., and Borovik, A. S. (2016) Reactivity of an Fe(IV)-oxo complex with protons and oxidants, *J. Am. Chem. Soc. 138*, 13143-13146.

[278] Briois, V., Lützenkirchen-Hecht, D., Villain, F., Fonda, E., Belin, S., Griesebock, B., and Frahm, R. (2005) Time-resolved study of the oxidation of ethanol by

cerium(IV) using combined quick-XANES, UV−Vis, and Raman spectroscopies, *J. Phys. Chem. A 109*, 320-329.
[279] Demars, T. J., Bera, M. K., Seifert, S., Antonio, M. R., and Ellis, R. J. (2015) Revisiting the solution structure of ceric ammonium nitrate, *Angew. Chem. Int. Ed. 54*, 7534-7538.
[280] Beineke, T. A., and Delgaudio, J. (1968) Crystal structure of ceric ammonium nitrate, *Inorg. Chem. 7*, 715-721.
[281] Costas, M., Tipton, A. K., Chen, K., Jo, D.-H., and Que, L., Jr. (2001) Modeling rieske dioxygenases: The first example of iron-catalyzed asymmetric cis-dihydroxylation of olefins, *J. Am. Chem. Soc. 123*, 6722-6723.
[282] Rohde, J.-U., Torelli, S., Shan, X., Lim Mi, H., Klinker Eric, J., Kaizer, J., Chen, K., Nam, W., and Que, L., Jr. (2004) Structural insights into nonheme alkylperoxoiron(III) and oxoiron(IV) intermediates by X-ray absorption spectroscopy, *J. Am. Chem. Soc. 126*, 16750-16761.
[283] Do, L. H., Xue, G., Que, L., and Lippard, S. J. (2012) Evaluating the identity and diiron core transformations of a (μ-oxo)diiron(III) complex supported by electron-rich tris(pyridyl-2-methyl)amine ligands, *Inorg. Chem. 51*, 2393-2402.
[284] Cicero, R. L., Zhao, D., and Protasiewicz, J. D. (1996) Polymorphism of ((tosylimino)iodo)-o-toluene: Two new modes of polymeric association for ArINTs, *Inorg. Chem. 35*, 275-276.